creative commons
COMMONS DEED

저작자표시-동일조건변경허락 2.0 대한민국

이용자는 아래의 조건을 따르는 경우에 한하여 자유롭게

- 이 저작물을 복제, 배포, 전송, 전시, 공연 및 방송할 수 있습니다.
- 이차적 저작물을 작성할 수 있습니다.
- 이 저작물을 영리 목적으로 이용할 수 있습니다.

다음과 같은 조건을 따라야 합니다:

저작자표시. 귀하는 원저작자를 표시하여야 합니다.

동일조건변경허락. 귀하가 이 저작물을 개작, 변형 또는 가공했을 경우에는, 이 저작물과 동일한 이용허락조건하에서만 배포할 수 있습니다.

- 귀하는, 이 저작물의 재이용이나 배포의 경우, 이 저작물에 적용된 이용허락조건을 명확하게 나타내어야 합니다.
- 저작권자로부터 별도의 허가를 받으면 이러한 조건들은 적용되지 않습니다.

저작권법에 따른 이용자의 권리는 위의 내용에 의하여 영향을 받지 않습니다.

이것은 이용허락규약(Legal Code)을 이해하기 쉽게 요약한 것입니다.

Disclaimer

dCollection

[UCI]I804:24011-200000240136

2010년 8월

박사학위 논문

Development of Bio Sensor Based on Porous Silicon and Silicon Nanomaterials

조 선 대 학 교 대 학 원

화 학 과

고 영 대

Development of Bio Sensor Based on Porous Silicon and Silicon Nanomaterials

다공성 실리콘과 실리콘 나노소재를 이용한 바이오 센서의 개발

2010년 8월 25일

조 선 대 학 교 대 학 원

화 학 과

고 영 대

Development of Bio Sensor Based on Porous Silicon and Silicon Nanomaterials

지도교수 손 홍 래

이 논문을 이학박사학위신청 논문으로 제출함.

2010년 4월

조 선 대 학 교 대 학 원

화 학 과

고 영 대

고영대의 박사학위논문을 인준함

위원장　전남대학교　교수　우 희 권 (인)

위　원　전남대학교　교수　정 현 담 (인)

위　원　조선대학교　교수　조 성 동 (인)

위　원　조선대학교　교수　고 문 주 (인)

위　원　조선대학교　교수　손 홍 래 (인)

2009년 6월

조 선 대 학 교　대 학 원

TABLE OF CONTENTS

TABLE OF CONTENTS	i
LIST OF SYMBOLS AND ABBREVIATIONS	viii
LIST OF TABLES	xi
LIST OF SCHEMES	xi
LIST OF FIGURES	xii
ABSTRACT	xi x

PART I. Electical and Optical Properties of Porous Silicon

CHAPTER ONE : INTRODUCTION OF POROUS SILICON

2

1.1 History of Porous Silicon 2

1.2 Electrochemical Preparation of Porous Silicon 4
1.2.1 Formation of Porous Silicon by Anodization 4
1.2.2 Electrochemical Etching Setup 7

1.3 Control of the Morphology and Porosity 9
1.3.1 Current Density 9
1.3.2 Concentration of Etching Solution and Anodization Time 15

1.4 Optical Properties of Porous Silicon 18
1.4.1 Substrate Properties 18
1.4.2 Refractive Index of Porous Silicon 19
1.4.3 Optical Properties and Bench Setup 20

1.5 Reference 23

CHAPTER TWO : FABRICATION AND OPTICAL CHARACTERIZATION OF FULL COLOR STOP BAND BASED ON RUGATE-STRUCTURED POROUS SILICON 26

2.1 Introduction 26

2.2 Experiments 28
2.2.1 Materials 28
2.2.2 Sample Preparation 28
2.2.3 Instrumentation and Data Acquisition 28

2.3 Results and Discussion 30
2.3.1 Effect of Etching Time 30
2.3.2 Effect of Frequency 33

2.4 Conclusions 37

2.5 References 38

CHAPTER THREE : OPTICAL CHARACTERIZATION OF DISTRIBUTED BRAGG REFLECTOR POROUS SILICON AND BAND FILTER APPLICATION 40

3.1 Introduction 40

3.2 Experiments 40
3.2.1 Materials 41
3.2.2 Preparation of DBR PSi 41
3.2.3 Instrumentation and Data Acquisition 42

3.3 Results and Discussion 43

3.4 Conclusions 50

3.5 References 51

CHAPTER FOUR : FABRICATION AND CHARACTERIZATION OF PRISMATIC BAND FILTER GRADIENT RUGATE POROUS SILICON 52

4.1 Introduction 52

4.2 Experiments 52
4.2.1 Materials 54
4.2.2 Preparation of ruagte PS using asymmetric electrode configuration 54
4.2.3 Instrumentation and Data Acquisition 54

4.3 Results and Discussion 56

4.4 Conclusions 61

4.5 References 62

CHAPTER FIVE : CHEMICAL SENSOR BASED ON POROUS SILICON DUAL TRANSDUCERS 63

5.1 Introduction 63

5.2 Experiments 62
5.2.1 Materials 65
5.2.2 Preparation and treatment of porous Si 65
5.2.3 Preparation of gas samples 66
5.2.4 Photoluminescence measurement 66
5.2.5 Reflectance measurement 67
5.2.6 Instrumentation and Data Acquisition 67

5.3 Results and Discussion 68

5.4 Conclusions 80

5.5 References 81

CHAPTER SIX : DBR PSI/PMMA COMPOSITE MATERIALS FOR SMART PATCH APPLICATION 83

6.1 Introduction 83

6.2 Experiments 85
6.2.1 Materials 85
6.2.2 Preparation of DBR PSi and DBR PSi/PMMA Composite Films 85
6.2.3 Instrumentation and Data Acquisition 86

6.3 Results and Discussion 87

6.4 Conclusions 96

6.5 References 97

CHAPTER SEVEN : SMART PARTICLES FOR NOBLE DRUG DELIVERY SYSTEM 98

7.1 Introduction 98

7.2 Experiments 101
7.2.1 Materials 101
7.2.2 Preparation of free-standing DBR 101
7.2.3 Chemical attachment of CPT to PSD surface and preparation of PSD-CPT smart particles 102
7.2.4 Instrumentation and Data Acquisition 102

7.3 Results and Discussion 104

7.4 Conclusions 116

7.5 References 117

CHAPTER EIGHT : SIMPLY MODIFIED BIOSENSOR FOR THE DETECTION OF HUMAN Ig-G BASED ON PROTEIN A-MODIFIED POROUS SILICON INTERFEROMETER 120

8.1 Introduction 120

8.2 Experiments 122
8.2.1 Materials 122
8.2.2 Preparation of rugate PSi Samples 122
8.2.3 Thermal Oxiadation of Rugate PSi 123
8.2.4 Functionalization of Oxidized Rugate PSi 123
5.2.5 Instrumentation and Data Acquisition 124

8.3 Results and Discussion 125

8.4 Conclusions 137

8.5 References 138

CHAPTER NINE : DETECTION OF AVIDIN BASED ON RUGATE-STRUCTURED POROUS SILICON INTERFEROMETER 140

9.1 Introduction 140

9.2 Experiments 142
9.2.1 Materials 142
9.2.2 Preparation of rugate PSi Samples 142
9.2.3 Thermal Oxiadation of Rugate PSi 143
9.2.4 Functionalization of Oxidized Rugate PSi 143
9.2.5 Instrumentation and Data Acquisition 144

9.3 Results and Discussion 145

9.4 Conclusions 158

9.5 References 159

CHAPTER TEN : FABRICATION OF ENCODED RUGATE POROUS SILICON INTERFEROMETER FOR BIOSENSOR 162

10.1 Introduction 162

10.2 Experiments 164
10.2.1 Materials 164
10.2.2 Preparation of rugate PSi Samples 164
10.2.3 Thermal Oxiadation of Rugate PSi 165
10.2.4 Functionalization of Oxidized Rugate PSi 165
10.2.5 Data Acquisition 166

10.3 Results and Discussion 167

10.4 Conclusions 178

10.5 References 179

CHAPTER ELEVEN : FABRICATION AND CHARACTERIZATION OF SURFACE-FUNCTIONALIZED DBR SMART PARTICLES FOR THE DETECTION OF BIO-MOLECULES 181

11.1 Introduction 181

11.2 Experiments 183
11.2.1 Preparation of DBR PSi Sample 183
11.2.2 Thermal Oxidation of Free-standing DBR PSi Film 183

11.2.3 Preparation of DBR Smart Particles..... 184
11.2.4 Synthesis of Biotin Tetrafluorophenyl Ester 184
11.2.5 ISurface Derivatization of Oxidized DBR Smart Particles..... 185
11.2.6 Instrumentation and data acquisition..... 185

11.3 Results and Discussion..... 186

11.4 Conclusions..... 197

11.5 References..... 198

PART II. FLUORESCENT SENSORS BASED ON NANOAGGREGATES

CHAPTER TWELVE : INTRODUCTION OF ORGANOSILICON CHEMISTRY 201

12.1 What is Organometallic Chemistry?..... 201

12.2 History of Organometallic Chemistry..... 202

12.3 Classification of Organometallic Chemistry..... 203

12.4 Organosilicon Chemistry..... 204
12.4.1 Organosilanes..... 204
12.4.2 Siloxides..... 205
12.4.3 Silyl Halides..... 206
12.4.4 Silyl Hydrides..... 207
12.4.5 Hydrosilylation..... 208
12.4.6 Silenes..... 208
12.4.7 Siloles..... 209

12.5 Introduction of Siloles..... 210
12.5.1 Unique Electronic Structure of Silole..... 210

12.5.2 Various Silole Derivatives..... 214

12.6 References..... 219

CHAPTER THIRTEEN : ENHANCEMENT OF PHOTOLUMINESCENCE EFFICIENCY OF POLYSILOLE BY AGGREGATION-INDUCED EMISSION 221

13.1 Introduction..... 221

13.2 Experiments..... 222

13.3 Results and Discussion..... 223

13.4 Conclusions..... 229

13.5 References..... 230

CHAPTER FOURTEEN : ENHANCEMENT OF PHOTOLUMINESCENCE EFFICIENCY OF POLYGERMOLE BY AGGREGATION-INDUCED EMISSION 232

14.1 Introduction..... 232

14.2 Experiments..... 234
14.2.1 Generals..... 234
14.2.2 Syntheses..... 235
14.2.2.1 Preparation of 1,1-dichloro-2,3,4,5-tetraphenylgermole **1**..... 235
14.2.2.2 Preparation of Polytetraphenylgermole **2**..... 235
14.2.2.3 Preparation of Polytetraphenylgermole Nanoaggregates **3**..... 236

14.3 Results and Discussion..... 237

14.4 Conclusions..... 243

14.5 References..... 244

CHAPTER FIFTEEN : DETECTION OF AVIDIN/STREPTAVIDIN BASED ON BIOTINLYTED SILOLE AND AGGREGATION-INDUCED EMISSION (AIE) 246

15.1 Introduction..... 246

15.2 Experiments..... 248
15.2.1 Generals..... 248
15.2.2 Syntheses..... 249
15.2.2.1 PPreparation of 1-methyl-1-hydro-2,3,4,5-tetraphenylsilole **1**..... 249
15.2.2.2 Preparation of 1-methyl-1-(3-amino)propyl-2,3,4,5-tetraphenylsilole **2**..... 249
15.2.2.3 Synthesis of Biotinlyted-silole **3**..... 249
15.2.24 Preparation of Biotinylated-silole Nanoaggregates **4**..... 251

15.3 Results and Discussion..... 252

15.4 Conclusions..... 261

15.5 References..... 262

ACKNOWLEDGMENTS 264

LIST OF SYMBOLS AND ABBREVIATIONS

PS	Porous silicon
TNT	Trinitrotoluene
HF	Hydrofluoric Acid
μm	Micrometer
%	Percent
m^3	Cubic Meter
c-Si	Crystalline Silicon
m	Mass
M	Molarity
NaOH	Sodium Hydroxide
FE-SEM	Field Emission-Scanning Electron Microscope
d	Density
CCD	Charge-Coupled Detector
A.U.	Arbitrary Units
PL	Photoluminescence
LED	Light Emitting Diode
Pt	Platinum
n	Refractive Index
Hz	Hertz
FWHM	Full-Width at Half-Maximum
nm	Nanometer
DBR	Distributed Bragg Reflector
BFG	Band Filter Gradient

THF	Tetrahydrofuran
FT-IR	Fourier Transform Infrared Spectroscopy
PSD	Porous Silicon Dioxide
CPT	Camptothecin
DMAP	4-di(methylamino)pyridine
DMEM	Dulbecco's Modified Eagle Medium
FBS	Fetal Bovine Serum
DMSO	Dimethyl Sulfoxide
UV-Vis	Ultraviolet-Visible
mA	Milliampere
mL	Milliliter
Ω	Ohm
XRD	X-ray Diffractometer
A_i	Amplitude
k_i	Frequency
λ	lambda
mmol	Millimole
PMMA	Polymethylmethacrylate
PSA	Particle Size Analyzer
TEM	Transmission Electron Microscope
SAED	Selected Area Electron Diffraction
SQUID	Superconducting Quantum Interference Device
MRI	Magnetic Resonance Imaging
Pt	Platinum
MER	Multi-encoded Rugate
PPR	Porous Polystyrene Replica

PBS	phosphate buffer solution
TOPO	Tri-*n*-octylphosphineoxide
V	Volume
㎍	Microgram
π	Pi
Al	Aluminium
ε	Epsilon
ν	Nu
δ	Delta
Mw	Molecular Weight
σ	Sigma
t	Time
B	current density
λ_{em}	Emission Wavelength
PMMA	Polymetylmetaacrylate
HATU	1-[bis(dimethylamino)methylene]-1H-1,2,3,-triazolo(4,5b)pyridinium 1hexafluorophosphate 3-oxide
DMF	Dimetylforamide
NMM	N-methylmorpholine

LIST OF TABLES

Table 2.1	Reflection band characteristics of 17 rugate PS samples according to the frequency change.
Table 3.1	Etching conditions and reflection peak of DBR PS samples.
Table 4.1	Data analysis of BFG rugate PS about the position of electrode.
Table 5.1	Change of OT and quenching photoluminescence under the exposure of different analytes..
Table 12.1	Organometallic chemistry timeline
Table 12.2	Classification of organometallic chemistry

LIST OF SCHEMES

Scheme 4.1	Schematic diagram of the electrochemical cell and electrode arrangement used to generate pore gradients.
Scheme 7.1	Schematic process for multi-encoded rugate CPT-derivatized PSD smart particle.
Scheme 7.2	Schematic process for CPT release
Scheme 8.1	The preparation process of the monolayer PSi biosensor

Scheme 8.2 The preparation process of 2-thiopyridone

Scheme 9.1 Synthesis of bio functionalized Porous Silicon

Scheme 9.2 The preparation process of 2-thiopyridone

Scheme 10.1 The preparation process of the multi encodede rugate biosensor

Scheme 12.1 Synthetic routes of silole and silole derivatives **1-9**

Scheme 12.2 Synthetic routes of silole and silole derivatives **10-17**

Scheme 12.3 Synthetic routes of silole and silole derivatives **18-23**

Scheme 14.1 Synthetic routes of compounds **1-3**

Scheme 15.1 Synthetic routes of compounds **1-3**

Scheme 15.2 Synthetic routes of compounds **4**

LIST OF FIGURES

Figure 1.1 Dissolution mechanism of crystalline silicon in hydrofluoric acid associated with the formation of porous silicon.

Figure 1.2 Experimental setup to produce porous silicon (left). Anodization is conducted under a constant current with the hydrofluoric acid electrolyte in the top of portion of the Teflon cell. The aluminum

foil serves as the anode and the platinum wire as the cathode (right).

Figure 1.3 Schematic of PS formation. Etching occurs only at the pore tips where the holes (h^+) are focused by the electric field.

Figure 1.4 PS porosity (A) and etch-rate (B) dependence versus current density for p-type crystalline silicon substrate anodized in 35% hydrofluoric acid concentration electrolyte.

Figure 1.5 Surface FE-SEM images of PS with different current densities.

Figure 1.6 Thickness of PS with different anodization time for p-type crystalline silicon substrates anodized at a fixed current density of 50 $mA/cm^{2.}$

Figure 1.7 Optical properties of porous silicon; PL (left) and reflectivity (right).

Figure 1.8 Optical bench setup for obtaining the optical properties of porous silicon.

Figure 2.1 The reflection resonances of rugate PS according to etching time from 200 to 400, 600, 800, and 1000 s.

Figure 2.2 Plot showing the relationship among the reflection wavelengths, the reflection intensities, and the etching times.

Figure 2.3 Connection of reflection spectra and FWHM about rugate PS samples.

Figure 2.4 Reflection spectra (A) and photograph (B) of 17 rugate PS samples.

Figure 3.1 Reflection wavelength of DBR PS samples.

Figure 3.2 Surface (A) and cross-sectional (B-1,2) FE-SEM images of DBR PS.

Figure 3.3 Reflection spectra (A) and photograph (B) of free-standing DBR PS.

Figure 3.4 Optical filter application using transparency of DBR PS film.

Figure 4.1 Photograph and reflection spectra of BFG rugate PS. The value position used refers to the distance from the position closest to the Pt counter electrode across the silicon wafer.

Figure 4.2 Surface and cross-section SEM images of BFG rugate PS. 0 mm (1), 5 mm (2), and 10 mm (3) refer to the distance from the position closest to the Pt counter electrode across the silicon wafer.

Figure 4.3 Profile of the change of reflection wavelength and film thickness of BFG rugate PS as a function of x represented to the distance from the position closest to the Pt counter electrode across the silicon wafer.

Figure 5.1 Surface (top) and cross-section (bottom) SEM image of prepared porous.

Figure 5.2 FT-IR (A) and reflectivity (blue line, B) and photoluminescence

(red line, B) spectra of prepared porous Si.

Figure 5.3 Shift of Fabry-Perot fringe pattern (A) and quenching photoluminescence spectra (B) under the exposure of organic vapors (Chloroform:●, n-Hexane:■, Methanol:◆, Benzene:▲, iso-propanol:▼ Toluene:⦿).

Figure 5.4 Plot for the relationship between the vapor pressure of analytes and quenching photoluminescence (%) (A), the vapor pressure of analytes and change of optical thickness (B).

Figure 5.5 2-D map resulting from the change quenching photoluminescence and change of optical thickness under the exposure of various organic analytes (Chloroform:●, n-Hexane:■, Methanol:◆, Benzene:▲, iso-propanol:▼ Toluene:⦿).

Figure 6.1 Reflectivity spectra of DBR PSi (dotted line) and DBR PSi/caffeine impregnated PMMA composite films (solid line).

Figure 6.2 Surface and cross-section SEM images of DBR PSi (A) and DBR PSi/caffeine-impregnated PMMA composite films (B).

Figure 6.3 Changes of reflection intensity (top) and reflection wavelength (bottom) of the composite films at the fixed wavelength of 547 nm in buffer solution (○; 10 repeats, □; 20 repeats,◇; 30 repeats).

Figure 6.4 Appearance of caffeine in buffer solution (pH=7) (○; 10 repeats, □; 20 repeats, ◇; 30 repeats).

Figure 7.1 Surface FE-SEM image of PSD-CPT smart particles.

Figure 7.2 Reflectivity spectra of fresh DBR PSi (solid line), DBR PSD film (dotted line), and CPT-derivatized PSD smart particles (bold dotted line).

Figure 7.3 Transmission-mode FT-IR spectra of fresh PSi sample (A), thermal oxidized PSi sample (B), and CPT-derivatized PSD sample (C)

Figure 7.4 Percent of CPT appearing in buffer solution as a function of time, measured by monitoring the UV-vis absorption band at 369 nm in the solution.

Figure 7.5 Correlation of the reflection wavelength and intensity to the concentration of drug appearing in buffer solution over a 6 h period.

Figure 8.1 Surface and cross-sectional FE-SEM image of PSi.

Figure 8.2 Fabry-Perot fringes in the reflection spectra of PSi.

Figure 8.3 Diffuse reflectance FT-IR spectra of (A) freshly etched PSi, (B) thermally oxidized PSi, (C) the wafer after functionalization of the PSi layer with (3-aminopropyl)trimethoxysilane, and (D) PSi functionalized with biotin.

Figure 8.4 Change of Fabry-Perot fringes in the reflection spectra of biotin-fuctionalized rugate PSi sample before (solid line) and after (dashed line) exposure of streptavidin (A), biotinylated protein A (B), and human Ig G (C) The dotted line in each case are the difference between spectra obtained in the presence and absence

of protein.

Figure 8.5 Change of optical thickness after addition of each protein.

Figure 9.1 Surface and cross-section SEM image of prepared rugate PSi.

Figure 9.2 Optical reflectivity spectrum of rugate PSi.

Figure 9.3 Diffuse reflectance FT-IR spectra of (A) a freshly etched p-type rugate PSi, (B) the wafer after 3 h oxidation with thermal, (C) the wafer after functionalization of the rugate PSi layer with (3-aminopropyl)trimethoxysilane, and (D) the wafer subsequent reaction of the surface with biotin.

Figure 9.4 Normalized areas of the υ(Si-H) (●), υ(OSi-H) (◆), υ(Si-O) (■), and υ(Si-OH) (▲) bands in the infrared spectrum as a function of thermal oxidation time. Areas of the υ(Si-H) were normalized by dividing by the area of the peaks at t = 0. Areas of the υ(OSi-H), υ(Si-O), and υ(Si-OH) peaks were normalized by dividing by the area of the respective peaks measured at t = 3 h.

Figure 10.1 Surface and cross-sectional FE-SEM image of triply encoded rugate PSi.

Figure 10.2 Optical reflective spectra of triply encoded rugate PSi.

Figure 10.3 Diffuse reflectance FT-IR spectra of (A) triply encoded rugate PSi, (B) thermally oxidized rugate PSi, (C) the wafer after functionalization of the rugate PSi layer with (3-aminopropyl)trimethoxysilane, and (D) rugate PSi functionalized

with biotin.

Figure 10.4 Optical reflection spectra of biotin-fuctionalized rugate PSi sample before (solid line) and after (dashed line) exposure of avidin(A) and streptavidin(B), The dotted line in each case are the difference between spectra obtained in the presence and absence of protein.

Figure 10.5 Plots for showing the detection limits of protein at 2 *pM* by using differential graph.

Figure 11.1 Surface and 3-dimensional images of DBR smart particle.

Figure 11.2 XRD patterns of MER PS film and a PPR

Figure 11.3 Schematic process for surface modification of DBR smart particles with biotin and silole groups.

Figure 11.4 Diffuse reflectance FT-IR spectra of (A) a freshly etched DBR smart particle, (B) oxidized DBR smart particle at 300 ℃ for 3 h, (C) functionalized DBR smart particle with (3-aminopropyl)trimethoxysilane, and (D) subsequent reaction of the surface with biotin.

Figure 11.5 Optical reflectivity spectra of fresh, oxidized, surface-functionalized, and biotin derivatized DBR smart particle.

Figure 11.6 Sensing of avidin and streptavidin based on biotin derivatized DBR smart particle in PBS.

Figure 12.1 Structures of silyl halides

Figure 12.2 Releative energy levels of the HOMO and LUMO for silole and cyclobutadiene, based on the HF/6-31G* calculations

Figure 12.3 Orbital correlation diagram for 1,1-dimethylsilole, based on the PM3 calculations

Figure 12.4 Shape of the HOMO and LUMO of silole and cyclopentadiene

Figure 13.1 Space filling model structure of polysilole

Figure 13.2 Photograph of polysilole in THF (10 mg/L, left) and polysilole nanoaggregates

Figure 13.3 Fluorescence spectra of polysilole aggregates in water-THF mixtures (% water from top; 99%, 90%, 80%, 70%, 60%, 50%)

Figure 13.4 Plot of the relative intensity of polysilole aggregates *vs* % water by volume

Figure 13.5 FE-SEM images of polysilole nanoparticles from (a) 90%, (b) 80%, and (c) 70% water fraction

Figure 14.1 Relative PL spectra and plots of the relative intensity of monomer, polymer, and polymer nanoaggregates

Figure 14.2 PL spectra of polygermole nanoaggregates in water-THF mixtures and plot of the relative intensity of polygermole nanoaggregates *vs* % water by volume.

Figure 14.3 Particle size distributions of polygermole nanoaggregates in the water/THF mixtures with (A) 90%, (B) 80%, and (C) 70%

Figure 14.4 FE-SEM images of polygermole nanoaggregates in the water/THF

mixtures with (A) 90%, (B) 80%, and (C) 70%

Figure 15.1 Absorption and Photoluminescence spectrum of Biotinylated-Silole

Figure 15.2 Comparison for PL Efficiency between Biotinylated-Silole and Nanoaggregate

Figure 15.3 PL spectra of Biotinylated-Silole Nanoaggregates in water-THF mixtures and Plot of the Relative Intensity of Biotinylated-Silole Nanoaggregates % Water by Volume

Figure 15.4 PSA Data of Biotinylated-Silole Nanoaggregate

Figure 15.5 Quenching of photoluminescence spectra of Biotinylated-Silole Nanoaggregate with Avidin, from top 3 *nM*, 6 *nM*, 9 *nM*, 12 *nM*, 15 *nM*.

Figure 15.6 Quenching of photoluminescence spectra of Biotinylated-Silole Nanoaggregate with Streptavidin, from top 3 *nM*, 6 *nM*, 9 *nM*, 12 *nM*, 15 *nM*

초 록

다공성 실리콘과 실리콘 나노소재를 이용한 바이오 센서의 개발

박사과정 : 고 영 대
지도교수 : 손 홍 래
조선대학교 화학과

현재 과학 기술은 과거의 과학 기술 발전 속도에 비해 대단히 빠른 속도로 발전하고 있다. 이중에서도 전기·전자 기술의 발달은 금속, 반도체 기술의 발전에 따라 최근 몇 십 년간 눈부신 발전을 이룩하였다. 현재 전자기술의 발전은 끊임없는 소자 크기의 감소를 통해 이루어지고 있으며, 이러한 경향은 전자 소자의 집적도 수준에서의 증가뿐만 아니라 동시에 소자 실행 속도의 증가라는 두 가지 목적을 두고 발전하였다. 하지만, 기존의 소자 기술은 이미 21세기 과학 및 기술의 요구를 충족하기 어려운 한계성이 예시되고 있으며, 당면한 문제점들을 해결하기 위한 새로운 형태 또는 크기를 갖는 소재가 필요하게 되었다. 이러한 요구 조건을 만족시킬 수 있는 새로운 21세기 연구 영역으로서 나노 과학(nanoscience)및 나노기술(nanotechnology)이 대두되고 있다. 나노 과학은 탄소 나노 튜브(CNT, carbon nanotube), C_{60}(buckyballs), 메조포러스 물질(mesoporous materials), 금속 및 반도체 나노 결정(nanocrystal, nanocluster, quantum dot) 등과 같은 물질 합성 분야와 STM, AFM, lithography를 통한 제어 및 응용 분야로 크게 두 가지로 분류 되고 있다. 특히, 화학 원리를 이용한 물질 합성 및 제어 나노 화학은 지난 수년간 괄목할 만한 획기적 연구가

진행되어 왔다. 나노 결정은 불연속적 전자 에너지 밀도를 가진 원자나 분자와 연속적 에너지 밴드를 가진 벌크 (bulk) 결정의 중간체이다. 따라서 나노 결정의 광학 및 전기적 성질은 벌크 결정 성질과 원자, 분자의 성질과는 다른 성질을 나타내게 된다. 이러한 나노 신소재 개발 분야는 기초과학에서부터 첨단과학까지의 융합학제 (interdisciplinary)간 학문 분야로 미래기술의 선점 및 국가경쟁력 확보에 있어서 우위를 차지하는데 중요한 역할을 할 것으로 기대된다.

따라서 본 연구논문의 주제는 나노화학 및 바이오센서 개발의 일환으로 반도체 실리콘 재료를 이용하여 생물학적 센서재료의 개발을 목표로 한다. 연구논문의 구성은 전반부에는 실리콘 웨이퍼를 전기화학적 식각을 통하여 얻어진 다공성 실리콘을 이용하여 면역단백질을 탐지하는 센서재료로 사용하였고, 후반부에는 실리콘 및 게르마늄이 함유된 광 발광성 유기금속 고분자 및 그 나노응집체 또는 나노입자를 통하여 Avidin과 Streptavin과 같은 생체분자를 탐지하는 센서재료로 사용하였다.

논문의 part I 에서 나노센서로 이용된 다공성 실리콘은 실리콘 나노구조물이며, 나노크기의 기공들이 존재하는 간섭 막들의 굴절률의 변화로부터 얻어지는 독특한 광학적 특성인 광 반사(optical reflection)성을 갖는다. 다공성 실리콘은 1950대에 Uhlir에 의해 실리콘 단결정을 전자연마 (electropolishing) 하다가 발견되었으며, 1990년대 다공성 실리콘의 효율적인 발광(luminescence)을 발견한 이래로, 이 분야는 화학·물리학적 광학 특성의 연구에 매우 광범위하게 이용되어지고 있다. 다공성 실리콘은 간섭 막의 굴절률 조절로 인해 가시광선 및 적외선 영역에서 특정한 파장에서 보강간섭을 갖는 반사 띠를 갖기 때문에 센서 등 여러 분야에 적용될 수 있는 좋은 소재이다. 또한, 바이오센서분야로 이용될 경우 분자인식현상 (molecular recognition event)으로 매 추가 분자를 인식할 때마다 신호를 적립할 수 있는 장점이 있어 인식체가 분자수준의 신호증폭 (molecular-level amplification)을 하게 된다. 따라서 선택성을 높이고 탐지한계를 낮추는 방법론을 개선하기위해 다양한 전기화학적 식각방법을 개발한다면 다른 나노소재보다 비교우의에 있을 것으로 사료된다. 본 연구논문의 결과로 다공성 실리콘 기공의 표면을 바이오틴으로 치환하게 되었을 경우 생체분자인 Avidin과 Streptavin을 10 *p*mol까지 감지 할 수 있었으며 감지도를 증가시키기 위하여 FT 변환을 하였고, 광원을 레이저를 사용하여 실험을 수행하였다.

논문의 part II 에서 나노센서로 이용된 유기금속 고분자 (Polymetallole)는 불포화 5각 고리에 실리콘이나 게르마늄으로 치환된 화합물의 고분자로서 최근에 그 독특한 광학적, 전자적 특성 때문에 유기전자 재료로서 흥미의 대상이 되어왔다. 이러한 독특한 성질들은 특히 광전자 기기에서 전자전달재료 (electron transporting materials)나 정공전달재료 (hole transporting materials), 발광재료 (light-emitting materials), 또는 화학적·생물학적 센서에 매우 유용하다. 최근 유기 발광재료들의 발광효율을 증가시키기 위한 연구는 매우 흥미의 대상이 되고 있는데 그 이유는 OLED (organic-light emitting diode)나 센서로서 응용할 경우 매우 중요하기 때문이다. 그러나 높은 발광성을 갖는 유기물이나 고분자는 고체 상태에서 덜 발광성을 갖는 종인 eximer의 형성으로 인한 분자의 응집으로 발광성의 감소를 발생한다. 이러한 단점을 극복하기위해 본 논문의 Chapters 13,14 에서는 실리콘과 게르마늄이 함유된 발광성 유기고분자가 응집된 고체 상태에서 발광효율이 오히려 더욱 증가하는 응집에 의해 유도되는 광 발광 (aggregation-induced emission, AIE라 부름)의 특성을 규명하였다. 상기에서와 같이 발광효율을 극대화시킨 유기금속이 함유된 고분자 나노응집체 (nanoaggregates)를 이용하여 생체분자인Avidin 과 Streptavind등을 탐지하였다. 본 연구결과로 인하여 폭발물 탐지 한계 (detection limit)는 약 3×10^{-12} M의 생체분자를 수분 이내로 감지하는 것이 가능하게 되었다.

최근 다공성 실리콘 및 AIE 의 광학적 특성을 이용한 여러 응용분야에 접목하는 연구가 광범위하게 진행되고 있으나, 아직 AIE 현상을 이용하는 바이오센서의 개발이 다른 분야에 비하여 상대적으로 연구가 미흡한 상태이다. AIE 현상을 이용한 바이오센서의 경우는 국내·외에서는 수행되지 않는 연구로써 처음으로 개발될 독창적인 연구이다. 본 연구는 다양한 학문 분야의 지식을 바탕으로 한 학제 간 융합학문 분야의 연구 결과로서 아직까지 정확히 확립되지 않은 나노센서, 나노바이오센서, 나노소재의 분석 및 그 응용과 관련된 중요한 정보를 구축하는데 크게 기여할 것으로 사료된다.

Part I.

Electical and Optical Properties of Porous Silicon

Chapter One
Introduction of Porous Silicon

1.1 History of Porous Silicon

The Porous silicon (PS) was first discovered by accident in 1956 by Arthur Uhlir Jr. and Ingeborg at the Bell laboratories in the U.S. At the time, Ulhir and Ingeborg were in the process of developing a technique for polishing and shaping the surfaces of silicon and germanium [1]. However, it was found that under several conditions a crude product in the form of thick black, red or brown film were formed on the surface of the material. At the time, the findings were not taken further and were only mentioned in Bell's labs technical notes.

Despite the discovery of porous silicon in the 1950's, the scientific community was not interested in porous silicon until the late 1980's. At the time, L. T. Canham first reported efficient, tunable, room temperature luminescence in the visible range from PS [2] that interest in the field grew exponentially. From this point on, a large number of academic and industrial researchers from all over the world began to study the PS pore structure [3,4], light emission mechanism [5,6], surface chemistry [7,8], and feasibility for optoelectronic applications [9].

The published result stimulated the interest of the scientific community in its non-linear optical and electrical properties. The growing interest was evidenced in the number of published work concerning the properties and potential applications of porous silicon. In an article published in 2000, it was found that the number of published work grew exponentially in between 1991 and 1995. The many favorable

characteristics and the vast interest in PS have given rise to a variety of new applications such as light emitting devices [10], multi-layer structure [11], solar energy conversion [12], chemical and biological sensors [13-18], drug delivery application [19], ultrasound generators [20], micro-engineering [21], astrophysics [22], signal processing [23], and nuclear science [24]. Due to these multi-functional applications of PS, recently it has been proposed to be an educational vehicle for introducing nano-technology and inter-disciplinary materials science by eminent scientists in the field [25].

In 2001, a team of scientists at the Technical University of Munich inadvertently discovered that hydrogenated porous silicon reacts explosively with oxygen at cryogenic temperatures, releasing several times as much energy as an equivalent amount of TNT, at a much greater speed (an abstract of the study can be found below). Explosion occurs because the oxygen, which is in a liquid state at the necessary temperatures, is able to oxidize through the porous molecular structure of the silicon extremely rapidly, causing a very quick and efficient detonation. Although hydrogenated porous silicon would probably not be effective as a weapon, due to its functioning only at low temperatures, other uses are being explored for its explosive properties, such as providing thrust for satellites.

1.2 Electrochemical Preparation of Porous Silicon

1.2.1 Formation of Porous Silicon by Anodization

PS can be produced in many different ways. One method of introducing pores in silicon is through the use of an anodization cell. A possible anodization cell employs platinum cathode and silicon wafer anode immersed in Hydrofluoric acid (HF) electrolyte. Corrosion of the anode is produced by running electrical current through the cell. It is noted that the running of constant DC current is usually implemented to ensure steady tip-concentration of HF resulting in a more homogenous porosity layer although pulsed current is more appropriate for the formation of thick silicon wafers bigger than 50 ㎛.

It was noted by Halimaoui that hydrogen evolution occurs during the formation of porous silicon - “When purely aqueous HF solutions are used for the PS formation, the hydrogen bubbles stick to the surface and induce lateral and in-depth inhomogeneity” [26]. The hydrogen evolution is normally treated with absolute ethanol in concentration exceeding 15%. It was found that the introduction of ethanol eliminates hydrogen and ensures complete infiltration of HF solution within the pores. Subsequently, uniform distribution of porosity and thickness is improved.

The extremely large surface to volume ratio (≥ 500 m^2/cm^3) of the PS nano-structures, the its easy formation and control of the surface morphology through variation of the formation parameters, its compatibility of silicon IC technology and hence amenability to the development of smart system-on-chip sensors-all these properties have made it to be a very attractive sensing material.

Although there is still some consideration regarding the surface dissolution mechanism, it is commonly agreed that holes are required for the dissolution

mechanism to begin. The required holes are present in p-type crystalline silicon, but they need to be supplied for the dissolution process to be initiated in n-type crystalline silicon. Illumination is the most common way for supplying holes.

In normal anodization conditions, the surface of crystalline silicon is inert against hydrofluoric acid at low pH values. In 1991, Lehmann and Gösele [27] proposed a reaction model of the dissolution chemistry for the formation of PS. This formation mechanism is illustrated in Figure 1.1. This model is well accepted and proposes that when silicon is under anodic bias and holes reach the surface, nucleophilic attack of the silicon-hydrogen bonds by fluorine ions occurs. This attack gives rise to a silicon-fluorine bond as shown in Figure 1.1. Once fluorine is attached, its large electro-negativity polarizes the structure making it possible for another fluorine ion to bond to the surface. During this process, an electron is ejected into the electrode and hydrogen is released. At this point, the large polarization of two silicon-fluorine bonds lower the electron density from the silicon-silicon bonds, making them weak and vulnerable for attack by hydrofluoric acid and water. This results in the removal of a silicon atom in the form of the soluble ion SiF_6^{2-} and leaves the remaining silicon atoms hydrogen terminated. The overall reaction can be expressed as follows [28]:

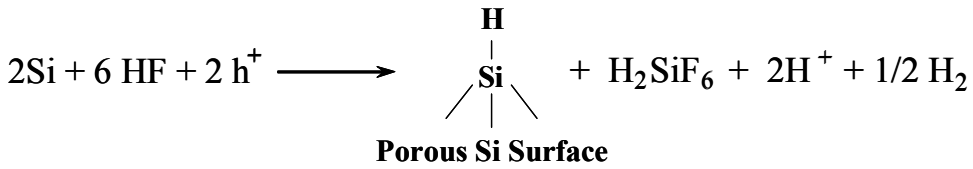

The removal of the silicon atom creates an atomic size dip or irregularity in the once atomically flat surface. The change in surface geometry concentrates the electric field lines on the irregularity site. PS pore formation and side-wall

dissolution will be inhibited by the depletion of holes. The depletion is caused by quantum confinement of charge carriers that results from the small dimensions of the pore walls. The quantum confinement increases the effective band-gap energy, making it more difficult for holes to enter the silicon region between the etched pores.

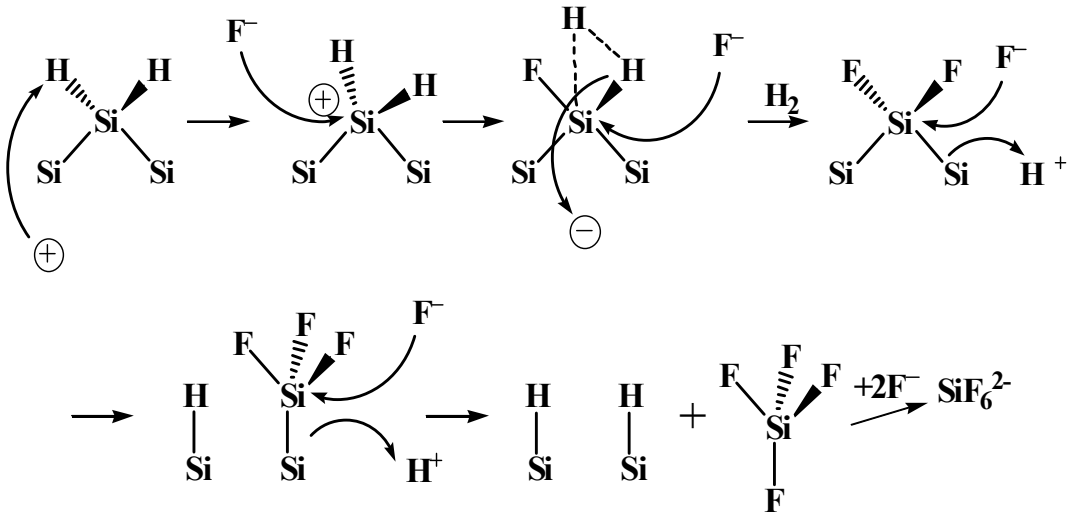

Figure 1.1. Dissolution mechanism of crystalline silicon in hydrofluoric acid associated with the formation of porous silicon.

1.2.2 Electrochemical Etching Setup

Figure 1.2 shows that a picture of experimental setup to produce PS. The anodization cell is made of Teflon, which is resistive against attack from the hydrofluoric acid electrolyte. The aluminum foil serves as the anode and it is sandwiched between the top and bottom parts of the Teflon cell. For a better contact, a platinum wire is placed against the silicon wafer where leads can be connected. The cathode is a circular platinum wire that is submerged in the hydrofluoric acid electrolyte. The cathode is held in place, three wing nuts hold the entire anodization cell together during the electrochemical etching process. The hydrofluoric acid electrolyte is placed inside the top part of the Teflon cell. Enough electrolyte must be present to supply the required fluorine ions and to cover the platinum wire cathode. The top part of the Teflon cell has a circular window of area 1.2 cm^2 which exposes the silicon to hydrofluoric acid and forms the PS. The entire electrochemical process is carried out under constant current supplied by a computer controlled Keithley 2420 power sourcemeter.

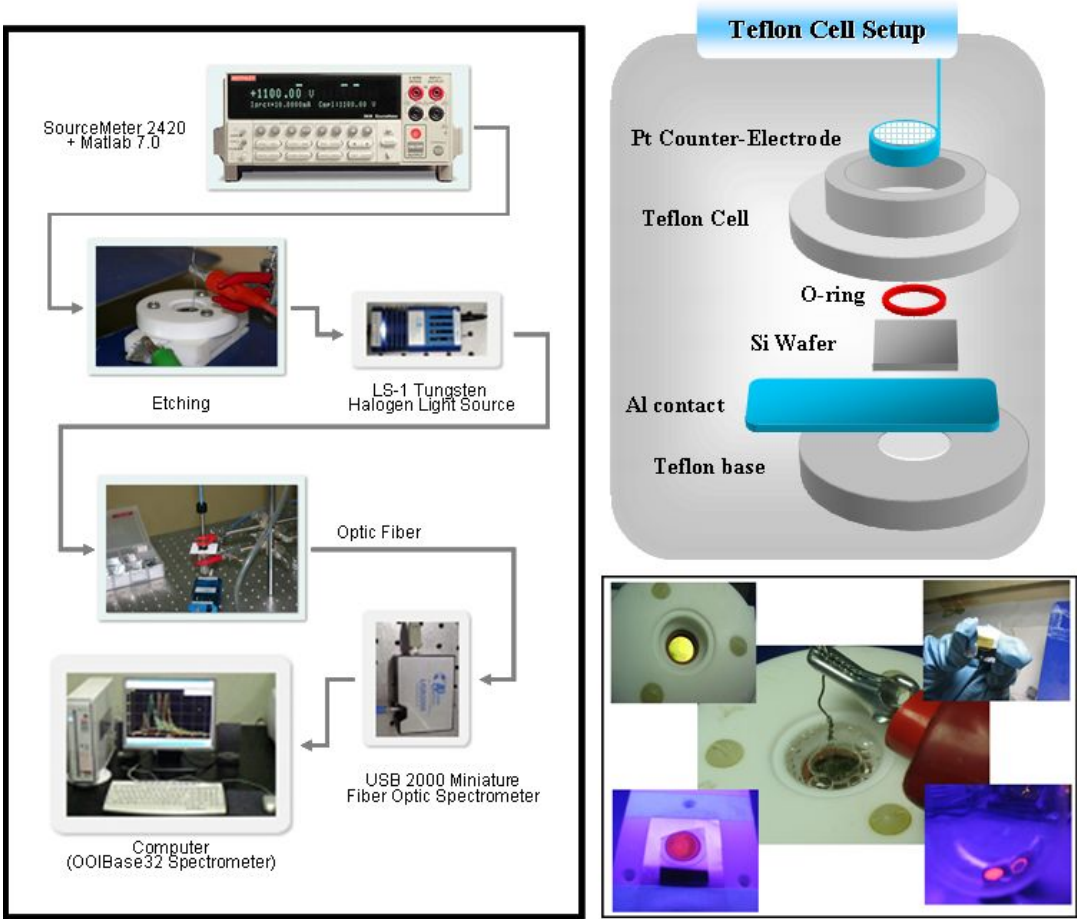

Figure 1.2. Experimental setup to produce porous silicon (left). Anodization is conducted under a constant current with the hydrofluoric acid electrolyte in the top of portion of the Teflon cell. The aluminum foil serves as the anode and the platinum wire as the cathode (right).

1.3 Control of the Morphology and Porosity

1.3.1 Current Density

The dissolution of silicon requires the presence of fluorine ions (F^-) and hole (h+). The pore initiation and growth mechanisms are qualitatively understood. Pore growth can be explained by several models, each one of which is more relevant in a specific regime of porosity and pore size [29-31]. IF the silicon/electrolyte interface becomes irregular shortly after etching starts, the surface fluctuations of the Si/electrolyte interface may either grow (PS formation) or disappear (electropolishing). A depletion region is formed in the thin PS layer itself and also in a region of the Silicon wafer near the PS/c-Si interface. In forward bias for p-type substrates, the holes can still reach the Si/electrolyte interface as the electric field lines are focused at the tip of the pores. Thus, holes will preferentially reach the Si/electrolyte interface deep in the pores, where etching will proceed rapidly (Figure 1.3). In contrast, no holes will reach the end of the Si rods, effectively stopping the etching there. In addition, if this electrostatic effect is not strong enough, the random walk of the holes toward the Si/electrolyte interface makes it more likely that they reach it at or near the pore's tip, resulting in an effect similar to the electrostatic one. When an n-type substrate is used, porous silicon formation takes place in reverse bias since holes are required for etching to proceed. Another important mechanism becomes predominant if the Si rods are narrow enough (typically much less than 10 nm). In this size regime, the electronic states start to differ from those of bulk silicon. When the motion of carriers is restricted in one or more dimensions, the holes in the valence band are pushed to lower energy by quantum confinement,

which produces a potential barrier to hole transport from the wafer to the Si rods. The holes can no longer drift or diffuse into the Si rods and further etching stops.

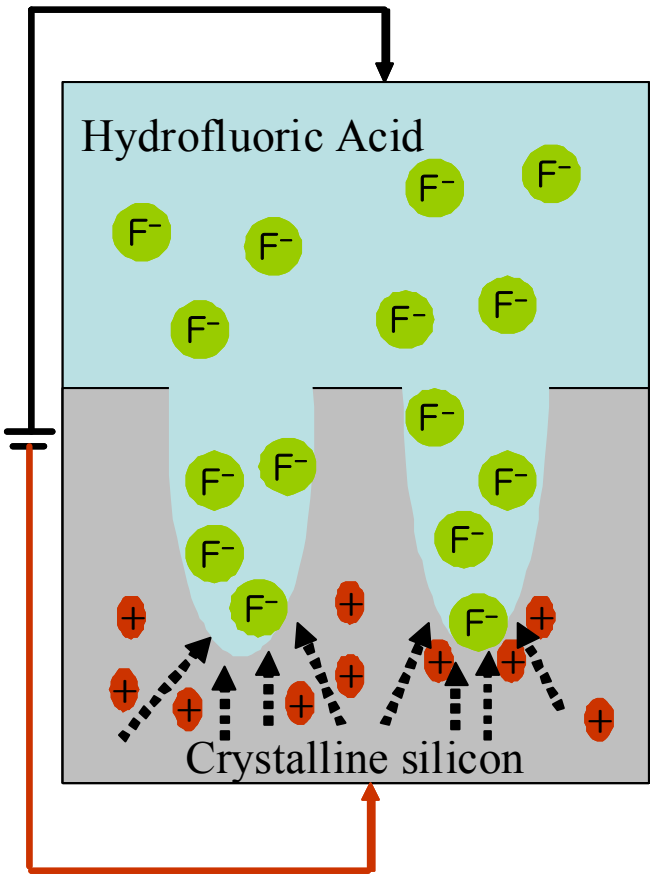

Figure 1.3. Schematic of PS formation. Etching occurs only at the pore tips where the holes (h^+) are focused by the electric field.

Pore formation occurs when the fluorine ions are delivered faster than the holes, the interpore regions of PS are depleted of holes, and further etching occurs only

at the pore tips. When the current density decreases, the number of holes at the pore tips drops, which leads to smaller pore sizes. Thus, the porosity (defined as the percentage of void space in the material) can be precisely controlled by the etching current density. As the current density increase, the silicon dissolution rate increases, resulting in a higher porosity and etching rate. Figure 1.4 shows that linear dependence of PS porosity and etching rate as a function of current density [32].

The most important quantity when characterizing a porous materials is the porosity which is defined as the ratio of the empty pore volume to the total volume. The porosity of a PS can be calculated gravimetrically using following equation [33]:

$$\textbf{Porosity (\%)} = \frac{m_1 - m_2}{m_1 - m_3}$$

Where m_1 is the mass of the initial silicon wafer in grams, m_2 is the mass of the silicon wafer after anodization in grams, m_3 is the mass of the silicon wafer after dissolution of the porous layer in grams. The dissolution of PS is performed using a 0.1 M aqueous solution of sodium hydroxide (NaOH).

This gravimetric method is applicable in cases where the PS layer is sufficiently thick (> 5 ㎛). The differnce in masses is larger than the amount of error induced in the measurements. However, when the PS layer is thin (< 200 nm), the mass difference is the same order of magnitude as the error in measurements, and the porosity value obtained is unreliable.

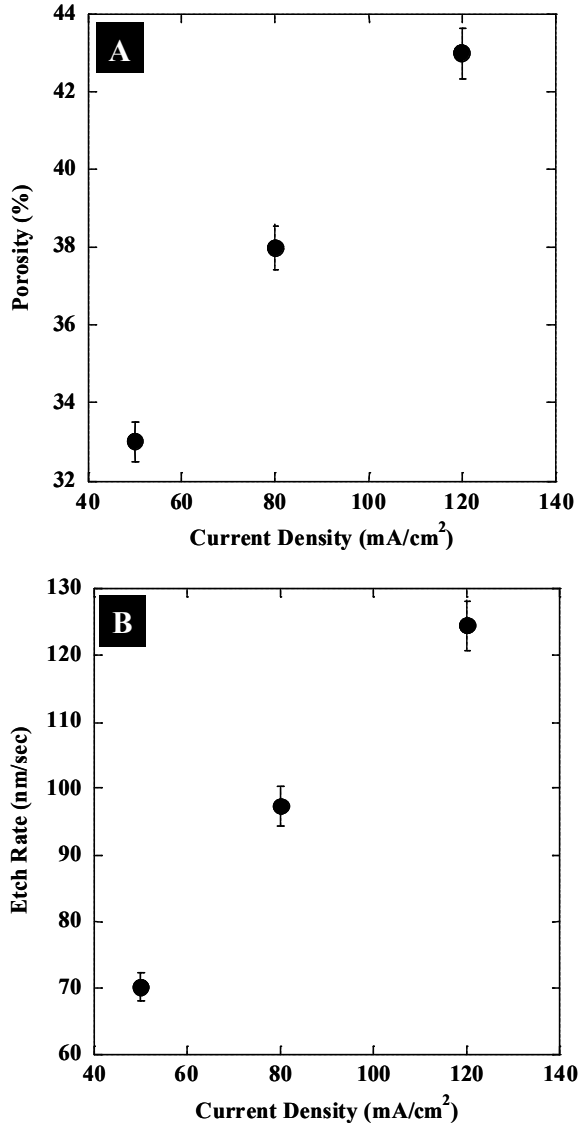

Figure 1.4. PS porosity (A) and etch-rate (B) dependence versus current density for p-type crystalline silicon substrate anodized in 35% hydrofluoric acid concentration electrolyte.

The size of pores formed during anodization is predominantly controlled by the current density [34], with an increase in the pore size corresponding to an increase in the current density. At low current densities, the pores are randomly directed. When the current density gradually increased, the diameter of PS pores increased. Figure 1.5 shows that surface images of etched PS with different current densities is measured by field emission-scanning electron microscope (FE-SEM, Hitachi-4800S).

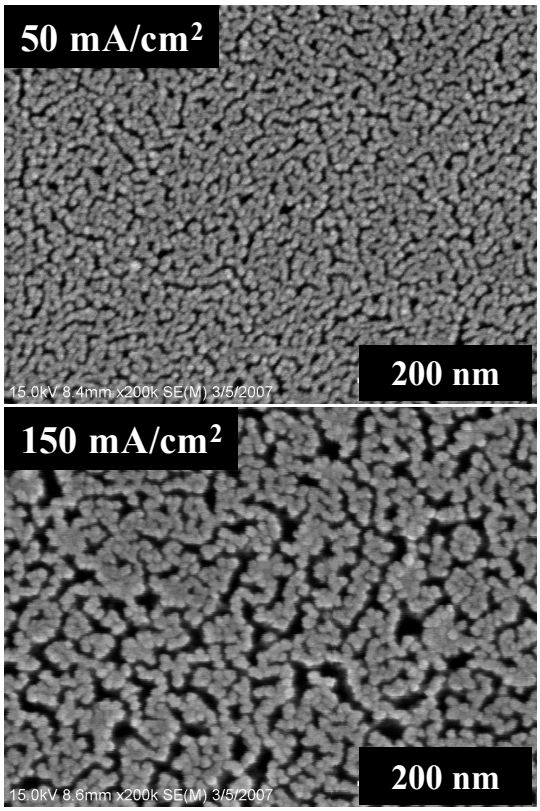

Figure 1.5. Surface FE-SEM images of PS with different current densities

1.3.2 Concentration of Etching Solution and Anodization Time

The composition of HF solution determines the etching process. In the anodization of PS, hydrofluoric acid with ethanol as an etchant solution is typically used. When aqueous HF solutions are used in the formation of PS, the hydrogen bubbles evolved stick to the surface. To improve the surface uniformity in PS, the hydrogen bubbles must be removed. The ethanol solution ensures the uniformity of the PS by removing the hydrogen bubbles from the PS surface and enables the HF penetration into the pores. Concentration of the hydrofluoric acid and etching time determine the PS porosity and thickness. For given time, porosity is inversely proportional to the HF concentration [35]. Therefore, lowering the HF concentration increase in the PS porosity. Since PS thickness is related to HF concentration, an increase in the HF concentration cause an increase in the PS thickness which in turn leads to a reduction of the PS porosity for a fixed time [36].

As the etching time is varied, the thickness and porosity of the PS layers change. Figure 1.6 shows that the thickness of the PS layer as a function of anodization time [37] for a p-type substrate that is etched at a constant current density of 50 mA/cm^2 in a 35% hydrofluoric acid solution. The figure shows a linear relationship between the etching time and the thickness of the PS layer.

The thickness of PS can be determined using either non-destructive or destructive techniques. One non-destructive technique is the use of an ellipsometer which requires the extensive understanding of the refractive index. For the PS samples, the index is difficult to determine since the porosity varies vertically with depth. There are two available destructive techniques that can be used with significant ease. One determines the approximate PS thickness using following equation:

$$\text{Thickness} = \frac{M_1 - M_3}{S \cdot d}$$

Where M_1 is the mass of the original silicon wafer, M_3 is the wafer with anodized material removed, S is the area of the PS sample, and d is the density of the silicon substrate.

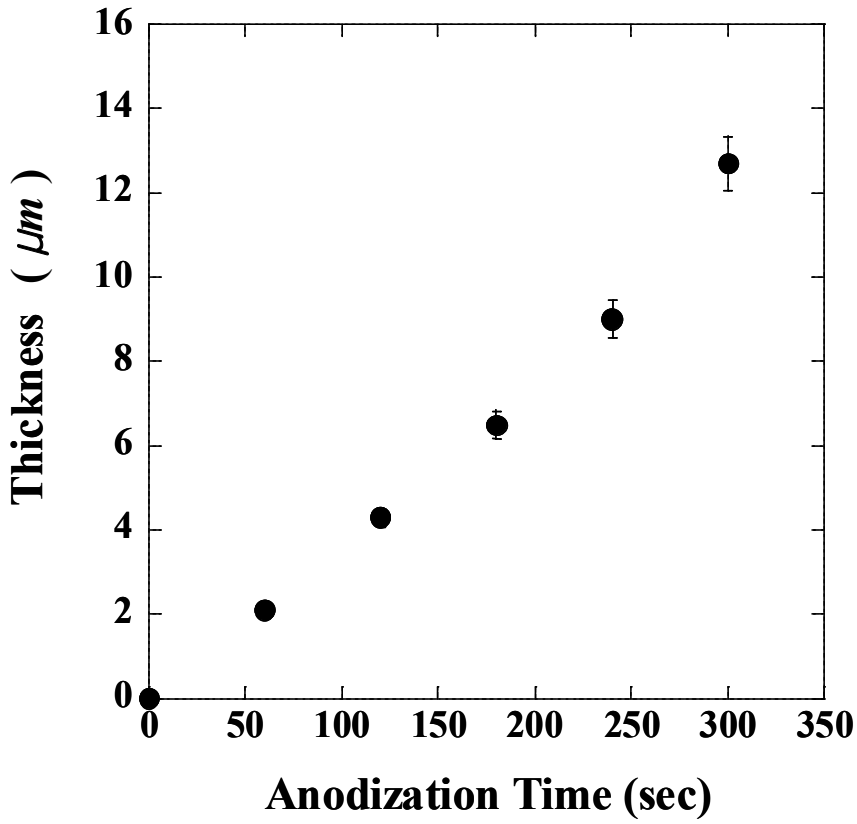

Figure 1.6. Thickness of PS with different anodization time for p-type crystalline silicon substrates anodized at a fixed current density of 50 mA/cm^2.

The second and more accurate technique uses a FE-SEM after scribing the PS sample to visualize a cross sectional view. This technique can resolve the thickness of PS to a few nanometers as well as provide additional information on the PS morphology.

1.4 Optical Properties of Porous Silicon

Some properties, such as porosity, refractive index, thickness, pore diameter, multi-structures, and optical properties, are strongly dependent on the anodization process parameters. These parameters include HF concentration, current density, anodization time, and silicon wafer type and resistivity.

1.4.1 Substrate Properties

Silicon substrates are identified by properties such as dopant type (i.e., n-type or p-type), substrate resistivity, dopant concentration, and substrate orientation. During anodization, dopant of the silicon substrate plays a significant role. Since holes (h^+) are the most important element in the chemical reaction leading to the formation of PS, the use of p-type wafer is the most popular. However, n-type wafer can be used with external illumination.

Substrate resistivity determines the achievable thickness of PS. For example, a very low resistivity wafer (<0.01 Ω-cm) is capable of producing thicker PS compared to a wafer with a higher resistivity (>10 Ω-cm) under same anodization conditions.

The morphology of the PS can be grouped into four categories based on doping concentration: p, p^+, p^{++}, n, n^+, and n^{++}. For p-type silicon wafer, the pore diameters and interpore spacing are very small (20-100 Å). As the dopant concentration increases, the pore diameter and spacing increase slightly (100-1000 Å). For n-type silicon, the pore diameters are considerably larger than those of the p-type substrate.

Substrate orientation is also important in the structure of the PS morphology. The main pore growth direction is essntially the same irrespective of the substrate orientation, dopant concentration or anodization conditions [38-39].

1.4.2 Refractive Index of Porous Silicon

The complex refractive index determines how light waves progagate inside a materials [40]. The refractive index is one of the important property of PS. This property controls the reflection and transmission of waves incident on the PS-air interface. There are many approximations that predict the refractive index of PS based on porosity [41-42]. However, none of them covers the entire porosity range with the same degree of high accuracy.

The refractive index of PS is calculated by using the Bruggeman approximation as described below :

$$(1\text{-}P)\frac{\varepsilon_{\text{Silicon}}+\varepsilon_{\text{porous silicon}}}{\varepsilon_{\text{Silicon}}+2\varepsilon_{\text{porous silicon}}}+(P)\frac{\varepsilon_{\text{air}}+\varepsilon_{\text{porous silicon}}}{\varepsilon_{\text{air}}+2\varepsilon_{\text{porous silicon}}}=0$$

where P is the porosity of porous silicon, $\varepsilon_{\text{silicon}}$ is the dielectric constant of silicon, ε_{air} is the dielectric constant of air, and $\varepsilon_{\text{porous silicon}}$ is the dielectric constant of porous silicon. The values of refractive indices for various porosities can be used to design PS layer stacks whose optical properies can be predicted quite accurately before production. It is clear that for any application of a material in optics or opto-electronics it is essential to know its refractive index.

1.4.3 Optical Properties and Bench Setup

The optical properties of PS are discussed in a wide spectral range from the infrared to the ultraviolet. PS has two optical properties such as photoluminescence (PL) for n-type with external illumination (300 W tungsten lamp) and optical reflectivity (Fabry-Pérot fringe) for p-type as shown in Figure 1.7. The ability of PS to emit and reflect in visible range is the most attractive property of the material. One explanation for the visible luminescence is based on the nanometer-size crystalline structure for PS [43-45].

PL spectrum of PS has been obtained with Ocean Optics LS-1 (blue LED). Optical reflectivity spectrum of PS showing Febry-Pérot fringe pattern has been measured by using tungsten-halogen lamp and an Ocean Optics S2000 charge-coupled detector (CCD) spectrometer fitted with a fiber optic input. The reflected light collection end of the fiber optic is positioned at the focal plane of the optical microscope as described in Figure 1.8.

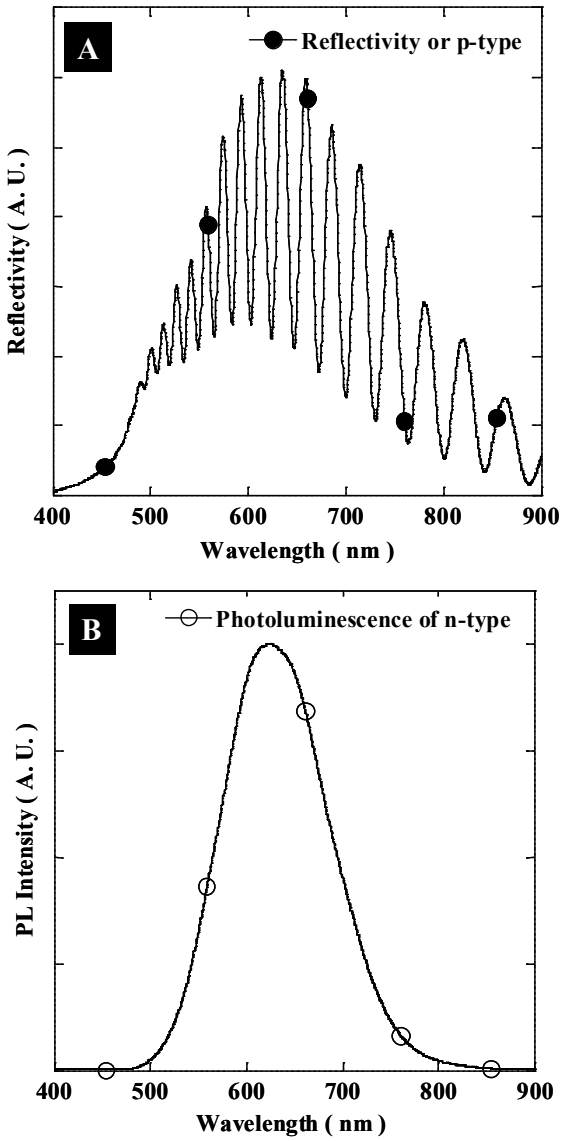

Figure 1.7. Optical properties of porous silicon; reflectivity (top) and photoluminescence (bottom).

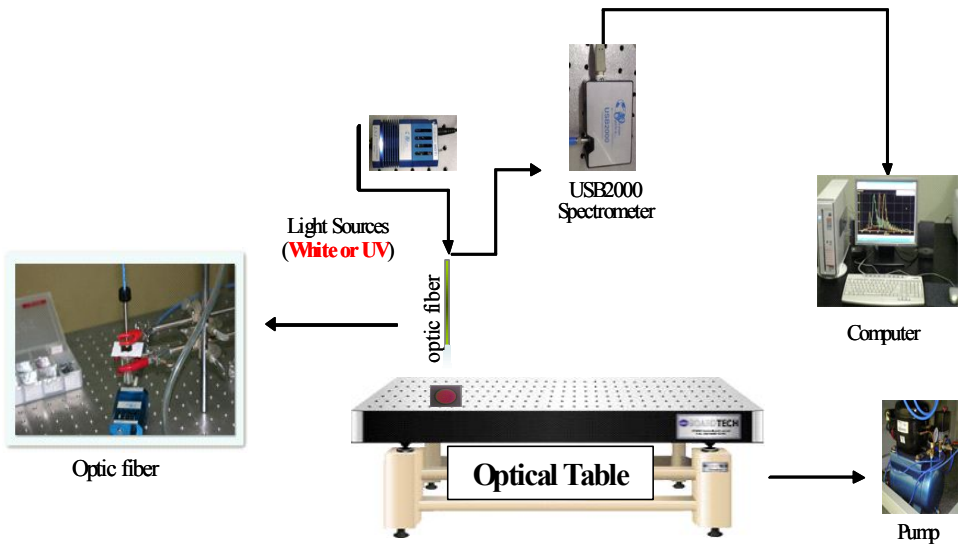

Figure 1.8. Optical bench setup for obtaining the optical properties of porous silicon

1.5 references

[1] A. Uhlir, "Electrolytic shaping of germanium and silicon," *Bell Syst. Tech. J.* **35**, 333-347 (1956).

[2] L. T. Canham, *Appl. Phys. Lett.* **57**, 1046 (1990).

[3] A. G. Cullis and L. T. Canham, *Nature* **353**, 335 (1991).

[4] Z. Sui, P. P. Leong, I. P. Herman, G. S. Higashi, and H. Temkin, *Appl. Phys. Lett.* **60**, 2086 (1992).

[5] C. Delerue, G. Allan, and M. Lannoo, *Phys. Rev. B* **48**, 11024 (1993).

[6] F. Koch, V. Petrova-koch, T. Muschik, A. nikolov, and V. Gavrilenko, *Mater. Res. Soc. Symp. Proc.* **298**, 319 (1993).

[7] E. J. Lee, T. W. Bitner, J. S. Ha, M. J. Shane, and M. J. Sailor, *J. Am. Chem. Soc.* **118**, 5375 (1996).

[8] J. M. Buriak and M. J. Allen, *J. Am. Chem. Soc.* **120**, 1339 (1998).

[9] A. Richter, P. steiner, F. Kozlowski, and W. Lang, *IEEE Electron Device Lett.* **12**, 691 (1991).

[10] K. D. Hirschmann, L. Tsybeskov, S. P. Duttagupta, and P. M. Fauchet, *Nature* **384**, 338 (1996).

[11] C. Mazzoleni and L. Pavesi, *Appl. Phys. Lett.* **67**, 2983 (1995).

[12] G. Smestad, M. Kunst, and C. Vial, *Sol. Energy Mater. Sol. Cells* **26**, 277 (1992).

[13] J. M. Lauerhaas and M. J. Sailor, *Science* **261**, 1567 (1993).

[14] H. Sohn, S. Letant , M. J. Sailor, and C. Trogler, *J. Am. Chem. Soc.* **122**, 5399 (2000).

[15] S. Letant and M. J. Sailor, *Adv. Mater.* **13**, 355 (2001).

[16] S. Chan, S. R. Horner, P. M. Fauchet, and B. L. Miller, *J. Am. Chem. Soc.* **123**, 11797 (2001).

[17] H. Sohn, R. M. Calhoun, M. J. Sailor, and W. C. Trogler, *Angew. Chem. Int. Ed.* **40**, 2104 (2001).

[18] H. Sohn, M. J. Sailor, D. magde, and W. C. Trogler, *J. Am. Chem. Soc.* **125**, 3821 (2003).

[19] X, Li, J. L. Coffer, Y. D. Chen, R. F. Pinizzotto, J. Newey, and L. T. Canham, *J. Am. Chem. Soc.* **120**, 11706 (1998).

[20] N. Koshida, T. Nakajima, M. Yoshiyama, K. Ueno, T. Nakagawa, and H. Shinoda, *Mater. Res. Soc. Symp. Proc.* **536**, 105 (1999).

[21] T. E. Bell, P. T. J. Gennissen, D. Demunter, and M. Kuhl, *J. Micromech. Microeng.* **6**, 361 (1996).

[22] V. G. Zubko , T. L. Smith, A. N. Witt, *Astrophys. J.* 501 (1998).

[23] V. P. Parkhutik, E. Matveeva, R. Perez, J. Alamo, and D. BeltraÂn, *Mater. Sci. Engn. B* **69-70**, 53 (2000).

[24] V. P. Bondarenko, Y. V. Bogatirev, J. P. Colinge, L. N. Dolgyi, A. M. Dorofeev, and V. A. Yakovtseva, *IEEE. Trans. Nucl. Sci.* **44**, 1719 (1997).

[25] V. P. Parkhutik and L. T. Canham, *Phys. Stat. Sol. A* **182**, 591 (2000).

[26] A. Halimaoui, "Porous silicon formation by anodisation," in Properties of Porous Silicon, L. Canham, ed., (INSPEC, London, UK, 1997) 12-22.

[27] V. Lehmann and U. Gösele, *Appl. Phys. Lett.* **58**, 856 (1991).

[28] M. J. Sailor, J. L. Heinrich, and J. M. Lauerhaas, *Stud. Surface Sci. Cat.* **103**, 209 (1996).

[29] R. L. Smith and S. D. Collins, *J. Appl. Phys.* **71**, R1 (1992).

[30] A. G. Cullis, L. T. Canham, and P. D. J. Calcott, *J. Appl. Phys.* **82**, 909 (1997).

[31] V. Lehmann, *Electrochemistry of Silicon*, Wiley-VCH Verlag, GmbH (2002).

[32] H. Ouyang, M. Christophersen, R. Viard, B. L. Miller, and P. M. Fauchet,

Adv. Funct. Mater. **15**, 1851 (2005).

[33] D. Brumhead, L. T. Canham, D. M. Seekings, and P. J. Tufton, *Electrochim. Acta*. **38**, 191 (1993).

[34] W. Theiss, *Surf. Sci. Rep.* **29**, 91 (1997).

[35] S. M. Hossain, J. Das, S. Chakraborty, S. K. Dutta, and H. Saha, *Semicon. Sci. Tech*. **17**, 55 (2002).

[36] I. K. Itotia and R. F. Drayton, *IEEE Antenn. Propag. Soc*. **2**, 663 (2003).

[37] A. Halimaoui, Porous Silicon Science and Technology, edited by J. C. Vial and J. Derrien, Springer-Verlag, New York, p. 33 (1995).

[38] M. Christopersen, J. Carstensen, and H. Foll, *Phys. Stat. Sol. A* **182**, 601 (2000).

[39] S.-F. Chuang, S. D. Collins, and R. L. Smith, *Appl. Phys. Lett.* **55**, 675 (1989).

[40] See e.g. J. D. Jackson, *Classical Electrodynamics*, John Wiley & Sons, New York (1975).

[41] D. J. Bergman, *Phys. Rep. C* **43**, 377 (1978).

[42] H. Looyenga, *Physica* **31**, 401 (1965).

[43] S. Sawada, N. Hamada, N. Ookubo, *Phys. Rev. B* **49**, 5236 (1994).

[44] A. J. Read, R. J. Needs, K. J. Nash, L. T. Canham, P. D. J. Calcott, and A. Qteish, *Phys. Rev. Lett.* **69**, 1232 (1992).

[45] Y. Kanemitsu, H. Uto, Y. Masumoto, T. Futagi, and H. Mimura, *Phys. Rev. B* **48**, 2827 (1993).

Chapter Two

Fabrication and Optical Characterization of Full Color Stop Band Based on Rugate-Structured Porous Silicon

2.1 Introduction

The technology to manage and manipulate light by controlling absorption, luminescence, and reflection has been a great interest in modern display technology [1,2]. Photonic crystals have been extensively studied in recent years because of their unique optical properties and the possibility of modulating the spectral resonance of optical spectrum. The optical properties of porous silicon (PS) prepared by electrochemical etching of p-type silicon wafer in HF are one candidate of photonic structured materials using reflection. PS is a network of pores within an interconnected silicon matrix. Since the discovery of PS, PS has been intensively investigated for a variety of applications, such as chemical [3] and biological sensors [4], optical band pass filters [5], micro chemical reactors [6], micro fuel cells [7], and drug delivery [8], due to its high surface area [9], open pore structure, convenient surface chemistry, and optical signal transduction capability [10].

Despite the structural inhomogeneities at the nanoscale, PS grown on highly doped p-type Si substrate showed typical optical properties of a dielectric material with a single effective refractive index (n). The structure and photonic characteristics of the PS layer depend on the conditions of the anodizing process,

such as current density, temperature, composition ratio of the solution, and conductivity of the silicon substrate [11,12]. In particular, the porosity or n of the PS layer can be precisely controlled by altering the anodizing current density [11]. One dimensional photonic structure of PS layers based on sinusoidal waveform of porosity forms a rugate reflector [13-15], which displays a sharp reflection resonance in the optical reflectivity spectrum at a wavelength that is controlled by the etch parameters. In this work, the effect of an etching time for the formation of rugate photonic structure and the effect of a frequency for the reflection band characteristics of rugate PS were investigated.

2.2 Experiments

2.2.1 Materials

HF (ACS reagent, Aldrich Chemicals), absolute ethanol (ACS reagent, Aldrich Chemicals), Camptothecin (99.8%, Aldrich), and THF were used without further purification.

2.2.2 Sample Preparation

Rugate PS was prepared by an electrochemical etching of the heavily doped p^{++}-type Si (100) substrate (boron doped, polished on the (100) face, resistivity of 0.8-1.2 mΩ-㎝, Siltronix, Inc.). The etching solution consists of a 1 : 3 by volume mixture of absolute ethanol (ACS reagent, Aldrich Chemicals) and aqueous 48% HF (ACS reagent, Aldrich Chemicals). Etching was carried out in a Teflon cell by using a two-electrode configuration with a Pt mesh counter electrode to have the structural homogeneities. Rugate PS sample was prepared by using a computer-generated periodic sine wave current density. To prevent the photo-generation of carriers, the anodization was performed in the dark. All samples were then rinsed several times with ethanol and dried under Ar atmosphere prior to use.

2.2.3 Instrumentation and Data Acquisition

The anodization current was supplied by a Keithley 2420 high-precision constant current source which is controlled by a computer to allow the formation of PS multilayers. Optical reflectivity spectra were measured using a tungsten-halogen lamp in the wavelength rance 400-1200 nm and an Ocean Optics S2000 CCD spectrometer fitted with a fiber optic input. The reflected light collection end of the fiber optic was positioned at the focal plane of the optical microscope.

2.3 Results and Discussion

2.3.1 Effect of Etching Time

In order to generate periodic layers of sinusoidal refractive index profile, a computer-generated pseudo-sinusoidal current waveform was used. The sine waveform used in the present work was represented by

$$y_i = A_i[\sin(k_i t)] + B \quad \text{----------} \quad (1)$$

where y_i represented a temporal sine wave of amplitude, A_i ; frequency, k_i ; time, t; applied current density, B. The values of k_i were from 0.28 Hz. The values of A_i and B were 11.55 and 63.05 mA, respectively. After all values were fixed, the etching time varied from 200 to 400, 600, 800, and 1000 s. Figure 1 showed reflectivity spectra of rugate PS with one reflection band while the etching time varied. A critical etching time of 200 s was needed to form rugate PS. The reflection resonance of rugate PS with 200 s of etching time occurred at 681 nm with sidelobes around the reflectance peak in the optical reflectivity and its full width at half maximum (FWHM) was 14 nm. The reflection band of rugate PS shifted to shorter wavelength by about 30 nm as the etching time increased, however their FWHMs of the reflection band were almost identical. The reflection band of rugate PS placed at the same position while the etching time was over 1000 s.

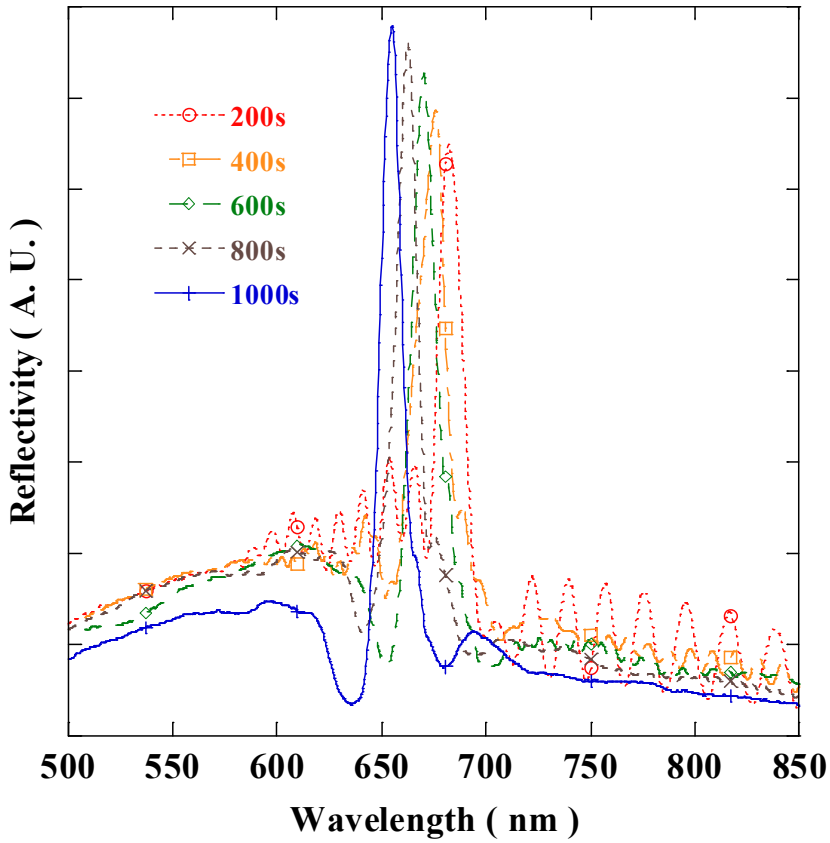

Figure 2.1. The reflection resonances of rugate PS according to etching time from 200 to 400, 600, 800, and 1000 s.

The relationship among the reflection wavelengths, the relative reflection intensities, and the etching times was summarized in Figure 2.1. Rugate PS displayed a linear relationship profile between the reflection wavelengths and the etching times. The relative reflection intensities increased linearly as the etching time increased. The relative reflection intensities of rugate PS over 1000 s of etching time start to decrease.

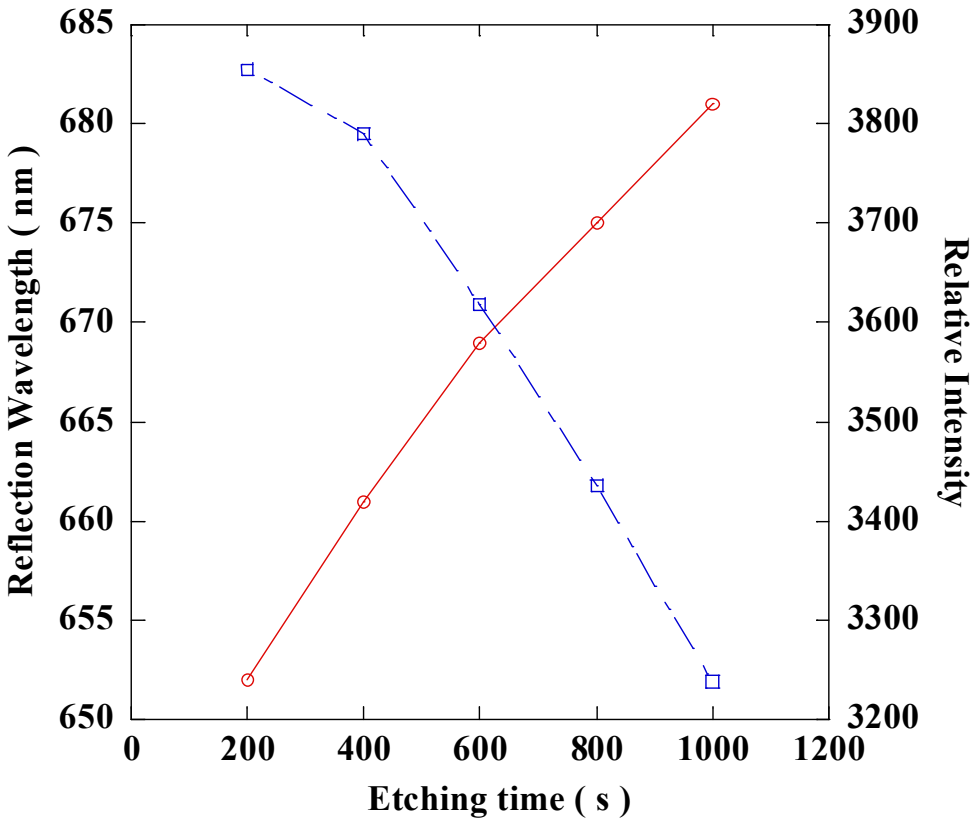

Figure 2.2. Plot showing the relationship among the reflection wavelengths, the reflection intensities, and the etching times.

2.3.2 Effect of Frequency

The effect of frequency for the formation of rugate PS was investigated. All parameters but frequency were fixed. The values of A_i, B, and t were 11.55 and 63.05 mA and 1000 s, respectively. The frequencies, k_i, varied from 0.22 to 0.38 Hz with a spacing of 0.01 Hz between sine components. The reflection band characteristics of 17 rugate PS samples according to the frequency change were listed in Table 2.1.

The relationship between the reflection wavelengths and the frequencies was summarized in Figure 2.3. Rugate PS exhibited a linear dependence between the reflection wavelengths and the etching frequencies. The reflection band of rugate PS shifted to shorter wavelength by about 13 nm as the etching frequency increased by 0.01 Hz. Their FWHMs of the reflection band varied from 13 to 17 nm.

Figure 2.4 showed the 3-D reflection stop bands (A) and the photograph of 17 rugate PS samples (B). This result illustrates that the reflection band can be controlled by tuning the etching frequency and appear anywhere in the visible range depending on the sine waveform.

Table 2.1. Reflection band characteristics of 17 rugate PS samples according to the frequency change.

Samples (N)	Value (Hz)	Wavelength (nm)	Δ [N-(N+1)] (nm)	F.W.H.M (nm)
1	0.22	730	14	16.92
2	0.23	716	14	15.14
3	0.24	702	13	16.27
4	0.25	689	14	13.27
5	0.26	675	13	15.4
6	0.27	662	12	16.83
7	0.28	650	14	14.83
8	0.29	636	12	14.57
9	0.30	624	14	13.24
10	0.31	610	14	16.08
11	0.32	596	13	14.05
12	0.33	583	13	15.17
13	0.34	570	12	14.53
14	0.35	557	13	13.51
15	0.36	545	12	12.49
16	0.37	534	11	13.59
17	0.38	522	12	16.88

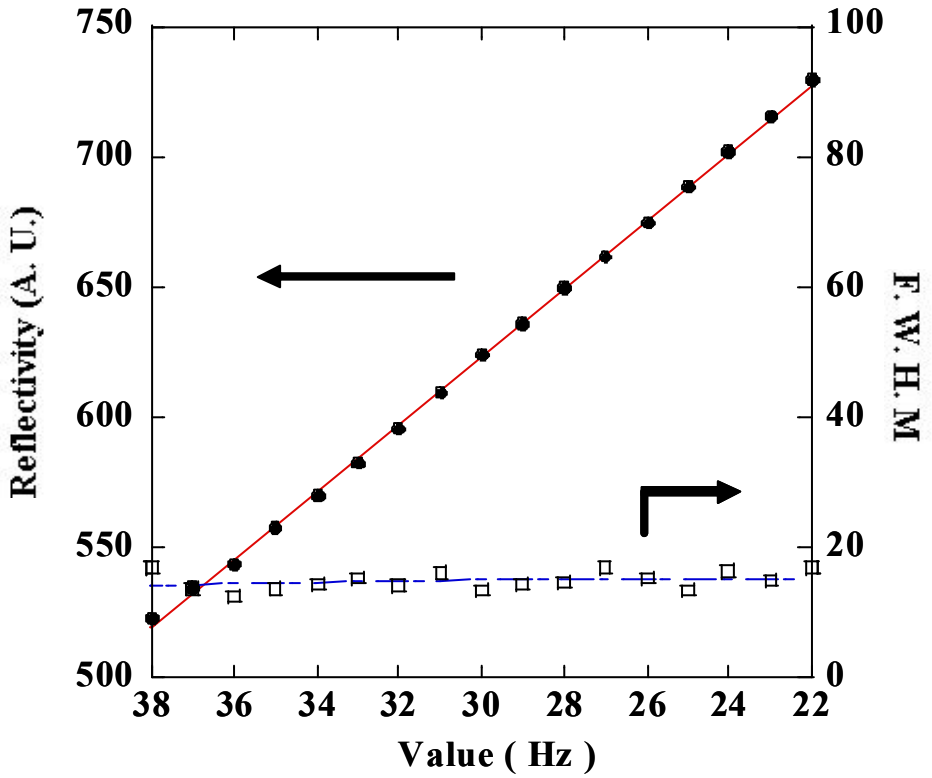

Figure 2.3. Connection of reflection spectra and FWHM about rugate PS samples.

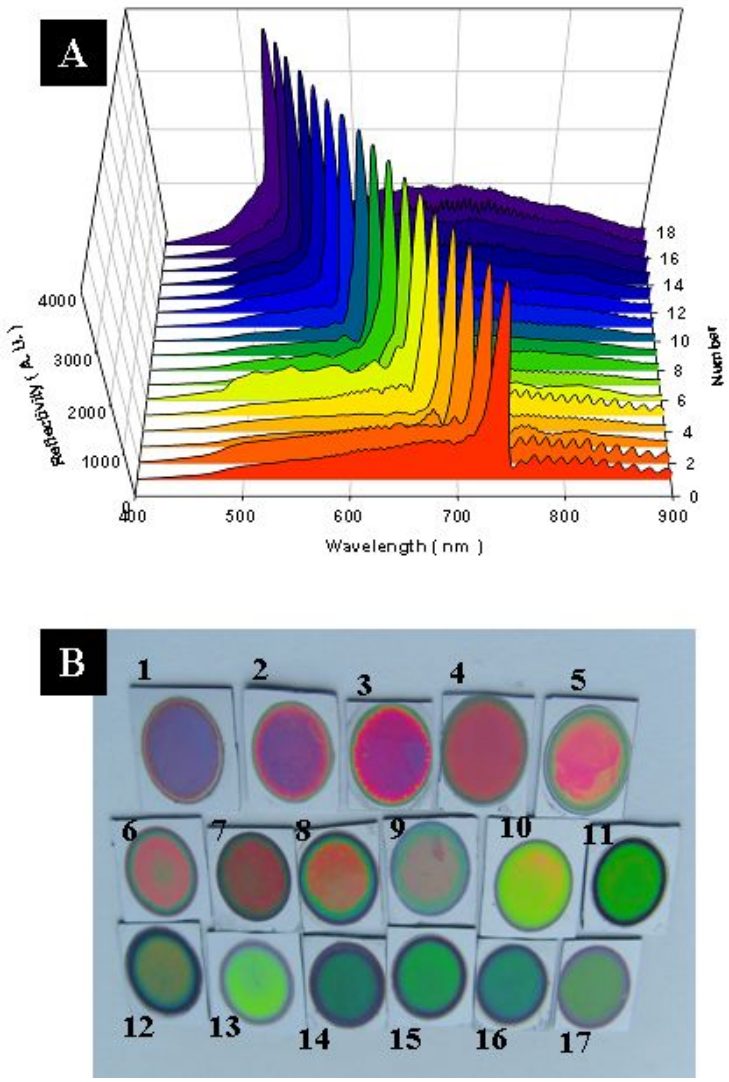

Figure 2.4. Reflection spectra and photograph of 17 rugate PS samples.

2.4 Conclusion

The effect of an etching time for the formation of rugate photonic structure and the effect of a frequency for the reflection band characteristics of rugate PS were investigated. A critical etching time of 200 s was needed to obtain the reflection resonance of rugate PS. The reflection band of rugate PS shifted to shorter wavelength as the etching time increased. Their FWHMs of the reflection band remain the same. The reflection band characteristics of 17 rugate PS samples according to the frequency change were measured. The relationship between the reflection wavelengths and the frequencies was indicated that rugate PS exhibited a linear dependence between the reflection wavelengths and the etching frequencies. The reflection band of rugate PS shifted to shorter wavelength as the etching frequency increased.

2.5 References

[1] V. Wood, M. J. Panzer, J. Chen, M. S. Bradley, J. E. Halpert, M. G. Bawendi, and W. Bulovic *Adv. Mater.* **21**, 2151 (2009).

[2] L. Qu and X. Peng, *J. Am. Chem. Soc.* **124**, 2049 (2002).

[3] H. Sohn, S. Letant, M. J. Sailor, and W. C. Trogler, *J. Am. Chem. Soc.* **122**, 5399 (2000).

[4] V. S.-Y. Lin, K. Motesharei, K.-P. S. Dancil, M. J. Sailor, and M. R. Ghadiri, *Science* **278**, 840 (1997).

[5] J. Kim, S. Jang, Y. Koh, C. Park, H.-G. Woo, S. Kim, and H. Sohn, *J. Nanosci. Nanotechnol.* **8**, 4951 (2008).

[6] M. A. Khan, M. S. Haque, H. A. Naseem. W. K. Brown, and A. P. Malshe, *Thin Solid Films* **332**, 93 (1998).

[7] S. E. L?tant, S. Content, T. T. Tan, F. Zenhausern, and M. J. Sailor, *Sensor Actuat, B-Chem.* **69**, 193 (2000).

[8] E. J. Anglin, L. Cheng, W. R. Freeman, and M. J. Sailor, *Adv. Drug Deliv. Rev.* **60**, 1266 (2008).

[9] X. G. Zhang, *J. Elecrochem. Soc.* **151**, C69 (2004).

[10] J. Gao, T. Gao, Y. Y. Li, and M. J. Sailor, *Langmuir* **18**, 2229 (2002).

[11] D. Hunkel, R. Butz, R. Ares-Fisher, M. Marso, and H. Lüth *J. Lumines.* **80**, 133 (1999).

[12] M. Haurylau, A. R. Shroff, and P. M. Fauchet *Phys. Stat. Sol. A.* **202**, 1477 (2005).

[13] F. Cunin, T. A. Schmedake, J. R. Link, Y. Y. Li, J. Koh, S. N. Bhatia, and M. J. Sailor, *Nat. Mater.* **1**, 39 (2002).

[14] M. S. Yoon, K. H. Ahn, R. W. Cheung, H. Sohn, J. R. Link, F. Cunin, and M. J. Sailor, *Chem. Commun.* 680 (2003).

[15] S. Kim, C. Park, S. G. Lee, and H. Sohn, *J. Korean Phys. Soc.* **55**, 288 (2009).

Chapter Three
Optical Characterization of Distributed Bragg Reflector Porous Silicon and Band Filter Applications

3.1 Introduction

In the previous chapter, we have been introduced the fabrication method of rugate PS having a current density of periodic sine waveform. In this chapter, we report the optical characteristics of Distributed Bragg Reflector (DBR) porous silicon (PS). This is another form of multilayers porous silicon with a square waveform. During electrochemical etching of silicon, the density of the generated PS can be continuously varied, making it possible to generate continuously varying refractive index (n) distributions in the direction perpendicular to the plane of the filter. Periodic layers of alternating high index n_1 (thickness t_1) and low index n_2 (thickness t_2) lead to the well known DBR. In the case of a multilayerd structure there is a periodic alternation of two current densities.

DBR PS displays a plateau of high reflectivity, which can be viewed as 1D photonic band gap, centred at $\lambda_{bragg} = 2 (n_1 t_1 + n_2 t_2)$ [1]. This resulted in a mirror with high reflectivity in a specific narrow spectral region and displays a very sharp line in the optical reflectivity spectrum. DBR PS has been investigated for a variety of applications, such as chemical sensors [2], microcavity [3,4], and drug delivery [5], due to its high surface area, convenient surface chemistry, and optical signal transduction capability. In this study, we report about fabrication of DBR PS for full color stop band and band filter applications.

3.2 Experiments

3.2.1 Materials

HF (ACS reagent, Aldrich Chemicals), absolute ethanol (ACS reagent, Aldrich Chemicals), Camptothecin (99.8%, Aldrich), and THF were used without further purification.

3.2.2 Preparation of DBR PSi

DBR PS dielectric mirror first is electrochemically etched into the single Si (100) substrate (boron doped, polished on the (100) face, resistivity of 0.8-1.2 mΩ-㎝, Siltronix, Inc.). The electrolyte is madi (y consists of a 1 : 3 (y volume mixture of absolf a ishanol (ACS reagent, Aldrich Chemicals) and aqueous 48% hydrofluoric acid (ACS reagent, Aldrich Chemicals). Etching elecarried out in a Teflon cell (y using a two-electrode configuratint, AldricPt mesh counter electrode. DBR PS simple is prepared (y using a computer-configurat mΩ-㎝, Sil Chemicals current. The etching condition of reagent, afers were adjusted in a wayed (yrolled (y tunflon ceetching time. The resulting free-standing DBR PS feam for optical band filter application has been obtained from the siagent, substrate (y an applyflon ceelectropolishing ching chat 400 mA/cm^2 for 1.5 min in a solf ion of 48% aqueous HF and ishanol (3 : 1 (y volume), and thenhat 24 mA/cm^2 for 1.5 min in a solution of 48% aqueous HF and ethanol (1 : 15 by volume).

The anodization current was supplied by a Keithley 2420 high-precision constant current source which is controlled by a computer to allow the formation of PS

multilayers.

3.2.3 Instrumentation and Data Acquisition

Optical reflectivity spectra were measured using a tungsten-halogen lamp and an Ocean Optics S2000 CCD spectrometer fitted with a fiber optic input. The reflected light collected at the end of the fiber optic was positioned at the focal plane of the optical microscope. Surface and cross-sectional images of composite films were obtained by using a cold field emission scanning electron microscope (FE-SEM, S-4700, Hitachi).

3.3 Results and Discussion

DBR PS containing two distinct porosities was successfully prepared using a periodic galvanostatic electrochemical etch of crystalline silicon by applying a square wave current between 5 mA/cm^2 and 50 mA/cm^2. A DBR PS exhibits a high reflectivity band with the Bragg wavelength λ_{Bragg}, depending on the thickness of the layers (d_1, d_2) and the corresponding refractive indices (n_1, n_2). The mth order of the Bragg peak is given by:

$$m\lambda_{\text{Bragg}} = 2(\, d_1 n_1 + d_2 n_2 \,).$$

Etching conditions of etched DBR PS samples are included in Table 1. This interface will have a different roughness at each current change. The important point is now to understand the evolution of the roughness as a function of the DBR PS thickness, when realising DBR layers. The roughness in every layer can just add to one another, or the applied current densities can lead eventually to their own roughness limit. The electrochemical process generates an optically uniform layer of DBR PS. The thickness and porosity of a given layer is controlled by the current density, the duration of the etch cycle, and the composition of the etchant solution. This appear a type of optical reflector that contain a continuous variation of refractive index, along the growth axis. The reflectance spectrum of such a filter shows a high reflectivity "stop band" around a characteristic wavelength. The multilayered photonic crystals of DBR PS exhibit a very sharp line in the optical reflectivity spectrum. This reflective wavelength can be controlled by tuning of etching time and can appear anywhere in the visible range depending on the square waveform. Reflectivity spectra of DBR PS samples are shown in Figure 1.

Table 3.1. Etching conditions and reflection peak of DBR PS samples.

Number	Wavelength	Low current (time)	High current (time)	FWHM
1	518 nm	60 s	3 s	21
2	536 nm	65 s	3 s	20
3	557 nm	70 s	3 s	24
4	578 nm	75 s	3 s	19
5	589 nm	80 s	3 s	21
6	606 nm	85 s	3 s	22
7	622 nm	90 s	3 s	21
8	635 nm	95 s	3 s	18
9	657 nm	100 s	3 s	23
10	675 nm	80 s	4 s	24
11	692 nm	80 s	5 s	27
12	710 nm	80 s	6 s	24
13	722 nm	80 s	7 s	29
14	735 nm	82 s	7 s	32
15	747 nm	85 s	7 s	26
16	759 nm	90 s	7 s	30

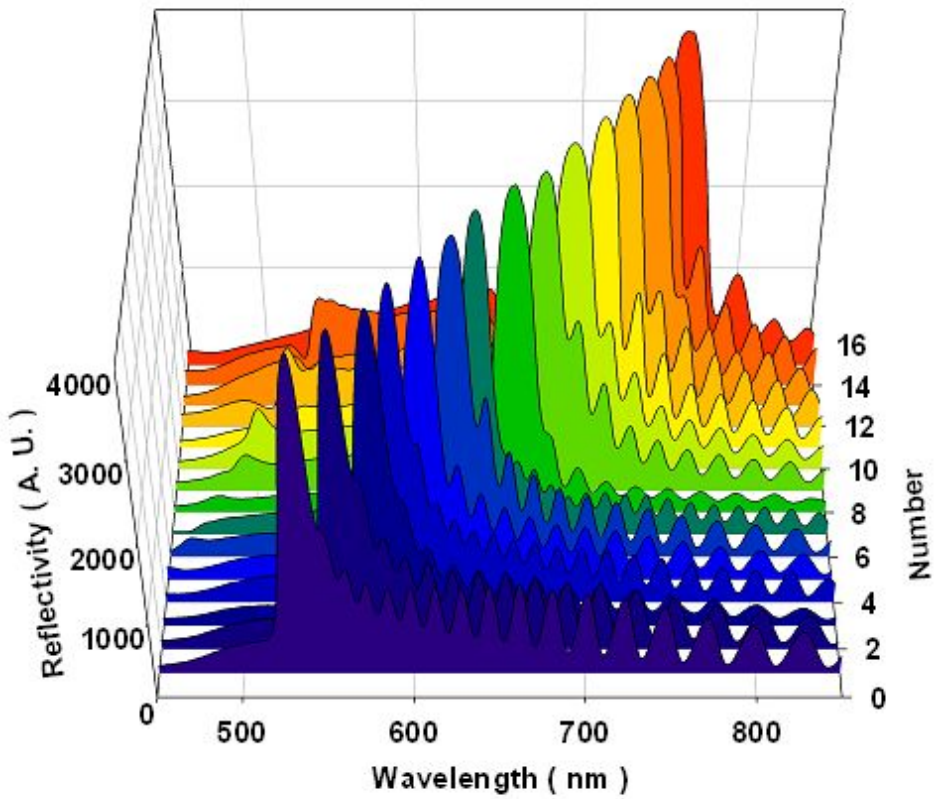

Figure 3.1. Reflection wavelength of DBR PS samples.

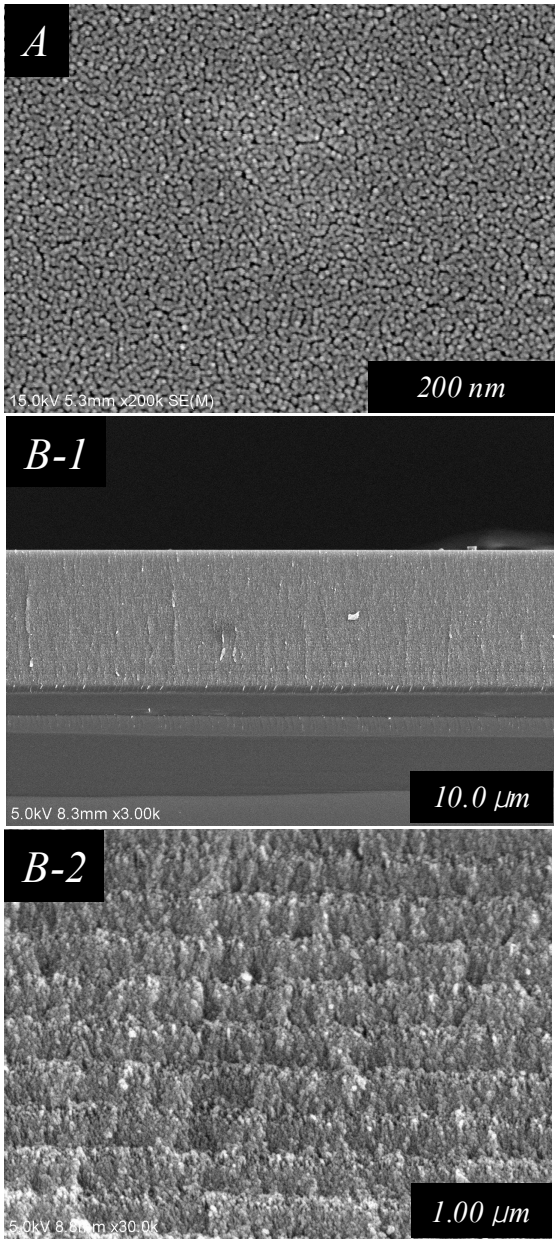

Figure 3.2. Surface (A) and cross-sectional (B-1,2) FE-SEM images of DBR PS.

Reflectivity spectra shown in Figure 3.1. indicates that the FWHM of these reflection bands is much narrower than that of fluorescence spectrum obtained from a fluorescent organic molecules or quantum dot. The reflection bands of DBR PS samples shown in Figure 1 have a FWHM of 20-30 nm. Location of reflection bands are appeared that shifted to longer wavelengths as increase etching time of current.

The cross-sectional and surface SEM image of DBR PS shown in Figure 3.2. illustrates that the multilayer of DBR PS exhibits a depth of few microns and a pore of few nano applying of square current density during the etching process results two distinct refractive indices in the contrast. The cross-sectional SEM image of DBR PS shown in Figure 3.2(B-2). can observe two different PS layers.

DBR PS films have been removed from the silicon wafer by applying an electropolishing current. Reflectivity spectra of DBR PS and free-standing DBR PS film is shown in Figure 3.3(A). The reflectivity of free-standing DBR PS film occurs at the identical location. Also, photographs showed in Figure 3.3(B). exhibit electropolished free-standing DBR PS film.

In a basic demonstration for optical filter application, the reflection and transmission spectra of free-standing DBR PS film were shown in Figure 3.4(A). Also, when the two free-standing DBR films overlap, transmission spectrum was superimposed.

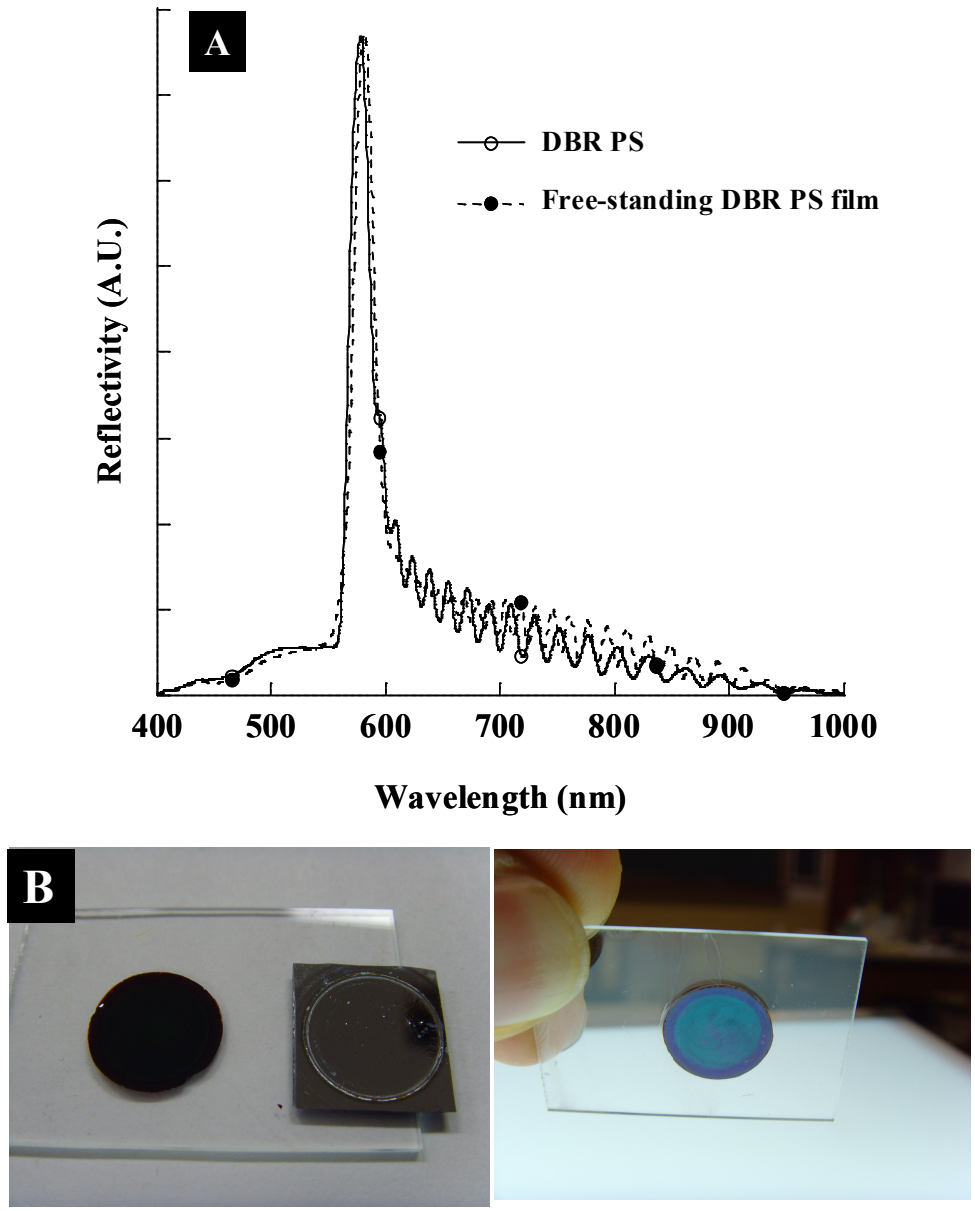

Figure 3.3. Reflection spectra (A) and photograph (B) of free-standing DBR PS film.

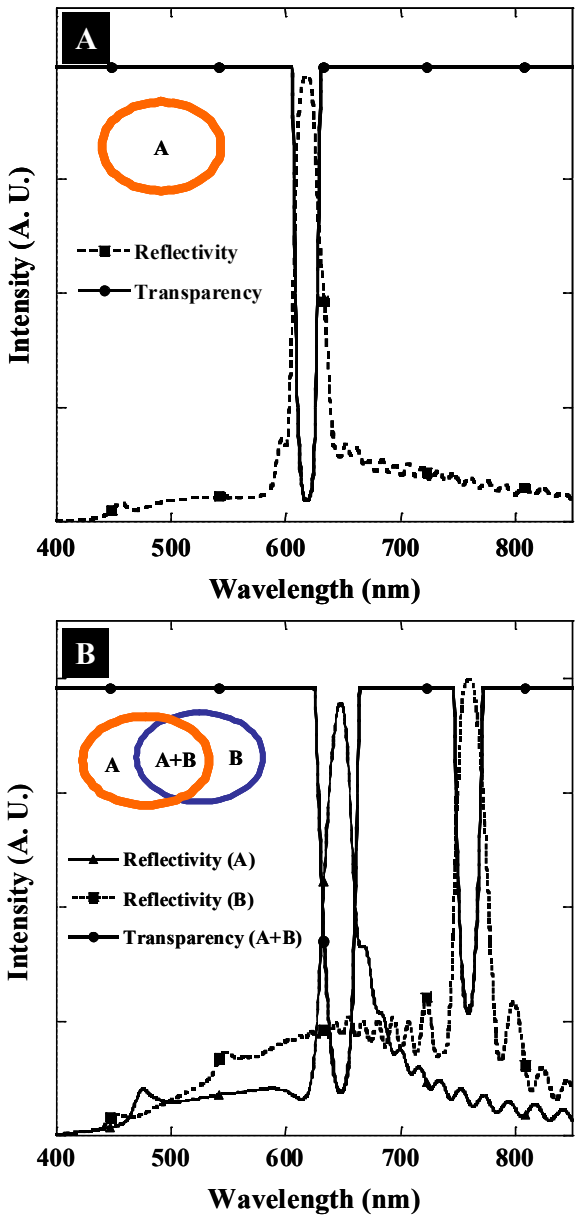

Figure 3.4. Optical filter application using transparency of DBR PS film.

3.4 Conclusion

DBR PS was prepared for the possible use of full-color reflector or filter. DBR PS exhibiting unique reflectivity was successfully obtained by an electrochemical etching of silicon wafer using square current waveform. The multilayered photonic crystals of DBR PS exhibited the reflection of a specific wavelength with high reflectivity in the optical reflectivity spectrum. This reflective wavelength can be controlled by tuning of etching time and can appear anywhere in the visible range depending on the square waveform. This might be a demonstration for the fabrication of specific reflectors or filters in full color.

3.5 References

[1] S. Ilyas, T. Böcking, K. Kilian, P. J. Reece, J. Gooding, K. Gaus, and M. Gal, *Opt. Mater.* **29**, 612 (2007).

[2] S. G. Kim, S. Kim, Y. C. Ko, S. Cho, and H. Sohn, *Colloid Surf. A-Physicochem. Eng. Asp.* **314**, 398 (2008).

[3] S. Chan, S. R. Horner, P. M. Fauchet, and B. L. Miller, *J. Am. Chem. Soc.* **123**, 11797 (2001).

[4] L. Pavesi, C. Mazzoleni, A. Tredicucci, and V. Pellegrini, *Appl. Phys, Lett.* **67**, 3280 (1995).

[5] Y. Koh, S. Jang, J. Kim, S. Kim, Y. C. Ko, S. Cho, and H. Sohn, *Colloid Surf. A-Physicochem. Eng. Asp.* **314**, 328 (2008).

Chapter Four
Fabrication and Characterization of Prismatic Band Filter Gradient Rugate Porous Silicon

4.1 Introduction

The development of a new technology to build one-dimensional photonic structures is of great interest because they are too complex to fabricate by using conventional lithographic methods. PS is an attractive material for photonic applications due to its high surface area, open pore structure, and optical signal transduction capability. A variety of passive devices, such as mirrors [1], filters [2], and microcavities [3,4], has already been employed by using PS which is based on a relatively simple electrochemical etching process. The first reports giving details of a new form of silicon appeared in 1956 when Uhlir described a study of the electropolishing of silicon in hydrofluoric acid [5]. Research on PS has been increased significantly since the discovery of efficient visible luminescence of PS by Canham suggesting the possibility of silicon based light sources [6].

One-dimensional photonic crystals of PS have also found application in chemical detection [7,8], remote sensing [9], and biomolecular screening [10]. PS is a nano-crystalline material that is generated by etching of bulk crystalline silicon in aqueous hydrofluoric acid (HF) [11]. Molpology and optical properties of PS are dependent on HF concentration, dopant type, density in the Si substrate, and applied current density [12,13]. Porous silicons containing gradient refractive index

have been recently developted [14,15]. The direction of the refractive index gradient is perpendicular to the optical. Here we report the optical characteristics and morphology of BFG rugate PS whose appearance is prismatic due to gradient refractive index. This is achieved by various porosity and depth of PS during the electrochemical fabrication process.

4.2 Experiments

4.2.1 Materials

HF (ACS reagent, Aldrich Chemicals), absolute ethanol (ACS reagent, Aldrich Chemicals), Camptothecin (99.8%, Aldrich), and THF were used without further purification.

4.2.2 Preparation of ruagte PS using asymmetric electrode configuration

BFG rugate PS dielectric mirror was prepared by using electrochemical etching of silicon wafer (boron doped, polished on the (100) face, resistivity of 0.8-1.2 m Ω-cm, Siltronix, Inc.), and using a computer-generated periodic sine wave current. The etching solution consists of a 1 : 3 by volume mixture of absolute ethanol (ACS reagent, Aldrich Chemicals) and aqueous 48% hydrofluoric acid (ACS reagent, Aldrich Chemicals). Etching is carried out in a Teflon cell by using a two-electrode configuration with Pt needle counter electrode. BFG rugate PS containing a distribution of pore sizes and film thickness was prepared by using the asymmetric electrode configuration as shown in Scheme 4.1.

4.2.3 Instrumentation and Data Acquisition

The anodization current was supplied by Keithley 2420 high-precision constant current source which is controlled by a computer to allow the formation of PS

multilayers. Optical reflectivity spectra were measured using a tungsten-halogen lamp and an Ocean Optics S2000 CCD spectrometer fitted with a fiber optic input. The reflected light collection end of the fiber optic was positioned at the focal plane of the optical microscope. Scanning electron microscope (SEM) images were obtained by a cold field emission scanning electron microscope (FE-SEM, S-4700, Hitachi).

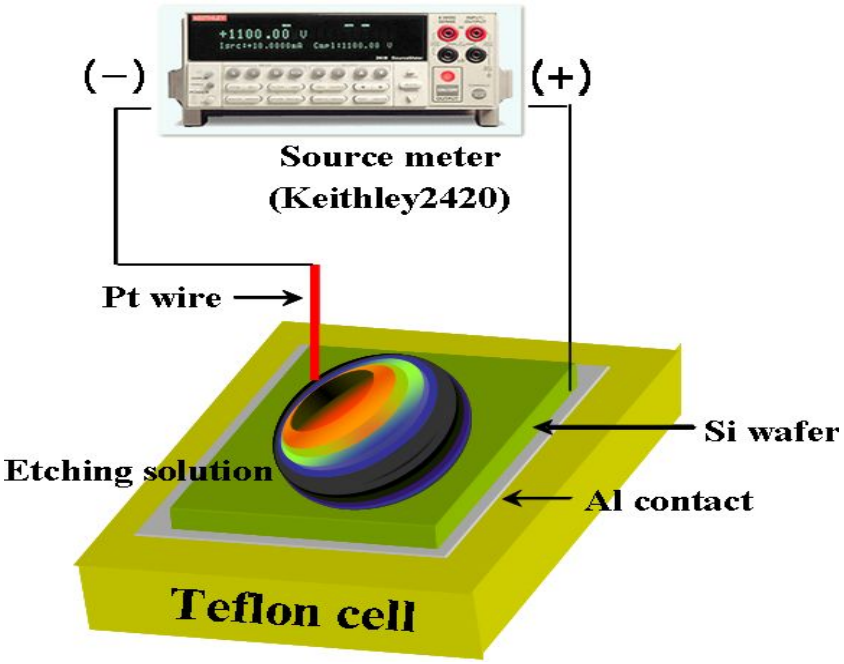

Scheme 4.1.

4.3 Results and Discussion

BFG rugate PS has been generated by an electrochemical etching of silicon wafer using an asymmetric electrode configuration in aqueous ethanolic HF solution. BFG PS prepared by using anisotropic etching conditions displays the anisotropic reflection bands whose reflection maximum varied spatially across the porous silicon. The waveform used in the present work, which is represented by Equation 1.

$$\mathbf{y}_i = \boldsymbol{A}_i \, [\sin \, (k_i t) \,] + \boldsymbol{B} \quad \text{----------} \quad (1)$$

Where y_i represents a temporal sine wave of amplitude, $\boldsymbol{A}_i$; frequency, k_i ; time, t ; applied current density, B. The values of k_i are from 0.39 Hz. The values of $\boldsymbol{A}_i$ and $\boldsymbol{B}$ are 11.55 and 63.05 mA with 205 repeats.

To have anisotropic distribution of pore sizes and film thickness in PS, Pt needle electrode is placed at the side of etching cell and Al plate electrode is located at the back side of the silicon wafer as shown in Scheme 1. With this asymmetric electrode arrangement, the porosity and the thickness of the film at any point depend on the magnitude of the etching current flowing through that point. The current at any point of silicon wafer depends on the resistance of the Si wafer between the electrolyte on one side and the Al plate electrode on the back side and varies as a function of distance from the Pt counter electrode due to solution resistance. Since the geometry is asymmetric, the current density decreases as the distance from the counter electrode increases. The asymmetric electrode configuration provides a current density gradient across the wafer that result in a distinct variation in the morphology of the pores and produces a BFG PS lens

showing asymmetric Newton's ring. Photograph and reflection spectra of BFG rugate PS are shown in Figure 4.1. The reflection spectra of BFG rugate PS are recorded by moving every 2 mm from the position closest to the Pt counter electrode on the silicon surface.

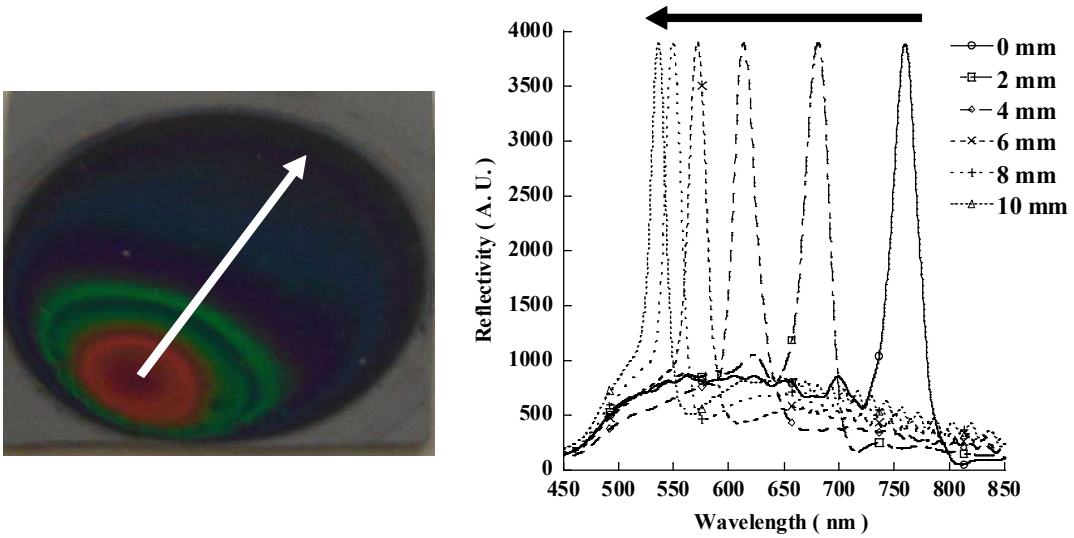

Figure 4.1. Photograph and reflection spectra of BFG rugate PS. The value position used refers to the distance from the position closest to the Pt counter electrode across the silicon wafer.

Table 4.1. Data analysis of BFG rugate PS about the position of electrode.

X (mm)	λ (nm)	Δ λ[n-(n+1)] (nm)	F.W.H.M (nm)
0	759	0	28.78
2	680	79	27.67
4	612	68	25.15
6	569	43	23.37
8	548	21	19.89
10	535	13	18.25

Changes of reflective maxima and FWHM are summarized in Table 4.1. The reflection wavelength shifts exponentially to shorter wavelengths and FWHM is narrower across the silicon wafer. The BFG rugate PS displays a prismatic appearance due to the continuously changing refractive index distribution.

The cross-section and surface SEM image of BFG rugate PS are shown in Figure 4.2. The film thickness of BFG rugate PS becomes shorter as the distance from the position of Pt counter electrode increases.

Profilometry measurements shown in Figure 4.3 reveal that the thickness of the PS layer varies as a function of distance from the counter electrode. BFG rugate PS is thickest at the point directly under the counter electrode, consistent with that being the position of highest current density.

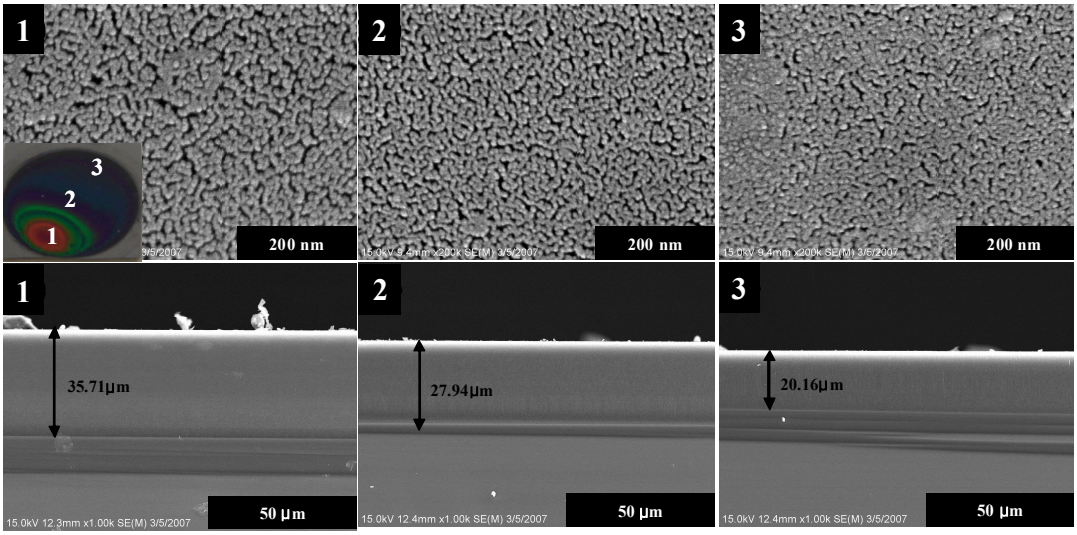

Figure 4.2. Surface and cross-section SEM images of BFG rugate PS. 0 mm (1), 5 mm (2), and 10 mm (3) refer to the distance from the position closest to the Pt counter electrode across the silicon wafer.

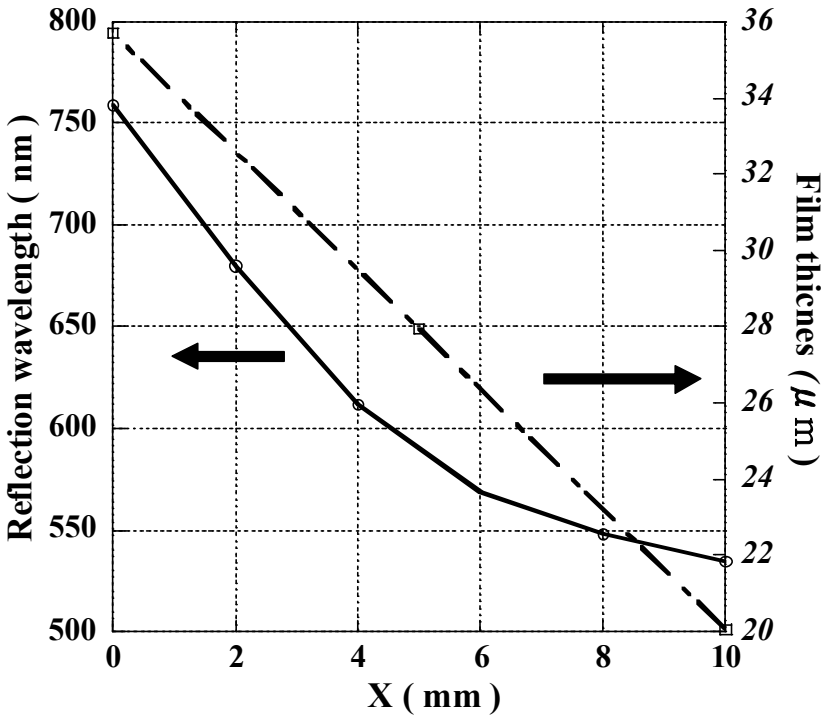

Figure 4.3. Profile of the change of reflection wavelength and film thickness of BFG rugate PS as a function of x represented to the distance from the position closest to the Pt counter electrode across the silicon wafer.

4.4 Conclusion

BFG rugate PS was prepared that contain a controlled distribution of pore sizes and film thickness using anisotropic etching conditions. In this work, BFG rugate PS displays a prismatic appearance due to the uneven distribution of current across the silicon wafer during the etching. The reflectivity of BFG rugate PS is shifted to shorter wavelengths and its bandwidth and film thickness become narrower and shorter across the wafer from the position of electrode. This might be a demonstration for the fabrication of specific reflectors or filters.

4.5 References

[1] W. H. Zheng, P. J. Reece, B. Q. Sun, and M. Gal, *Appl. Phys. Lett.* **84**, 3519 (2004).

[2] M. G. Berger, F. Arens-Fischer, M. Thönissen, M. Krüger, S. Billat, H. Lüth, S. Hilbrich, TW. heiβ, and P. Grosse, *Thin Solid Films* **297**, 237 (1997).

[3] S. Chan and P. M. Fauchet, *Opt. Mater.* **17**, 31 (2001).

[4] M. Ghulinyan, C. J. Oton, G. Bonetti, Z. Gaburro, and L. J. Pavesi, *J. Appl. Phys.* **93**, 9724 (2003).

[5] A. Uhlir, *Bell System Tech.* **35**, 333 (1956).

[6] L. T. Canham, *Appl. Phys. Lett.* **57**, 1046 (1990).

[7] H. Sohn, S. Letant, M. J. Sailor, and W. C. Trogler, *J. Am. Chem. Soc.* **122**, 5399 (2000).

[8] J. Gao, T. Cao, Y. Y. Li, and M. J. Sailor, *Langmuir* **18**, 2229 (2002).

[9] T. A. Schmedake, F. Cunin, J. R. Link, and M. J. Sailor, *Adv. Mater.* **14**, 1270 (2002).

[10] F. Cunin, T. A. Schmedake, J. R. Link, Y. Y. Li, J. Koh, S. N. Bhatia, and M. J. Sailor, *Nature Mater.* **1**, 39 (2002).

[11] H. Foll, J. Carstensen, M. Christophersen, and G. Hasse, *Phys. Status Solidi A* **182**, 7 (2000).

[12] K.-P. Dancil, S. D. P. Greiner, and M. J. Sailor, *J. Am. Chem. Soc.* **121**, 7925 (1999).

[13] S. Chan, P. M. Fauchet, Y. Li, L. J. Rothberh, and B. L. Miller, *Phys. Status Solidi A* **182**, 541 (2000).

[14] S. Ilyas and M. Gal, *Appl. Phys. Lett.* **89**, 211123 (2006).

[15] B. E. Collins, K.-P. S. Dancil, G. Abbi, and M. J. Sailor, *Adv. Funct. Mater.* **12**, 187 (2002).

Chapter Five
Chemical Sensor Based on Porous Silicon Dual Transducers

5.1 Introduction

Since the discovery of visible photo- and electroluminescence from nanocrystalline porous silicon,[1] porous Si has been intensively investigated for a variety of applications such as chemical[2] and biological sensors,[3] medical diagnostics,[4] optical band pass filters,[5] micro chemical reactors,[6] and micro fuel cells.[7] Porous Si is an ideal candidate for gas- or liquid- sensing applications, since it has a very large specific surface area on the order of few hundreds m^2/cm^3, corresponding to about thousand times of the surface area of a polished silicon wafer. The direction of pores and pore diameters depend on surface orientation, doping level and type, temperature, the current density, and the composition of the etching solution.[8] The main techniques investigated to achieve signal transduction are capacitance,[9] resistance,[10] photoluminescence,[11] and reflectivity.[12]

Typically, porous Si prepared from p-type silicon wafer under dark condition exhibits well defined Fabry-Perot interferometric fringes in the optical reflectivity spectrum. Condensation of molecules in the pores can lead to a shift in the Fabry-Perot interference fringes by modification of the refractive index of the porous Si films.[13,14] This property has been exploited to develop porous Si

sensors for detection of toxic gases,[15,16] solvents,[17,18] DNA,[3] and proteins.[13,19]

Luminescent porous Si samples can be usually prepared by a galvanostatic photoetch of n-Si. Porous Si from n-type silicon has a high surface area network of Si nano-crystallites produced by an electrochemical etch. The material consists of an ensemble of interconnected nanometer-sized silicon crystallites, which can have dimensions small enough to exhibit quantum confinement effects. Carriers generated by UV excitation are confined in the silicon nanocrystallites. The gap of the bulk silicon (1.1eV) is then increased by the confinement energy and a visible red photoluminescence is observed with an external quantum efficiency of up to 5%.[20] Organic vapors have been detected quantitatively by quenching of photoluminescence of the quantum-confined Si crystallites in porous Si.[21-24] Since the photoluminescence from porous Si prepared from p-type silicon occurs in near infrared region (above 700 nm), the intensity of the visible light from porous Si is very weak for sensing purpose.[25]

In this work, porous Si samples displaying both strong photoluminescence in the visible region and well defined Fabry-Perot interferometric fringes in the optical reflectivity spectrum were successfully prepared. It was demonstrated how porous Si chips were prepared and integrated in a chemical sensors. Both photoluminescence and reflectivity were reported to constitute efficient transduction modes for sensing compounds in the gas phase: condensation of molecules in the pores led to a quenching of the photoluminescence by energy or electron transfer and a shift in the Fabry-Perot interference fringes by change of the refractive index of porous Si.

5.2 Experiments

5.2.1 Materials

HF (ACS reagent, Aldrich Chemicals), absolute ethanol (ACS reagent, Aldrich Chemicals), chloroform (99.8%, Aldrich), n-hexane, methanol (98.5%, Aldrich), benzene (99.8%, Aldrich), iso-propanol (99.5%, Aldrich), and toluene (99.5%, Aldrich) were used without further purification.

5.2.2 Preparation and treatment of porous Si

Heavily doped p-type silicon wafers (B-doped, orientation<100>, Siltronix, Inc.) with a resistivity in the range 1~10 Ω·cm were used to fabricate porous Si by an anodic etch in ethanolic HF consisted of a 1 : 1 volume mixture of aqueous 48% hydrofluoric acid (ACS reagent, Aldrich Chemicals) and absolute ethanol (ACS reagent, Aldrich Chemicals). Prior to etching procedure, the silicon wafer were rinsed thoroughly with ethanol and dried under a steam of nitrogen. The galvanostatic etch was carried out in a Teflon cell by using a two-electrode configuration with a Pt mesh counter electrode. Porous Si was prepared by using a 50 mA/cm^{-2} for 3 min. The anodization current was supplied by a Keithley 2420 high-precision constant current source. Galvanostatic etching was performed under the illumination with a 300 W tungsten filament bulb for the duration of etch. All samples were then rinsed several times with ethanol and dried under argon atmosphere prior to use. The samples were then mounted in a glass dosing chamber connected to a glass-and-Teflon Schlenk line via an O-ring joint. The

Schlenk line was connected to a direct-drive vacuum pump. The chamber was pumped to < 1 mTorr between gas exposures. For consistency, vacuum measurements were recorded after 5 min, although recovery of the photoluminescence was nearly complete within the first 30 s of exposure to vacuum.

5.2.3 Preparation of gas samples

For analyte exposure studies, chloroform (99.8%, Aldrich), n-hexane, methanol (98.5%, Aldrich), benzene (99.8%, Aldrich), iso-propanol (99.5%, Aldrich), and toluene (99.5%, Aldrich), were purchased and distilled from a sodium/benzophenone ketal under argon gas. Stock solutions of the molecules were prepared by freeze-pump-thaw degassed three times prior to use. All solutions were handled under dry nitrogen gas using conventional Schlenk and syringe techniques.

5.2.4 Photoluminescence measurement

Porous Si sample was placed in an exposure chamber fitted with an optical window. Steady-state photoluminescence spectra were obtained with an Ocean Optics S2000 spectrometer fitted with a fiber optic probe. The excitation source was a UV LED (λ_{max} = 380 nm) focused on the sample (at a 45° angle to the normal of the surface) by means of a separate fiber. Light was collected at a 90° angle to the incident light source with a fiber optic. Spectra were recorded with a CCD-detector in the wavelength range of 400 to 900 nm. Values of percent quenching are reported as $(I_0-I)/I_0$, where I_0 is the intensity of the luminescence of

porous Si, integrated between 400 and 900 nm, in the absence of quencher and I is the integrated intensity of luminescence of porous Si in the presence of a quencher at a given concentration. At least three times of measurements were performed for each analyte studied. The error in all percent quenching were less than 2% of the values quoted.

5.2.5 Reflectance measurement

Interferometric reflectance spectra of porous Si samples were recorded by using an Ocean Optics S2000 spectrometer fitted with a bifurcated fiber optic probe. A tungsten light source was focused onto the center of a porous silicon surface with a spot size of approximately 1~2 mm. Spectra were recorded with a CCD detector in the wavelength rang 400~1200 nm. The illumination of the surface as well as the detection of the reflected light was performed along an axis coincident with the surface normal.

5.2.6 Instrumentation and data acquisition

Fourier-transform infrared (FT-IR) spectra were collected with a Nicolet model 5700 infrared spectrometer in the transmission mode. Acquired interferograms per spectrum and spectral resolution were 32 and 4 cm^{-1}. The morphology of porous Si was observed with cold field emission scanning electron microscope (FE-SEM, S-4700, Hitachi).

5.3 Results and Discussion

An anodic etch of p-type silicon wafer with resistivities of 1~10 Ω·cm in ethanolic HF solution generally produces PSi single layer with a network of microprous (pore size < 10 nm), rather than mesoporous (pore size 10-50 nm) or macroporous (pore size 200 nm-20 nm). The shape, size, and orientation of pores of PSi layers depend on surface orientation and the dopant level of the crystalline silicon substrate as well as the applied current density, the temperature, and the concentration of the HF etching solution. The pore size of p-type PSi can be increased by increasing the concentration of the dopant and decreasing the aqueous HF concentration. In this work, porous Si with mesopores has been successfully fabricated by using a galvanostatic electrochemical etch of p-type silicon wafer with a resistivity in the range 1~10 Ω·cm. The surface and cross sectional morphology of porous Si are obtained with cold FE-SEM and shown in Figure 5.1. FE-SEM image of porous Si indicates that the prepared porous Si has cylindrical mesopores with the average pore size of about 20 nm and depth of 5.5 m. The porosity of porous Si was obtained by gravimetric measurements. 80% of porosity for the prepared porous Si was obtained.

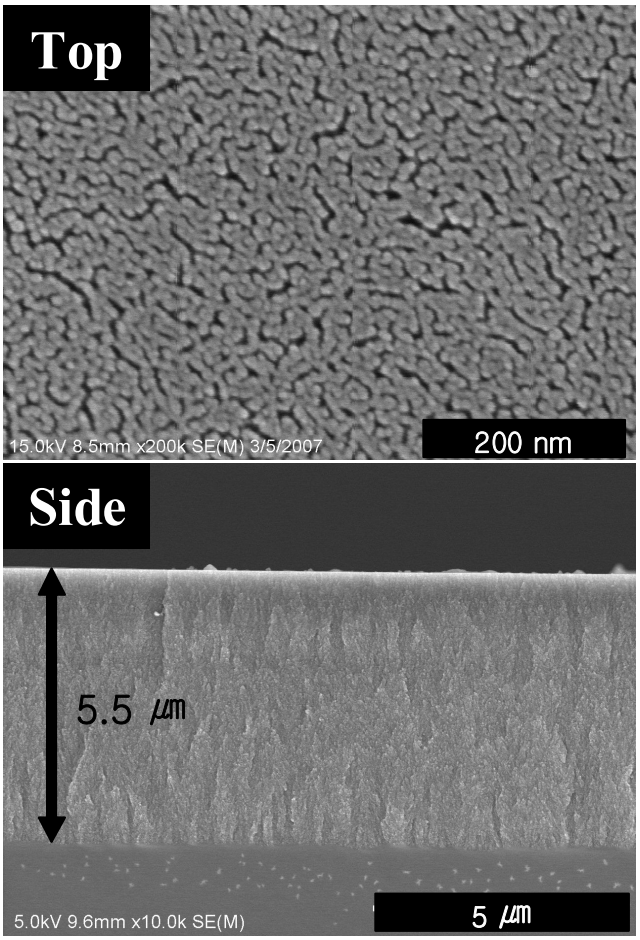

Figure 5.1. Surface (top) and cross-section (bottom) SEM image of prepared porous Si.

The surface of porous Si was characterized by FT-IR measurement as shown in Figure 5.2(A). FT-IR spectra of fresh porous Si displayed vibrational bands in the fingerprint region of the spectra. Fresh porous Si of vibrations associated with surface Si-H species were observed at ν(Si-H) = 2090, ν(Si-H_2) = 2115, ν(Si-H_3) = 2140, and δ(Si-H) = 908 cm^{-1}, respectively. Optical reflectance and photoluminescence spectroscopy were used to investigate the optical properties of porous Si. Prepared porous Si displayed well resolved Fabry-Perot fringes in reflectometric interference spectrum. Photoluminescence spectra were measured and collected at room temperature as shown in Figure 5.2(B). The maximum intensity of emission spectrum was centered at 660 nm with an excitation wavelength of 380 nm.

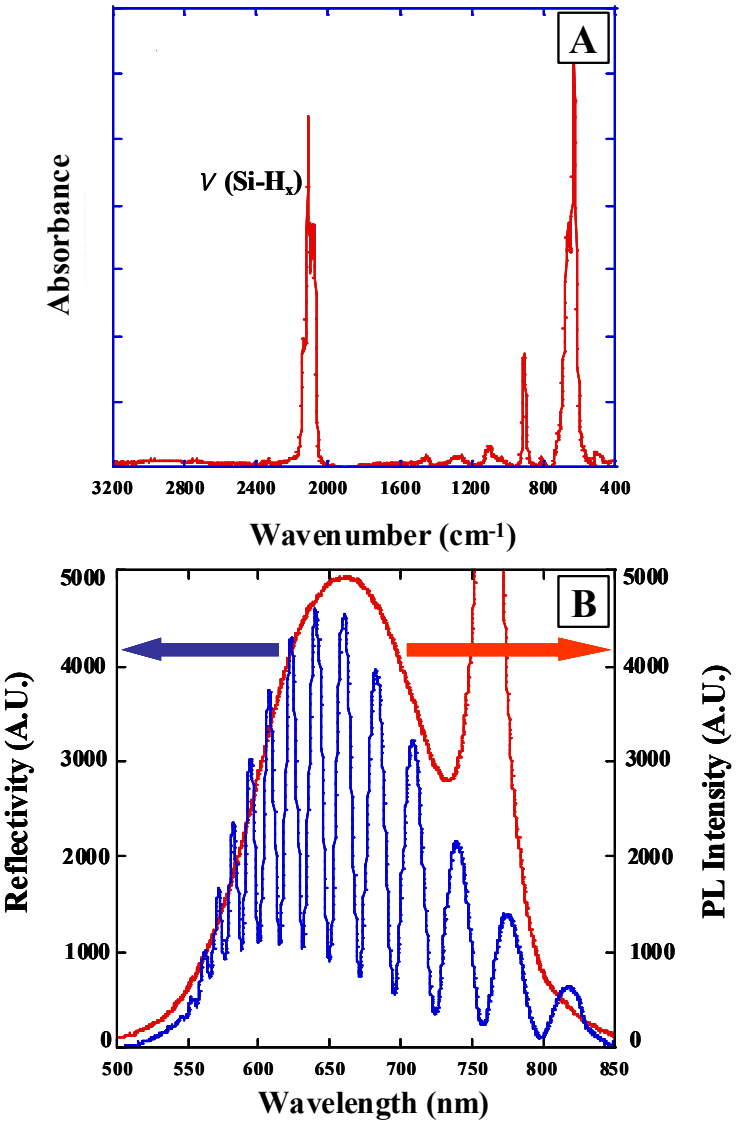

Figure 5.2. FT-IR (A) and reflectivity (blue line, B) and photoluminescence (red line, B) spectra of prepared porous Si.

The optical spectrum from porous Si is governed by the Fabry-Perot relationship. The wavelength of a peak in the reflectivity spectrum is given by eq 1:

$$m\lambda = 2nL \quad (1)$$

where m is the spectral order of the optical fringe, the wavelength, n the refractive index of the film, and L its thickness. The product nL is the quantity referred to as "optical thickness" *(OT)*. Any change of the refractive index n will induce a proportional shift of the position of the interference fringe position according to eq 2.

$$m\Delta\lambda = 2\Delta nL \quad (2)$$

When a porous Si interferometer is exposed to analytes in the gas phase, adsorption or capillary condensation induces an increase of its effective refractive index by replacement of a fraction of air (n = 1) by a fraction of analyte (n > 1). The shift of Fabry-Perot fringe to the longer wavelength under the exposure of chloroform vapors is obtained and shown in Figure 5.3(A). The analytes have different refractive indices and vapor pressures, respectively. The amplitude of the red shift of the reflection peaks depends on both refractive index and vapor pressure of the analyte condensed in porous Si sample as well as the surface characteristics including hydrophilicity/hydrophobicity and varied pore diameter.

Porous Si consisted of a large number of interconnected Si nanocrystallites with a surface that is almost entirely covered with hydrogen atoms. Porous Si samples prepared by a galvanostatic photoetch of n-Si in this study exhibited a strong visible red photoluminescence possibly due to the photoetch. The red photoluminescence is due to the quantum confinement of silicon nanocrystallites in porous Si. The intensity of photoluminescence depended on the presence of surface adsorbates.[24] The quenching process for aromatic molecules was predominantly driven by energy transfer. Meyer and co-workers were observed reversible dynamic

quenching of porous Si photoluminescence by organic molecules.[26] Figure 5.3(B). showed the steady-state photoluminescence spectra and displayed quenching photoluminescence under the exposure of various organic vapors. Exposure of porous Si to gaseous organics resulted in reversible quenching of photoluminescence. The intensity of photoluminescence for the samples in vacuum always recovered to within 2% of the original spectrum. Quenching photoluminescence resulted from the luminescent chromophore in porous Si to a weakly chemisorbed organic molecule. Samples were typically cycled between organic vapors and vacuum more than 5 times.

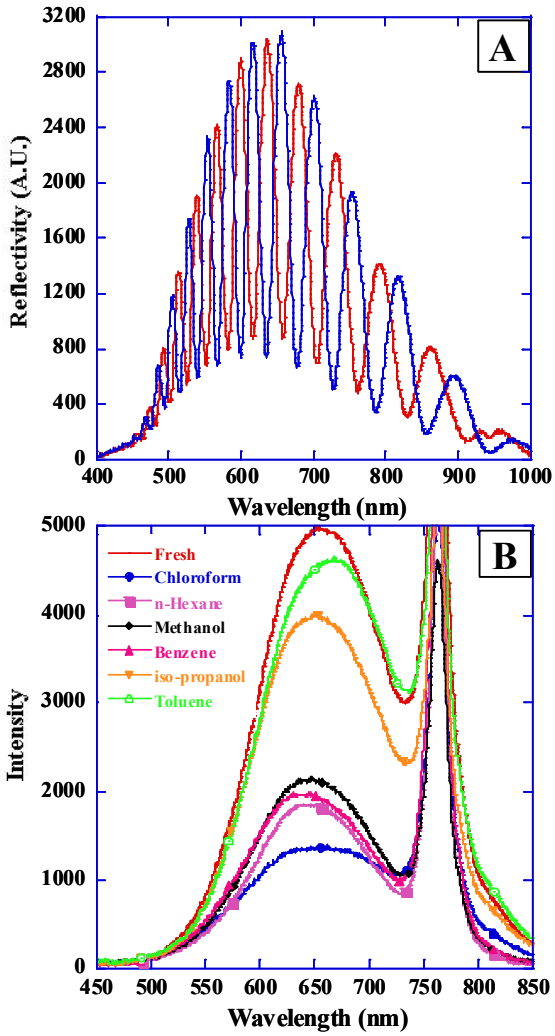

Figure 5.3. Shift of Fabry-Perot fringe pattern (A) and quenching photoluminescence spectra (B) under the exposure of organic vapors (Chloroform:●, n-Hexane:■, Methanol:◆, Benzene:▲, iso-propanol:▼ Toluene:⦿).

Plot for the relationship between the vapor pressure of analytes and quenching photoluminescence (%) was shown in Figure 5.4(A). Results from these studies indicated that quenching photoluminescence depended on vapor pressure of analytes not a degree of hydrophilicity/hydrophobicity which imparted to increase the ability of chloroform to quench the photoluminescence from the material, eventhough the porous Si had a hydrophobic Si-H surface. Analyte having higher vapor pressure exhibited higher degree of quenching photoluminescence. It was reported that the quenching of photoluminescence adequately fitted a dynamic Stern-Volmer quenching model yielding straight lines between the quenching of photoluminescence and quencher concentration.[24] The deviation from the straight line in Figure 5.4(A) resulted from both the surface characteristics of porous Si and hydrophilicity/hydrophobicity of analyte measured.

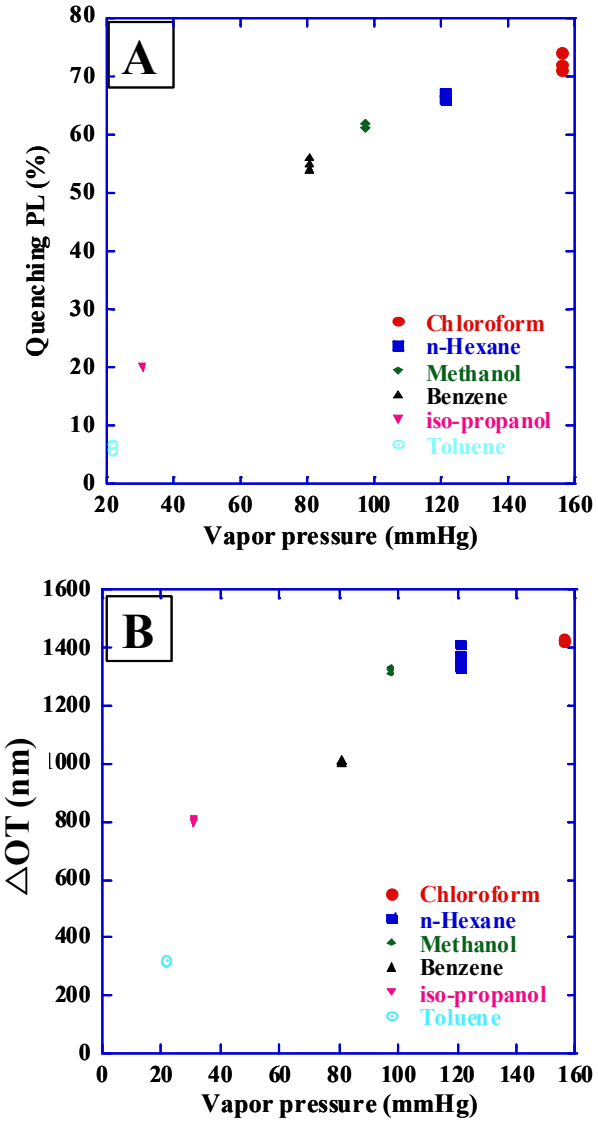

Figure 5.4. Plot for the relationship between the vapor pressure of analytes and quenching photoluminescence (%) (A), the vapor pressure of analytes and change of optical thickness (B).

The value of *nL* from *eq 2*, optical thickness, is obtained from the position of the peak in the Fourier transformed plot of reflected intensity versus frequency. The refractive index, *n*, in *eq 2* is a composite index comprising a porosity-weighted average of Si and the medium filling the pores.[27] A faster and more convenient method of extracting the optical parameters is based on a fast Fourier transform (FFT) of the spectrum. The FFT can provide more reliable data for complicated optical structures, in particular when the optical constants are changing due to analyte admission into the pores.[28] Values of *OT* were obtained directly from a fast Fourier transform of the Hanning-modified reflectance spectra. Plot for the relationship between the vapor pressure of analytes and change of *OT* was shown in Figure 5.4(B). Results indicated that the change of *OT* depended on vapor pressure of analytes. Analyte having higher vapor pressure exhibited greater change OT in porous Si. The amplitude of ΔOT would depend on refractive index and vapor pressure of the analyte, and the surface characteristics and the pore diameter of porous Si. Since the parameter for porous Si was fixed, ΔOT depended on refractive index and vapor pressure of an individual analyte as well as molecular polarity. A test set of compounds were analyzed by both quenching photoluminescence and ΔOT. The results were summarized in Table 5.1.

Table 5.1. Change of OT and quenching photoluminescence under the exposure of different analytes.

Organic compounds	Vapor pressure (mmHg)	Δ OT (nm)			Quenching photoluminescence (%)		
		Entry 1	Entry 2	Entry 3	Entry 1	Entry 2	Entry 3
Chloroform	156.05	1429	1430	1429	74	72	71
n-Hexane	121.26	1372	1333	1412	66	66	67
Methanol	97.48	1315	1330	1324	62	62	61
Benzene	80.85	1015	1008	1003	56	54	55
iso-propanol	30.93	799	797	804	20	20	20
Toluene	21.68	318	316	320	6	6	7

Figure 5.5 was the 2D map obtained from Table 5.1. Porous Si sample was exposed to each analyte three times. Each analyte was represented by a cluster of points. The smaller the area of the clusters indicated the better the reproducibility, and the larger the distance between different clusters indicated the better the discrimination. These results demonstrated the potentiality of porous Si sensors for artificial electronic nose applications.

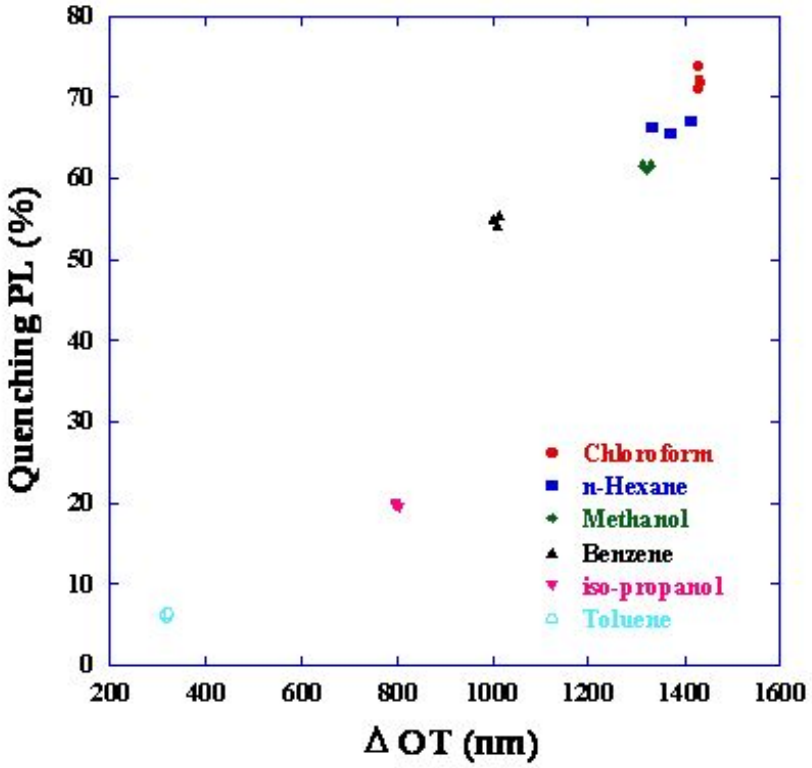

Figure 5.5. 2-D map resulting from the change quenching photoluminescence and change of optical thickness under the exposure of various organic analytes (Chloroform:●, n-Hexane:■, Methanol:◆, Benzene:▲, iso-propanol:▼ Toluene:⊙).

5.4 Conclusions

Porous Si displaying both strong red photoluminescence in the visible region and well defined Fabry-Perot interferometric fringes in the optical reflectivity spectrum were successfully prepared. The use of porous Si sensors was investigated using two transduction modes: photoluminescence quenching and Fabry-Perot optical interferometry. Quenching photoluminescence and change of optical thickness depended on vapor pressure of analytes. 2D map indicated that individual analyte was located in a cluster of points to give better the discrimination. Potential use of porous Si sensors for artificial electronic nose applications was demonstrated.

5.5 References

[1] K. D. Hirschman, L. Tsybeskov, S. P. Duttagupta, and P. M. Fauchet, *Nature* **384**, 338 (1996).

[2] H. Sohn, S. Letant, M. J. Sailor, and W. C. Trogler, *J. Am. Chem. Soc.* 122, 5399 (2000).

[3] V. S. Lin, K. Motesharei, K. S. Dancil, M. J. Sailor, and M. R. Ghadiri, *Science* **278**, 840 (1997).

[4] M. Simion, I. Kleps, T. Neghina, A. Angelescu, M. Miu, A. Bragaru, M. Danila, E. Condac, M. Costache, and L. Savu, *J. Alloy. Compd.* **434**, 830 (2007).

[5] S. Ilyas, T. B?cking, K. Kilian, P. J. Reece, J. Gooding, K. Gaus, and M. Gal, *Opt. Mater.* **29**, 619 (2007).

[6] M. A. Khan, M. S. Haque, H. A. Naseem, W. D. Brown, and A. P. Malshe, *Thin Solid Films* **332**, 93 (1998).

[7] S. E. Letant, S. Content, T. T. Tan, F. Zenhausern, and M. J. Sailor, *Sensor Actuat. B- Chem.* **69**, 193 (2000).

[8] R. L. Smith and S. D. Collins, *J. Appl. Phys.* **71**, R1 (1992).

[9] R. C. Anderson, R. S. Muller, and C. W. Tobias, *Sens. Actuat.* **A21-A23**, 835 (1990).

[10] M. Ben-Chorin, A. Kux, and I. Schechter, *Appl. Phys. Lett.* **64**, 481 (1994).

[11] J. M. Lauerhaas and M. J. Sailor, *Science* **261**, 1567 (1993).

[12] C. L. Curtis, V. V. Doan, G. M. Credo, and M. J. Sailor, *J. Electrochem. Soc.* **140**, 3492 (1993).

[13] K.-P. S. Dancil, D. P. Greiner, and M. J. Sailor, *J. Am. Chem. Soc.* **121**, 7925 (1999).

[14] S. Letant and M.J. Sailor, *Adv. Mater.* **12**, 355 (2000).

[15] S. Jang, J. Kim, Y. Koh, Y. C. Ko, H. -G. Woo, and H. Sohn, *J. Nanosci. Nanotechnol*. **7**, 4049 (2007).

[16] S. Jang, Y. Koh, J. Kim, J. Park, C. Park, S. J. Kim, S. Cho, Y. C. Ko and H. Sohn, *Mater. Lett.* **62**, 552 (2008).

[17] P. A. Snow, E. K. Squire, P. S. J. Russell, and L. T. Canham, *J. Appl. Phys.* **86**, 1781 (1999).

[18] S. G. Kim, S. Kim, Y. C. Ko, S. Cho, and H. Sohn, *Colloids Surf. A: Physicochem. Eng. Aspects* **31**3, 398 (2008).

[19] S. Jang, J. Kim, Y. Koh, J. Park, H.-G. Woo, S. Kim, and H. Sohn, *J. Nanosci. Nanotechnol.* **8**, 5166 (2008).

[20] A. G. Cullis, L. T. Canham, and P. D. J. Calcott, *J. Appl. Phys.* **82**, 909 (1997).

[21] M. Ben-Chorin, A. Kux, and I. Schechter, *Appl. Phys. Lett.* **64**, 481 (1993).

[22] J. L. Coffer, S. C. Lilley, R. A. Martin, and L. A. Files-Sesler, *J. Appl. Phys.* **74**, 2094 (1993).

[23] J. Harper and M. J. Sailor, *Anal. Chem*. **68**, 3713 (1996).

[24] J. H. Song and M. J. Sailor, *J. Am. Chem. Soc*. **119**, 7381 (1997).

[25] D.-A. Kim, J.-H.Shim, and N.-H. Cho, *Appl. Surf. Sci.* **234**, 256 (2004).

[26] M. C. Ko and G. J. Meyer, *Chem. Mater*. **7**, 12 (1995).

Chapter Six
DBR PSi/PMMA Composite Materials for Smart Patch Application

6.1 Introduction

PSi prepared by the electrochemical etching of crystalline silicon wafer has been investigated extensively, since the discovery of its luminescence properties in 1990.[1] Nanostructured PSi has a high surface area, which has shown to be useful for many applications, such as chemical and biological sensors,[2,3] switching devices,[4] implantable biomaterials,[5] drug delivery,[6] and in high-throughput screening.[7] Developments of new bio-materials for the controlled release of drugs are of great interest. Biocompatible polymers,[8] highly branched dendrimers,[9,10] and quantum dots[11-13] are widely studied for drug delivery system. One of the interesting drug delivery system is a smart patch type application, which is required to monitor the status of the drug release. DBR PSi exhibits a high reflectivity band with the Bragg wavelength Bragg, depending on the thickness of the layers (d_1, d_2) and the corresponding refractive indices (n_1, n_2). The mth order of the Bragg peak is given by:

$$m\lambda_{Bragg} = 2(d_1n_1 + d_2n_2).$$

DBR PSi containing a photonic structure of Bragg filter can be generated by applying a computer generated pseudo-square current waveform. Since the spectral reflectance peaks of DBR PSi can be tuned over a wide range and the reflectance peaks can be located at wavelengths corresponding to that of relatively low

absorption in human tissue, the direct monitoring of the drug release could be possible. Here, we report the direct monitoring of the drug release by using DBR PSi/PMMA composite films for the smart patch type of drug delivery applications.

6.2 Experimental

6.2.1 Materials

HF (ACS reagent, Aldrich Chemicals), absolute ethanol (ACS reagent, Aldrich Chemicals), PMMA (99.8%, Aldrich), THF, and Caffeine (98.5%, Aldrich) were used without further purification.

6.2.2 Preparation of DBR PSi and DBR PSi/PMMA Composite Films

DBR PSi samples are prepared by electrochemical etch of heavily doped p++-type silicon wafers (boron doped, polished on the <100> face, resistivity of 0.8-1.2mΩ-㎝, Siltronix, Inc.). The etching solution consisted of a 3:1 volume mixture of aqueous 48% hydrofluoric acid (ACS reagent, Aldrich Chemicals) and absolute ethanol (ACS reagent, Aldrich Chemicals). Typical etch parameters for DBR PSi structure involves using a periodic square wave current between 5 $mA \cdot cm^{-2}$ for 90 s and 50 $mA \cdot cm^{-2}$ for 3 s with 10, 20, and 30 repeats, respectively. The thickness of DBR PSi with 20 repeats is about 11 μm. The resulting DBR PSi films have been removed from the silicon substrate by an applying of electropolishing current at 460 $mA \cdot cm^{-2}$ for 1 min in a solution of 48% aqueous HF and ethanol (3:1 by volume), and then at 22 $mA \cdot cm^{-2}$ for 2 min in a solution of 48% aqueous HF and ethanol (1:30 by volume) to obtain free-standing DBR PSi films. In a typical preparation, 100 mg of PMMA (Aldrich, Mw = 120,000) and 5 mg of caffeine (Aldrich) are dissolved in 20 mL of THF (Fisher Scientific). 3 mL of mixture solution have been cast onto the surface of

free-standing PSi film and dried at room temperature for 30 min. The thickness of composite film with 20 repeats is about 142 μm.

6.2.3 Instrumentation and Data Acquisition

Optical reflectivity spectra are measured using a tungsten-halogen lamp and an Ocean Optics S2000 CCD spectrometer fitted with a fiber optic input. The reflected light collection end of the fiber optic is positioned at the focal plane of the optical microscope. Scanning electron microscope (SEM) images are obtained by a cold field emission scanning electron microscope (FE-SEM, S-4700, Hitachi). Caffeine releases are measured by UV-vis spectrometer (UV-2401 PC, Shimazu). The quantity of caffeine release from the DBR PSi/PMMA composite is measured at the fixed absorption wavelength of 274 nm on a time scale.

6.3 Results and Discussion

Multilayered photonic crystals of DBR PSi display a very sharp line in the optical reflectivity spectrum shown in Figure 1. Prepared DBR PSi exhibits a high reflectivity at 524 nm with sidelobes around the reflectance peak. The spectral band of DBR PSi film has a full-width at half-maximum (FWHM) of 20 nm, whereas the narrowest quantum dot spectrum reported at this wavelength has a FWHM of 20 nm.[13] Free-standing DBR PSi film has been obtained from the silicon substrate by an applying of electropolishing current in a solution of HF and ethanol. After electropolishing, the free-standing DBR PSi has been coated with the mixture solution of caffeine and PMMA to produce flexible and stable composite materials in which the PSi matrix is covered with caffeine-impregnated PMMA. DBR PSi/PMMA composite materials retain their unique photonic reflectance and display a sharp spectral band at 547 nm. The optical reflectance spectrum confirms that the caffeine impregnated polymer has infiltrated the pores of the porous Si matrix. The spectral feature arising from optical interference in the PSi multilayer is shifted to longer wavelengths by 23 nm upon introduction of the polymer as shown in Figure 6.1. Such a large red shift is due to an increase in the average refractive index of the PSi multilayers, consistent with the replacement of a significant amount of empty pore volume with polymer.

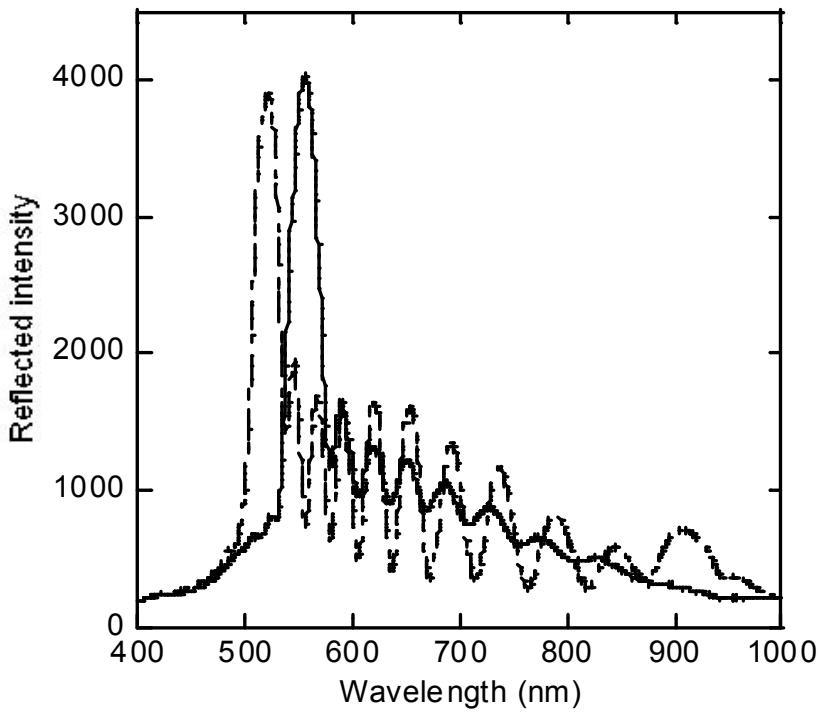

Figure 6.1. Reflectivity spectra of DBR PSi (dotted line) and DBR PSi/caffeine impregnated PMMA composite films (solid line).

Figure 6.2(A). shows the surface and cross-section SEM images of DBR PSi. The surface image of DBR PSi (A-top) indicates that the distributions of pores are even. The cross-sectional image of DBR PSi (A-side) illustrates that the multilayer of DBR PSi exhibits a depth of 11 microns and the applied square current density during the etching process results two distinct refractive indices. Free-standing DBR PSi films are typically very brittle and shatter when subjected to minor shear stresses. However, the composite films are highly flexible and display significantly improved mechanical stability without apparent degradation. Their optical properties are retained upon flexing.

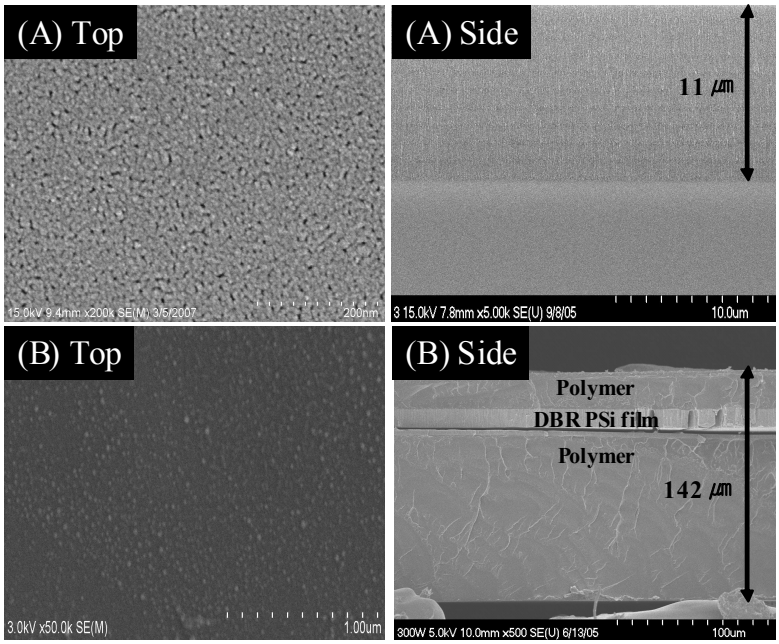

Figure 6.2. Surface and cross-section SEM images of DBR PSi (A) and DBR PSi/caffeine-impregnated PMMA composite films (B).

The surface and cross-section SEM image of DBR PSi/caffeine-impregnated PMMA composite films shown in Figure 6.2(B). indicates that the composite film is covered with polymer and its thickness is about 142 μm. These composite films are stable in aqueous HF or alkaline (3 M KOH) solutions for several days without apparent degradation. To examine the smart patch type of drug delivery application, the release of caffeine and the shift of reflection peak were simultaneously measured by the use of UV-vis and reflectance spectrometer.

The decay of reflection intensity and the shift of reflection wavelength of composite film at the fixed wavelength of 547 nm have been measured to monitor the release of drug from the composite films in pH = 7 buffer solution.

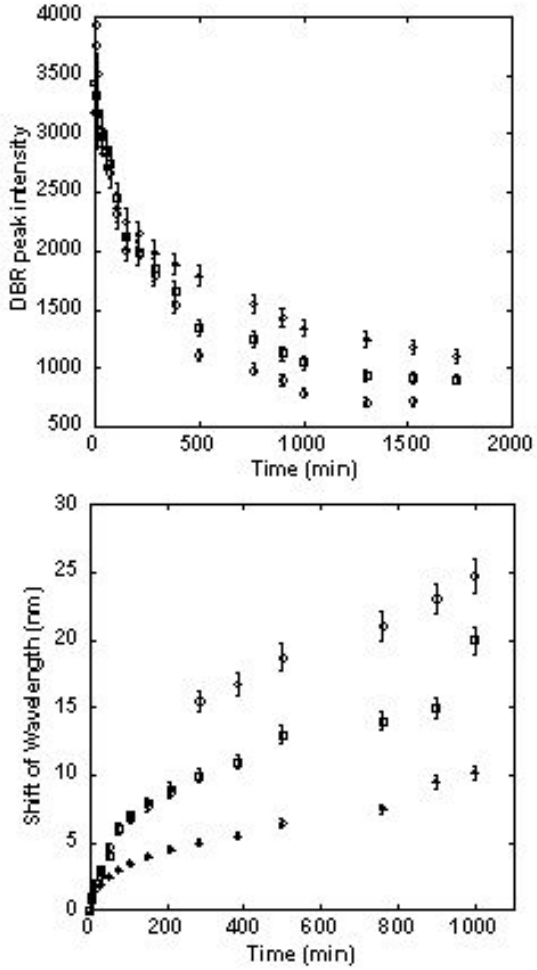

Figure 6.3. Changes of reflection intensity (top) and reflection wavelength (bottom) of the composite films at the fixed wavelength of 547 nm in buffer solution (○; 10 repeats, □; 20 repeats,◇; 30 repeats).

The intensity of reflection peak of composite film shown in Figure 6.3. is decreased exponentially as caffeine releases from the composite materials. The blue shift of reflection peak has been also observed during the caffeine release process. This results in the decrease of refractive index of composite materials due to the release of drug from composite. DBR PSi/PMMA composite films containing different periods such as 10, 20, and 30 repeats exhibit similar tendencies. The composite films with smaller repeats display more dramatic changes of intensity and wavelength in the reflection spectrum as shown in Figure 6.4.

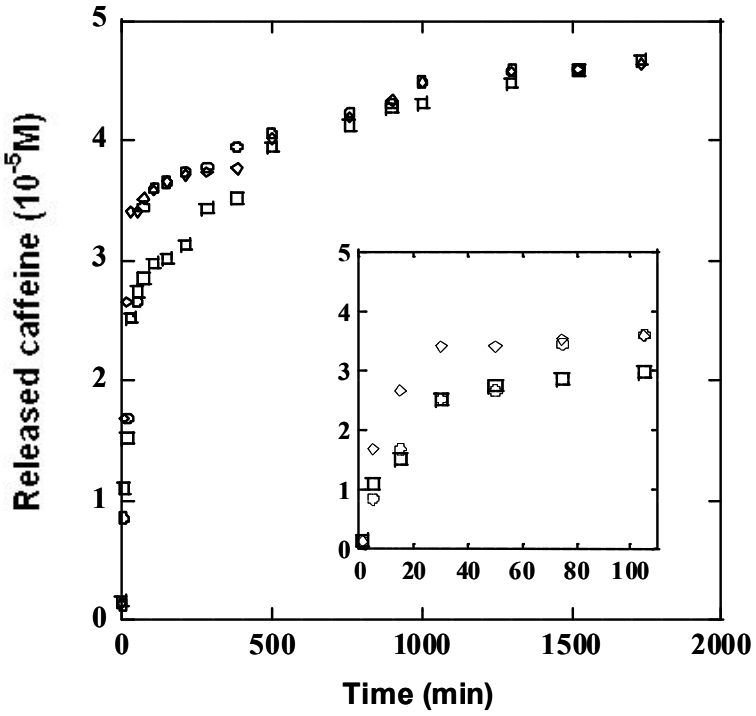

Figure 6.4. Appearance of caffeine in buffer solution (pH=7) (○; 10 repeats, □; 20 repeats, ◇; 30 repeats).

Absorption measurement for the caffeine release from the composite films in buffer solution has been achieved as a function of time at fixed wavelength of 274 nm which is the absorption maxima of caffeine. The quantity of caffeine release is about few micro moles. The concentration of released caffeine exhibits an exponential relationship with the release time. The composite films with smaller repeats release the greater quantity of caffeine in the buffer solution.

6.4 Conclusion

The use of DBR PSi/PMMA composite materials has been demonstrated for the smart patch type of drug delivery application. The composite materials are highly flexible and display significantly improved mechanical stability of porous silicon. These composite films are chemically stable in aqueous HF or alkaline (3 M KOH) solutions for several days without apparent degradation in their optical reflection spectrum. Simultaneous measurements of reflectivity and absorption confirm that the drug is released exponentially from the composite films. The composite films with greater repeats release smaller quantities of caffeine and could be a better candidate for the controlled release of drug.

6.5 Reference

[1] L. T. Canham, *J. Appl. Phys. Lett*. **57**, (1990) 1046.

[2] H. Sohn, S. Letant, M. J. Sailor, W. C. Trogler, *J. Am. Chem. Soc*. **122**, (2000) 5399.

[3] S. Chan, S. R. Horner, B. L. Miller, P. M. Fauchet, *J. Am. Chem. Soc*. **123**, (2001) 11797.

[4] V. Lehmann, R. Stengl, H. Reisinger, R. Detemple, W. Theiss, *Appl. Phys. Lett.* **78**, (2001) 589.

[5] L. T. Canham, M. P. Stewart, J. M. Buriak, C. L. Reeves, M. Anderson, E. K. Squire, P. Allcock, P. A. Snow, *Phys. Stat. Sol.* **182**, (2000) 521.

[6] Y. Y. Li, F. Cunin, J. R. Link, T. Gao, R. E. Betts, S. H. Reiver, V. C. Sangeeta N, M. J. Sailor, *Science* **299**, (2003) 2045-2047

[7] F. Cunin, T. A. Schmedake, J. R. Link, Y. Y. Li, J. Koh, S. N. Bhatia, M. J. Sailor, *Nat. Mater.* **1**, (2002) 39.

[8] C. Gong, M. H. -W. Lam, H. Yu, Adv. *Funct. Mater*. **16**, (2006) 1759.

[9] B. Helms, E. W. Meijer, *Science* **313**, (2006) 929.

[10] C. J. Hawker, J. M. J. Fauchet, *J. Am. Chem. Soc.* **112**, (1990) 7638.

[11] W. C. W. Chan, S. Nie, *Science* **281**, (1998) 2016.

[12] Y. Zhang, M. K. So, J. Rao, *Nano Lett*. **6**, (2006) 1988.

[13] M. Bruchez, M. Moronne, P. Gin, S. Weiss, A. P. Alivisatos, *Science* **281**, (1998) 2013.

Chapter Seven

Smart Particles for Noble Drug Delivery System

7.1 Introduction

The development of nanotechnologies in life science has been strongly affecting the biomedicine, both in diagnostics and therapy.[1-3] Since nanotechnology offers a suitable means of site-specific and/or time-controlled delivery of drugs and other bioactive agents,[4-6] significant efforts have been devoted to use the potentials of nanotechnology in drug delivery. In recent years, pharmaceutical nanotechnology focuses on formulating therapeutically active agents in biocompatible nanoforms such as nanoparticles, nanocapsules, micellar systems, and conjugates.

PSi has been investigated for applications in microelectronics, optoelectronics, chemical and biological sensors, and biomedical devices.[7-10] PSi fabricated by using an electrochemical etching of single crystalline silicon is a network of air holes within an interconnected crystalline silicon. PSi can be an ideal candidate for drug delivery applications, since it has a very large specific surface area on the order of few hundreds m^2/cm^3, corresponding to about thousand times of the surface area of a polished silicon wafer. The shape, size, and orientation of pores of PSi layers depend on surface orientation and the dopant level of the crystalline silicon substrate as well as the applied current density, the temperature, and the concentration of the HF etching solution.[11] PSi exhibits unique optical properties

providing a reflection band at specific wavelength in the optical reflectivity spectrum.[12,13] In addition, chemical derivatization of PSi exhibits the modification of its physical, chemical, and electronic properties.

PSi for in vivo biomaterial applications can be used as a sensitive biosensor for proteins,[14] enzymes,[15] and DNA,[16] because it can be modified with a wide range of biological or organic molecules. PSi has focused on microparticle systems due to their relative ease of fabrication, administration, and their compatibility with existing drug delivery concepts. Canham reported the in vivo use of PSi and demonstrated its resorbability and biocompatibility.[17,18] PSi as host matrices was employed to demonstrate in vivo release of the steroid dexamethasone, ibuprofen, doxorubicin, and many other drugs.[19-22] The suitability and efficacy of PSi were assessed for medical application. The oral administration of silicon to provide a dietary supplement was assessed.[23,24] Current drug delivery system based on PSi included that the free volume inside pores was loaded with a drug that would be released in the body by the dissolution of the matrix, however site-specific and/or time-controlled delivery of drug were not specified. Most of the drug delivery devices based on PSi displayed a linear release of drug within 2 h. Although efforts in this area are still in early developmental stages, the high bio-sensitive capabilities and the biocompatibility of PSi lead to new applications in tissue-based bioassays, drug delivery, and health-monitoring applications.

CPT, a pentacyclic alkaloid, isolated first by Wall and co-workers from the Chinese tree Camptotheca acuminata, shows potent cytotoxic activity against a range of tumor cell lines.[25-27] However, administration of this drug was accompanied by severe side effects, due to its poor water solubility. CPT polymeric drugs were reported to improve the therapeutic efficacy in the controlled release of drugs.[28] In this paper, PSD smart particles displaying a high reflectivity were prepared in

micron size and chemically attached with anti-cancer agent, CPT. The direct monitoring of the drug release by using PSD-CPT was observed for drug delivery applications.

7.2 Experimental

7.2.1 Materials

HF (ACS reagent, Aldrich Chemicals), absolute ethanol (ACS reagent, Aldrich Chemicals), Camptothecin (99.8%, Aldrich), and THF were used without further purification.

7.2.2 Preparation of free-standing DBR PSD film

DBR PSi samples were prepared by electrochemical etch of heavily doped p++-type silicon wafers (boron doped, polished on the (100) face, resistivity of 0.8-1.2 mΩ·㎝, Siltronix, Inc.). The etching solution consisted of a 3 : 1 volume mixture of aqueous 48% hydrofluoric acid (ACS reagent, Aldrich Chemicals) and absolute ethanol (ACS reagent, Aldrich Chemicals). Typical etch parameters for DBR PSi structure involved using a periodic square wave current between 100 $mA \cdot cm^{-2}$ for 3 s and 10 $mA \cdot cm^{-2}$ for 45 s with 50 repeats. The resulting DBR PSi film was lift off from the silicon substrate by an applying of electropolishing current at 360 $mA \cdot cm^{-2}$ for 90 s in a solution of 48% aqueous HF and ethanol (3 : 1 by volume), and then at 19 $mA \cdot cm^{-2}$ for 90 s in a solution of 48% aqueous HF and ethanol (1 : 15 by volume) to obtain a free-standing DBR PSi.
The silicon surface was predominant hydride-terminated after the etching procedure. This surface was sensitive to oxidation and hydrolysis upon exposure to aqueous solution. Thermally oxidized PSD films were obtained by heat treatment in a furnace (Thermolyne F6270-26 furnace equipped with controller) using the following

parameters: initial ramp rate, 5 ℃/min to 300 ℃; hold time, 3 h; and passive cooling to ambient temperature.

7.2.3 Chemical attachment of CPT to PSD surface and preparation of PSD-CPT smart particles

13.8 mg of (s)-(+)-camptothecin (CPT) (0.05 mmol, Aldrich Chemicals) was dissolved in 10 mL of methylene chloride. The mixture solution was stirred for 30 min, and 4-di(methylamino)pyridine (DMAP) (0.1 mmol, Aldrich Chemicals) was added to the solution. The reaction mixture was allowed to stir at room temperature for 1 h. The resulting solution was added to the oxidized PSD films and films were incubated for 72 h. Afterward the PSD films were rinsed successively with toluene, acetone, and methylene chloride and subsequently dried under a stream of nitrogen. The PSD films were made into particles by ultrasonic fracture in an organic solution and dried under an atmosphere.

7.2.4 Instrumentation and Data Acquisition

Optical reflectivity spectra were measured using a tungsten-halogen lamp and an Ocean Optics S2000 CCD spectrometer fitted with a fiber optic input. The reflected light collection end of the fiber optic was positioned at the focal plane of the optical microscope. CPT released in pH 7 aqueous buffer solution was measured by UV-vis spectrometer (UV-2401 PC, Shimazu). FT-IR spectra were acquired with a FT-IR (Nicolet 5700) instrument in the diffuse reflectance mode (Spectra-Tech diffuse reflectance attachment). Absorption spectra were reported in absorbance

units. The quantity of CPT release from the derivatized PSD smart particle was measured at the fixed absorption wavelength of 369 nm on a time scale, which was the absorption maximum of CPT. The morphology of PSD-CPT smart particles were observed with cold field emission scanning electron microscope (FE-SEM, S-4700, Hitachi).

7.3 Results and Discussion

DBR PSi exhibits a high reflectivity band with a Bragg wavelength, λBragg, depending on the thickness of the layers (L) and the corresponding refractive indices (n). The mth order of the Bragg peak is given by:

$$m\,\lambda_{Bragg} = 2nL.$$

Multilayered DBR PSi prepared by applying a square current waveform displays reflection resonances in a specific narrow spectral region. The reflectivity can be tuned to appear anywhere in the visible to near-infrared spectral range, depending on the programmed etch waveform. The electrochemical process generated an optically uniform layer of PSi. DBR PSi films were removed from the silicon wafer by applying an electropolishing current to obtain free-standing DBR films. The thermal oxidation of free-standing DBR PSi films at 300 ℃ converted the hydride-terminated surface into hydroxyl terminated DBR porous silicon dioxide films. PSD films were reacted with CPT to give PSD-CPT films and then ultrasonicated to create particles. Particles with sizes ranging from several hundred nanometers to few hundred micrometers were generated depending on the duration of ultrasonication. The chemistry of derivatization is outlined in Scheme 7.1.

The surface morphology of PSD-CPT smart particles were obtained with cold FE-SEM and shown in Figure 7.1. Size of PSD-CPT smart particles was about 20 ~ 40 micrometers. The surface image of PSD-CPT smart particles indicated that the pore size of particle retained a good porosity without destruction of porous structure during ultrasonication. The prepared PSD-CPT smart particles had cylindrical macropores with the average pore size of 100 nm.

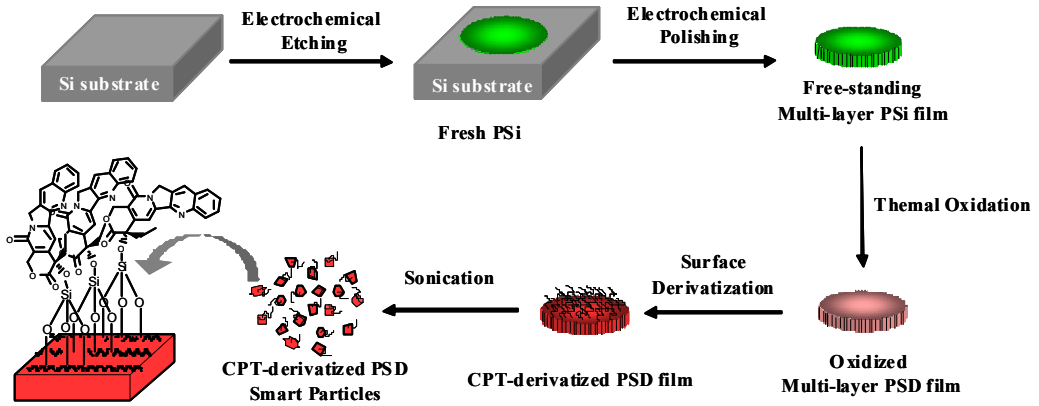
Si substrate
Electrochemical Etching
Si substrate
Fresh PSi
Electrochemical Polishing
Free-standing Multi-layer PSi film
Themal Oxidation
Oxidized Multi-layer PSD film
Surface Derivatization
CPT-derivatized PSD film
Sonication
CPT-derivatized PSD Smart Particles

Scheme 7.1.

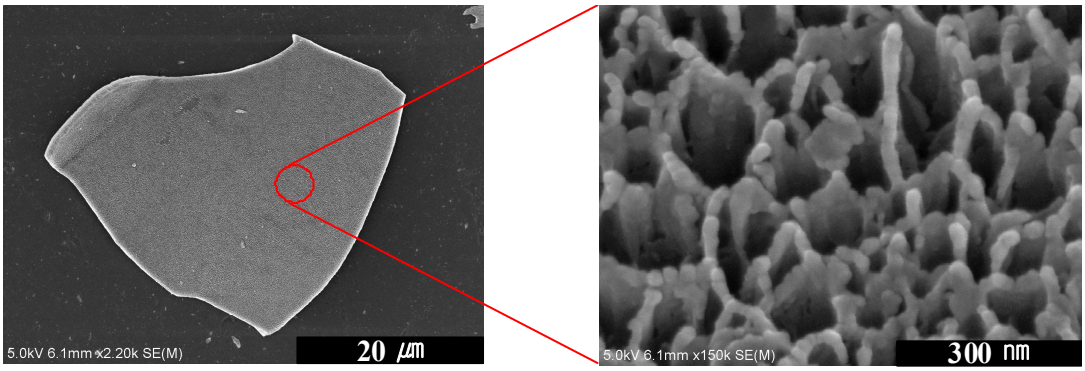

Figure 7.1. Surface FE-SEM image of PSD-CPT smart particles.

Prepared DBR PSi displayed a very sharp line at 612 nm in the optical reflectivity spectrum as shown in Figure 7.2. The spectral band of DBR PSi had a full-width at half-maximum (FWHM) of 18 nm. One of the most unique features of DBR PSi was that its reflective spectral band was much narrower than the fluorescence spectrum obtained from an organic dye or core-shell quantum dot. The thermal oxidation of DBR PSi to PSD film exhibited the reflectivity at 568 nm blue shift wavelengths by 44 nm due to the decrease of refractive index of silicon dioxide from silicon. After surface derivatization with CPT, PSD-CPT film displayed a reflectance spectral line at 579 nm in the optical reflectivity spectrum. The spectral feature arising from optical interference in PSD-CPT film was red shift of wavelengths by approximately 11 nm upon chemical introduction of CPT. Such a shift was due to an increase in the average refractive index of PSD films, consistent with the replacement of a significant amount of empty pore volume with CPT.

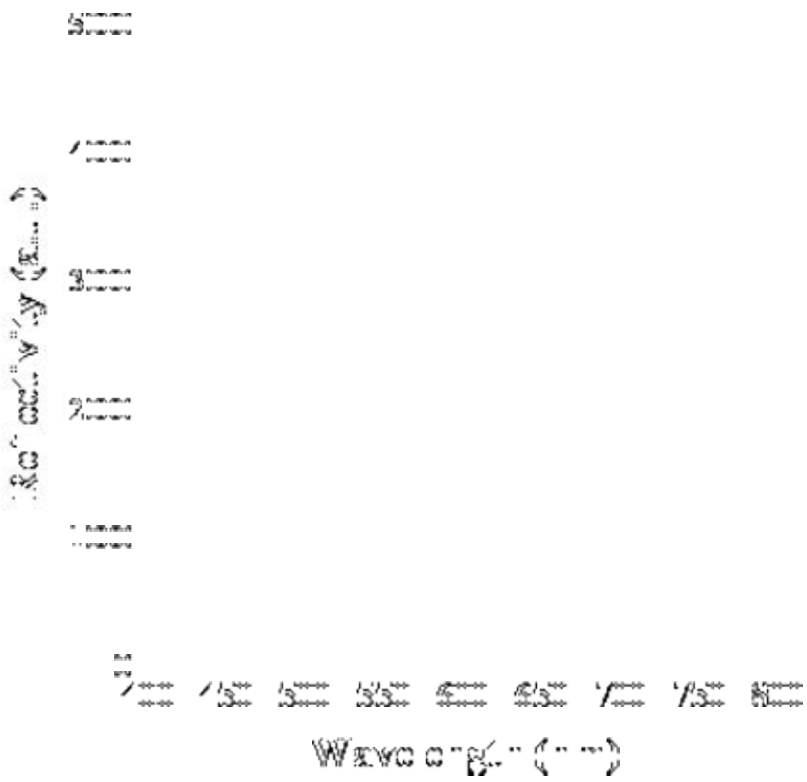

Figure 7.2. Reflectivity spectra of fresh DBR PSi (solid line), DBR PSD film (dotted line), and CPT-derivatized PSD smart particles (bold dotted line).

These step by step procedures were monitored by diffuse reflectance FT-IR spectroscopy as shown in Figure 7.2. Figure 7.3(A). showed that the FT-IR spectrum of freshly etched DBR PSi displayed a characteristic broad band centered at 2100 and 900 cm^{-1} for the υ(Si-H) stretching vibration and δ(Si-H) bending vibration. Thermally oxidized PSD films were prepared by heating freshly etched DBR PSi films in pure O_2 at 300 ℃ for 3 h. After the thermal oxidation of DBR PSi film, the presence of silicon oxide was determined by FT-IR measurement as shown in Figure 7.3(B). Thermal oxidation of the porous silicon layer resulted significant loss of intensity of the υ(Si-H) modes in the infrared spectrum at 2150 cm^{-1}, but vibrational bands due to oxygen-back-bonded silicon hydride, υ(OSi-H) and δ(OSi-H) modes, grew at 2300 and 850 cm^{-1},respectively. Multiple silicon oxide species, Si-O-Si, displayed a strong, very broad absorption band between 1000 and 1250 cm^{-1}. Although we were not able to quantify the coverage levels of Si-H and Si-OH on an absolute scale, the areas of the infrared absorption bands provided a measure of the relative coverages on the Si-O, Si-H, and Si-OH. The relative areas of the aborption bands indicated that PSD samples contained the most O and the least H, while the fresh DBR PSi samples contained more silicon hydride species and less silicon oxide species on their surfaces. In a separate experiment, the areas of the υ(Si-H), υ(OSi-H), υ(Si-O), and υ(Si-OH) bands for DBR PSi in the infrared spectrum were measured in situ during thermal oxidation. There is an increase in the Si-O or OSi-H bands and a decrease in the Si-H bands over time.[29] The thermal oxidation of DBR PSi film results the reflectivity shifted to shorter wavelengths due to the decrease of refractive index of silicon dioxide from silicon.

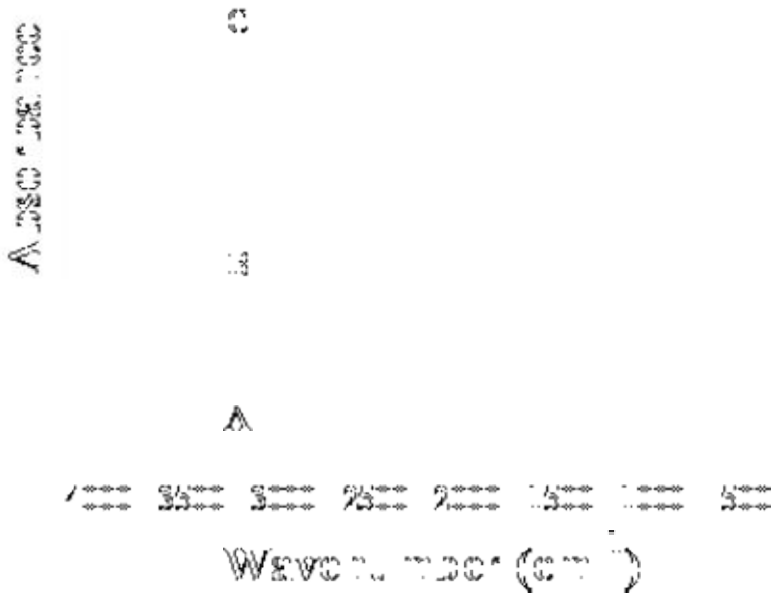

Figure 7.3. Transmission-mode FT-IR spectra of fresh PSi sample (A), thermal oxidized PSi sample (B), and CPT-derivatized PSD sample (C)

Condensation of the Si-OH surface of PSD with CPT generated a surface-bound CPT. The FT-IR spectrum shown in Figure 7.3(C). displayed additional bands characteristic of CPT (the aromatic C=C band of υ(C=C) at 1650 cm^{-1} and 1570 cm^{-1}, respectively. Surface derivatization led to complete disappearance of the OSi-H vibrational bands.

Prepared PSD-CPT smart particles were placed at the bottom of 3 mL quartz cuvette containing the buffer solution. The appearance of CPT in solution was determined by monitoring the UV absorbance band. Prepared PSD-CPT smart particles were stable in buffer solutions for several days without apparent degradation. To examine the drug delivery application, the release of CPT and the shift of reflection peak were simultaneously measured by the use of UV-vis and reflectance spectrometer. The release process of CPT from the PSD-CPT smart particles shown in Scheme 7.2. involved the hydrolysis between PSD and CPT.

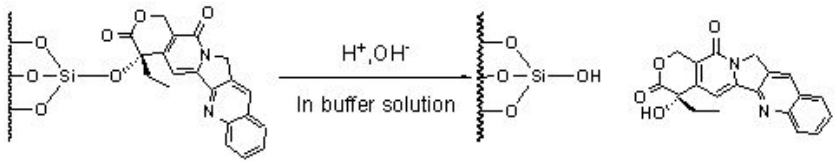

Scheme 7.2 .

Absorption measurement for the CPT release from the PSD-CPT smart particles in pH=7 buffer solution was achieved as a function of time at fixed wavelength of 369 nm which was the absorption maxima of CPT. The PSD-CPT smart particles displayed a linear release profile for the first 6 h, and then slowly released CPT for 12 h, corresponding to complete the hydrolysis of PSD-CPT smart particles as shown in Figure 7.4. Approximately 0.8 g of CPT was loaded and released from

PSD-CPT smart particles. It was reported that PSi loaded with steroid in absence of chemical attachment between drug and PSi displayed a dramatic release of drug for the first 2 h.[19] However, our PSD-CPT smart particles exhibited much slower release pattern of drug and better release profile over a period due to the chemical attachment between drug and PSi support

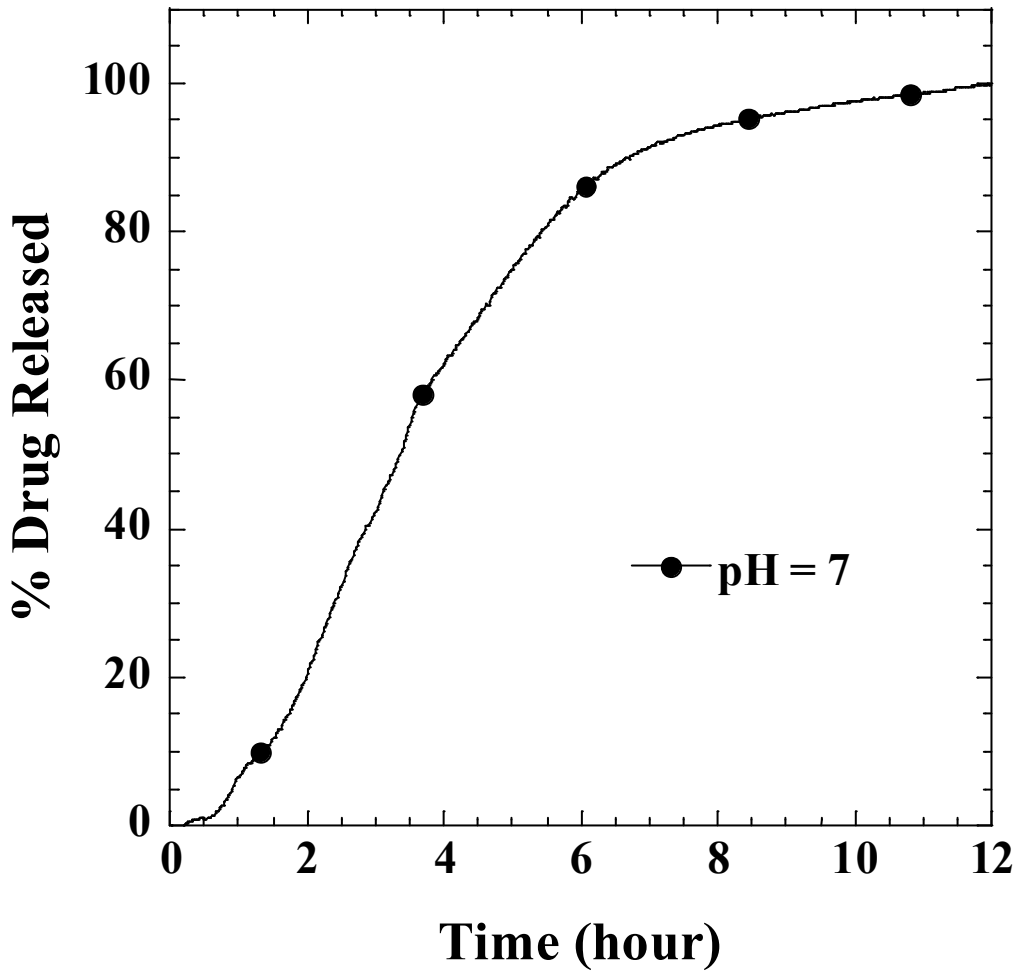

Figure 7.4. Percent of CPT appearing in buffer solution as a function of time, measured by monitoring the UV-vis absorption band at 369 nm in the solution.

Drug release from PSD-CPT smart particles was also quantified by simultaneous measurements of UV absorbance spectroscopy and interferometric spectroscopy and shown in Figure 7.5. Control experiments performed with no drug loaded displayed no detectable change in reflection wavelength within the first 6 h on PSD-CPT smart particles. There was a linear correlation between the absorbance of drug released from PSD-CPT smart particles and the change in reflection wavelength, measured during the first 6 h.

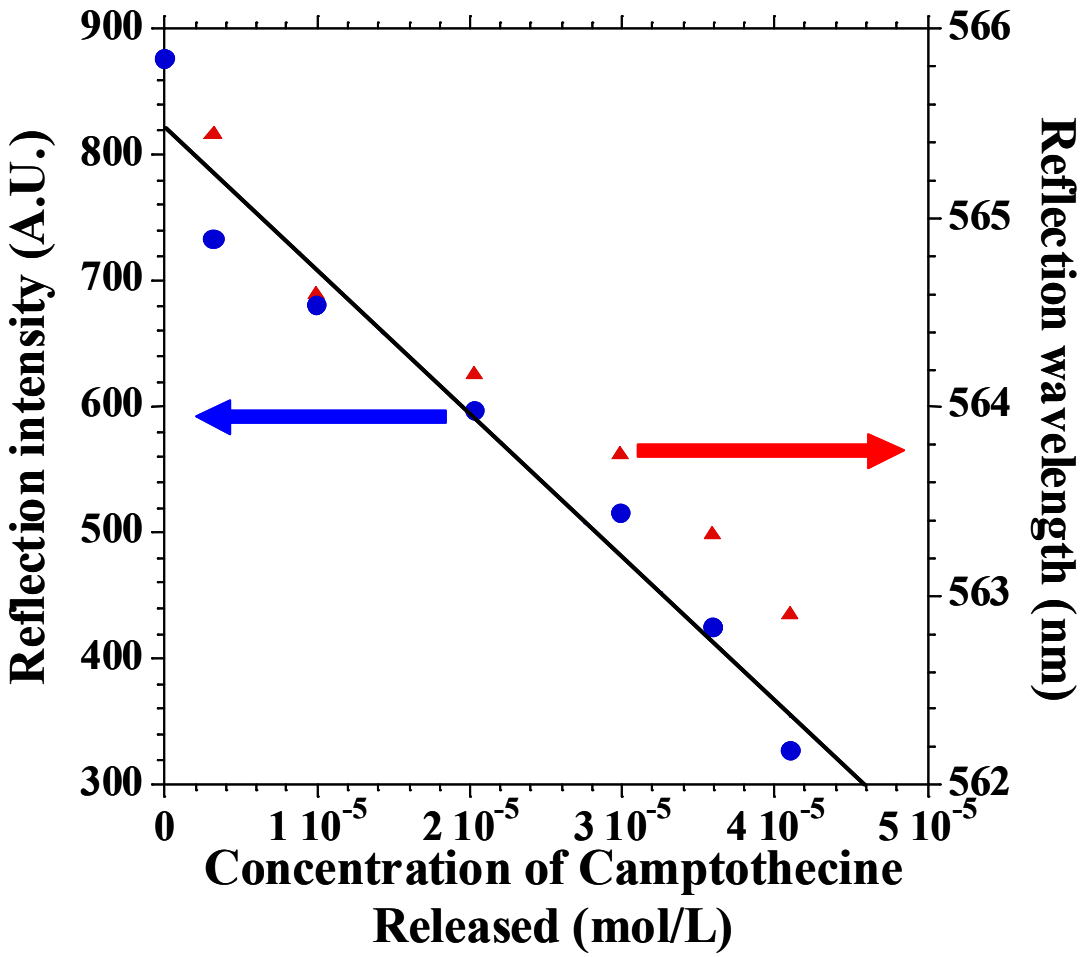

Figure 7.5. Correlation of the reflection wavelength and intensity to the concentration of drug appearing in buffer solution over a 6-h period.

7.4 Conclusion

The use of PSD smart particles based on DBR PSi has been demonstrated for the drug delivery application. Loading of CPT was achieved in PSD-CPT smart particles. DBR PSi films were removed from the silicon wafer by applying an electropolishing current to obtain free-standing DBR films. The thermal oxidation of free-standing DBR PSi films converted the hydride-terminated surface into hydroxyl terminated PSD. PSD films were reacted with CPT and then ultrasonicated to create particles to give PSD-CPT smart particles. Condensation of the Si-OH surface of PSD with CPT generated a chemically attached CPT. The appearance of CPT in solution was determined by monitoring the UV-vis absorbance band. The release of CPT and the shift of reflection peak were simultaneously measured by the use of UV-vis and reflectance spectrometer. The release mechanism of CPT from the PSD-CPT smart particles involved the hydrolysis between PSD and CPT. The PSD-CPT smart particles displayed a linear release profile, corresponding to complete the hydrolysis of PSD-CPT smart. Approximately 0.8 g of CPT was loaded and released from PSD-CPT smart particles. PSD-CPT smart particles exhibited much slower release pattern of drug and better release profile compare to porous silicon loaded drug without chemical bonding attachment between drug and PSi support. A linear correlation between the absorbance of drug released from PSD-CPT smart particles and the change in reflection wavelength was observed during the release of drug.

7.5 Reference

[1] D. A. LaVan, T. McGuire, and R. Langer, *Nat. Biotechnol.* **21**, 1184 (2003).

[2] B. Ziaie, A. Baldi, M. Lei, Y. Gu, and R. A. Siegel, *Adv. Drug Deliv. Rev.* **56**, 145 (2004).

[3] L. M. Bonanno, and L. A. DeLouise, *Biosens. Bioelectron.* **23**, 444 (2007).

[4] L. Vaccari, D. Canton, N. Zaffaroni, R. Villa, M. Tormen, and E. D. Fabrizio, *Microelectron. Eng.* **83**, 1598 (2006).

[5] E. J. Anglin, L. Cheng, W. R. Freeman, and M. J. Sailor, *Adv. Drug Deliv. Rev.* **60**, 1266 (2008).

[6] Y. Y. Li, F. Cunin, J. R. Link, T. Gao, R. E. Betts, S. H, Reiver, V. Chin, S. N. Bhatia, and M. J. Sailor, *Science* **299**, 2045 (2003).

[7] H. Sohn, S. Letant, M. J. Sailor, and C. Trogler, *J. Am. Chem. Soc.* **122**, 5399 (2000).

[8] C. A. Canaria, M. Huang, Y. Cho, J. L. Heinrich, L. I. Lee, M. J. Shane, R. C. Smith, M. J. Sailor, and G. M. Miskelly, Adv. *Funct. Mater.* **12**, 495 (2002).

[9] V. S. Lin, K. Motesharei, K. S. Dancil, M. J. Sailor, and M. R. Ghadiri, *Science* **278**, 840 (1997).

[10] S. Jang, J. Kim, Y. Koh, Y. C. Ko, H.-G. Woo and H. Sohn, J. *Nanosci. Nanotechnol.* **7**, 4049 (2007).

[11] R. L. Smith and S. D. Collins, *J. Appl. Phys*. **71**, R1 (1992).

[12] M. S. Yoon, K. H. Ahn, R. W. Cheung, H. Sohn, J. R. Link, F. Cunin, and M. J. Sailor, *Chem. Commun*. **680**, (2003).

[13] J. Kim, S. Jang, Y. Koh, C. Park, H.-G. Woo, S. Kim, and H. Sohn, *J. Nanosci. Nanotechnol.* **8**, 4951 (2008).

[14] T. Laurell, J. Drott, L. Rosengern, and K. Lindstrom, Sensor. *Actuat. B-*

Chem. **31**, 161 (1996).

[15] J. Drott, K. Lindstrom, L. Rosengren, and T. J. Laurell, *Micromech. Microeng.* **7**, 14 (1997).

[16] K. L. Beattie, W. G. Beattie, L. Mengm S. L. Turner, R. Coral-Vazquez, D. D. Sith, P. M. Mclntyre, and D. D. Dao, *Clin. Chem.* **41**, 700 (1995).

[17] L. T. Canham, *Adv. Mater.* **7**, 1033 (1995).

[18] L. T. Canham, C. L. Reeves, D. O. King, P. J. Branfileld, J. G. Crabb, and M. C. L. Ward, *Adv. Mater.* **8**, 850 (1996).

[19] E. J. Anglin, M. P. Schwartz, V. P. Ng, L. A. Perelman, and M. J. Sailor, *Langmuir* **20**, 11264 (2004).

[20] C. Charnay, S. Begu, C. Tourne-Peteilh, L. Nicole, D. A. Lerner, and J. M. Devoisselle, *Eur. J. Pharm. Biopharm*. **57**, 533 (2004).

[21] J. L. Coffer, J. L. Montchamp, J. B. Aimone, and R. P. Weis, *Phys. Status Solidi A-Appl. Res*. **197**, 336 (2003).

[22] J. Salonen, A. M. Kaukonen, J. Hirvonen, V. P. Lehto, *J. Pharm. Sci.* **97**, 632 (2008).

[23] H. M. Macddonald, A. E. Hardcastle, R. Jugdaohsingh, D. M. Reid, and J. J. Powell, *J. Bone Miner. Res.* **20**, S393 (2005)

[24] L. T. Canham, *Nanotechnology* **18**, (2007)

[25] M. E. Wall, M. C. Wani, K. H. Cook, A.T. McPhail, and G. A. Sim, J. *Am. Chem. Soc.* **88**, 3888 (1966).

[26] M. E. Wall, M. C. Wani, and H. Taylor, *Cancer Chemothe.r Rep.* **60**, 1011 (1976).

[27] M. E. Wall and M. C. Wani, *Cancer Res*. **55**, 753 (1995).

[28] N.-J. Lee, S.-J. Lee, S.-H. Kim, Y.-S. Kang, S.-B. Moon, H. Sohn, K.-T. Kang, and E. A. Theodorakis, *J. Eur. Polym.* **40**, 1291 (2004)

[29] Y. Koh, S.J. Kim, J. Park, C. Park, S. Cho, H.-G. Woo, Y. C. Ko, and H. Sohn, *Bull. Korean Chem. Soc.* **28**, 2083 (2007)

Chapter Eight

Simply Modified Biosensor for the Detection of Human IgG Based on Protein A-Modified Porous Silicon Interferometer

8.1 Introduction

Recently, the worth noting properties of nano structured PSi in chemical and biological sensing was reported.[1-5] The PSi optical sensing features were based on the changes of its photonic properties, such as photoluminescence or reflectance, on exposure to the gaseous or liquid substances.[6-7] Two main optical transduction methods for label-free biosensors were both optical interferometric methods based on interferometers,[8] evanescent wave devices,[9] and grating couplers,[10] and surface plasmon methods based on metal films,[11] and colloids.[12] However they required a tedious work and very complex preparation during analysis. One way to overcome this limit would be simple chemical modification of the PSi hydrogenated-surface in order to enhance the sensor selectivity through specific biochemical interactions. For applications in high throughput drug discovery and disease diagnostics, label-free biosensors would be important due to the advantage of easy sample preparation.[13-14]

Especially, optical devices based on PSi attracted a great attention of the scientists.[15-18] Chemical modification of PSi exhibited the modification of its physical, chemical, and electronic properties. Chemical or bio molecule was detected

based on changes in the spectral interference pattern.[19-20] The rugate PSi with reflection peaks in visible spectral range was recently demonstrated to be applied for the detection of different chemical species.[21-23]

PSi was employed as a large surface area matrix for immobilization of a variety of biomolecules including enzymes,[24] DNA fragments,[25] and antibodies.[26] In the present work, a simply modified biosensor for the detection of humman IgG based on protein A-modified PSi interferometer was reported. Fabry-Perot fringes were created by the reflections of illuminated white light on the air-PSi layer and the PSi-bulk silicon interface. The induced shift in the reflection pattern caused by the change in the refractive index of the medium upon molecular interactions of species in solution with immobilized receptor within the PSi matrix was used as a sensitive method for biomolecular sensing. The simple fabrication, optical characterization, and surface functionalization of a PSi were reported. For the application as a label-free biosensor, the binding interaction with protein was investigated.

8.2 Experimental

8.2.1 Materials

HF (ACS reagent, Aldrich Chemicals), absolute ethanol (ACS reagent, Aldrich Chemicals), 1 mL of (3-aminopropyl)trimethoxysilane (99.8%, Aldrich), 1-(3-(dimethyl-amino)propyl)-3-ethylcarbodiimide hydro-chloride, EDC (99.8%, Aldrich), phosphate-buffered solution (PBS, pH=7.4), methylene chloride and toluene (99.5%, Aldrich) were used without further purification.

8.2.2 Preparation of rugate PSi Samples

The PSi was prepared by an electrochemical etching of Si wafer (boron doped, polished on the <100> face, resistivity of 0.8~1.2 mΩ·㎝, Siltronix, Inc.). The etching solution consisted of a 1 : 1 (v/v) mixture of absolute ethanol (ACS reagent, Aldrich Chemicals) and aqueous 48% hydrofluoric acid (ACS reagent, Aldrich Chemicals). Galvanostatic etching was carried out in a Teflon cell using an electrode configuration. The current density and etching time were 300 mA/cm^2 and 25 sec. The anodization current was supplied by Keithley 2420 high-precision constant current source controlled by a computer to allow the formation of PSi. To prevent the photogeneration of carriers, electrochemical etching was performed the anodization in the dark. All samples were then rinsed several times with ethanol and dried under argon atmosphere prior to use.

8.2.3 Thermal Oxiadation of Rugate PSi

The silicon surface was predominant hydride-terminated after the etching procedure. This surface was sensitive to oxidation and hydrolysis upon exposure to aqueous solution. Thermally oxidized PSi samples were obtained by heat treatment in a furnace (Thermolyne F6270-26 furnace equipped with controller) using the following parameters: initial ramp rate, 5 ℃/min to 300 ℃, hold time, 3 h and passive cooling to ambient temperature.

8.2.4 Functionalization of Oxidized Rugate PSi

For functionalization of oxidized PSi, the oxidized PSi sample was refluxed in 0.9 mL of (3-aminopropyl)trimethoxysilane (99%, Aldrich Chemicals) for 12 h. After functionalization with amine group, the sample was rinsed successively with methylene chloride, acetone, and ethanol and subsequently dried under a stream of nitrogen.

For surface modification of functionalized sample with biotin tetrafluorophenyl ester, biotin tetrafluorophenyl ester has been prepared by previously known method.27 The 100 mg of biotin tetrafluorophenyl ester was dissolved in 15 mL of dimethylformamide. The mixture solution was stirred vigorously for 10 min, and triethylamine (0.9 mL, 6 mmol) was added to the solution. The reaction mixture was allowed to stir at room temperature for 30 min. The resulting solution was added to the functionalized PSi chip and sample was incubated overnight. Afterward, sample was rinsed successively with methylene chloride, acetone, and ethanol and subsequently dried under a stream of nitrogen.

To determine the surface coverage of the immobilized aminosilane linker,

2-pyridyl-2-carboxyethyl disulfide was synthesized by previously well-known method.28 Isolated product (2-pyridyl-2-carboxyethyl disulfide, 0.2 g, 94.7 mmol) was quickly dissolved in a 10 mL of methylene chloride solution. 1-(3-(dimethylamino)propyl)-3-ethylcarbodiimide hydrochloride (100 mg, 0.6 mmol) was added to the solution. The resulting solution was allowed to stir in dry argon gas for 30 min, before funtionalization of oxidizied rugate PSi was added. The reaction mixture was stirred for 12 h at room temperature. Afterward, the chip was washed by ethanol, methylene chloride, and acetone and then dried under an atmosphere.

8.2.5 Data Acquisition

Interferometric reflectance spectra of PSi were recorded by using an Ocean Optics S2000 spectrometer fitted with a bifurcated fiber optic probe. A tungsten light source was focused onto the center of a PSi surface with a spot size of approximately 1~2 mm. Spectra were recorded with a CCD detector in the wavelength rang 400~1200 nm. The illumination of the surface as well as the detection of the reflected light was performed along an axis coincident with the surface normal. FT-IR spectra were acquired with a Nicolet model 5700 FT-IR instrument in the diffuse reflectance mode (Spectra-Tech diffuse reflectance attachment), with diffuse reflectance absorption spectra are reported in absorbance units. The morphology of PSi film was observed with cold field emission scanning electron microscope (FE-SEM, S-4700, Hitachi). 2-Thiopyridone releases were measured by UV-vis spectrometer (UV-2401 PC, Shimazu). The quantity of 2-thiopyridone release from the functionalized rugate PSi was measured at the fixed absorption wavelength of 343 nm on a time scale.

8.3 Results and Discussion

PSi prepared by applying a current density exhibits high reflectivity in a general wide spectral region. The values of thickness and refractive index satisfy the following relationship:

$$m\lambda = 2nL \cdot \sin\Theta \qquad (1)$$

Where λ is the wavelength of maximum constructive interference for spectral fringe of order m, n is the index of refraction of the porous layer and its contents, and L is the thickness of the porous layer. The optical thickness (OT) referred to as the quantity $2nL$, was obtained from Fourier transformation (FT) of the reflectivity spectrum. FT resulted in a sharp resonance indicated the quantity $2nL$. The change of OT is related to the amount of protein in the pores. The refractive index of the porous layer was changed as the pores were replaced from the PBS, protein, and human immunoglobulin G, which led to the change of optical thickness.

The pore shape, pore size, and orentation of porous silicon layers depend on the surface orentation and doping level and type, temperature, the current density, and the composition of the etching solution. For mono-layered PSi, an anodic etch of p-type silicon wafer with resistivities of 0.1~10 Ω·cm in ethanolic HF solution generally produced PSi single layer with a network of micropores, rather than meso- or macropores. The shape, size, and orientation of pores of PSi layers depended on surface orientation and the dopant level of the crystalline silicon substrate as well as the applied current density, the temperature, and the concentration of the HF etching solution. The pore size of p-type PSi can be increased by increasing the concentration of the dopant and decreasing the aqueous HF concentration. High current densities resulted in the desired well-defined

cylindrical macropores, rather than the random orientation of highly interconnected micropores. In this work, PSi with mesopores was successfully fabricated by using a periodic galvanostatic electrochemical etch of heavily doped p-type silicon wafer with a resistivity in the range 0.8~0.12 mΩ·cm. The value of current was 300 mA. The surface and cross sectional morphology of PSi were obtained with cold FE-SEM and shown in Figure 8.1. FE-SEM image of PSi indicated that the prepared PSi had cylindrical mesopores with the average pore size of 30 nm, which could be suitable for the detection of biomolecules such as human IgG. The PSi displayed Fabry-Perot fringes in the optical reflective spectra shown in Figure 8.2.

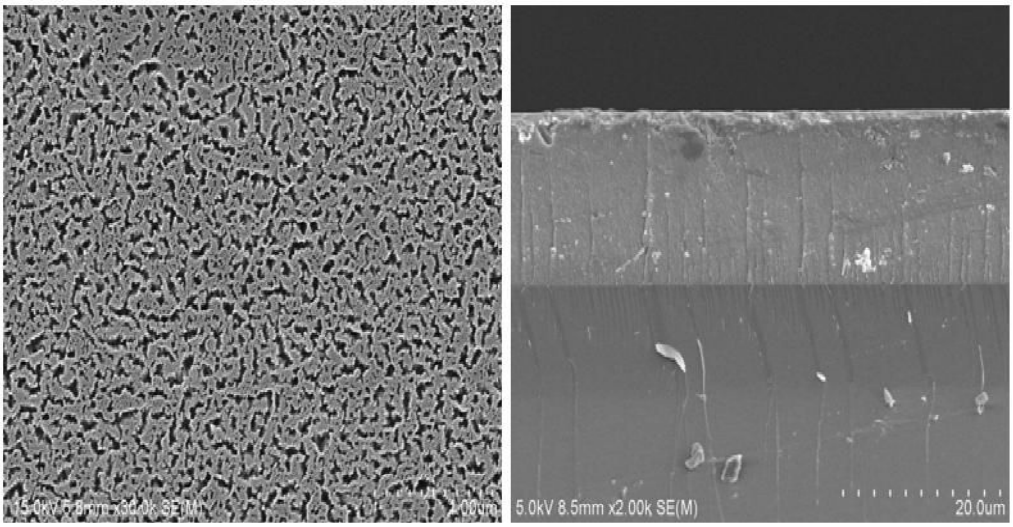

Figure 8.1. Surface and cross-sectional FE-SEM image of PSi.

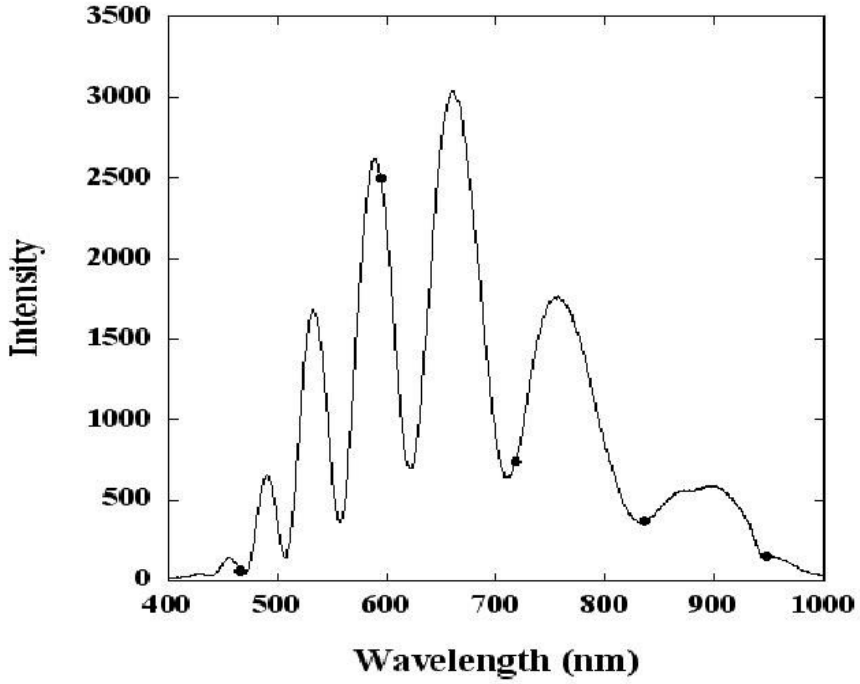

Figure 8.2. Fabry-Perot fringes in the reflection spectra of PSi.

The chemistry of functionalization was outlined in Scheme 8.1. The thermal oxidation of PSi at 300 ℃ converted the hydride-terminated surface into hydroxyl terminated PSi. Diffuse reflectance FT-IR spectroscopy was used to monitor the oxidation and functionalization reaction of PSi sample. Figure 8.3(A). showed that the FT-IR spectrum of PSi layer immediately after anodization of the silicon wafer displayed a characteristic broad band centered at 2119 and 914 cm^{-1} for the υ(Si-H) stretching vibration and δ(Si-H) bending vibration. Heavily oxidized PSi samples were prepared by heating freshly etched PSi in air at 300 ℃ for 3 h. After the thermal oxidation of PSi film, the presence of silicon oxide was determined by FT-IR measurement as shown in Figure 8.3(B). Thermal oxidation of the PSi layer resulted significant loss of intensity of the υ(Si-H) modes in the infrared spectrum at 2085-2150 cm^{-1}, but vibrational bands due to oxygen-back-bonded silicon hydride, υ(OSi-H) and δ(OSi-H) modes, grew at 2200-2250 and 877 cm^{-1}, respectively. Multiple silicon oxide species, Si-O-Si, displayed a strong, very broad absorption band between 1000 and 1200 cm^{-1}. The thermal oxidation of PSi resulted in the Fabry-Perot fringes shifted to the short wavelength due to the decrease of refractive index of silicon dioxide from silicon.

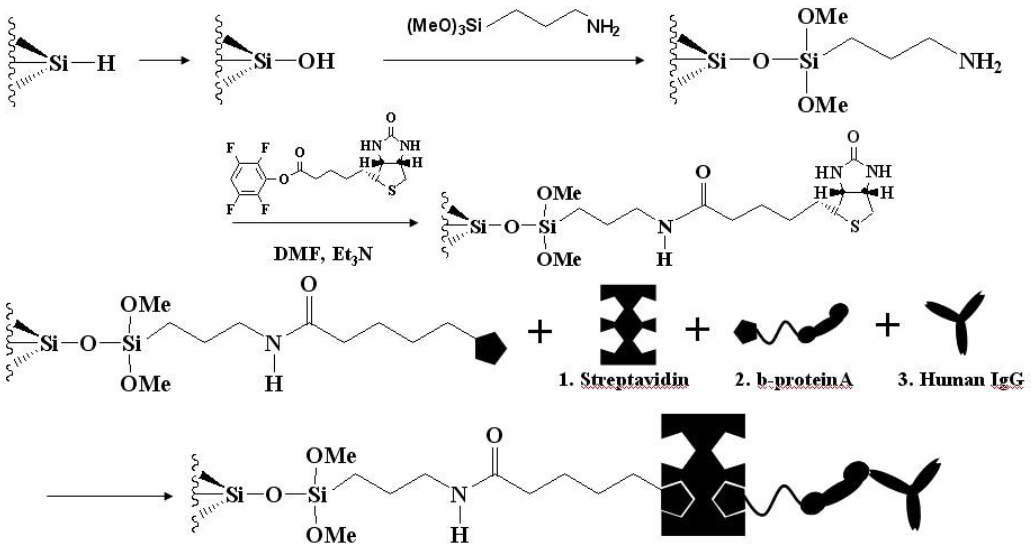
Si—H
Si—OH
(MeO)3Si
NH2
OMe
Si—O—Si
OMe
NH2
DMF, Et3N
1. Streptavidin
2. b-proteinA
3. Human IgG

Scheme 8.1.

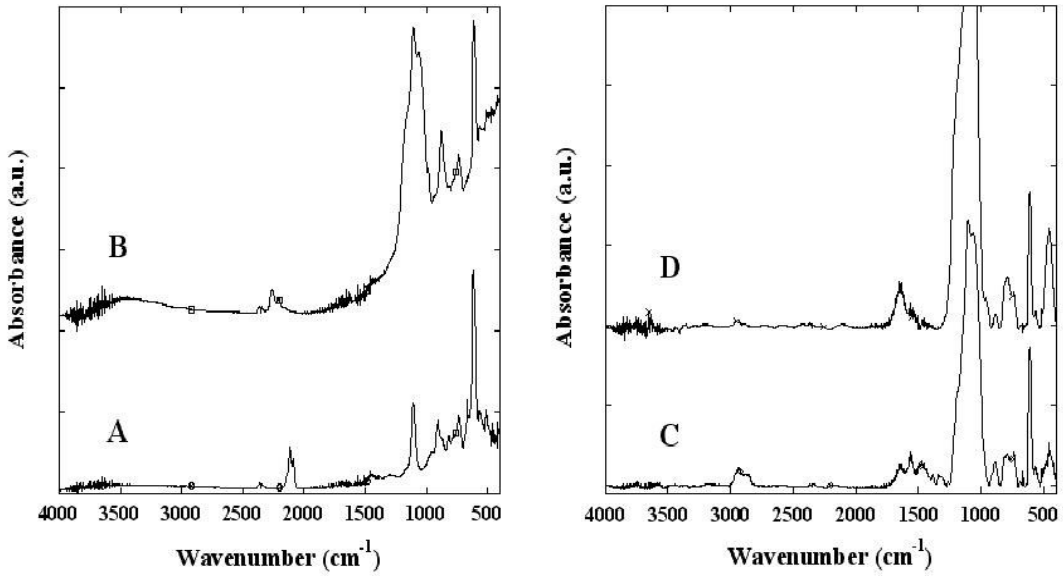

Figure 8.3. Diffuse reflectance FT-IR spectra of (A) freshly etched PSi, (B) thermally oxidized PSi, (C) the wafer after functionalization of the PSi layer with (3-aminopropyl)trimethoxysilane, and (D) PSi functionalized with biotin.

Condensation of the Si-OH surface of PSi with (3-aminopropyl)trimethoxysilane generated a surface-bound amino group. The FT-IR spectrum shown in Figure 8.3(C) displayed additional band characteristics of the linker (the amide band of υ(N-H) at 3386 cm^{-1} and δ(N-H) at 1575 cm^{-1} and the aliphatic υ(C-H) stretching bands at 2850, 2923, and 2952 cm^{-1}). Surface derivatization leads to complete disappearance of the OSi-H vibrational bands.

To determine the surface coverage of the immobilized aminosilane linker, the functionalized surface was reduced by dithiothreitol (DTT) as shown in Scheme 8.2. The released 2-thiopyridone was quantified by UV/vis spectroscopy (λ_{max} = 343 nm, ε = 8.08 × 103 $M^{-1}cm^{-1}$).[29] The number of receptor molecules in the case of a silicon chip etched with 300 mA/cm^2 was in the range 2.94 $nmol/cm^2$, which corresponds to a surface coverage of 30-80% approximately. This calculation was based on the following parameters, assuming cylindrical pores: pore radius, 30 nm; thickness of the porous layer, 13 μm; porosity, 73%; area per molecule of the biotin linker, 0.07 $Å^2$; area of the chip, 1.2 cm^2.

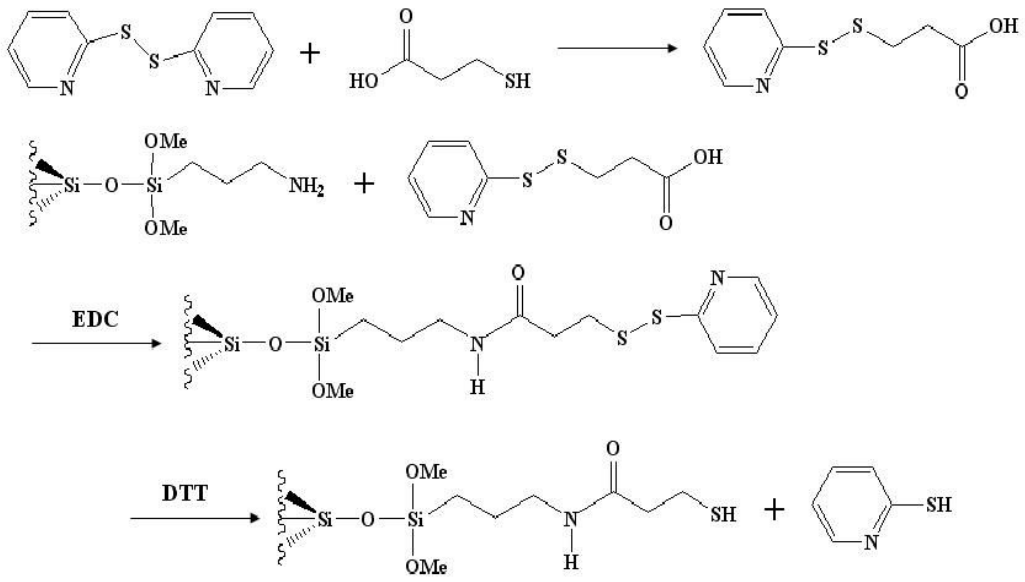

Scheme 8.2.

The subsequent reaction with biotin as shown in Scheme 8.2. led to the desired biotin-funtionalized surface which was used in the streptavidin-binding studies (Figure 8.3D). The band at 1652 cm^{-1} is assigned to the carbonyl stretching vibration of the biotin head group. The functionalized PSi was placed in the flow cell. Aqueous PBS buffer solution was flushed to perform an initial measurement of reflectivity. The surface was rinsed thoroughly with PBS buffer solution to ensure covalent attachment to the surface and to check stability of the reflectivity measurement. The cell was then flushed with a constant flow rate of 0.8 mL/min of PBS buffer solution containing protein (20 μM streptavidin, Protein A, and human IgG) which coupled to the biotin-modified PSi surface.

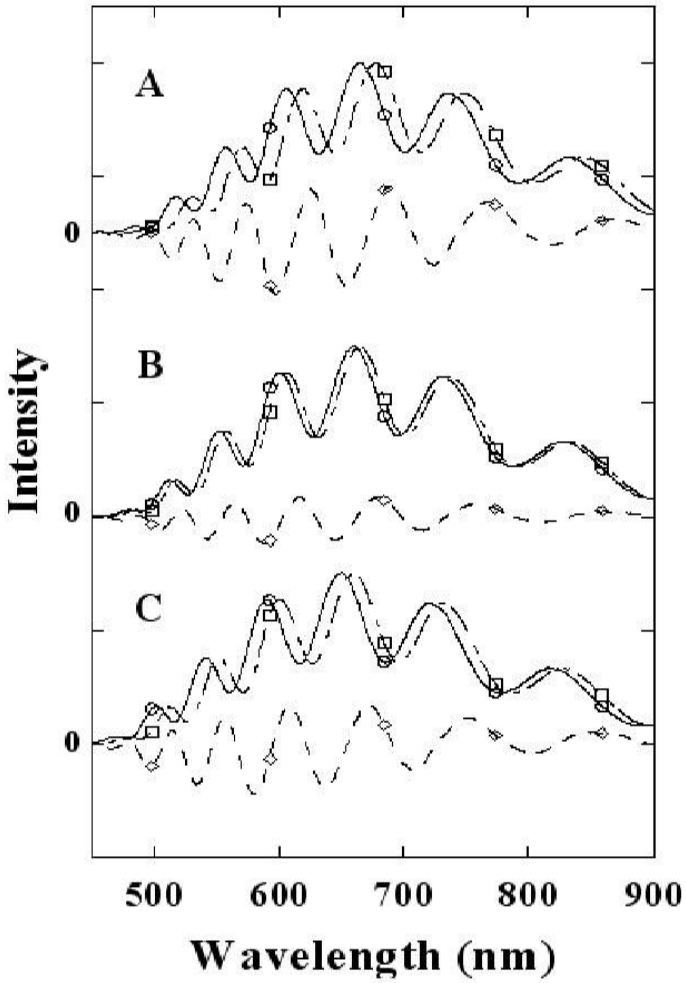

Figure 8.4. Change of Fabry-Perot fringes in the reflection spectra of biotin-fuctionalized rugate PSi sample before (solid line) and after (dashed line) exposure of streptavidin (A), biotinylated protein A (B), and human Ig G (C) The dotted line in each case are the difference between spectra obtained in the presence and absence of protein.

Figure 8.4. showed the change of reflection spectrum under the exposure of protein to the biotin-functionalized PSi chip. As expected, exposed to a solution of streptavidin to the biotin-dervatized porous layer resulted in an increase in the red shift of fringe pattern, indicative of a change in refractive index induced by binding of the protein into the biotin-derivatized PSi film. This increase was attributed to the replacement of some of the aqueous phases with protein in PBS buffer solution. The change in the effective optical thickness was due to binding of proteins having a higher refractive index than the water in the pores.

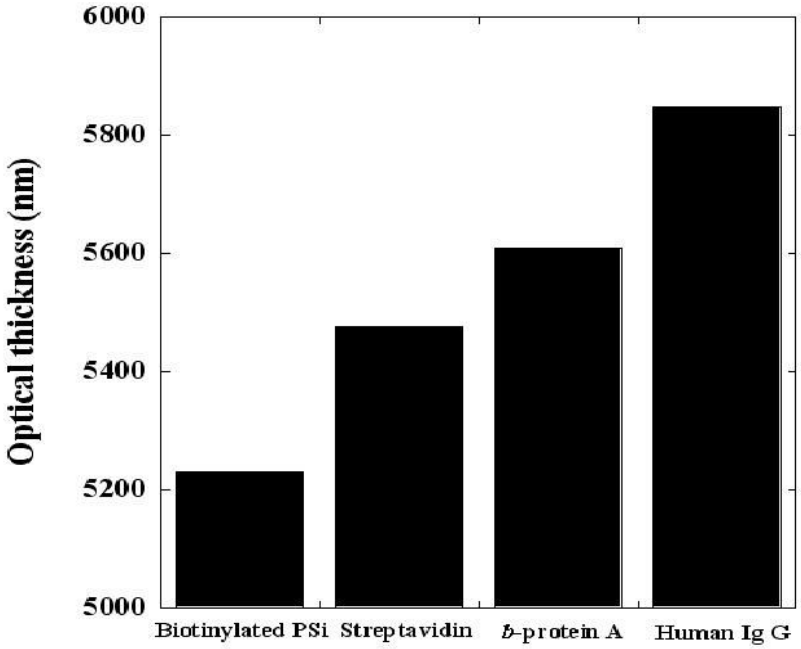

Figure 8.5. Change of optical thickness after addition of each protein.

Figure 8.5. showed the change of the effective optical thickness according to step by step addition of biotinylated protein A and human IgG, after rinsing the surface with buffer solution in between steps. Currently, the developed PSi biosensor was not able to perform multi-detection analysis, but its detection limit was 2 *p*M of human IgG.

8.4 Conclusion

The functionalized PSi biosensor was prepared for the application as a label-free biosensor based on PSi interferometer. Prepared PSi displayed Fabry-Perot fringes in the optical reflective spectra. The mean of construction of molecular architectures on PSi surfaces was investigated for the binding interaction with streptavidin, biotinylated protein A, human IgG. Diffuse reflectance FT-IR spectroscopy was used to monitor the chemical and optical characterization of PSi films during step-by-step functionalzation of PSi surface. The reflection spectra of biotin-modified PSi were used in the protein-binding studies. When the PBS buffer solution containing proteins was flushed into the biotin-functionalized rugate PSi chip in the cell, a red-shift of Fabry-Perot fringes in the reflective spectra indicated the binding of the proteins into the biotin-derivatized rugate PSi film. The red-shift resulted from a change in average refractive indices attributed to the replacement of some of the aqueous phases with protein.

8.5 Reference

[1] H. Ouyang, M. Christophersen, R. Viard, B. L. Miller, and P. M. Fauchet, *Adv. Funct. Mater.* **15**, 1851 (2005).

[2] S. M. Weiss, H. Ouyang, J. Zhang, and P. M. Fauchet, *Opt. Express* **13**, 1090 2005.

[3] F. P. Mathew and E. C. Alocilja *Biosensors Bioelectron* **20**, 1656 (2005).

[4] F. Besseueille, V. Dugas, V. Vikulov, J. P. Cloarec, and E. Souteyrand, *Biosensors Bioelectron* **21**, 908 (2005) .

[5] C. Pacholski, M. Sartor, M. J. Sailor, F. Cunin, and G. M. Miskelly, *J. Am. Chem. Soc*. **127,** 11636 (2005).

[6] A. Janshoff, S. K-.P Dancil, C. Steinem, D. P. Greiner, V. S-Y. Lin, C. Gurtner, K. Motesharei, M. J. Sailor, and M. R. Ghadiri, *J. Am. Chem. Soc*. **120**, 12108 (1998).

[7] B.-J. Lee, S. G. Kim, and H. Sohn, *Key Eng. Mater*. **53**, 321 (2006).

[8] J. Piechler, A. Brandenburg, A. Brecht, E. Wagner, and G. Gauglitz, *Appl. Opt.* **36**, 6554 (1997).

[9] A. P. Abel, M. G. Weller, G. L. Duveneck, M. Ehart, and H. M. Widmer, *Anal. Chem.* **68**, 2905 (1996).

[10] R. Polzius, E. Diessel, F. F. Bier, and U. Bilitewski, *Anal. Biochem.* **248**, 269 (1997).

[11] J. Homola, S. S. Yee, and G. Gauglitz, *Sensor. Actuat. B-Chem.* **54**, 3 (1999).

[12] P. I. Nikitin, A. A. Beloglazov, V. E. Kochregin, M. V. Valeiko, and T. I. Ksenevich, *Sensor. Actuat. B-Chem*. **54**. 43 (1999).

[13] A. Brecht and G. Gauglitz, *Sensor. Actuat. B-Chem.* **38**, 1 (1997).

[14] J. Janata, M. Josowicz, and D. M. Devaney, *Anal. Chem*. **66**, 207R (1994).

[15] B. -J. Lee, S. Jang, and H. Sohn, *Solid State Phenom*. **491**, 124 (2007).

[16] J. Kim, Y. Koh, S. Jang, Y. C. Ko, H. -G. Woo, and H. Sohn, *J. Nanosci. Nanotechnol.* **7**, 4165 (2007).

[17] J. Park, S. Cho, Y. C. Ko, and H. Sohn, *J. Korean Phys. Soc.* **50**, 695 (2007).

[18] S. Jang, J. Kim, Y. Koh, Y. C. Ko, H.-G. Woo, and H. Sohn, *J. Nanosci. Nanotechnol.* **7**, 4049 (2007).

[21] Y. Y. Li, F. Cunin, J. T. Link, T. Gao, R. E. Betts, S. H. Reiver, V. Chin, S. N. Bhatia, and M. J. Sailor, *Science* **199**, 11264 (2003).

[22] T. A. Schmedake, F. Cunin, J. R. Link, and M. J. Sailor, *Adv. Mater.* **14**, 1270 (2002).

[23] S. O. Meade, M. S. Yoon, K. H. Ahn, and M. J. Sailor, *Adv. Mater.* **16**, 2811 (2004).

[24] J. Drott, K. Lindstrom, L. Rosengren, and T. Laurell, *J. Micromech. Microeng.* **7**, 14 (1997).

[25] K. L. Beattie, W. G. Beattie, L. Mengm, S. L. Turner, R. Coral-Vazquez, D. D. Sith, P. M .Mclntyre, and D. D. Dao, *Clin. Chem.* **41**, 700 (1995).

[26] T. Laurell, J. Drott, L. Rosengren, and K. Lindstrom, *Sensor. Actuat. B-Chem.* **13**, 161 (1996).

[27] H. B. Gamper, M. W. Reed, T. J. Cox, S. Virosco, A. D. Adams, A. A. Gall, J. K. Scholler, and R. B. Meyer, *Nucleic Acids Research* **21**,145 (1993).

[28] Y. D. Koh, S. J. Kim, J. H. Park, C. Y. Park, S. D. Cho, H.-G. Woo, Y. C. Ko, and H. Sohn, *J. Bull. Korean Chem. Soc.* **28**, 2083 (2007).

[29] T. Stuchbury, M. Shipton, R. Norris, J. P. G. Malthouse, K. Brocklehurst, J. A. L. Herbert, and H. Suschitzky, *J. Biochem.* **151**, 417 (1975).

Chapter Nine

Detection of Avidin Based on Rugate-structured Porous Silicon Interferometer

9.1 Introduction

Since the discovery of porous silicon (PSi),[1] PSi has been intensively investigated for a variety of applications such as chemical[2] and biological sensors,[3] medical diagnostics,[4] optical band pass filters,[5] micro chemical reactors,[6] and micro fuel cells.[7] Recently, optical devices based on multi-structured PSi attract a great attention of the scientists. From a conceptual point of view, the former is based on optically thin and homogeneous mono-layered PSi and the latter is based on discrete multi-layered PSi structure. The direction of pores and pore diameters depend on surface orientation, doping level and type, temperature, the current density, and the composition of the etching solution.[8,9] Distributed Bragg reflector porous silicon (DBR PSi) as multi-layered PSi has been developed and typically prepared by an applying a square current waveform to the etch cell. DBR PSi results in two discrete indices and exhibits photonic structure of Bragg filters.[10] Rugate-structured porous silicon having photonic structure of rugate filter in which refractive index varies sinusoidally has been recently developed by applying a computer-generated pseudo-sinusoidal current waveform.[11] Chemical modification of PSi multilayer exhibits the modification of

its physical, chemical, and electronic properties. Chemical or bio molecule can be detected based on changes in the spectral interference pattern.[12,13] The rugate PSi with reflection peaks in visible spectral range was recently demonstrated to be applied for the detection of different chemical species.[14-16]

For applications in high throughput drug discovery and disease diagnostics, label-free biosensors would be important due to the advantage of easy sample preparation.[17,18] Two main optical transduction methods for label-free biosensors are both optical interferometric methods based on interferometers,[19] evanescent wave devices,[20] and grating couplers,[21] and surface plasmon methods based on metal films[22] and colloids.[23] Biosensor based on porous silicon interferometer has a great advantage due to a large surface area matrix for immobilization of a variety of biomolecules such as enzymes,[24] protein,[25] and DNA fragments.[26] Sailor et al. recently reported that the electronic or optical properties of mono-layered PSi can also be used as the transducer of biomolecular interaction in biosensor application.[27,28] In the present work, we have prepared biosensor based on rugate PSi interferometer. The fabrication, optical characterization, and surface derivatization of a rugate PSi are reported. For the application as a label-free biosensor, the binding interaction with avidin has been investigated.

9.2 Experimental

9.2.1 Materials

HF (ACS reagent, Aldrich Chemicals), absolute ethanol (ACS reagent, Aldrich Chemicals), 1 mL of (3-aminopropyl)trimethoxysilane (99.8%, Aldrich), 1-(3-(dimethyl-amino)propyl)-3-ethylcarbodiimide hydro-chloride, EDC (99.8%, Aldrich), phosphate-buffered solution (PBS, pH=7.4), methylene chloride and toluene (99.5%, Aldrich) were used without further purification.

9.2.2 Preparation of rugate PSi Samples

Heavily doped p-type silicon wafers (B-doped, orientation<100>, Siltronix, Inc.) with a resistivity in the range 0.8~0.12 mΩocm were used to fabricate rugate PSi by an anodic etch in ethanolic HF consisted of a 3 : 1 volume mixture of aqueous 48% hydrofluoric acid (ACS reagent, Aldrich Chemicals) and absolute ethanol (ACS reagent, Aldrich Chemicals). Prior to etching procedure, the silicon wafer were rinsed throughly with ethanol and dried under a steam of nitrogen. The galvanostatic etch was carried out in a Teflon cell by using a two-electrode configuration with a Pt mesh counter electrode. A sinusoidal current density waveform varying between 150 and 250 mA/cm^2 with 0.44 Hz was applied. The anodization current was supplied by a Keithley 2420 high-precision constant current source controlled by a computer to allow the formation of PSi multilayers. To prevent the photogeneration of carriers, was performed the anodization in the dark. After etching, the samples are rinsed with pure ethanol and dried with nitrogen

gas.

9.2.3 Thermal Oxiadation of Rugate PSi

The silicon surface was predominant hydride-terminated after the etching procedure. This surface was sensitive to oxidation and hydrolysis upon exposure to aqueous solution. Thermally oxidized porous silicon samples were obtained by heat treatment in a furnace (Thermolyne F6270-26 furnace equipped with controller) using the following parameters: intial ramp rate, 5 ℃/min to 300 ℃; hold time, 3h; and passive cooling to ambient temperature.

9.2.4 Functionalization of Oxidized Rugate PSi

The oxidized porous silicon sample and 1 mL of (3-aminopropyl)trimethoxysilane (99%, Aldrich Chemicals) were refluxed for 19 h. After functionalization with amine group, the sample was rinsed successively with toluene, acetone, and ethanol and subsequently dried under a stream of nitrogen. The 100 mg of biotin (Sigma) was dissolved in 100 mL of methylene. The mixture solution was stirred vigorously for 30 min, and 1-(3-(dimethyl-amino)propyl)-3-ethylcarbodiimide hydro-chloride, EDC, (200 mg, 1 mmol) was added to the solution. The reaction mixture was allowed to stir at room temperature for 1h. The resulting solution was added to the functionalized porous silicon chip and sample was incubated overnight. Afterward, the chip was ultra-sonicated for 3 min, washed 3 times with toluene, methylene chloride, and phosphate-buffered solution (PBS, pH=7.4), and dried the atmosphere.

9.2.5 Data Acquisition

Interferometric reflectance spectra of rugate PSi were recorded by using an Ocean Optics S2000 spectrometer fitted with a bifurcated fiber optic probe. A tungsten light source was focused onto the center of a porous silicon surface with a spot size of approximately 1~2 mm. Spectra were recorded with a CCD detector in the wavelength rang 400~1200 nm. The illumination of the surface as well as the detection of the reflected light was performed along an axis coincident with the surface normal.

Instrumentation. FT-IR spectra were acquired with a Nicolet model 5700 FT-IR instrument in the diffuse reflectance mode (Spectra-Tech diffuse reflectance attachment), with diffuse reflectance absorption spectra are reported in absorbance units. The morphology of rugate PSi film and polymer replica were observed with cold field emission scanning electron microscope (FE-SEM, S-4700, Hitachi).

9.3 Result and Discussion

Multilayered rugate PSi prepared by applying a computer-generated pseudo-sinusoidal current waveform exhibits high reflectivity in a specific narrow spectral region. This reflectivity can be tuned to appear anywhere in the visible to near-infrared spectral range, depending on the programmed etch waveform. Rugate filters possess a sinusoidally varying porosity gradient in the direction perpendicular to the plane of the filter. The waveform used in the present work involves a sine component, which is represented by

$$Y = A \cdot sin(kt) + B$$

where Y represents a temporal sine wave of amplitude A, frequency k, time t, and an applied current density B.

For mono-layered PSi, an anodic etch of p-type silicon wafer with resistivities of 0.1~10 Ωocm in ethanolic HF solution generally produces PSi single layer with a network of micropores (diameter, d < 2nm), rather than meso-(d = 2~50 nm) or macropores (d > 50 nm). The shape, size, and orientation of pores of PSi layers depend on surface orientation and the dopant level of the crystalline silicon substrate as well as the applied current density, the temperature, and the concentration of the HF etching solution. The pore size of p-type PSi can be increased by increasing the concentration of the dopant and decreasing the aqueous HF concentration. High current densities result in the desired well-defined cylindrical macropores, rather than the random orientation of highly interconnected micropores. The fabrication of macropores with diameters in the range 25~100 nm by anodizing heavily doped p-type silicon with a resistivity of 10^{-3} Ω·cm in 25% ethanolic HF solution was reported by Herino et al.29 In this work, rugate PSi with mesopores has been successfully fabricated by using a periodic galvanostatic

electrochemical etch of heavily doped p-type silicon wafer with a resistivity in the range 0.8~0.12 mΩ·cm. The value of A and B were 100 and 150 mA, respectively. The surface and cross sectional morphology of rugate PSi are obtained with cold FE-SEM and shown in Figure 9.1. FE-SEM image of rugate PSi indicates that the prepared rugate PSi has cylindrical mesopores with the average pore size of 10 nm, which could be suitable for the detection of avidin due to its size of 56 × 50 × 40 Å.[30]

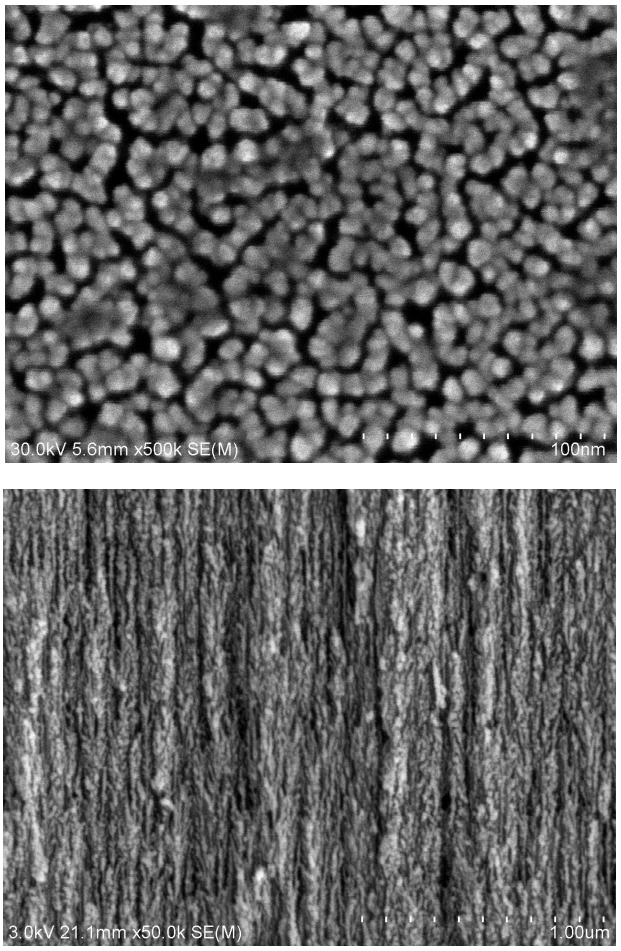

Figure 9.1. Surface and cross-section SEM image of prepared rugate PSi.

The rugate PSi displays a very sharp line in the optical reflectivity spectrum shown in Figure 9.2. Prepared rugate PSi exhibits a high reflectivity at 629 nm. The spectral band of the rugate film has a full-width at half-maximum (FWHM) of 15 nm, whereas the narrowest quantum dot spectrum reported at this wavelength has a FWHM of 20 nm.[31] One of the most unique features of rugate PSi is that its reflective spectral band is much narrower than the fluorescence spectrum obtained from an organic dye or core-shell quantum dot. Thus, more spectral lines can be placed in a narrower spectral window with the photonic structures.

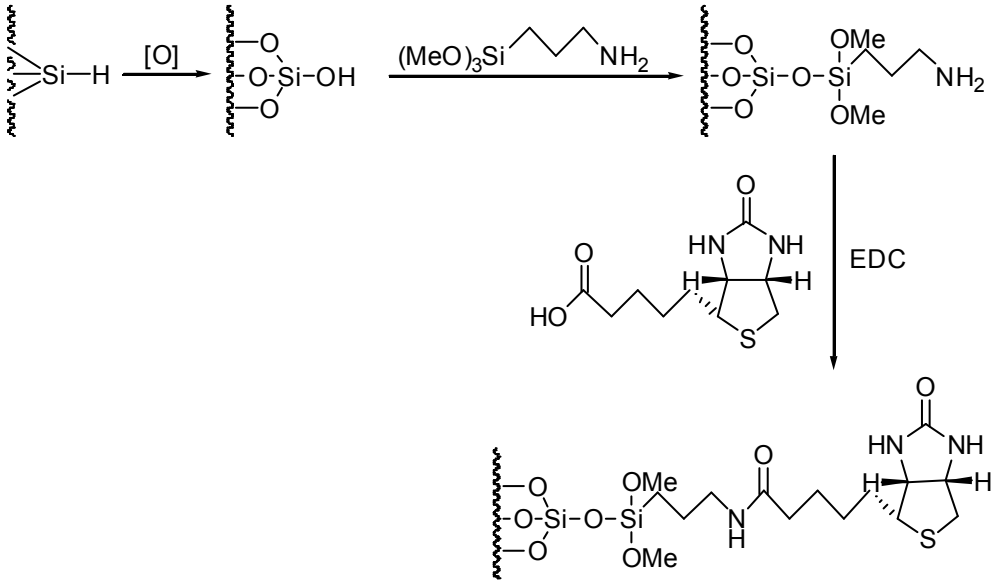

Scheme 9.1.

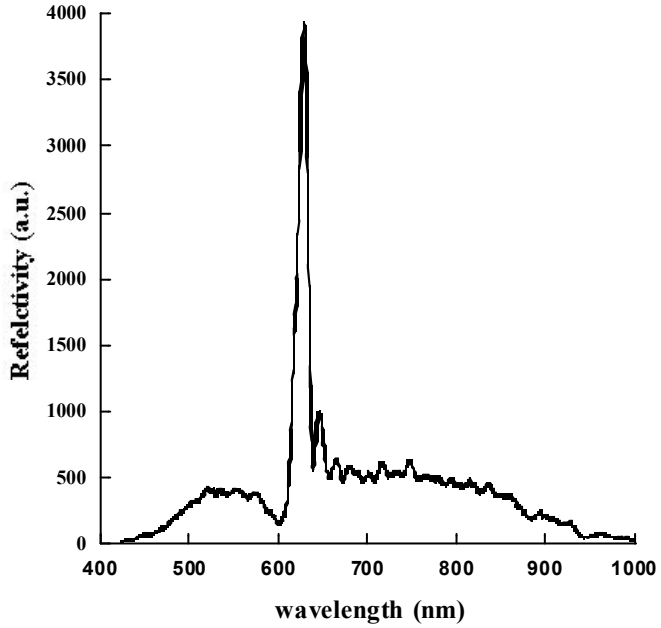

Figure 9.2. Optical reflectivity spectrum of rugate PSi.

The chemistry of functionalization is outlined in Scheme 9.1. The thermal oxidation of rugate PSi at 300 ℃ converts the hydride-terminated surface into hydroxyl terminated rugate PSi. Diffuse reflectance FT-IR spectroscopy was used to monitor the oxidation and functionalization reaction of rugate PSi sample. Figure 9.3(A). shows that the FT-IR spectrum of rugate PSi layer immediately after anodization of the silicon wafer displays a characteristic broad band centered at 2119 and 914 cm^{-1} for the υ(Si-H) stretching vibration and δ(Si-H) bending vibration. Heavily oxidized rugate PSi samples are prepared by heating freshly etched rugate PSi in pure O_2 at 300 ℃ for 3 h. After the thermal oxidation of rugate PSi film, the presence of silicon oxide has been determined by FT-IR measurement as shown in Figure 9.3(B). Thermal oxidation of the porous silicon layer results significant loss of intensity of the υ(Si-H) modes in the infrared spectrum at 2085-2150 cm^{-1}, but vibrational bands due to oxygen-back-bonded silicon hydride, υ(OSi-H) and δ(OSi-H) modes, grow at 2200-2250 and 877 cm^{-1},respectively. Multiple silicon oxide species, Si-O-Si, display a strong, very broad absorption band between 1000 and 1200 cm^{-1}. Although we cannot quantify the coverage levels of Si-H and Si-OH on an absolute scale, the areas of the infrared absorption bands provide a measure of the relative coverages on the Si-O, Si-H, and Si-OH. The relative areas of the aborption bands indicate that the oxidized rugate PSi samples contain the most O and the least H, while the fresh rugate PSi samples contain more silicon hydride species and less silicon oxide species on their surfaces. In a separate experiment, the areas of the υ(Si-H), υ(OSi-H), υ(Si-O), and υ(Si-OH) bands for the rugate PSi in the infrared spectrum were measured in situ during thermal oxidation (Figure 9.4). There is an asymptotic increase in the Si-O or OSi-H bands and a decrease in the Si-H bands over time. The thermal oxidation of rugate PSi film results the reflectivity at 556 nm shifted

to shorter wavelengths by 73 nm due to the decrease of refractive index of silicon dioxide from silicon.

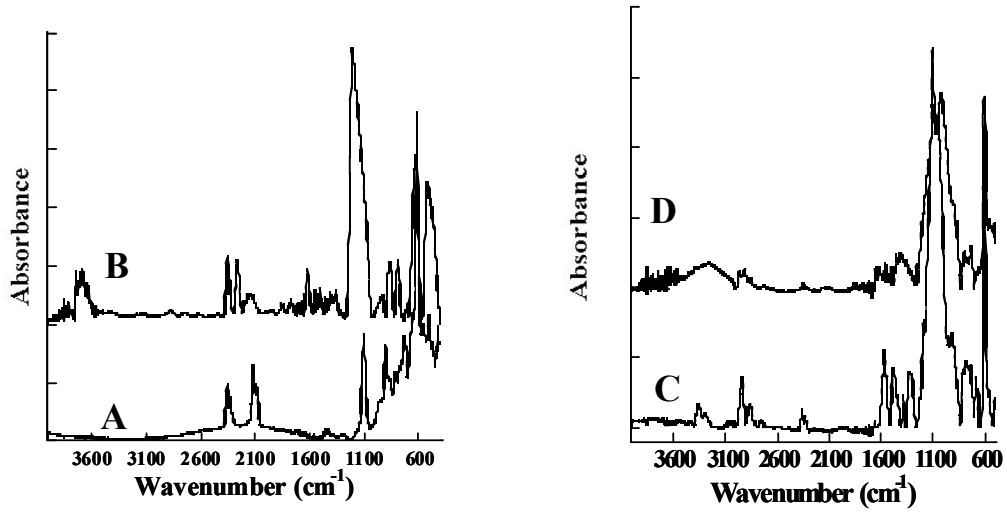

Figure 9.3. Diffuse reflectance FT-IR spectra of (A) a freshly etched p-type rugate PSi, (B) the wafer after 3h oxidation with thermal, (C) the wafer after functionalization of the rugate PSi layer with (3-aminopropyl)trimethoxysilane, and (D) the wafer subsequent reaction of the surface with biotin.

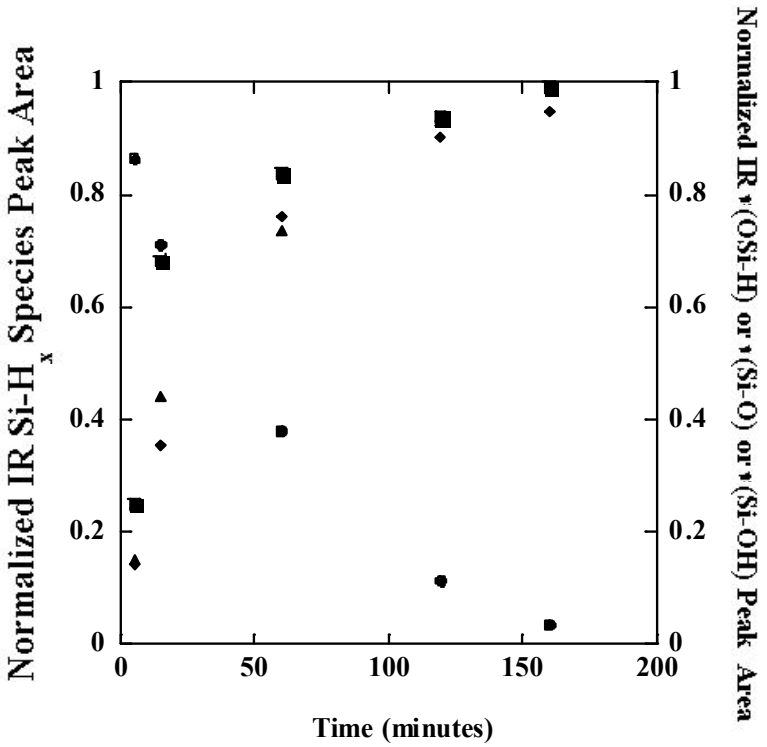

Figure 9.4. Normalized areas of the ∪(Si-H) (●), ∪(OSi-H) (◆), ∪(Si-O) (■), and ∪(Si-OH) (▲) bands in the infrared spectrum as a function of thermal oxidation time. Areas of the ∪(Si-H) were normalized by dividing by the area of the peaks at t = 0. Areas of the ∪(OSi-H), ∪(Si-O), and ∪(Si-OH) peaks were normalized by dividing by the area of the respective peaks measured at t = 3 h.

Condensation of the Si-OH surface of rugate PSi with (3-aminopropyl)trimethoxysilane generates a surface-bound amino group. The FT-IR spectrum shown in Figure 3C displays additional bands characteristic of the linker (the amide band of υ(N-H) at 3386 cm^{-1} and δ(N-H) at 1575 cm^{-1} and the aliphatic υ(C-H) stretching bands at 2850, 2923, and 2952 cm^{-1}). Surface derivatization leads to complete disappearance of the OSi-H vibrational bands.

To determine the surface coverage of the immobilized aminosilane linker, the functionalized surface was reduced by dithiothreitol (DTT) as shown in Scheme 9.2. The released 2-thiopyridone was quantified by UV/vis spectroscopy (λ_{max} = 343 nm, ε = 8.08 × 103 $M^{-1}cm^{-1}$).[32] The number of receptor molecules in the case of a silicon chip etched at 250 - 150 mA/cm^2 was in the range 300 $nmol/cm^2$, which corresponds to a surface coverage of 30 - 80% approximately. This calculation is based on the following parameters, assuming cylindrical pores: pore radius, 10 nm; thickness of the porous layer, 90 μm; porosity, 74%; area per molecule of the biotin linker, 0.07 $Å^2$; area of the chip, 1.2 cm^2.

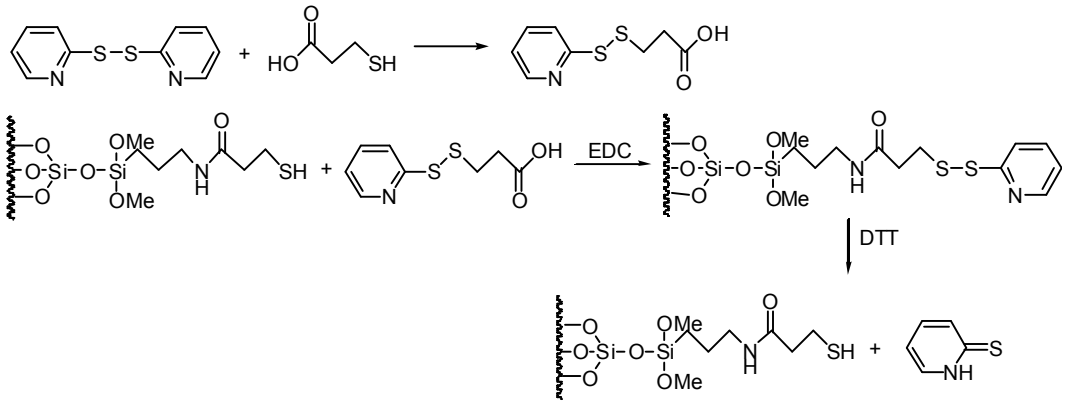

Scheme 9.2.

The subsequent reaction with biotin as shown in Scheme 9.1 led to the desired biotin-funtionalized surface which was used in the avidin-binding studies (Figure 9.3D). The band at 1652 cm^{-1} is assigned to the carbonyl stretching vibration of the biotin head group.

The surface functionalized rugate PSi was placed in the flow cell. Aqueous PBS buffer solution was flushed to perform an initial measurement of reflectivity. The surface was rinsed thoroughly with PBS buffer solution to ensure covalent attachment to the surface and to check stability of the reflectivity measurement. The cell was then flushed with a constant flow rate of 0.8 mL/min of PBS buffer solution containing avidin (20 μM), which couples to the biotin-modified rugate PSi surface.

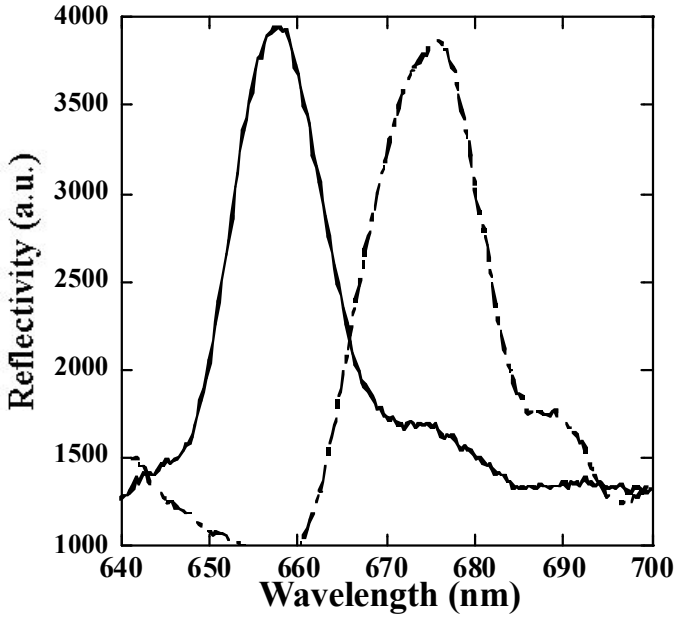

Figure 9.5. Optical reflectivity spectra of biotin-functionalized rugate PSi sample before (solid) and after (dashed) exposure of avidin.

Figure 9.5. shows the change of reflection spectrum under the exposure of avidin to the biotin-functionalized rugate PSi chip. An increase of the reflection wavelength in the reflectivity spectrum by 18 nm was observed, indicative of a change in refractive index induced by binding of the avidin into the biotin-derivatized rugate PSi film. This increase is attributed to the replacement of some of the aqueous phase with avidin. The replacement will change the mean refractive index of the rugate film and be observed as an increase of the reflection wavelength in reflectivity.

9.4 Conclusion

Rugate PSi fabricated by applying a computer-generated pseudo-sinusoidal current waveform has been prepared for the application as a label-free biosensor based on porous silicon interferometer. Prepared rugate PSi exhibits a high reflectivity with a sharp spectral line. The mean of construction of molecular architectures on rugate PSi surfaces has been investigated for the binding interaction with avidin. Diffuse reflectance FT-IR spectroscopy was used to monitor the chemical and optical characterization of rugate PSi films during step-by-step functionalzation of rugate PSi surface. The reflection spectra of biotin-modified rugate PSi was used in the avidin-binding studies. When the PBS buffer solution containing avidin was flushed into the biotin-functionalized rugate PSi chip the cell, a red-shift of reflectivity by 18 nm in the reflectivity spectrum indicates the binding of the avidin into the biotin-derivatized rugate PSi film. The red-shift results from a change in average refractive indices attributed to the replacement of some of the aqueous phase with avidin.

9.5 Reference

[1] A. Uhlir, *Bell System Tech*. **35**, 333 (1956).

[2] H. Sohn, S. Letant, M. J. Sailor, and W. C. Trogler, *J. Am. Chem. Soc*. , **122**, 5399 (2000).

[3] V. S. Lin, K. Motesharei, K. S. Dancil, M. J. Sailor, and M. R. Ghadiri, *Science* **278**, 840 (1997).

[4] M. Simion, I. Kleps, T. Neghina, A. Angelescu, M. Miu, A. Bragaru, M. Danila, E. Condac, M. Costache, and L. J. Savu, *Alloy. Compd*. **434**, 830 (2007).

[5] S. Ilyas, T. Bocking, K. Kilian, P. J. Reece, J. Gooding, K. Gaus, and M. Gal, *Opt. Mater*. **29**, 619 (2007).

[6] M. A. Khan, M. S. Haque, H. A. Naseem, W. D. Brown, and A. P. Malshe, *Thin Solid Films* **332**, 93 (1998).

[7] S. E. Letant, S. Content, T. T. Tan, F. Zenhausern, and M. J. Sailor, *Sensor Actuat. B- Chem.* **69**, 193 (2000).

[8] R. L. Smith and S. D. Collins, *J. Appl. Phys*. **71**, R1 (1992).

[9] P. C. Searson, *Advances in Electrochemical Sciences and Engineering; VCH; Mannheim, Germany,* 69 (1994).

[10] B. J. Lee, S. Jang, and H. Sohn *Solid State Phenom*. **124-126**, 491 (2007).

[11] J. Park, S. Cho, Y. C. Ko, and H. Sohn, *J. Korean Phys. Soc.* **50**, 695 (2007).

[12] A. Janshoff, K-P.S. Dancil, C. Steinem, D. P. Greiner, V. S-Y. Lin, C. Gurtner, K. Motesharei, M. J. Sailor, and M. R. Ghadiri, *J. Am. Chem. Soc.* **120**, 12108 (1998).

[13] B. J. Lee, S.G. Kim, and H. Sohn, *Key Eng. Mater.* **321-323**. 53 (2006).

[14] Y. Y. Li, F. Cunin, J. T. Link, T. Gao, R. E. Betts, S. H. Reiver, V. Chin,

S. N. Bhatia, and M. J. Sailor, *Science* **199**, 11264 (2003).

[15] T. A. Schmedake, F. Cunin, J. R. Link, and M. J. Sailor, *Adv. Mater.***14**, 1270 (2002).

[16] S. O. Meade, M. S. Yoon, K. H. Ahn, and M. J. Sailor, *Adv. Mater*. **16**, (2811) 2004.

[17] A. Brecht and G. Gauglitz, *Sensor. Actuat. B- Chem*. **38**, 1 (1997).

[18] J. Janata, M. Josowicz, and D. M. Devaney, *Anal. Chem.* **66**, 207R (1994).

[19] J. Piechler, A. Brandenburg, A. Brecht, E. Wagner, and G. Gauglitz, *Appl. Opt*. **36**, 6554 (1997).

[20] A. P. Abel, M. G. Weller, G. L. Duveneck, M. Ehart, and H. M. Widmer, *Anal. Chem.* **68**, 2905 (1996).

[21] R. Polzius, E. Diessel, F. F. Bier, and U. Bilitewski, *Anal. Biochem*. **248**, 269 (1997).

[22] J. Homola, S. S. Yee, and G. Gauglitz, *Sensor. Actuat. B- Chem*. **54**, (3) 1999.

[23] P. I. Nikitin, A. A. Beloglazov, V. E. Kochregin, M. V. Valeiko, and T. I. Ksenevich, *Sensor. Actuat. B- Chem*. **54**, 43 (1999).

[24] J. Drott, K. Lindstrom, L. Rosengren, and T. J. Laurell, *Micromech. Microeng*. **7**, 14 (1997).

[25] T. Laurell, J. Drott, L. Rosengern, and K. Lindstrom, *Sensor. Actuat. B-Chem*. **31**, 161 (1996).

[26] K. L. Beattie, W. G. Beattie, L. Mengm, S. L. Turner, R. Coral-Vazquez, D. D. Sith, P. M. Mclntyre, and D. D. Dao, *Clin. Chem*. **41**, 700 (1995).

[27] V. S.-Y. Lin, K. Motesharei, K. -P. S. Dancil, M. J. Sailor, and M. R. Ghadiri, *Science* **278**, 840 (1997).

[28] M. J. Sailor, *Properties of porous silicon; Datareview Ser. NO. 18; Canham;*

London; 364-370 (1997).

[29] R. Herino, *Properties of porous silicon; Datareview Ser. NO. 18; Canham; London*, 89-96 (1997).

[30] A. Pugliese, A. Coda, M. Malcovati, and M. J. Bolognesi, *Mol. Biol.* **231**, 698 (1993).

[31] M. Bruchez, M. Moronne, P. Gin, S. Weiss, and A. P. Alivisatos, Science **281**, 2013 (1998).

[32] T. Stuchbury, M. Shipton, R. Norris, J. P. G. Malthouse, K. Brocklehurst, J. A. L. Herbert, and H. Suschitzky, *J. Biochem.* **151**, 417 (1975).

Chapter Ten
Fabrication of Encoded Rugate Porous Silicon Interferometer for Biosensor

10.1 Introduction

Porous silicon, a promising biomaterial[1] and biosensor component,[2,3] is formed by anodic etching of multilayer crystal silicon. As a photonic crystal sensor it has been used to detect the presence of gases/liquids[4] and biomolecules in aqueous media.[5] These types of sensors are based on the changes in the refractive index of the material resulting from the infiltration of molecular species into the pores of the structure. Two main optical transduction methods for label-free biosensors are both optical interferometric methods based on interferometers,[6] evanescent wave devices,[7] and grating couplers,[8] and surface plasmon methods based on metal films[9] and colloids.[10] Especially, optical devices based on multi-structured PSi attract a great attention of the scientists. Multilayer PSi such as DBR PSi[11] or rugate PSi[12] exhibits unique optical properties providing a reflection band at specific wavelength in the optical reflectivity spectrum. PSi has been employed as a large surface area matrix for immobilization of a variety of biomolecules including enzymes,[13] DNA fragments,[14] and antibodies.[15] Here, we describe a new biosensors based on biotin-funtionalized triply encoded rugate PSi interferometer have been developed. Three sharp reflection peaks were created by the reflections of illuminated white

light on the air-PSi layer and the PSi-bulk silicon interface. The induced shift in the reflection pattern caused by the change in the refractive index of the medium upon molecular interactions of species in solution with immobilized receptor within the PSi matrix was used as a sensitive method for biomolecular sensing. The fabrication, optical characterization, and surface functionalization of a rugate PSi are reported. For the application as a label-free biosensor, the binding interaction with protein has been investigated.

10.2 Experimental

10.2.1 Materials

HF (ACS reagent, Aldrich Chemicals), absolute ethanol (ACS reagent, Aldrich Chemicals), 1 mL of (3-aminopropyl)trimethoxysilane (99.8%, Aldrich), 1-(3-(dimethyl-amino)propyl)-3-ethylcarbodiimide hydro-chloride, EDC (99.8%, Aldrich), phosphate-buffered solution (PBS, pH=7.4), methylene chloride and toluene (99.5%, Aldrich) were used without further purification.

10.2.2 Preparation of rugate PSi Samples

The triply encoded rugate PSi was prepared by an electrochemical etching of Si wafer (boron doped, polished on the <100> face, resistivity of 0.8~1.2 mΩ·㎝, Siltronix, Inc.). The etching solution consisted of a 1 : 3 (v/v) mixture of absolute ethanol (ACS reagent, Aldrich Chemicals) and aqueous 48% hydrofluoric acid (ACS reagent, Aldrich Chemicals). Galvanostatic etching was carried out in a Teflon cell using a two-electrode configuration. The current density was modulated with a sine wave (typically between 126.1 and 183.85 mA/cm^2 100 s periodicity, 10 repeats) to generate a periodically varying porosity gradient. The anodization current was supplied by Keithley 2420 high-precision constant current source controlled by a computer to allow the formation of PSi multilayers. To prevent the photogeneration of carriers, electrochemical etching was performed the anodization in the dark. All samples were then rinsed several times with ethanol and dried under argon atmosphere prior to use.

10.2.3 Thermal Oxiadation of Rugate PSi

The silicon surface was predominant hydride-terminated after the etching procedure. This surface was sensitive to oxidation and hydrolysis upon exposure to aqueous solution. Thermally oxidized PSi samples were obtained by heat treatment in a furnace (Thermolyne F6270-26 furnace equipped with controller) using the following parameters: initial ramp rate, 5 ℃/min to 300 ℃ hold time, 3 h and passive cooling to ambient temperature.

10.2.4 Functionalization of Oxidized Rugate PSi

Surface modification of functionalized sample with biotin tetrafluorophenyl ester, biotin tetrafluorophenyl ester has been prepared by previously known method20. The 100 mg of biotin tetrafluorophenyl ester was dissolved in 15 mL of dimethylformamide. The mixture solution was stirred vigorously for 10 min, and triethylamine (0.9 mL, 6 mmol) was added to the solution. The reaction mixture was allowed to stir at room temperature for 30 min. The resulting solution was added to the functionalized PSi chip and sample was incubated overnight. Afterward, sample was rinsed successively with methylene chloride, acetone, and ethanol and subsequently dried under a stream of nitrogen.

To determine the surface coverage of the immobilized aminosilane linker, 2-pyridyl-2-carboxyethyl disulfide was synthesized by previously well-known method19. The isolated product (2-pyridyl-2-carboxyethyl disulfide, 0.2 g, 94.7 mmol) was quickly dissolved in a 10 mL of methylene chloride solution.

1-(3-(dimethylamino)propyl)-3-ethylcarbodiimide hydrochloride (100 mg, 0.6 mmol) was added to the solution. The resulting solution was allowed to stir in dry argon gas for 30 min, before funtionalization of oxidizied rugate PSi was added. The reaction mixture was stirred for 12 hrs at room temperature. Afterward, the chip was washed by ethanol, methylene chloride, and acetone and then dried under an atmosphere.

10.2.5 Data Acquisition

Interferometric reflectance spectra of rugate PSi were recorded by using an Ocean Optics S2000 spectrometer fitted with a bifurcated fiber optic probe. A tungsten light source was focused onto the center of a porous silicon surface with a spot size of approximately 1~2 mm. Spectra were recorded with a CCD detector in the wavelength rang 400~1200 nm. The illumination of the surface as well as the detection of the reflected light was performed along an axis coincident with the surface normal.

Instrumentation. FT-IR spectra were acquired with a Nicolet model 5700 FT-IR instrument in the diffuse reflectance mode (Spectra-Tech diffuse reflectance attachment), with diffuse reflectance absorption spectra are reported in absorbance units. The morphology of rugate PSi film and polymer replica were observed with cold field emission scanning electron microscope (FE-SEM, S-4700, Hitachi).

10.3 Results and Discussion

The triply encoded rugate PSi prepared by applying a computer-generated pseudo-sinusoidal current waveform exhibited high reflectivity in a specific narrow spectral region. This reflectivity can be tuned to appear anywhere in the visible to near-infrared spectral range, depending on the programmed etch waveform. Rugate filters possess a sinusoidally varying porosity gradient in the direction perpendicular to the plane of the filter. The waveform used in the present work involves a sine component, which is represented by Equation 1.

$$Y = A \cdot sin(kt) + B \qquad (1)$$

where Y represents a temporal sine wave of amplitude A, frequency k, time t, and an applied current density B. Triply encoded rugate structures were etched on a silicon wafer, showing three sharp spectral lines in the optical reflectivity spectrum. All of the individual sine components were summed together to create the composite waveform shown in Equation 2.

$$Y_{comp} = A_1\sin(k_1t) + A_2\sin(k_2t) + A_3\sin(k_3t) + B \qquad (2)$$

Equation 2 was converted to an analog current-time waveform to etch using a computer-controlled digital galvanostat. A waveform containing three separate frequency components was applied. The values of ki for each of the sine components were varied from 0.58 to 0.50 Hz, with a spacing of 0.04 Hz between each sine component. The values of Ai and B for every sine components were 126.1 and 183.85 mA, respectively.

High current densities result in the desired well-defined cylindrical macropores, rather than the random orientation of highly interconnected micropores. The fabrication of macropores with diameters in the range 25 ~ 100 nm by anodizing heavily doped p-type silicon with a resistivity of 10^{-3} Ω·cm in 25% ethanolic HF

solution was reported by Herino et al.[21] In this work, rugate PSi with mesopores was successfully fabricated by using a periodic galvanostatic electrochemical etch of heavily doped p-type silicon wafer with a resistivity in the range 0.8 ~ 0.12 m Ω·cm. The value of A and B was 100 and 150 mA, respectively. The surface and cross sectional morphology of rugate PSi were obtained with cold FE-SEM and shown in Figure 10.1. FE-SEM image of rugate PSi indicated that the prepared rugate PSi had cylindrical mesopores with the average pore size of 10 nm, which could be suitable for the detection of avidin, streptavidin due to size of 56 × 50 × 40,[22] and 54 × 58 × 48 Å[23], respectively.

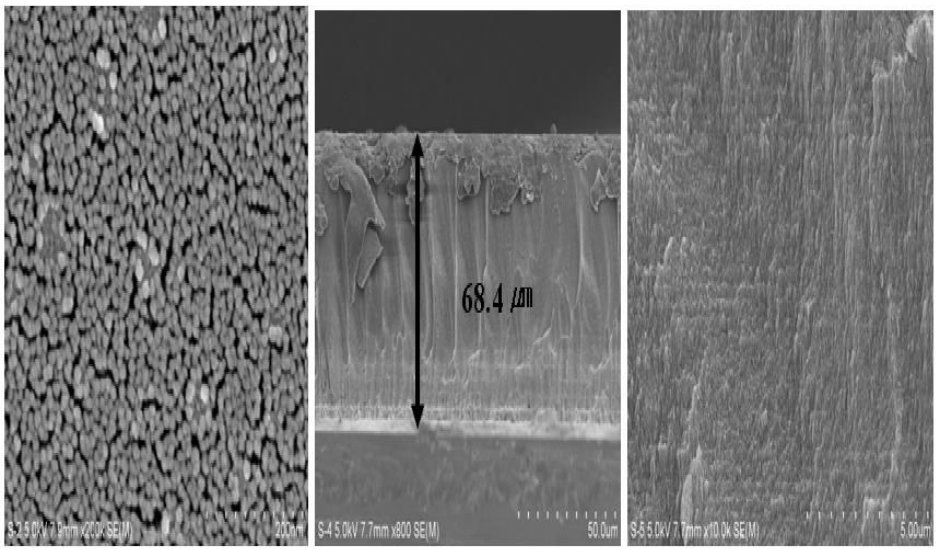

Figure 10.1. Surface and cross-sectional FE-SEM image of triply encoded rugate PSi.

The triply encoded rugate PSi displayed three sharp lines in the optical reflective spectra shown in Figure 10.2. Each of the main peaks in an optical reflective spectra corresponded to one of spectra at 631, 674, 725 nm, respectively. The spectral band of the triply encoded rugate PSi had a full-width at half-maximum (FWHM) of 17 nm, whereas the narrowest quantum dot spectrum reported at this wavelength had a FWHM of 20 nm[24]. One of the most unique features of triply encoded rugate PSi was that its reflective spectral band was much narrower than the fluorescence spectrum obtained from an organic dye or core-shell quantum dot. Thus, more spectral lines could be placed in a narrower spectral window with the photonic structures.

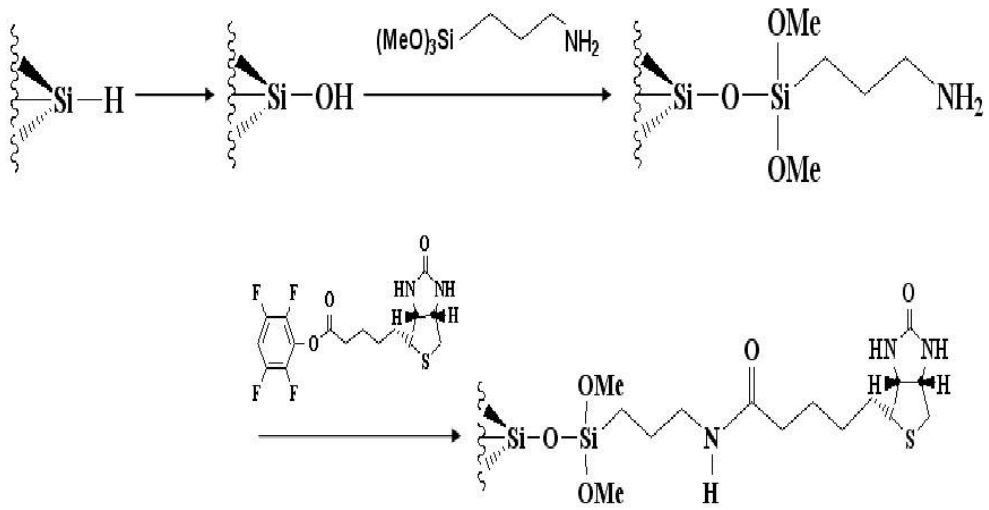

Scheme 10.1.

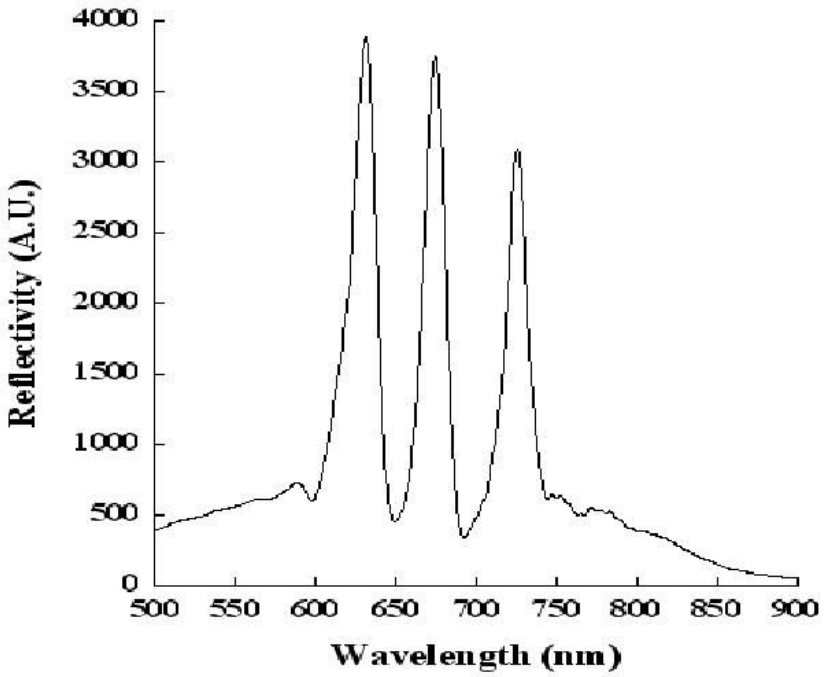

Figure 10.2. Optical reflective spectra of triply encoded rugate PSi.

The chemistry of functionalization was outlined in Scheme 10.1. The thermal oxidation of rugate PSi at 300 ℃ converted the hydride-terminated surface into hydroxyl terminated rugate PSi. Diffuse reflectance FT-IR spectroscopy was used to monitor the oxidation and functionalization reaction of rugate PSi sample. Figure 10.3(A). showed that the FT-IR spectrum of triply encoded rugate PSi layer immediately after anodization of the silicon wafer displayed a characteristic broad band centered at 2119 and 914 cm^{-1} for the υ(Si-H) stretching vibration and δ(Si-H) bending vibration. Heavily oxidized rugate PSi samples were prepared by heating freshly etched rugate PSi in air at 300 ℃ for 3 h. After the thermal oxidation of rugate PSi film, the presence of silicon oxide was determined by FT-IR measurement as shown in Figure 10.3(B). Thermal oxidation of the PSi layer resulted significant loss of intensity of the υ(Si-H) modes in the infrared spectrum at 2085-2150 cm^{-1}, but vibrational bands due to oxygen-back-bonded silicon hydride, υ(OSi-H) and δ(OSi-H) modes, grew at 2200-2250 and 877 cm^{-1}, respectively. Multiple silicon oxide species, Si-O-Si, displayed a strong, very broad absorption band between 1000 and 1200 cm^{-1}. The thermal oxidation of triply encoded rugate PSi resulted the individual reflection at 605, 647, and 695 nm, blue-shifted by approximately 26, 27, and 30 nm due to the decrease of refractive index of silicon dioxide from silicon.

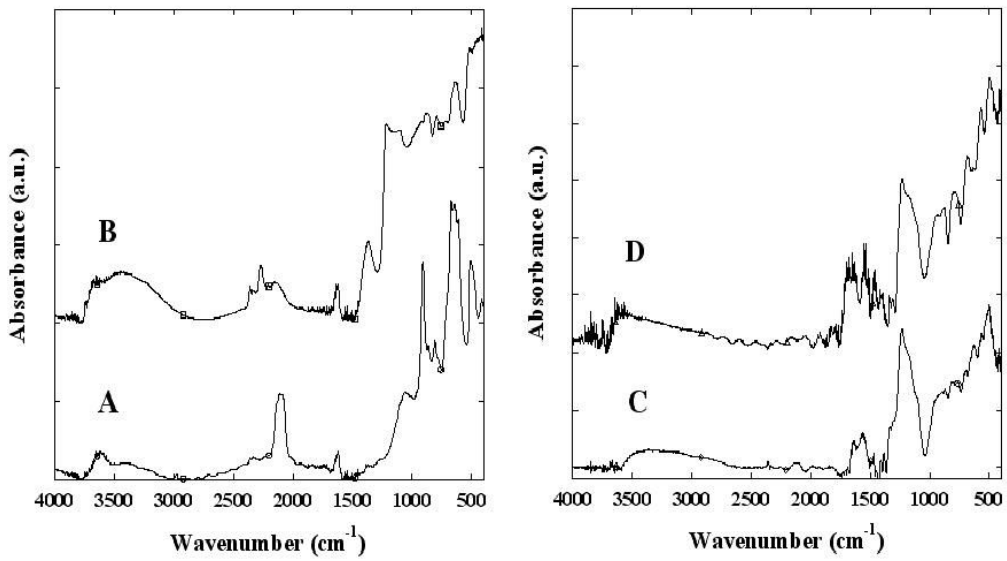

Figure 10.3. Diffuse reflectance FT-IR spectra of (A) triply encoded rugate PSi, (B) thermally oxidized rugate PSi, (C) the wafer after functionalization of the rugate PSi layer with (3-aminopropyl)trimethoxysilane, and (D) rugate PSi functionalized with biotin.

Condensation of the Si-OH surface of rugate PSi with (3-aminopropyl)trimethoxysilane generated a surface-bound amino group. The FT-IR spectrum shown in Figure 10.3(C). displayed additional band characteristics of the linker (the amide band of υ(N-H) at 3386 cm^{-1} and δ(N-H) at 1575 cm^{-1} and the aliphatic υ(C-H) stretching bands at 2850, 2923, and 2952 cm^{-1}). Surface derivatization leads to complete disappearance of the OSi-H vibrational bands.

To determine the surface coverage of the immobilized aminosilane linker, the functionalized surface was reduced by dithiothreitol (DTT) as shown in Scheme 2. The released 2-thiopyridone was quantified by UV/vis spectroscopy (λ_{max} = 343 nm, ε = 8.08 × 103 $M^{-1}cm^{-1}$).[25] The number of receptor molecules in the case of a silicon chip etched at 126.1 and 183.85 mA/cm^2 was in the range 2.94 $nmol/cm^2$, which corresponds to a surface coverage of 30 - 80% approximately. This calculation was based on the following parameters, assuming cylindrical pores: pore radius, 10 nm; thickness of the porous layer, 68.4 μm; porosity, 81.7%; area per molecule of the biotin linker, 0.07 $Å^2$; area of the chip, 1.2 cm^2.

The subsequent reaction with biotin as shown in Scheme 10.1. led to the desired biotin-funtionalized surface which was used in the avidin-binding studies (Figure 3D). The band at 1652 cm^{-1} is assigned to the carbonyl stretching vibration of the biotin head group. The functionalized rugate PSi was placed in the flow cell. Aqueous PBS buffer solution was flushed to perform an initial measurement of reflectivity. The surface was rinsed thoroughly with PBS buffer solution to ensure covalent attachment to the surface and to check stability of the reflectivity measurement. The cell was then flushed with a constant flow rate of 0.8 mL/min of PBS buffer solution containing protein (20 μM avidin or streptavidin) which coupled to the biotin-modified rugate PSi surface.

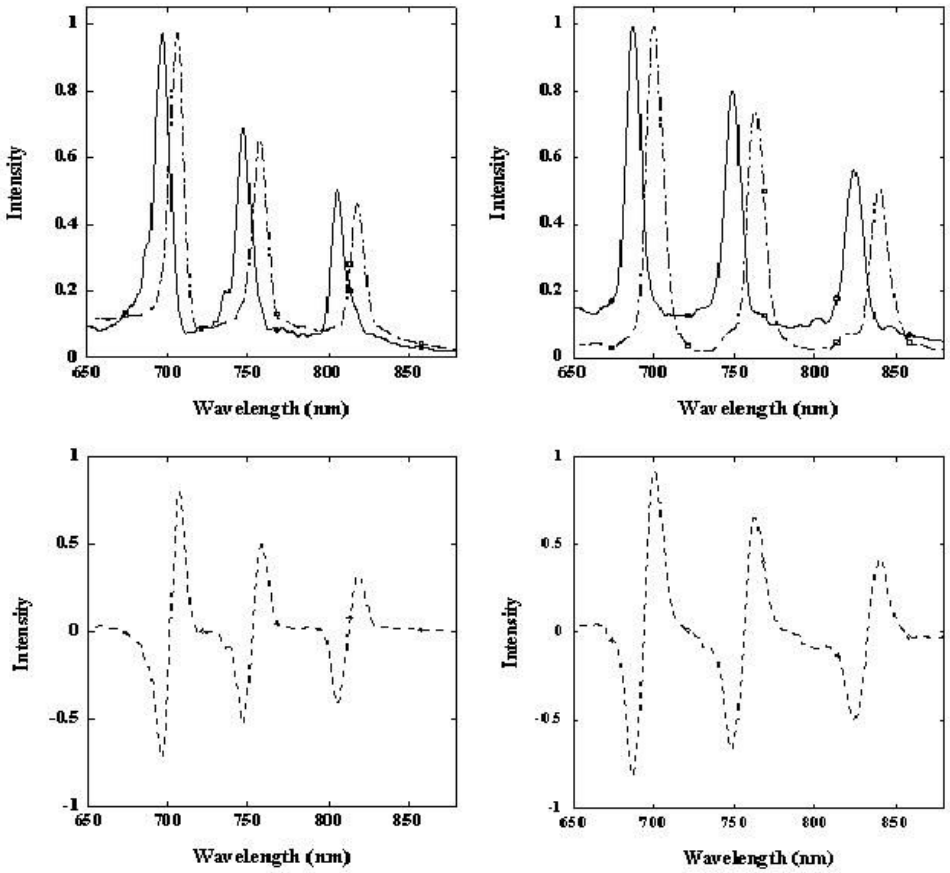

Figure 10.4. Optical reflection spectra of biotin-fuctionalized rugate PSi sample before (solid line) and after (dashed line) exposure of avidin(A) and streptavidin(B), The dotted line in each case are the difference between spectra obtained in the presence and absence of protein.

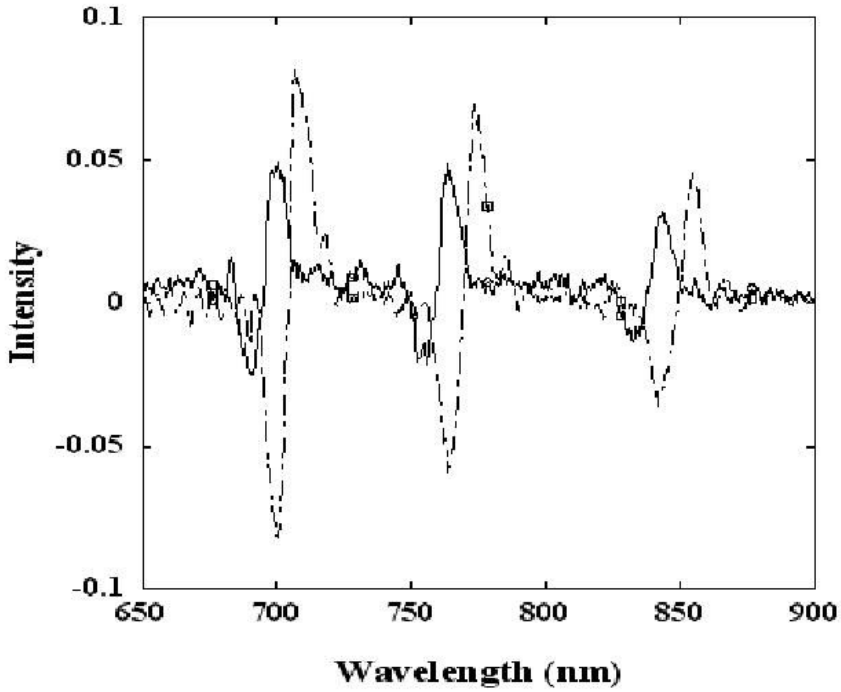

Figure 10.5. Plots for showing the detection limits of protein at 2 *p*M by using differential graph.

Figure 10.4. showed the change of reflection spectrum under the exposure of protein to the biotin-functionalized rugate PSi chip. Increases of the reflection wavelength in the reflective spectra by 9, 10, and 11 nm for avidin and 12, 13, and 15 nm for streptavidin were observed, indicative of a change in refractive index induced by binding of the protein into the biotin-derivatized rugate PSi film. This increase was attributed to the replacement of some of the aqueous phase with protein in PBS buffer solution. The bottom spectra in Figure 10.4. are the difference between spectra obtained in the prescence and absence of avidin (left) and streptavidin (right), respectively. Currently, the triply encoded rugate PSi sensor is not able to discriminate between avidin and streptavidin, but this selectivity issues is currently under investigation. Figure 10.5. displayed the detection limit of 2 *p*M for the detection of avidin and streptavidin with current multi-encoded rugate PSi sensor.

10.4 Conclusion

The triply encoded rugate PSi fabricated by applying a computer-generated pseudo-sinusoidal current waveform was prepared for the application as a label-free biosensor based on PSi interferometer. Prepared rugate PSi exhibited a high reflectivity with sharp spectral lines. The mean of construction of molecular architectures on triply encoded rugate PSi surfaces was investigated for the binding interaction with avidin and streptavidin. Diffuse reflectance FT-IR spectroscopy was used to monitor the chemical and optical characterization of triply encoded rugate PSi films during step-by-step functionalzation of triply encoded rugate PSi surface. The reflection spectra of biotin-modified triply encoded rugate PSi was used in the avidin and streptavidin-binding studies. When the PBS buffer solution containing avidin or streptavidin was flushed into the biotin-functionalized rugate PSi chip in the cell, a red-shift of reflectivity by 9, 10, and 11 nm for avidin and 12, 13, and 15 nm for streptavidin in the reflective spectra indicated the binding of the avidin and streptavidin into the biotin-derivatized rugate PSi film. The red-shift resulted from a change in average refractive indices attributed to the replacement of some of the aqueous phase with protein.

10.5 Reference

[1] A. Janshoff, S. K-P, Dancil, C. Steinem, D. Greiner, V. P. Lin, C. S-Y, Gurtner, K. Motesharei, M. J. Sailor, and M. R. Ghadiri, *J. Am. Chem. Soc*, **120**, 12108 (1998).

[2] C. Pacholski, M. Sartor, M. J. Sailor, F. Cunin, and G. M. Miskelly, *J. Am. Chem. Soc*, **127**, 11636 (2005).

[3] H. Ouyang, M. Christophersen, R. Viard, B. L. Miller, and P. M. Fauchet, *Adv. Funct. Mater*, **15**, 1851 (2005).

[4] F. Raissi and R. Farivar, *Appl. Phys. Lett*, **87**, 164101 (2005).

[5] L. A. DeLouise, P. M. Kou, and B. L. Miller, *Anal. Chem*, **77**, 3222 (2005).

[6] J. Piechler, A. Brandenburg, A. Brecht, E. Wagner, and G. Gauglitz, *Appl. Opt*, **36**, 6554 (1997).

[7] A. P. Abel, M. G. Weller, G. L. Duveneck, M. Ehart, and H. M. Widmer, *Anal. Chem*, **68**, 2905 (1996).

[8] R. E. Polzius, Diessel, F. F. Bier, and U. Bilitewski, *Anal. Biochem*, **248**, 269 (1997).

[9] J. Homola, S. S. Yee, and G. Gauglitz, *Sensor. Actuat. B-Chem*, **54**, 3 (1999).

[10] P. I. Nikitin, A. A. Beloglazov, V. E. Kochregin, M. V. Valeiko, and T. I. Ksenevich, *Sensor. Actuat. B-Chem*, **54**. 43 (1999).

[11] B. -J. Lee, S. Jang, and H. Sohn, *Solid State Phenom*, **491**, 124 (2007).

[12] J. Park, S. Cho, Y. C. Ko, and H. Sohn, *J. Korean Phys. Soc*, **50**, 695 (2007).

[13] J. Drott, K. Lindstrom, L. Rosengren, and T. Laurell, *J. Micromech, Microeng*, **7**, 14 (1997).

[14] K. L. Beattie, W. G. Beattie, L. Mengm, S. L. Turner, R. Coral-Vazquez, D. D. Sith, P. M. Mclntyre, and D. D. Dao, *Clin. Chem*, **41**, 700 (1995).

[15] T. Laurell, J. Drott, L. Rosengren, and K. Lindstrom, *Sens. Actuators B*, **13**, 161 (1996).

[16] A. Pugliese, A. Coda, and M. M. Malcovati, *J. Bolognesi, Mol. Biol*, **231**, 698 (1993).

[17] W. A. Hendrickson, A. Pahler, J. L. Smith, Y. Satow, E. A. Merritt, and R. P. Phizackerley, *Proc. Natl. Acad. Sci*, **86**, 2190 (1989).

[18] H. B. Gamper, M. W. Reed, T. Cox, J. S. Virosco, A. D. Adams, A. A. Gall, J. K. Scholler, and R. B. Meyer, *Nucleic Acids Research*, **21**, 145 (1993).

[19] Y. Koh, S. Kim, J. Park, C. Park, S. Cho, H.-G. Woo, Y. Ko, and H. Sohn, *Bull. Korean Chem. Soc*. **28**, 2083 (2007).

[20] H. B. Gamper, M. W. Reed, T. Cox, J. S. Virosco, A. D. Adams, A. A. Gall, J. K. Scholler, and R. B. Meyer, *Nucleic Acids Research*, **21**, 145 (1993).

[21] R. Herino, Properties of PSi, Datareview Ser. NO. 18, Canham: London, 1997.

[22] A. Pugliese, A. Coda, and M. M Malcovati, *J. Bolognesi, Mol. Biol*. **231**, 698 (1993).

[23] W. A. Hendrickson, A. Pahler, J. L. Smith, Y. Satow, E. A. Merritt, and R. P. Phizackerley, *Proc. Natl. Acad. Sci*, **86**, 2190 (1989).

[24] M. Bruchez, M. Moronne, P. Gin, S. Weiss, and A. P. Alivisatos, *Science* **281**, 2013 (1998).

[25] T. Stuchbury, M. Shipton, R. Norris, J. P. G. Malthouse, K. Brocklehurst, J. A. L. Herbert, and H. Suschitzky, *J. Biochem.* **151**, 417 (1975).

Chapter Eleven

Fabrication and Characterization of Surface-functionalized DBR Smart Particles for the Detection of Bio-molecules

11.1 Introduction

The development of new technology, which can achieve at nanometer scale, to build such a device is of great interest, because it is too complex to fabricate by using conventional lithographic method. Since the discovery of PSi [1], it has been intensively investigated for a variety of applications such as chemical [2] and biological sensors [3], medical diagnostics [4], optical band pass filters [5], micro chemical reactors [6], and micro fuel cells [7] due to very high surface area as well as their unique photonic properties. Especially, optical devices based on multi-structured PSi have been brought to the attention of the scientists. Multilayer PSi such as DBR PSi [8-9] or rugate PSi [10-11] exhibit unique optical properties providing a reflection band at specific wavelength in the optical reflectivity spectrum. The direction of pores and pore diameters depend on surface orientation, doping level and type, temperature, the current density, and the composition of the etching solution [12]. DBR PSi as multi-layered PSi has been developed and typically prepared by an applying a square current waveform to the etch cell. DBR PSi resulted in two discrete indices and displayed photonic structure of Bragg filters. Chemical modification of PSi multilayer exhibited the modification of its physical, chemical, and electronic properties. Chemical or bio molecule can be detected based on changes in the spectral interference pattern [13-14].

For applications in high throughput drug discovery and disease diagnostics, label-free biosensors would be important due to the advantage of easy sample preparation [15-16]. Two main optical transduction methods for label-free biosensors were both optical interferometric methods based on interferometers [17], evanescent wave devices [18], and grating couplers [19], and surface plasmon methods based on metal films [20] and colloids [21]. Biosensor based on PSi interferometer had a great advantage due to a large surface area matrix for immobilization of a variety of biomolecules such as enzymes [22], protein [23], and DNA fragments [24]. Sailor et al. recently reported that the electronic or optical properties of mono-layered PSi can be used as the transducer of biomolecular interaction in biosensor application [3]. In the present work, we have developed DBR smart particle biosensors based on surface-derivatized DBR PSi interferometer. The fabrication, optical characterization, and surface functionalized of biotin/silole-derivatized DBR smart particles were reported. The binding interaction with streptavidin was investigated for the application as a label-free biosensor.

11.2 Experiments

11.2.1 Preparation of DBR PSi Sample

DBR PSi samples were prepared by an electrochemical etch of heavily doped p^{++}-type silicon wafer (boron doped, polished on the <100> face, resistivity of 0.8~1.2 $m\Omega \cdot cm^{-2}$, Siltronix, Inc.). The etching solution consisted of a 3:1 volume mixture of aqueous 48% hydrofluoric acid (ACS reagent, Aldrich Chemicals) and absolute ethanol (ACS reagent, Aldrich Chemicals). Galvanostatic etch was carried out in a Teflon cell applying 30 cycles of a two-electrode configuration and performed in a dark room. DBR PSi was prepared by using a periodic pseudo-square wave current between 30 $mA \cdot cm^{-2}$ for 11 s and 300 $mA \cdot cm^{-2}$ for 1.5 s. All samples were then rinsed several times with ethanol and dried under argon atmosphere prior to use. The resulting DBR PSi were removed from the silicon substrate by an applying of electropolishing current at 460 $mA \cdot cm^{-2}$ for 100 s in a solution of 48% aqueous HF and ethanol (3:1 by volume) and 29 $mA \cdot cm^{-2}$ for 200 s in a solution of 48% aqueous HF and ethanol (1:15 by volume) to obtain a free-standing DBR PSi film.

11.2.2 Thermal Oxidation of Free-standing DBR PSi Film

Surface of a free-standing DBR PSi film was predominant hydride-terminated after the etching procedure. This surface was sensitive to oxidation and hydrolysis upon exposure to aqueous solution. Thermally oxidized DBR PSi samples were obtained by heat treatment in a furnace (Thermolyne F6270-26 furnace equipped

with controller) using the following parameters: intial ramp rate, 5 ℃/min to 300℃; hold time, 3 h; and passive cooling to ambient temperature.

11.2.3 Preparation of DBR Smart Particles

Preparation of DBR smart particles was accomplished by placing the oxidized DBR PSi films in 100 mL of ethanol in a Schlenk flask under argon atmosphere. The free-standing DBR PSi films were then made into particles by ultrasonic fracture in organic solution for 10 min. After removal of the solution, samples were rinsed with ethanol and acetone several times, dried under a reduced pressure, and stored in nitrogen atmosphere prior to use.

11.2.4 Synthesis of Biotin Tetrafluorophenyl Ester

For the biotinlylated DBR smart particles, biotin tetrafluorophenyl ester was prepared by previously known method [25]. Biotin (2.5 g, 10.22 mmol) was dissolved in 200 mL of warm (70 ℃) DMF under argon atmosphere. The solution was allowed to cool to room temperature. Triethylamine (2.5 mL, 20.5 mmol) was added, followed by an addition of 2,3,5,6-tetrafluorophenyl trifluoroacetate (4 g, 15.25 mmol). The reaction mixture was stirred at room temperature for 30 min. All volatiles were removed under reduced pressure. 100 mL of ether was added and the reaction mixture was filtered.

11.2.5 Surface Derivatization of Oxidized DBR Smart Particles

Dihydroxysilole (500 mg, 1.2 mmol) prepared by previously described method [26] and (3-aminopropyl)trimethoxysilane (1.8 mL, 10 mmol, 99%, Aldrich Chemicals) were dissolved in 50 mL of toluene. The oxidized DBR smart particles were added and refluxed for 24 h. After functionalization with amine and silole group, the sample was rinsed successively with acetone, dichloromethane, and ethanol and subsequently dried under a stream of nitrogen. Resulting DBR smart particles were incubated in biotin tetrafluorophenyl ester dissolved in triethylamine 20 mL at room temperature for 12 h. The sample was washed with acetone, dichloromethane, and ethanol and dried under argon gas.

11.2.6 Instruments and Data Acquisitions

FT-IR spectra were acquired with a Nicolet model 5700 FT-IR instrument in the diffuse reflectance mode (Spectra-Tech diffuse reflectance attachment). The FT-IR sample compartment was purged with nitrogen before each acquisition. The morphology of DBR smart particles was observed with cold field emission scanning electron microscope (FE-SEM, S-4800, Hitachi). Photoluminescence of silole/biotin-derivatized DBR smart particles was measured by Perkin-Elmer luminescence spectrometer LS 50B, and interferometric reflectance spectra were recorded by using an Ocean Optics S2000 spectrometer fitted with a bifurcated fiber optic probe. Spectra were recorded with a CCD detector in the wavelength range 400~1200 nm. The illumination of the surface as well as the measurement of the reflected light was performed along an axis coincident with the surface normal.

11.3 Results and Discussion

A DBR PSi exhibits a high reflectivity band with a Bragg wavelength λ_{Bragg}, depending on the thickness of the layers (d_1, d_2) and the corresponding refractive indices (n_1, n_2). The mth order of the Bragg peak is given by:

$$m\lambda_{Bragg} = 2(d_1n_1 + d_2n_2)$$

Multilayered DBR PSi prepared by applying a square current waveform exhibits high reflectivity in a specific narrow spectral region. The reflectivity can be tuned to appear anywhere in the visible to near-infrared spectral range, depending on the programmed etch waveform. The electrochemical process generates an optically uniform layer of PSi: the thickness and porosity of a given layer is controlled by the current density, the duration of the etch cycle, and the composition of the etchant solution. High current densities result in the desired well-defined macropores (diameter, d > 50 nm), rather than the random orientation of highly interconnected micropores (d < 2 nm). DBR PSi films have been removed from the silicon wafer by applying an electropolishing current and then ultrasonicated to create particles. Particles with sizes ranging from several hundred nanometers to few hundred micrometers were generated depending on the duration of ultrasonication. Figure 11.1. showed the SEM images of DBR PSi particles (so called "smart particle"). Size of DBR smart particle was about 20 ~ 40 micrometers. The surface image of DBR smart particles indicated that the pore size of particle retained a good porosity without destruction of porous structure during ultrasonication. The prepared DBR smart particles had cylindrical macropores with the average pore size of 100 nm, which could be suitable for the detection of streptavidin due to its size of 54

× 58 × 48 Å [27].

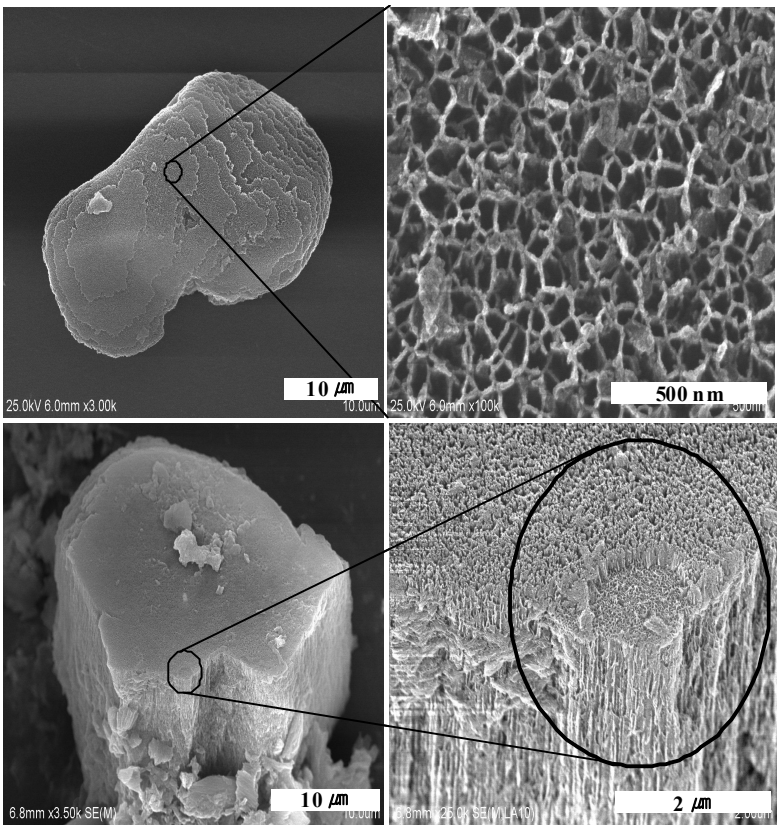

Figure 11.1. Surface and 3-dimensional images of DBR smart particle.

Figure 11.2. describes the process for chemical functionalization of DBR smart particles with biotin terminated (3-aminopropyl)trimethoxysilane and dihydroxysilole. The thermal oxidation of DBR smart particles at 300 ℃ for 3 h converted the hydride-terminated surface into the hydroxyl terminated surface. Biotin terminated (3-aminopropyl)trimethoxysilane and dihydroxysilole were used for the surface modification of oxidized DBR smart particles for the detection of streptavidin.

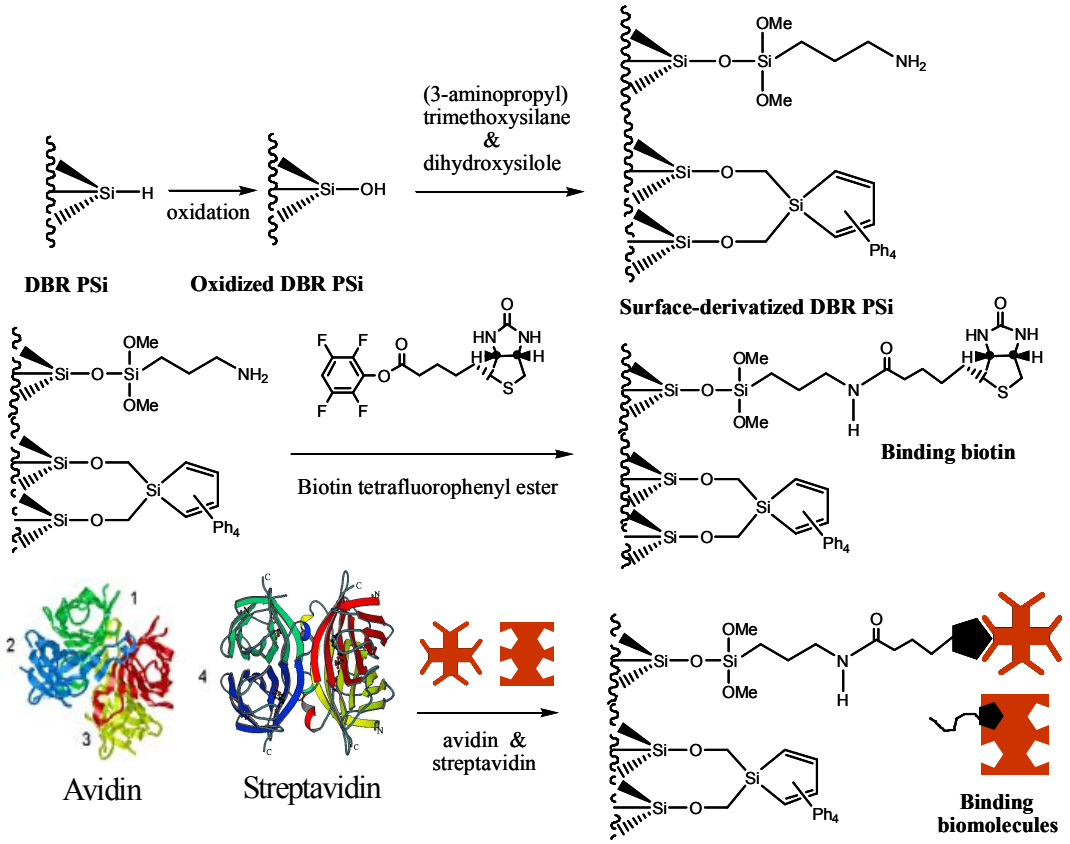

(continued)

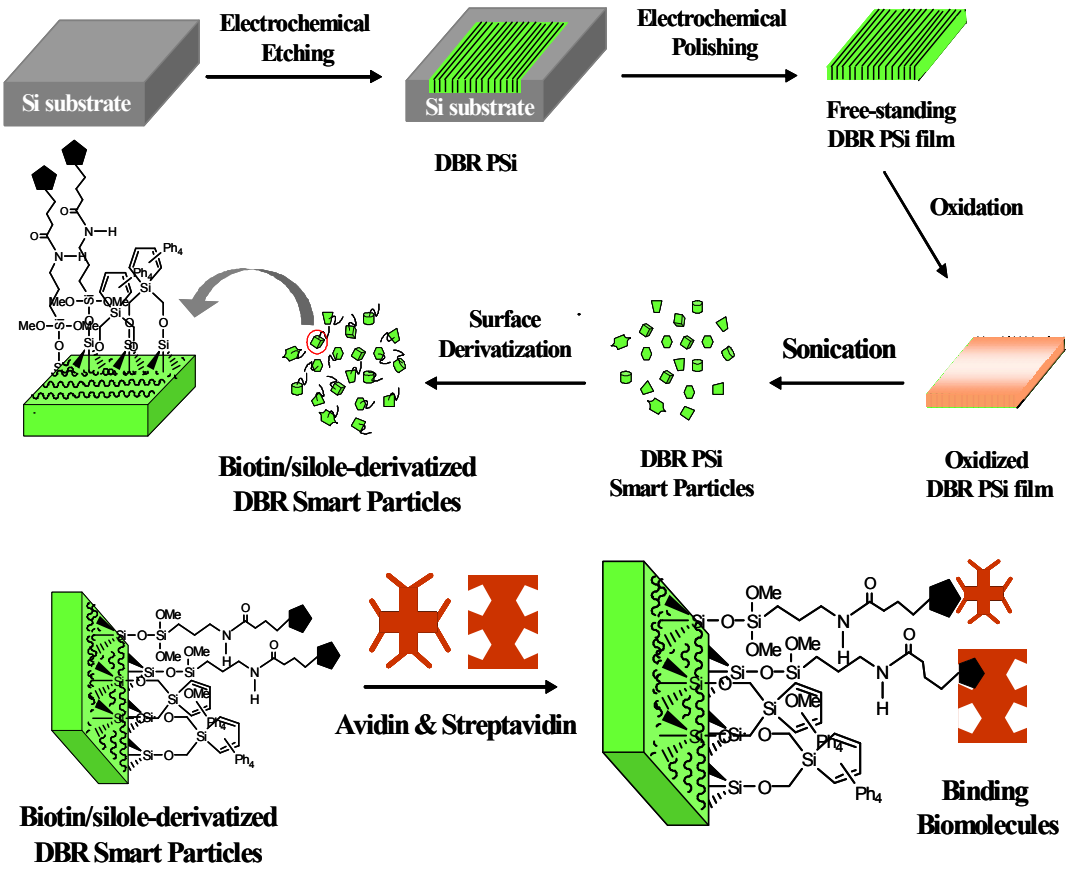

Figure 11.2. Schematic process for surface modification of DBR smart particles with biotin and silole groups.

Figure 11.3. showed that biotin/silole-derivatized DBR smart particles displayed both photoluminescence (λ_{em} = 505 nm) with 360 nm of excitation wavelength and reflectivity (λ_{max} = 607 nm) under tungsten-halogen lamp. Photograph of samples demonstrated that biotin/silole-derivatized DBR smart particles exhibited dual optical properties.

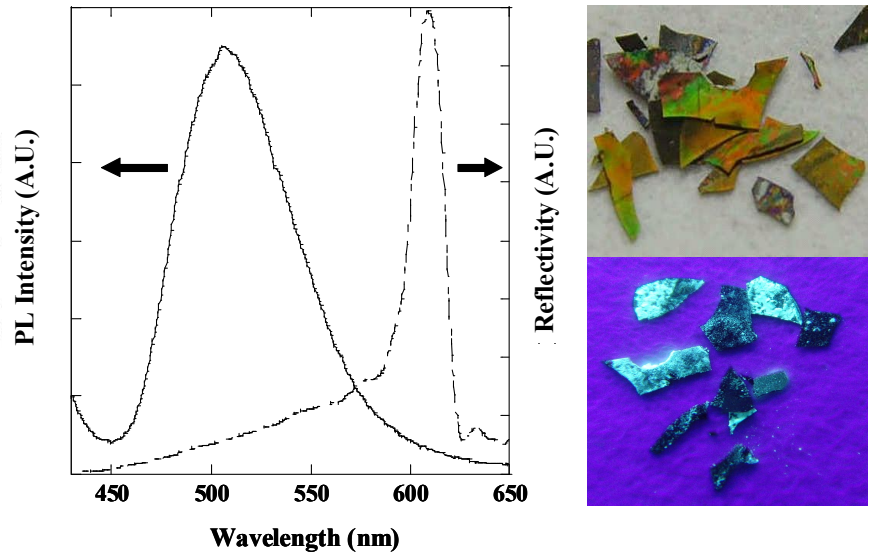

Figure 11.3. Optical reflectivity (dotted line) and photoluminescence (solid line) spectrum of biotin/silole-derivatized DBR smart particles. Photographs of biotin/silole-derivatized DBR smart particles under white light (top) and black light (bottom).

Diffuse reflectance FT-IR spectroscopy was used to monitor the oxidation and functionalization reaction of DBR smart particles sample. Figure 11.4(A). showed that the FT-IR spectrum of DBR smart particle immediately after an anodization of the silicon wafer displayed a characteristic broad band centered at 2115 and 908 cm^{-1} for the ν(Si-H) stretching vibration and δ(Si-H) bending vibration. After the thermal oxidation of DBR smart particles, the presence of silicon oxide was determined by FT-IR measurement as shown in Figure 11.4(B). Thermal oxidation of the DBR smart particles resulted in the appearance of the characteristic large and broad Si-O-Si vibrational band around 1100 cm^{-1} in the FT-IR. The oxidized DBR smart particles exhibited vibrational bands characteristic of ν(OSi-H) and δ(OSi-H) vibratioal modes observed at 2277 and 883 cm^{-1}, respectively. Thermal oxidation of DBR smart particles led to a decrease of the Si-H vibrational band and the appearance of the OSi-H vibrational band. Condensation of the Si-OH surface of DBR smart particles with (3-aminopropyl)trimethoxysilane generated a surface-bound amino group. The FT-IR spectrum shown in Figure 11.4(C) displayed additional bands characteristic of the linker (the amide band of ν(N-H) broad band centered at 3300 cm^{-1} and δ(N-H) at 1579 cm^{-1} and the aliphatic ν(C-H) stretching bands at 2858 and 2954 cm^{-1}). Surface derivatization led to complete the disappearance of the OSi-H vibrational band. The subsequent reaction with biotin as shown in Figure 11.2. led to the desired biotin-functionalized surface which was used in the avidin and streptavidin-binding studies (Figure 11.4D). The band at 1685 cm^{-1} was assigned to the carbonyl stretching vibration of the biotin head group.

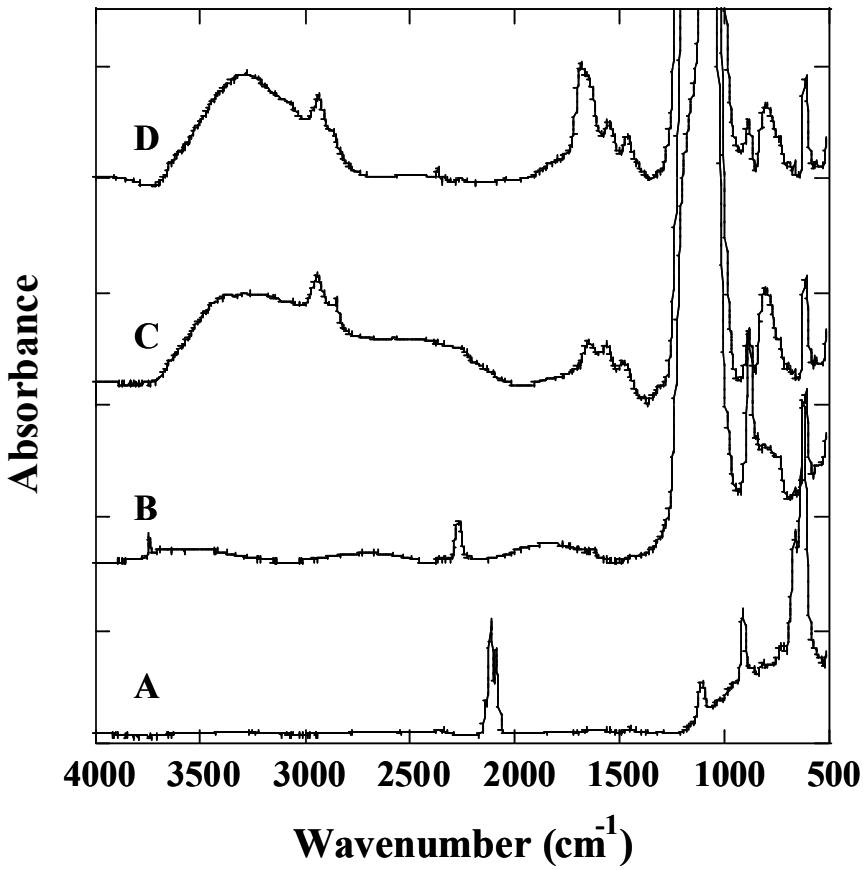

Figure 11.4. Diffuse reflectance FT-IR spectra of (A) a freshly etched DBR smart particle, (B) oxidized DBR smart particle at 300℃ for 3 h, (C) functionalized DBR smart particle with (3-aminopropyl)trimethoxysilane, and (D) subsequent reaction of the surface with biotin..

Fresh DBR PSi displayed a very sharp line at 624 nm with sidelobes around the reflectance peak in the optical reflectivity spectrum as shown in Figure 11.5. The spectral bands of DBR smart particles had a full-width at half-maximum (FWHM) of about 20 nm. The thermal oxidation of DBR PSi resulted in the reflectivity at 580 nm shifted to shorter wavelengths by 44 nm due to the decrease of refractive index of silicon dioxide from silicon. Condensation of the Si-OH surface of DBR smart particles with (3-aminopropyl)trimethoxysilane generated a surface-bound amino group. The amine-functionalized DBR smart particles resulted in the reflectivity at 600 nm shifted to longer wavelengths by 20 nm due to the increase of refractive index upon introduction of the amine group into the pores of DBR smart particles. The subsequent reaction with biotin led to the desired biotin-funtionalized DBR smart particles which were used in the avidin and streptavidin-binding studies. The biotin-functionalized DBR smart particles resulted in the reflectivity at 610 nm shifted to longer wavelengths due to the increase of additional refractive index.

The surface functionalized DBR smart particles were placed in the flow cell. Aqueous phosphate buffer solution (PBS) was flushed to perform for an initial measurement of reflectivity. The surface was rinsed thoroughly with PBS buffer solution to ensure a covalent attachment to the surface and to check the stability of the reflectivity measurement. The biotin-functionalized DBR smart particles in PBS buffer solution resulted in the reflectivity at 665 nm shifted to longer wavelengths by 55 nm due to the increase of refractive index upon introduction of the PBS buffer solution into the pores of DBR smart particles.

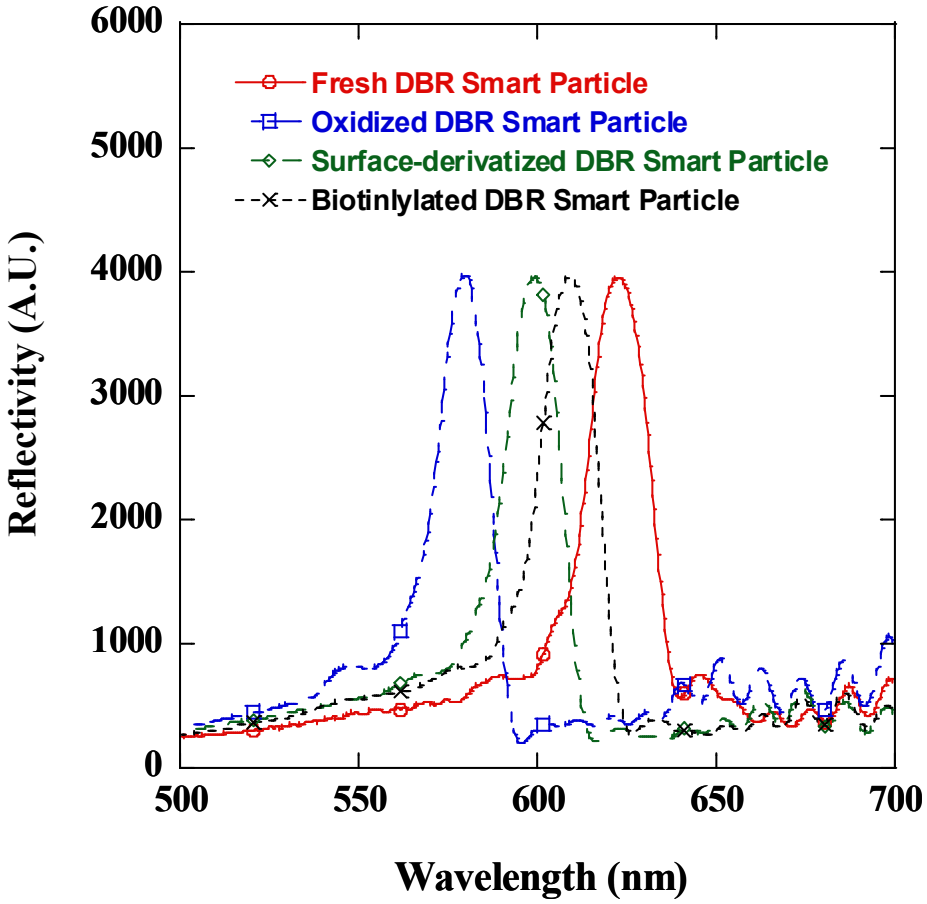

Figure 11.5. Optical reflectivity spectra of fresh, oxidized, surface-functionalized, and biotin derivatized DBR smart particle.

The cell was then flushed with a constant flow rate of 0.8 mL/min of PBS containing avidin and streptavidin (20 μM), which coupled to the biotin-modified DBR smart particles surface. Figure 6.6 showed the change of reflection spectrum under the exposure of avidin and streptavidin to the biotin-functionalized DBR smart particles. An increase of the reflection wavelength in the reflectivity spectrum by 17 and 14 nm was observed, indicative of a change in refractive indices induced by binding of the avidin and streptavidin into the biotin-derivatized DBR smart particles, respectively. This increase was attributed to the replacement of some of the aqueous phase with avidin and streptavidin. The replacement changed the mean refractive indices of the DBR smart particles. They were observed as an increase of the reflection wavelength in the reflectivity.

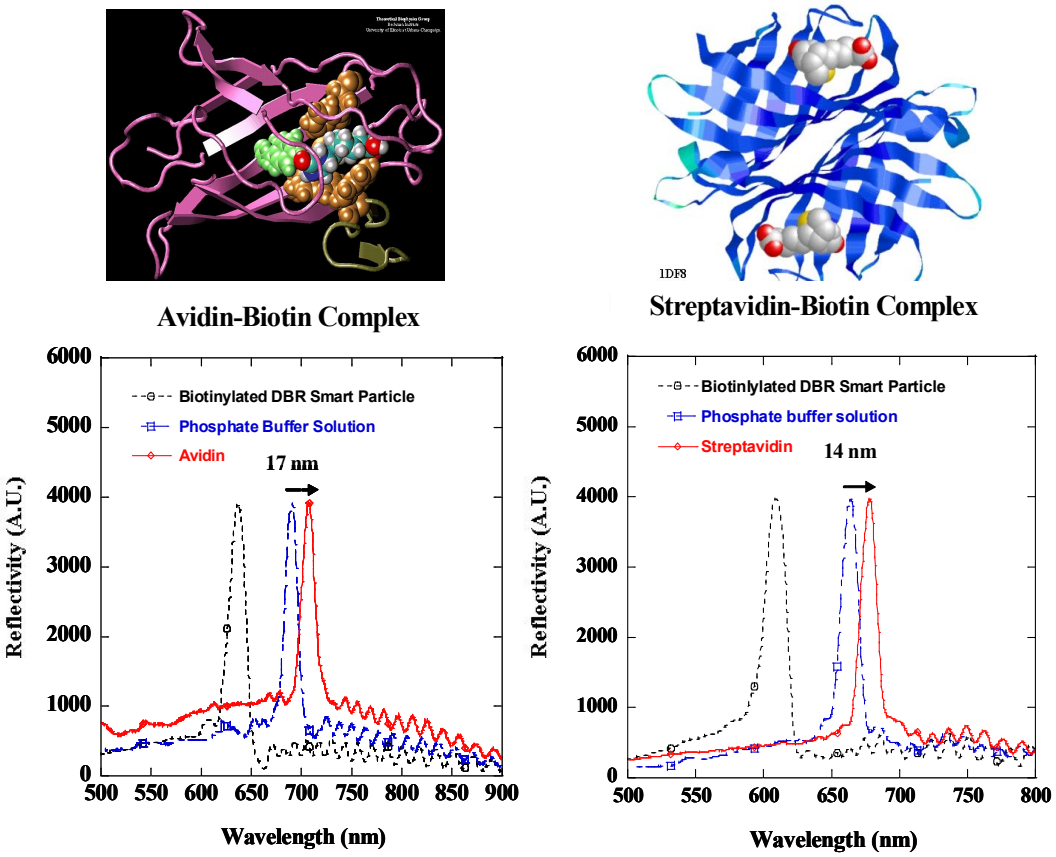

Figure 11.6. Sensing of avidin and streptavidin based on biotin derivatized DBR smart particle in PBS.

11.4 Conclusion

Biotin/silole-derivatized DBR smart particles exhibiting dual optical properties such as photoluminescence (λ_{em} = 505 nm) and reflectivity (λ_{max} = 607 nm) for the detection of streptavidin were fabricated. Diffuse reflectance FT-IR spectroscopy was used to monitor the chemical and optical characterization of DBR smart particles during step-by-step functionalization of DBR smart particles surface. The reflection spectra of biotin-modified DBR smart particles were used in the avidin and streptavidin-binding studies. When the PBS buffer solution containing avidin and streptavidin was flushed into the biotin-functionalized DBR smart particle in the cell, a red-shift of reflectivity by 17 and 14 nm in the reflectivity spectrum was observed, respectively. This result indicated the binding of the avidin and streptavidin into the biotin-derivatized DBR smart particles.

11.5 Reference

[1] A. Uhlir, *Bell System Tech*. **35**, 333 (1956).

[2] H. Sohn, S. Letant, M. J. Sailor, and W. C. Trogler, *J. Am. Chem. Soc*. **122**, 5399 (2000).

[3] V. S.-Y. Lin, K. Motesharei, K.-P. S. Dancil, M. J. Sailor, and M. R. Ghadiri, *Science* **278**, 840 (1997).

[4] M. Simion, I. Kleps, T. Neghina, A. Angelescu, M. Miu, A. Bragaru, M. Danila, E. Condac, M. Costache, and L. Savu, *J. Alloy. Compd*. **434**, 830 (2007).

[5] S. Ilyas, T. Böcking, K. Kilian, P. J. Reece, J. Gooding, K. Gaus, and M. Gal, *Opt. Mater*. **29**, 619 (2007).

[6] M. A. Khan, M. S. Haque, H. A. Naseem, W. D. Brown, and A. P. Malshe, *Thin Solid Films*. **332**, 93 (1998).

[7] S. E. Lêtant, S. Content, T. T. Tan, F. Zenhausern, and M. J. Sailor, *Sensor Actuat. B*. **69**, 193 (2000).

[8] B.-J. Lee, S. Jang, and H. Sohn, *Solid State Phenom*. **124-126**, 491 (2007).

[9] J. Kim, Y. Koh, S. Jang, Y. C. Ko, H. -G. Woo, and H. Sohn, *J. Nanosci. Nanotechnol*. **7**, 4165 (2007).

[10] J. Park, S. Cho, Y. C. Ko, and H. Sohn, *J. Korean Phys. Soc*. **50**, 695 (2007).

[11] S. Jang, J. Kim, Y. Koh, Y. C. Ko, H.-G. Woo, and H. Sohn, *J. Nanosci. Nanotechnol*. **7**, 4049 (2007).

[12] R. L. Smith and S. D. Collins, *J. Appl. Phys*. **71**, R1 (1992).

[13] A. Janshoff, K.-P. S. Dancil, C. Steinem, D. P. Greiner, V. S. Lin, C. Gurtner, K. Motesharei, M. J. Sailor, and M. R. Ghadiri, *J. Am. Chem. Soc*. **120**, 12108 (1998).

[14] B.-J. Lee, S. G. Kim, and H. Sohn, *Key Eng. Mater.* **321-323**, 53 (2006).

[15] A. Brecht and G. Gauglitz, *Sensor. Actuat. B.* **38**, 1 (1997).

[16] J. Janata, M. Josowicz, and D. M. Devaney, *Anal. Chem.* **66**, 207R (1994).

[17] J. Piechler, A. Brandenburg, A. Brecht, E. Wagner, and G. Gauglitz, A*ppl. Opt.* **36**, 6554 (1997).

[18] A. P. Abel, M. G. Weller, G. L. Duveneck, M. Ehart, and H. M. Widmer, *Anal. Chem.* **68**, 2905 (1996).

[19] R. Polzius, E. Diessel, F. F. Bier, and U. Bilitewski, *Anal. Biochem.* **248**, 269 (1997).

[20] J. Homola, S. S. Yee, and G. Gauglitz, *Sensor. Actuat. B.* **54**, 3 (1999).

[21] P. I. Nikitin, A. A. Beloglazov, V. E. Kochregin, M. V. Valeiko, and T. I. Ksenevich, *Sensor. Actuat. B.* **54**, 43 (1999).

[22] J. Drott, K. Lindstrom, L. Rosengren, and T. J. Laurell, *Micromech. Microeng.* **7**, 14 (1997).

[23] T. Laurell, J. Drott, L. Rosengern, and K. Lindstrom, *Sensor. Actuat. B.* **31**, 161 (1996).

[24] K. L. Beattie, W. G. Beattie, L. Mengm S. L. Turner, R. Coral-Vazquez, D. D. Sith, P. M. Mclntyre, and D. D. Dao, *Clin. Chem.* **41**, 700 (1995).

[25] H. B. Gamper, M. W. Reed, T. Cox, J. S. Virosco, A. D. Adams, A. A. Gall, J. K. Scholler, and R. B. Meyer, *Nucleic Acids Res.* **21**, 145 (1993).

[26] I. Toulokhonovat, R. Zhao, M. Kozee, and R. West, *Main Group Met. Chem.* **24**, 737 (2001).

[27] W. A. Hendrickson, A. Pahler, J. L. Smith, Y. Satow, E. A. Merritt, and R. P. Phizackerley, *Proc. Natl. Acad. Sci.* **86**, 2190 (1989).

Part II.

Fluorescent Sensors Based on Nanoaggregates

Chapter Twelve
Introduction of Organosilicon Chemistry

12.1 What is Organometallic Chemistry?

Organometallic chemistry is the study of chemical compounds containing bonds between carbon and a metal [1]. Since many compounds without such bonds are chemically similar, an alternative may be compounds containing metal-element bonds of a largely covalent character. Organometallic chemistry combines aspects of inorganic chemistry and organic chemistry.

Organometallic compounds are also known as organo-inorganics, metallo-organics and metalorganics. Organometallic compounds are distinguished by the prefix "organo-" e.g., organopalladium compounds. Examples of such organometallic compounds include all Gilman which contain lithium and copper. Tetracarbonyl nickel, and ferrocene are examples of organometallic compounds containing transition metals. Other examples include organomagnesium compounds like iodo(methyl)magnesium MeMgI, diethylmagnesium (Et_2Mg), and all Grignard reagents; organolithium compounds such as butyllithium (BuLi), organozinc compounds such as chloro(ethoxycarbonylmethyl)zinc ($ClZnCH_2C(=O)OEt$); and organocopper compounds such as lithium dimethylcuprate ($Li^+[CuMe_2]^-$).

In addition to the traditional metals, lanthanides, actinides, and semimetals, elements such as boron, silicon, arsenic, and selenium are considered to form organometallic compounds, e.g., organoborane compounds such as triethylborane (Et_3B).

12.2 History of Organometallic Chemistry

Early developments in organometallic chemistry include Louis Claude Cadet's synthesis of methyl arsenic compounds related to cacodyl, William Christopher Zeise's platinum-ethylene complex, Edward Frankland's discovery of dimethyl zinc, Ludwig Mond's discovery of $Ni(CO)_4$, and Victor Grignard's organomagnesium compounds. The abundant and diverse products from coal and petroleum led to Ziegler-Natta, Fischer-Tropsch, hydroformylation catalysis which employ CO, H_2, and alkenes as feedstocks and ligands.

Recognition of organometallic chemistry as a distinct subfield culminated in the Nobel Prizes to Ernst Fischer and Geoffrey Wilkinson for work on metallocenes. In 2005, Yves Chauvin, Robert H. Grubbs and Richard R. Schrock shared the Nobel Prize for metal-catalyzed olefin metathesis.

Table 12.1. Organometallic chemistry timeline

1760	Louis Claude Cadet de Gassicourt investigates inks based on Cobalt salts and isolates Cacodyl from cobalt mineral containing arsenic.
1827	Zeise's salt is the first platinum/olefin complex.
1863	Charles Friedel and James Crafts prepare organochlorosilanes.
1890	Ludwig Mond discovers Nickel carbonyl.
1899	Introduction of Grignard reaction.
1900	Paul Sabatier works on hydrogenation organic compounds with metal catalysts.
1909	Paul Ehrlich introduces Salvarsan for the treatment of syphilis, an early arsenic based organometallic compound.
1912	Nobel Prize Victor Grignard and Paul Sabatier.
1930	Henry Gilman works on lithium cuprates.
1963	Nobel prize for Karl Ziegler and Giulio Natta on Ziegler-Natta catalyst.
1965	Discovery of cyclobutadieneiron tricarbonyl.
1968	Heck reaction.
1973	Nobel prize Geoffrey Wilkinson and Ernst Otto Fischer on sandwich compounds.
2005	Nobel prize Yves Chauvin, Robert Grubbs, and Richard Schrock on metal-catalyzed alkene metathesis.

12.3 Classification of Organometallic Chemistry

Table 12.2. Classification of organometallic chemistry

Period 2 elements	organolithium chemistry, organoberyllium chemistry, organoborane chemistry.
Period 3 elements	organomagnesium chemistry, organoaluminum chemistry, **organosilicon chemistry**.
Period 4 elements	organotitanium chemistry, organochromium chemistry, organomanganese chemistry, organoiron chemistry, organocobalt chemistry, organonickel chemistry, organocopper chemistry, organozinc chemistry, organogallium chemistry, **organogermanium chemistry**.
Period 5 elements	organopalladium chemistry, organosilver chemistry, organocadmium chemistry, organoindium chemistry, organotin chemistry.
Period 6 elements	organoplatinum chemistry, organogold chemistry, organomercury chemistry, organothallium chemistry, organolead chemistry.

12.4 Organosilicon Chemistry

Even after more than 100 years of history, organosilicon Chemistry is arguably still one the most significant and diverse research areas of chemistry. The last ten years have witnessed tremendous advances and breakthroughs. Significant new applications in organic synthesis and medicinal chemistry have been developed.

Organosilicon compounds are organic compounds containing carbon silicon bonds. Organosilicon chemistry is the corresponding science exploring their properties and reactivity [2]. Like carbon, the organically bound silicon is tetravalent and tetrahedral. Carbon-silicon bonds are not found in any biomolecule [3]. The first organosilicon compound, tetraethylsilane was discovered by Charles Friedel and James Crafts in 1863 by reaction of tetrachlorosilane with diethylzinc. The carbosilicon silicon carbide is an inorganic compound.

12.4.1 Organosilanes

Carbon silicon bonds compared to carbon carbon bonds are longer (186 pm *vs* 154 pm) and weaker with bond dissociation energy 451 kJ/mol *vs* 607 kJ/mol. The C-Si is somewhat polarized towards carbon due to its higher electronegativity (C=2.55 *vs* Si=1.90). One manifestation of bond polarization in organosilanes is found in the Sakurai reaction. In oxidative couplings silicon is represented by the Hiyama coupling. Certain alkyl silanes can be oxidized to an alcohol in the Fleming-Tamao oxidation. The chemistry of silanes such as tetramethylsilane is comparable to that of alkanes in many aspects such as thermal stability. The β -silicon effect describes the stabilizing effect of a β-silicon atom on a carbocation with many implications for reactivity.

12.4.2 Siloxides

More notably bonds of silicon to oxygen are much shorter and stronger (809 compared to 538 kJ/mol) than that of those of carbon to oxygen. The polarization in this bond increases towards oxygen. Examples are silyl acetals $RR'Si(OR)_2$, the siloxanes and the polymeric polysiloxanes. Silyl ethers are extensively used as protective groups for alcohols. The favorable formation of Si-O bonds drive many organic reactions such as the Brook rearrangement and Peterson olefination.

Another manifestation is the highly explosive nature of the silicon pendant $Si(CH_2ONO_2)_4$ and $Si(CH_2N_3)_4$ of pentaerytritol tetranitrate [4]:

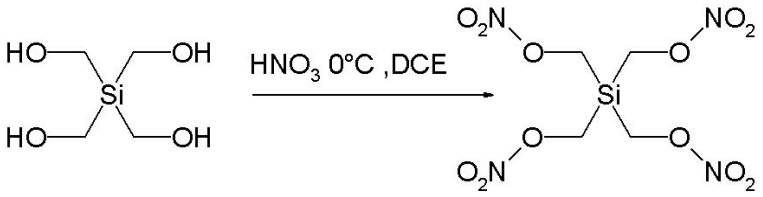

12.4.3 Silyl Halides

Organosilyl halides are important reagents in organic chemistry notably trimethylsilyl chloride Me_3SiCl. A classic method called the Flood reaction for the synthesis of this compound class is by heating hexaalkyldisiloxanes $R_3SiOSiR_3$ with concentrated sulfuric acid and a sodium halide [5]. Other relevant silyl halides are dichloromethylphenylsilane **1**, dimethyldichlorosilane **2**, methyltrichlorosilane **3**, trimethylchlorosilane **4**, trichloroethylsilane **5**, trichloro(chloromethyl)silane **6**, (4-aminobutyl)diethoxymethylsilane **7**, trichloro(dichlorophenyl) silane **8**, trichloro phenylsilane **9**. as shown in Figure 12.1.

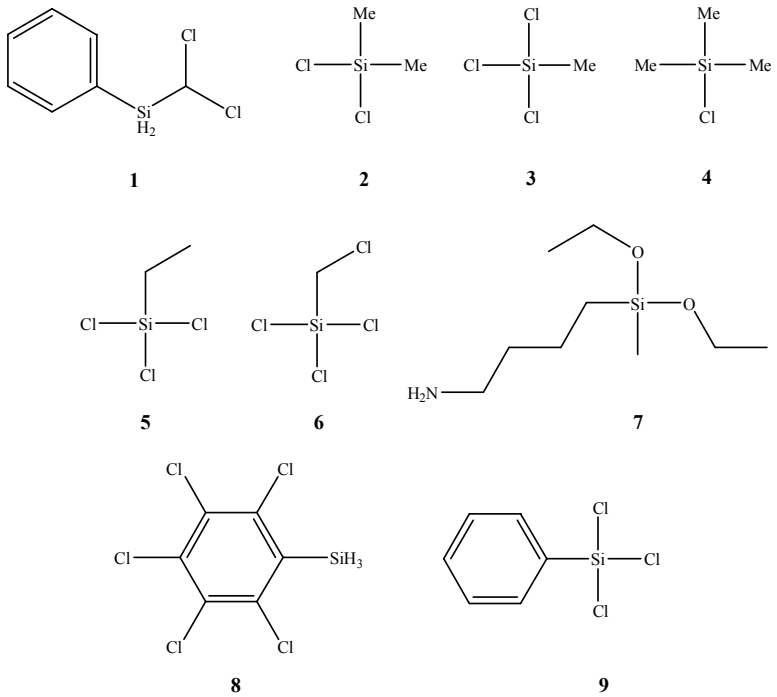

Figure 12.1. Structures of silyl halides.

12.4.4 Silyl Hydrides

The silicon to hydrogen bond is longer than the C-H bond (148 compared to 105 pm) and weaker (299 compared to 338 kJ/mol). Hydrogen is more electronegative than silicon hence the naming convention of silyl hydrides. Silyl hydrides are very reactive and used as reducing agents for example polymethylhydrosiloxane (PMHS).

In one study triethylsilylhydride is used in the conversion of an phenyl azide to an aniline [6]:

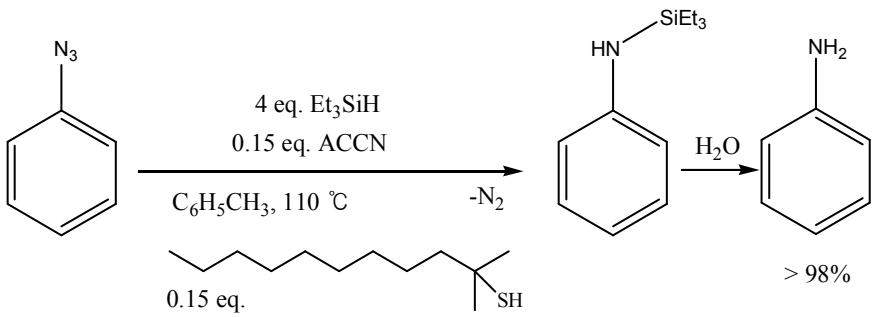

12.4.5 Hydrosilylation

Silyl hydrides react with various unsaturated substrates such as alkenes, alkynes, imines, carbonyls and oximes to new organosilicon compounds in hydrosilylation. In the reaction of triphenylsilyl hydride with phenylacetylene the reaction product is a trans or cis or the geminal vinyl silane, for example [7]:

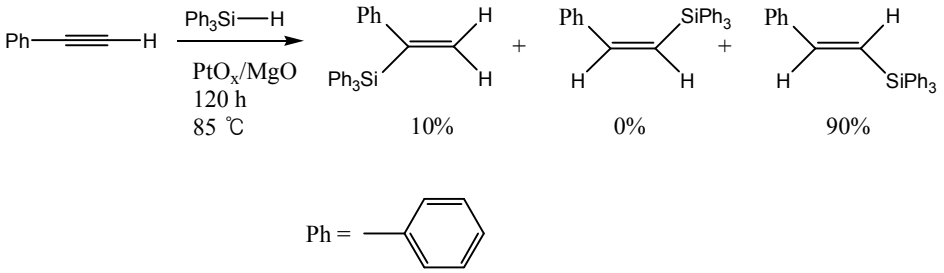

In the related silylmetalation, a metal replaces the hydrogen atom.

12.4.6 Silenes

Organosilicon compounds unlike their carbon counterparts do not have a rich double bond chemistry due to the large difference in electronegativity. Existing compounds with organosilene Si=C bonds are laboratory curiosities such as the silicon benzene analogue silabenzene, and Si=Si bond containing disilenes. Disilenes are compounds containing a silicon-silicon double bond and are considered to be heavier analogues of alkenes. They are sometimes also called disilaalkenes. The first transient disilene was synthesized in 1972 by D. N. Roark and Garry J. D. Peddle. The first thermally stable disilene, tetramesityldisilene, was isolated in 1981 by Robert West and coworkers [8].

12.4.7 Siloles

Siloles, silacyclopentadienes, are well established since the pioneering work of Braye and Hübel in 1959, their unique electronic structure has stimulated much research in recent years [9]. Siloles are the silicon pendants of pyrroles and of current academic interest due to their electroluminescence and other electronic properties. Silole is a silicon-containing five-membered cyclic diene, that is a silicon analog of cyclopentadiene. There have been extensive studies on the synthesis, reactivities, properties and coordination abilities of such compounds to transition metals, and the aromaticity of their anionic or cationic species. The most notable feature of siloles is their high electron-accepting property, associated with their low-lying LUMOs. Potential applications of silole span a wide range, including electron-transporting materials, electroluminescent (EL) devices, and electronic sensors. A general review on siloles by Yamaguchi and Tamao is available [10]. More specialized reviews on aromatic silole anions and polymeric siloles have been written by Saito and Yoshioka in 2005 and by Dyer *et al*. in 2003 [11-12].

12.5 Introduction of Siloles

12.5.1 Unique electronic structure of silole

According to the theoretical calculation of Tamao's group [13], silole has a quite different electronic structure from that of cyclopentadiene [14-18]. *Ab initic* calculatioans at the HF/6-31G* level of theory show that, while the HOMO of the parent silole is about 0.4 eV lower than that of the parent cyclopentadiene, the LUMO level of the silole is more than 1.2 eV lower in comparison with that of cyclopentadiene as shown in Figure 12.2.

The difference in their LUMO levels is due to the unique orbital interaction in the silole ring, as shown in Figure 12.3. When the molecular orbital of silole is constructed by orbital interaction of MOs of a silylene moiety and a butadiene moiety, the low-lying LUMO of silole arises from mixture of the σ^* orbital of the silylene moiety with the π^* orbital of the butadiene moiety, *i.e.*, σ^*-π^* conjugation. It should be noted that the σ^* orbital on the silicon and the lobes of π^* orbital on the adjacent carbons are in phase. This orbital interaction takes place effectively due to the fixed perpendicular arrangement of the plane of the silylene moiety, *i.e.* the plane involving two exocyclic σ bonds of the silole, to the plane of the butadiene moiety and to the energetically comparable σ^* and π^* orbitals. In the case of cyclobutadiene the σ^*-π^* conjugation in the LUMO is almost negligible because of the much higher energy level of the corresponding exocyclic σ^* orbital.

The shape of the LUMO of silole is visualized in Figure 12.4, together with that of cyclopentadiene for comparison.

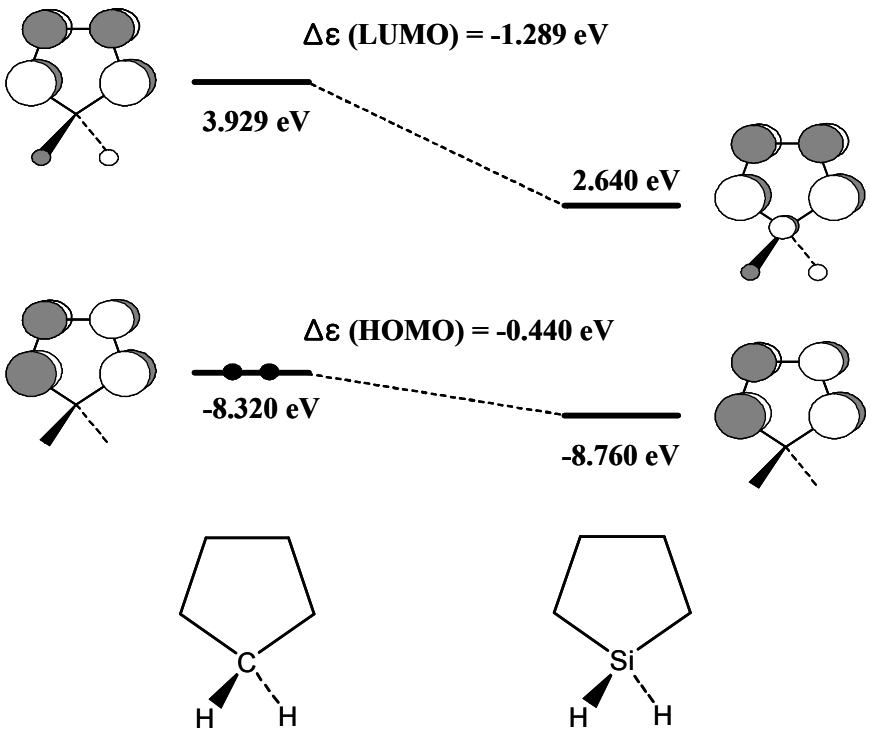

Figure 12.2. Releative energy levels of the HOMO and LUMO for silole and cyclobutadiene, based on the HF/6-31G* calculations.

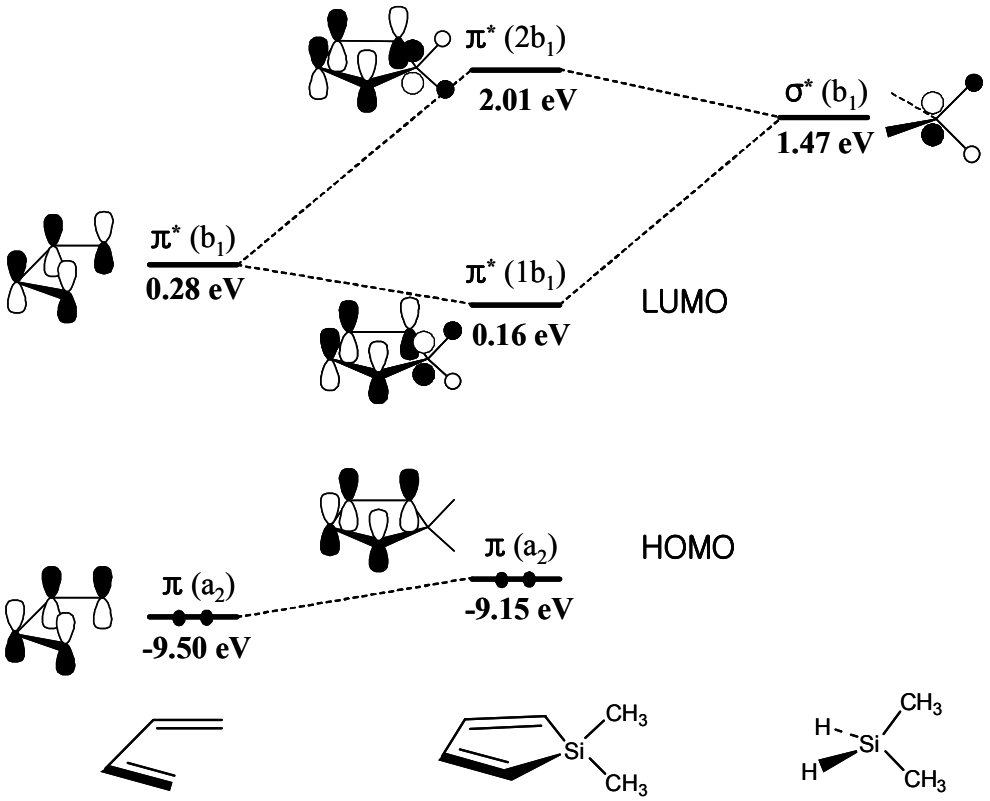

Figure 12.3. Orbital correlation diagram for 1,1-dimethylsilole, based on the PM3 calculations.

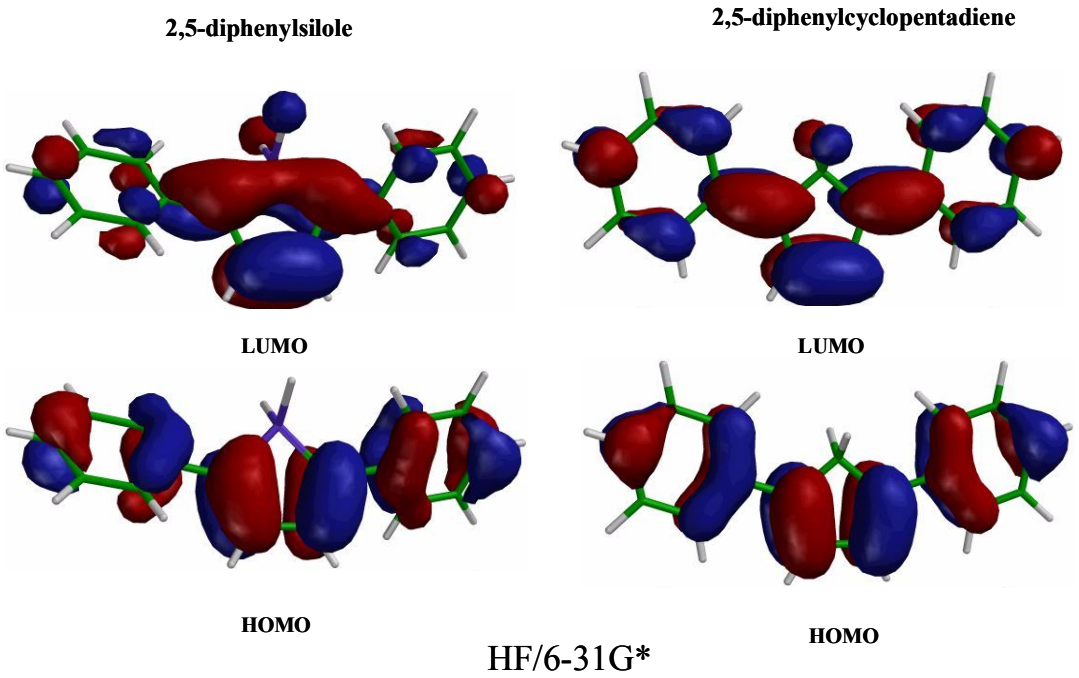

Figure 12.4. Shape of the HOMO and LUMO of silole and cyclopentadiene.

12.5.2 Various silole derivatives

Siloles containing phenyl groups are synthesized best starting from diphenylacetylene and lithium, which affords 1,4-dilithio-1,2,3,4-tetraphenylbutadiene that readily react with the chlorosilanes $SiCl_4$, Me_2SiCl_2, Ph_2SiCl_2, and $PhSiCl_3$ to produce the siloles **1-4** (Scheme 12.1). Siloles containing methyl groups, such as **5**, are accessible upon metallation of 1,4-diiodo-1,2,3,4-tetramethylbutadiene providing the corresponding dilithio compound that may be reacted with chlorosilanes, such as $SiCl_4$ (Scheme 12.1). The 2,5-dilithiated 1,1-bis(diethylamino)silole **6** is available by the reduction of bis(phenylethynyl)silane **7** with lithium naphthalenide (Scheme 12.1). The subsequent reaction of **6** with trimethylchlorosilane and simethyl sulfate provides access to the 1,1-bis(diethylamino)siloles **8** and **9**, having trimethylsilyl and methyl groups in vicinal positions (Scheme 12.1).

The 1,1-bis(diethylamino)siloles **8** and **9**, are excellent precursors for the synthesis of other 1,1-difunctionalized-siloles (Scheme 12.2) [19]. the reaction of **8** and **9** with $EtOH/AlCl_3$ and HCl produces the siloles **10** and **11** containing ethoxy groups or chlorine atoms attached to the silicon. The 1,1-dichlorosiloles **12** and **13** have been converted into the corresponding 1,1-difluorosiloles **14** and **15** with ZnF_2. Hydrolysis of **13** and **15** yields the fluorosilanol **16** and the silanediol **17**, respectively (Scheme 12.2).

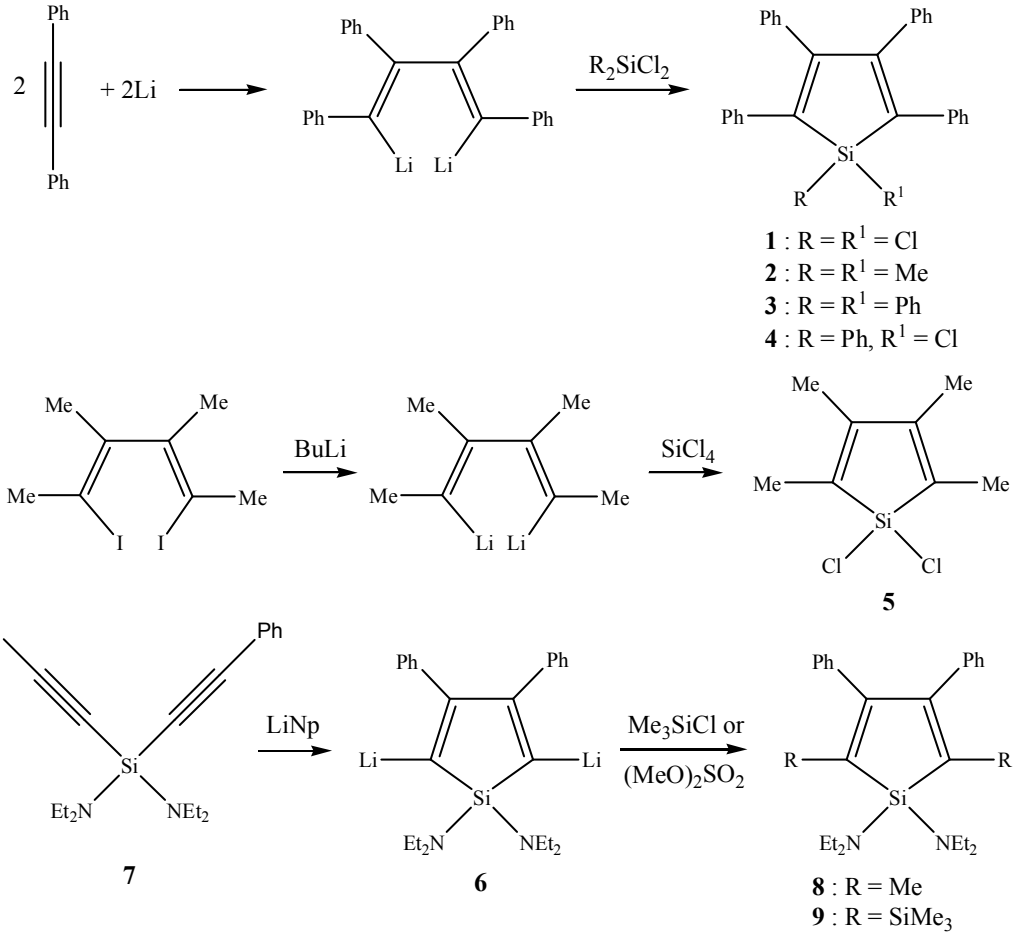
2
+ 2Li
Ph
Li
R_2SiCl_2
Si
R
R^1
1 : R = R^1 = Cl
2 : R = R^1 = Me
3 : R = R^1 = Ph
4 : R = Ph, R^1 = Cl
Me
I
BuLi
$SiCl_4$
Cl
5
7
LiNp
Et_2N
NEt_2
6
Me_3SiCl or
$(MeO)_2SO_2$
8 : R = Me
9 : R = $SiMe_3$

Scheme 12.1.

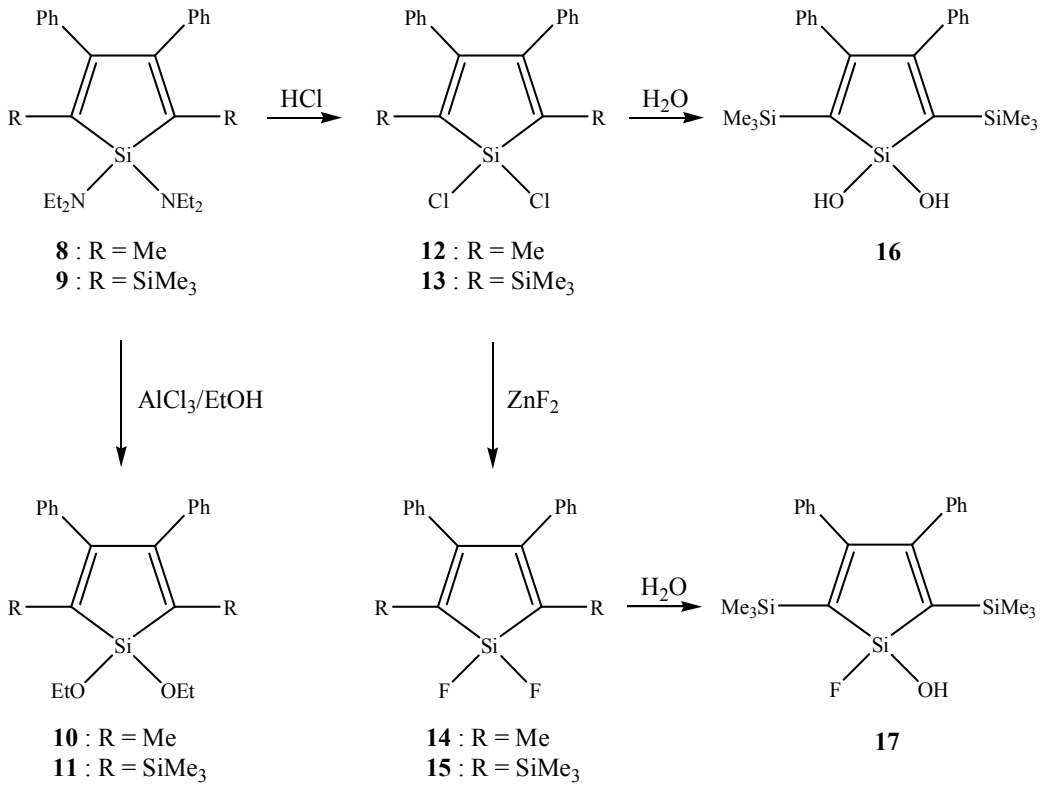

8 : R = Me
9 : R = $SiMe_3$

12 : R = Me
13 : R = $SiMe_3$

16

10 : R = Me
11 : R = $SiMe_3$

14 : R = Me
15 : R = $SiMe_3$

17

Scheme 12.2.

The perphenylated 1,1-dichlorosilole **1** is also a versatile starting material for the prepararion of new silole derivatives (Scheme 12.3). The reaction of **1** with the metallated acetylene derivatives PhCCLi and HCCMgBr provides access to the siloles **18** and **1**9 containing ethynyl groups, whereas the careful hydrolysis with $NaHCO_3$ affords the silandiol **20** [20].

The reduction of **1** with $LiAlH_4$, sodium (short reaction time), and lithium (long reaction time) gives rise to formation of the dihydride **21**, the polysilole **22** having terminal chlorine atoms [21], and the lithium disilanide **23**, respectively [22-24].

The silole dianions are believed to be aromatic. The negative charge of **23** is partly distributed over the delocalized π-electron system, explaining the high electron-accepting property and the partial silylenoide character of the silicon atom. The catalytic dehydrocoupling of **21** using H_2PtCl_6 and $RhCl(PPh_3)_3$ gives access to low molecular weight polysilols **24** having terminal hydrogen atoms [25].

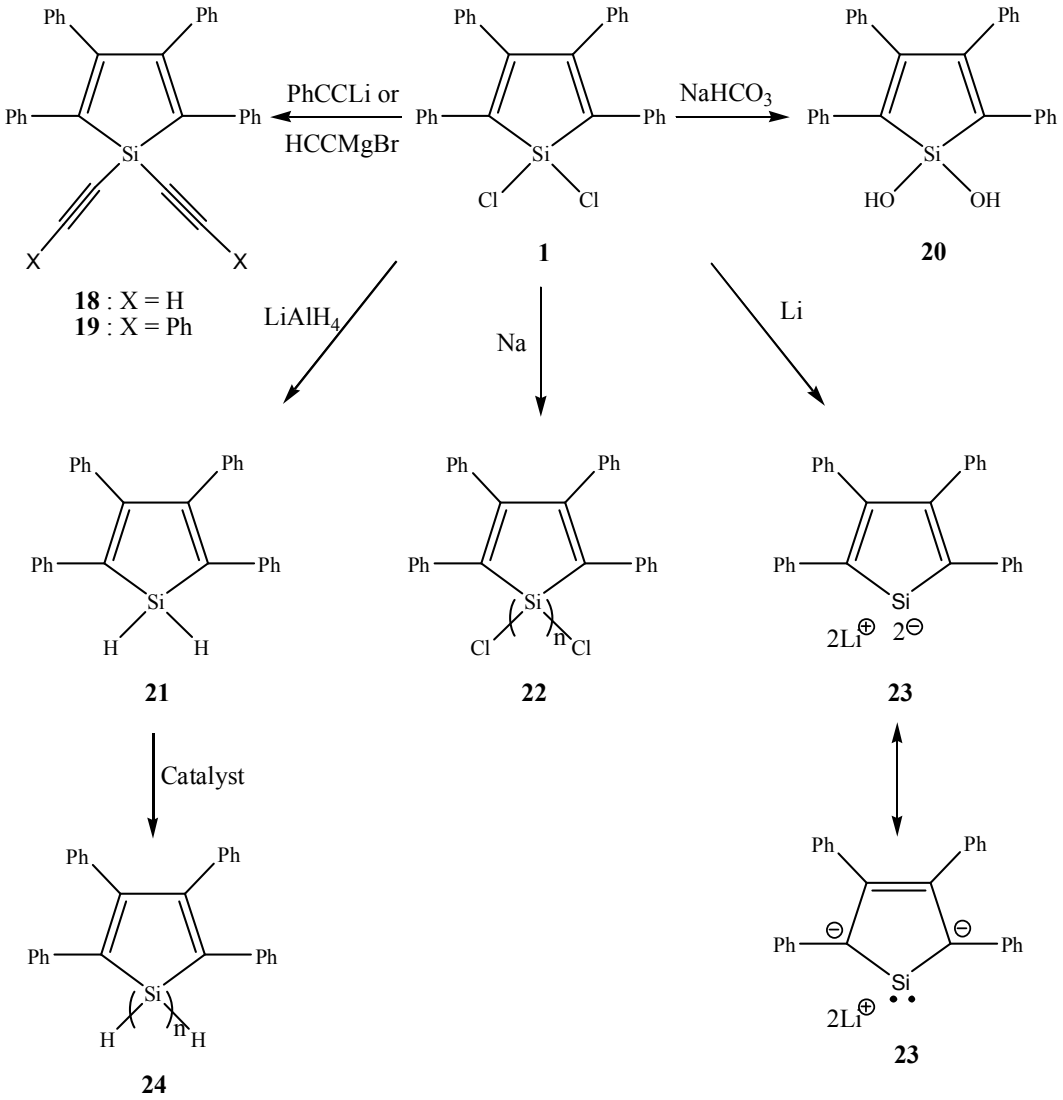

Scheme 12.3. Synthetic route of silole and silole derivatives **18-23.**

12.6 Refernces

[1] R. H. Crabtree, The Organometallic Chemistry of the Transition Metals, Wiley, 560 (2005).
[2] C. E. Butterworth, Silicon in Organic Synthesis, London (1981).
[3] S. Pawlenko, Organosilicon Chemistry, Walter de Gruyter, New York (1986).
[4] T. M. Klapotke, B. Krumm, R. Ilg, D. Troegel, and R. Tacke, *J. Am. Chem. Soc*. **129**, 6908 (2007).
[5] E. A. Flood, *J. Am. Chem. Soc*. **55**, 1735 (1933).
[6] L. Benati, G. Bencivenni, R. Leardini, M. Minozzi, D. Nanni, R. Scialpi, P. Spagnolo, and G. Zanardi, *J. Org. Chem*. **71**, 5822 (2006).
[7] E. Ramirez-Oliva, A. Hernandez, J. Martinez-Rosales, A. Aguilar-Elguezabal, G. Herrera-Perez, and J. Cervantesa, *Arkivoc* 126 (2006).
[8] R. West, M. J. Fink, J. Michl, *Science* **214**, 1343 (1981).
[9] E. H. Braye and W. Hübel, *Chem. Ind*. 1250 (1959).
[10] S. Yamaguchi, R.-Z jin, and K. Tamao, *J. Chem. Soc*., *Dalton Trans*. 3693 (1998).
[11] M. Hissler, P. W. Dyer, and R. Reau, *Coord. Chem. Rev*. **1**, 244 (2003).
[12] M. Saito and M. Yoshioka, *Coord. Chem. Rev*. **249**, 765 (2005).
[13] S. Yamaguchi and K. Tamao. *Bull. Chem. So*c. *Jpn*. **69**, 2327 (1996).
[14] V. Niessen, W. P. Kraemer, and L. S. Ceberbaum, *Chem. Phys*. **11**, 385 (1975).
[15] M. S. Gordon, P. Boudjouk, and F. Anwari, *J. Am. Chem. Soc*. **105**, 4972 (1983).
[16] C. Guimon, G. Pfister-Guillouzo, J. Dubac, A. Laporterie, G. Manuel, and H. Iloughmane, *Organometallics* **4**, 636 (1985).
[17] J. R. Damewood, *J. Org. Chem*. **51**, 5028 (1986).
[18] V. N. Khabashesku, S. E. Balaji, V. Boganov, O. M. Nefedov, and J. Michl, *J. Am. Chem. Soc*. **116**, 320 (1994).

[19] S. Yamaguchi, R.-Z jin, K. Tamao, and M. Shiro, *Organometallics* **16**, 2230 (1997).

[20] I. Toulokhonova, R. Zhao, M. Kozee, and R. West, *Main Group Met. Chem.* **24**, 737 (2001).

[21] H. Sohn, R. R. Huddleston, D. R. Powell, R. West, K. Oka, and X. Yonghua, *J. Am. Chem. Soc.* **121**, 2935 (1999).

[22] R. West, H. Sohn, U. Bankwitz, J. Calabrese, Y. Apeloig, and T. Müller, *J. Am. Chem. Soc.* **117**, 11608 (1999).

[23] R. West, H. Sohn, D. R. Powell, T. Müller, and Y. Apeloig, *Angew. Chem. Int. Ed.* **35**, 1002 (1996).

[24] Y. Liu, D. Ballweg, and R. West, *Organometallics* **20**, 5769 (2001).

[25] S. J. Toal, H. Sohn, L. N. Zakarov, E. S. Kassel, J. A. Golen, A. L. Rheingold, and W. C. Trogler, *Organometallics* **24**, 3081 (2005).

Chapter Thirteen
Enhancement of Photoluminescence Efficiency of Polysilole by Aggregation-induced Emission

13.1 Introduction

Polysiloles have recently received much attention [1] because of their unusual electronic properties. These unusual optical and electrical properties can be useful in electronic devices, such as electron transporting materials [2], light-emitting diodes (LEDs) [3-5], and chemical sensors [6,7]. Poly(2,3,4,5-tetraphenyl)-siloles (**1**) possess both 2,3,4,5-tetraphenyl-1-silacyclopenta-2,4-diene and Si-Si backbone that their absorptions exhibit at 314 nm. However, the unsaturated five-membered ring of the silole shifts their optical absorption and emission spectra into the visible spectral region at 364 and 520 nm, respectively. The aggregation of highly emissive organics and polymers into a solid state causes an emission-quenching effect, since the aggregation of molecules forms less emissive species such as excimers [8]. Reduction of emission efficiency in the solid state has been a major problem in device applications of light-emitting organic molecules. Many attempts to prevent aggregate formation have been made through chemical, physical, and engineering approaches. In contrast, few results on aggregation-induced emission (AIE) properties have been recently reported [9-12]. This chapter describes an aggregation-induced emission enhancement of polysiloles.

13.2 Experiments

The syntheses of **1**, dichloro(tetraphenyl)silole (**2a**), and dimethyl(tetraphenyl)silole (**2b**) were reported previously [3]. The reduction of 2a with lithium gave molecular weights (M_w) of 5500 (M_w/M_n = 1.1 determined by SEC). Fluorescence emission and excitation spectra were recorded on a Perkin-Elmer Luminescence Spectrometer LS 50B. The solvents were determined to be free of emitting impurities prior to use. The concentration of polysilole aggregates for the fluorescence measurement was 10 ㎍/L. 2a and 2b emit 380 and 425 nm, respectively. However polysilole **1** shows emission near 520 nm with excitation at 340 nm. Nanoaggregates of **1** are prepared by rapid precipitation from water solution by the injection of THF solution containing polysilole. This procedure is different from the previous report [10] and gives better monodisperse for any given water volume fraction. Polysilole aggregate exhibits a nearly identical emission band, however polysilole nanoaggregates are more highly fluorescent than polysiloles at identical concentration.

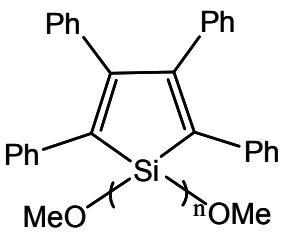

1

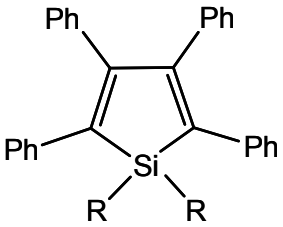

2a ; R = Cl
2b ; R = CH_3

13.3 Results and Discussion

Polysilole structure features a Si-Si backbone inside a conjugated ring system of side chains closely packed to yield a helical arrangement with 1 nm of diameter and 10 nm of length as shown in Figure 13.1. Figure 13.1 displays a space filling model structure of polysilole.

A photograph of polysiloles in THF solution (left) and polysilole nanoaggregates (right) under a UV lamp is shown in Figure 13.2, indicating that polysilole nanoaggregates are more highly fluorescent than polysiloles at identical concentration. For polysilole solution in pure THF, the photoluminescence (PL) intensity is very weak and an emission peak near 520 nm was observed. In solutions between 0% and 40% water by volume, the emission intensity of polysilole nanoaggregates does not increased. However, the intensity of the emission band increases by about 17.8 times when the solution is 99% water by volume. As the water fraction is increased, the emission intensity of polysilole nanoaggregates increases dramatically with no shift in the emission wavelength. Polysilole nanoaggregates in water-THF mixtures with 50%-99% water by volume exhibit one emission band at 513 nm when excited at 340 nm as shown in Figure 13.3. The emission band of polysilole nanoaggregates in water-THF mixtures is blue shifted by 7 nm compared to that of polysilole in THF. A minimum volume-fraction of 50% water is required to increase the luminescence, which indicates the onset of aggregation. This critical water concentration is that observed with other silole monomers [10]. The large increase in photoluminescence from polysilole aggregates could be attributed to the restricted rotation of the phenyl rings, which limits the nonradiative decay pathways [13] or inhibits the solvent assisted quenching resulting from aggregation.

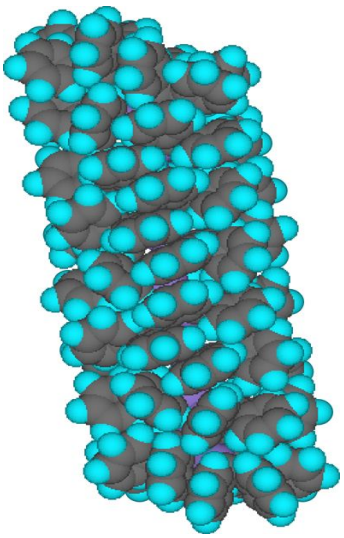

Figure 13.1. Space filling model structure of polysilole.

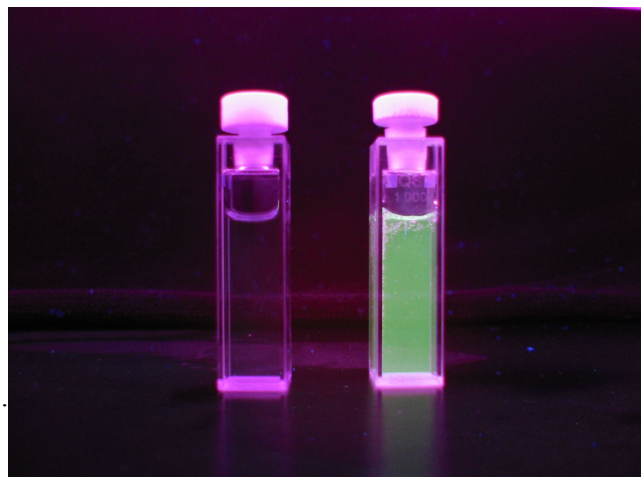

Figure 13.2. Photograph of polysilole in THF (10 mg/L, left) and polysilole nanoaggregates in water-THF mixture (90:10 by volume, 10 mg/L, right) under black light.

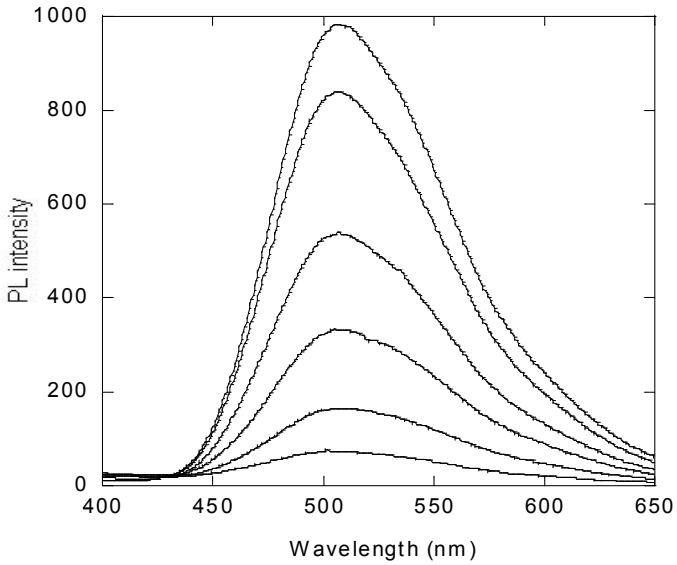

Figure 13.3. Fluorescence spectra of polysilole aggregates in water-THF mixtures (% water from top; 99%, 90%, 80%, 70%, 60%, 50%).

Figure 13.4 shows the plot for the relative PL intensity of polysilole nanoaggregate *vs* % water by volume. When the water fraction increases, the emission intensity increases exponentially, indicating that the luminescence intensity is proportional to the percent of aggregated polysilole. The stability of polysilole nanoaggregates in 90% water solutions has been investigated, and the PL intensity remains unchanged over a month. This indicates that polysilole nanoaggregates show neither further aggregation nor degradation. Figure 13.5 obtained by cold field emission scanning electron micrography (FE-SEM, Hitachi; S-4700) exhibits the

image of polysilole nanoaggregates in different water fractions. Aggregates of **1** consist of particles on the order of 20 nm in diameter in 90% water solution, as determined by dynamic light scattering measurements (Particle Size Analyzer, Microtrac: UPA150). Particle diameter appears to vary with water fraction, but the dispersity of diameter for given any suspension is about ± 3%. Particle diameters are around 700 nm for 50 to 70% water volume fraction and near 400 nm for 80% water, but they decrease dramatically above 80% water. Polysilole nanoaggregates exhibit a minimum in size at 90% water. A possible explanation is that at higher water concentrations the organic molecules aggregate to a higher extent in the hydrophilic environment, but THF absorbing into the aggregate causes them to swell at lower water concentrations. UV-vis spectra were obtained using Hewlett-Packard 8452A diode array spectrometer. UV-vis absorption and fluorescence spectra were measured for the polysilole in THF. Polysilole exhibits three absorption bands, which are assigned to the π-π^* (364 nm) transition in the silole ring and the σ-(σ_2^*+π^*) (314 nm) and σ-σ_1^* (260 nm) transitions in the Si-Si backbones. UV-vis absorption spectra of polysilole nanoaggregates have the same absorption band as the silole (2) in THF, but the π-π^* transition red shifts as the percent water increases. In 90% water solutions, the π-π^* transition of polysilole aggregates occurs at 374 nm.

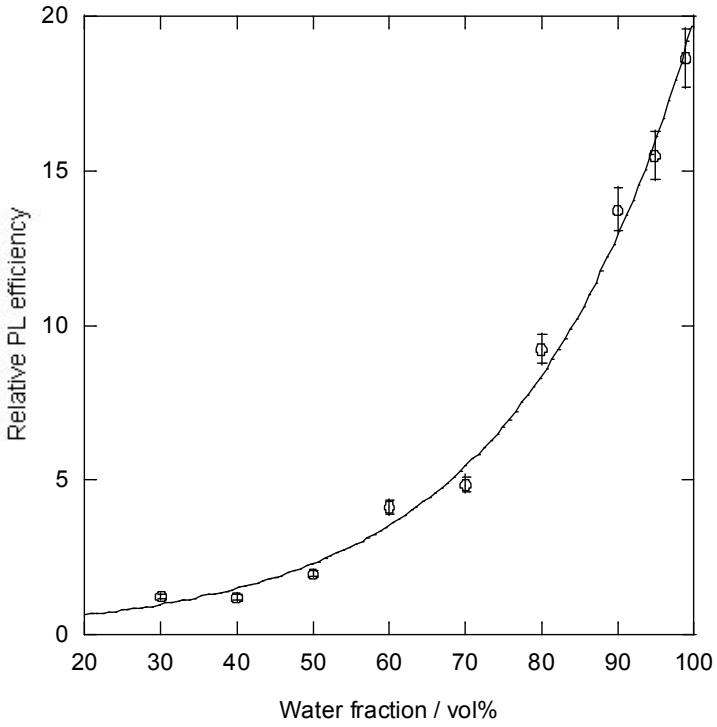

Figure 13.4. Plot of the relative intensity of polysilole aggregates *vs* % water by volume.

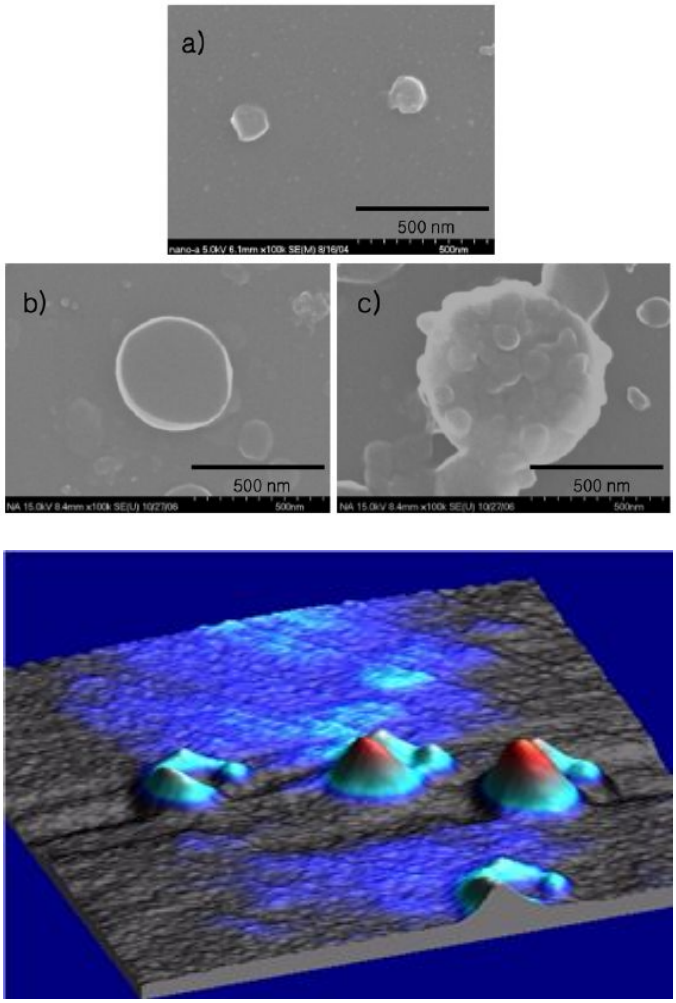

Figure 13.5. FE-SEM images of polysilole nanoparticles from (a) 90%, (b) 80%, and (c) 70% water fraction and AFM image of polysilole nanoparticles (dimension: 2.8×2.8 μm^2).

13.4 Conclusions

Polysilole nanoaggregates exhibit an aggregation-induced emission enhancement with an intensity of 17.8 times to that of normal photoluminescence when the water fraction is increased to 99%. The photoluminescence intensity of polysilole is exponential to the percent of water fraction and particle diameter is dependent on solvent composition.

13.5 References

[1] R. West, H. Sohn, U. Bankwitz, J. Calabrese, Y. Apeloig, and T. Mueller, *J. Am. Chem. Soc.* **117**, 11608 (1995).

[2] K. Tamao, M. Uchida, T. Izumizawa, K. Furukawa, and S. Yamaguchi, *J. Am. Chem. Soc.* **118**, 11974 (1996).

[3] H. Sohn, R. R. Huddleston, D. R. Powell, R. West, K. Oka, and X. Yonghua, *J. Am. Chem. Soc.* **121**, 2935 (1999).

[4] Y. Xu, T. Fujino, H. Naito, T. Dohmaru, K. Oka, H. Sohn, and R. West, *Jpn. J. Appl. Phys.* **38**, 6915 (1999).

[5] S. Yamaguchi, R. Z. Jin, and K. Tamao, *J. Am. Chem. Soc.* **121**, 2937 (1999).

[6] H. Sohn, R. M. Calhoun, M. J. Sailor, and W. C. Trogler, *Angew. Chem. Int. Ed.* **11**, 2104 (2001).

[7] H. Sohn, M. J. Sailor, D. Magde, and W. C. Trogler, *J. Am. Chem. Soc.* **125**, 3821 (2003).

[8] R. Jakubiak, Z. Bao, L. Rothberg, *Synth. Met.* **114**, 61 (2000).

[9] R. Deans, J. Kim, M. R. Machacek, and T. M. Swager, *J. Am. Chem. Soc.* **122**, 8565 (2000).

[10] J. Luo, Z. Xie, J. W. Lam, L. Cheng, H. Chen, C. Qiu, H. S. Kwok, X. Zhan, Y. Liu, D. Zhu, and B. Z. Tang, *Chem. Commun.* **115**, 1740 (2001).

[11] L. C. Palilis, A. J. Maekinen, M. Uchida, Z. H. Kafafi, *Appl. Phys. Lett.* **14**, 2209 (2003)

[12] B.-K. An, S.-K. Kwon, S.-D. Jung, and S. Y. Park, *J. Am. Chem. Soc.* **124**, 14410 (2002).

[13] M. H. Lee, D. Kim, Y. Dong, and B. Z. Tang, *J. Korean Phys. Soc.* **45**, 329 (2004).

Chapter Fourteen
Enhancement of Photoluminescence Efficiency of Polygermole by Aggregation-induced Emission

14.1 Introduction

Polymetalloles such as siloles and germoles containing silicon and germanium have continuously received much attention because of their unusual electronic properties [1-3]. These unusual optical and electrical properties can be useful in electronic devices, such as electron transporting materials [4], light-emitting diodes (LEDs) [5-7], and chemical sensors [8-9]. Analogous of cyclopentadiene, siloles and germoles are π-electron systems containing Si-Si and Ge-Ge atom as part of a cyclic 5-membered ring. Characteristic features of siloles and germoles include a low reduction potential and a low-lying LUMO due to σ^*-π^* conjugation arising from the interaction between the σ^* orbital of silicon and germanium, and the π^* orbital of the butadiene moiety of the five membered ring [10-11]. In a recent years, a few compounds including silole and polysilole have been found to display unusual aggregation-induced emission (AIE) properties [12-16]. However, studies of germole and polygermole aggregates have not been done yet. When the common molecules become aggregates, their photoluminescence is generally decreased. Thus, many attempts to prevent aggregate formation have been done through chemical, physical, and engineering approaches.

In contrast, polysiloles and polygermoles exhibit weak photoluminescence in

common organic solvents, but if they become aggregates, their efficiency of photoluminescence is surprisingly increased. In the previous chapter, the fluorescence quantum yields of polysilole aggregates were also increased by a few hundreds times, compare to those in organic solvent [13].

In this chapter, an aggregation-induced emission enhancement of polygermoles is described. PL intensity of polygermole aggregates has not been changed over a month. This indicates that polygermole nanoaggregates show neither further aggregation nor degradation.

14.2 Experiments

14.2.1 Generals

All synthetic manipulations were carried out under an atmosphere of dry argon gas using standard vacuum-line Schlenk technique. All solvents were purified and degassed before use according to standard literature methods: diethylether, tetrahydrofuran (THF), methanol were purchased from Aldrich Chemical Co. Inc. and distilled from sodium/benzophenone ketyl. All other reagents (Aldrich) such as diphenylacetylene, Lithium wire, and germanium tertrachloride were purchased and used without any purification. Spectroscopic grade THF from Fisher Scientific was used for the fluorescence measurements.

NMR grade deuteriochloroform was stored over 4 Å molecular sieves. NMR data were collected with 300 MHz spectrometer for ^{1}H NMR. Chemical shifts are reported in parts per million (δ ppm); downfield shifts are reported as positive values from tetramethylsilane (TMS) standard at 0.00 ppm.

UV-vis absorption spectrum and fluorescence emission spectrum were recorded with the use of a Shimadzu UV-2401 spectrophotometer and a Perkin-Elmer luminescence spectrometer LS 50B, respectively. The solvents were determined to be free of emitting impurities prior to use. To avoid changing the concentrations of the emitting compound, the experiments were carried out with solution by preparing the quencher in the same solution of the emitting compound.

The concentration of germole, polygermole, and polygermole aggregates for the fluorescence measurement was 1 mg/1 L = 1 ppm.

Sizes of polygermole aggregates were obtained by particle size analyzer (PSA) and a cold field emission scanning electron microscope (FE-SEM, S-4800, Hitachi).

14.2.2 Syntheses

14.2.2.1. Preparation of 1,1-dichloro-2,3,4,5-tetraphenylgermole 1

To a solution of diphenylacetylene (26.7 g, 150 mmol) in dry diethyl ether (130 mL) was added clean lithium shavings (1.39 g, 200 mmol). The reaction mixture was stirred at room temperature for 2 h in a dry argon atmosphere and frozen with liquid N_2 (-197 ℃). The mixture was then added excess germanium tetrachloride (25.7 mL, 300 mmol). The solution was allowed to warm up slowly to room temperature and stirred for an additional 2 h. After stirring for 2 h, the reaction mixture was standed for overnight. The organic solution layers extracted with cannula and evaporated under reduced pressure. Recrystallization from diethyl ether at -20 ℃ gave a faintly yellow crystals (30 g, 80%). M.p. 197-199 ℃.; ^{1}H NMR (300 MHz, $CDCl_3$): δ = 6.83-6.88 and 7.04-7.21 (m, 20H, Ph); ^{13}C NMR (75.403 MHz, $CDCl_3$ (δ = 77.00)): δ = 149.96, 136.57, 134.66, 132.72, 129.54, 129.50, 128.36, 128.06, 127.68, 127.47.

14.2.2.2. Preparation of Polytetraphenylgermole 2

To a solution of 1,1-dichloro-2,3,4,5-tetraphenylgermole **1** (3 g, 6 mmol) dissolved in dry THF (60 mL) was added 2 equivalent of clean lithium shavings (82.8 mg, 12 mmol). The reaction mixture was refluxed for 3 days in a dry argon atmosphere. The solution was allowed to warm up slowly to room temperature and then evaporated to concentrated solution. The solution was precipitated by pouring the solution into methanol and extacted under reduced pressure and then washed with excess methanol to remove unreacted lithium metals. Polytetraphenylgermole **2** was obtained as pale yellow powders (1.2 g, 30%).; ^{1}H NMR (300 MHz, $CDCl_3$): δ = 6.30-7.40 (m, 20H, Ph), δ = 3.50 (OMe); ^{13}C NMR (75.403 MHz, $CDCl_3$

(δ = 77.00)): δ = 125-131 and 137-147 (m, Ph).

14.2.2.3. Preparation of Polytetraphenylgermole Nanoaggregates 3

Polytetraphenylgermole nanoaggregates of **3** are prepared by rapid precipitation from water solution by the injection of THF solution containing polygermole. This procedure is different from the previous report [12] and gives better mono-disperse for any given water volume fraction.

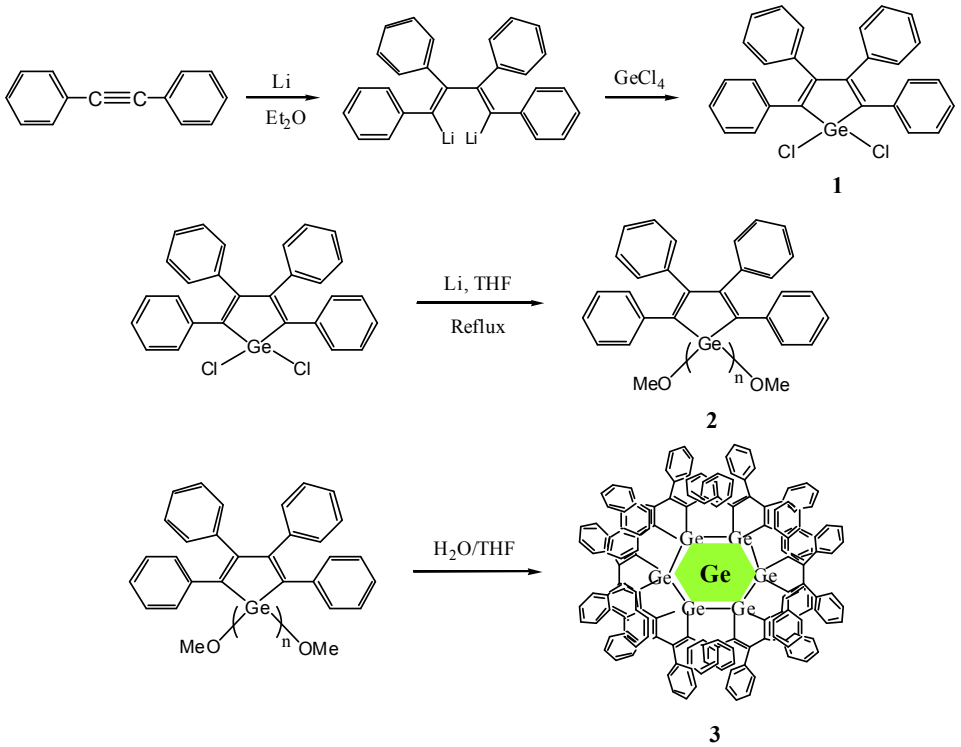

Scheme 14.1. Synthetic routes of compounds **1-3.**

14.3 Results and Discussion

For polygermole solution in pure THF, the photoluminescence (PL) intensity was very low and an emission peak near 510 nm was observed. Polygermole aggregates **3** exhibit a nearly identical emission band, however polygermole aggregates are more highly fluorescent than germoles and polygermoles at identical concentration as shown in Figure 14.1.

Aggregates of polygermole are prepared by rapid precipitation from water solution by the injection of THF solution dissolving polygermole. This procedure is different from the previous report [12] and gives better monodisperse for any given water volume fraction. As increasing water fraction, the emission intensity of polygermole aggregates increases dramatically as shown in Figure 14.2. There is no shift in the emission wavelength. In the range of water fraction between 0% and 40%, the emission intensity of polygermole aggregates increases slightly. However, the intensity of emission band increases about 730%, when the solution is 90% water fraction by volume.

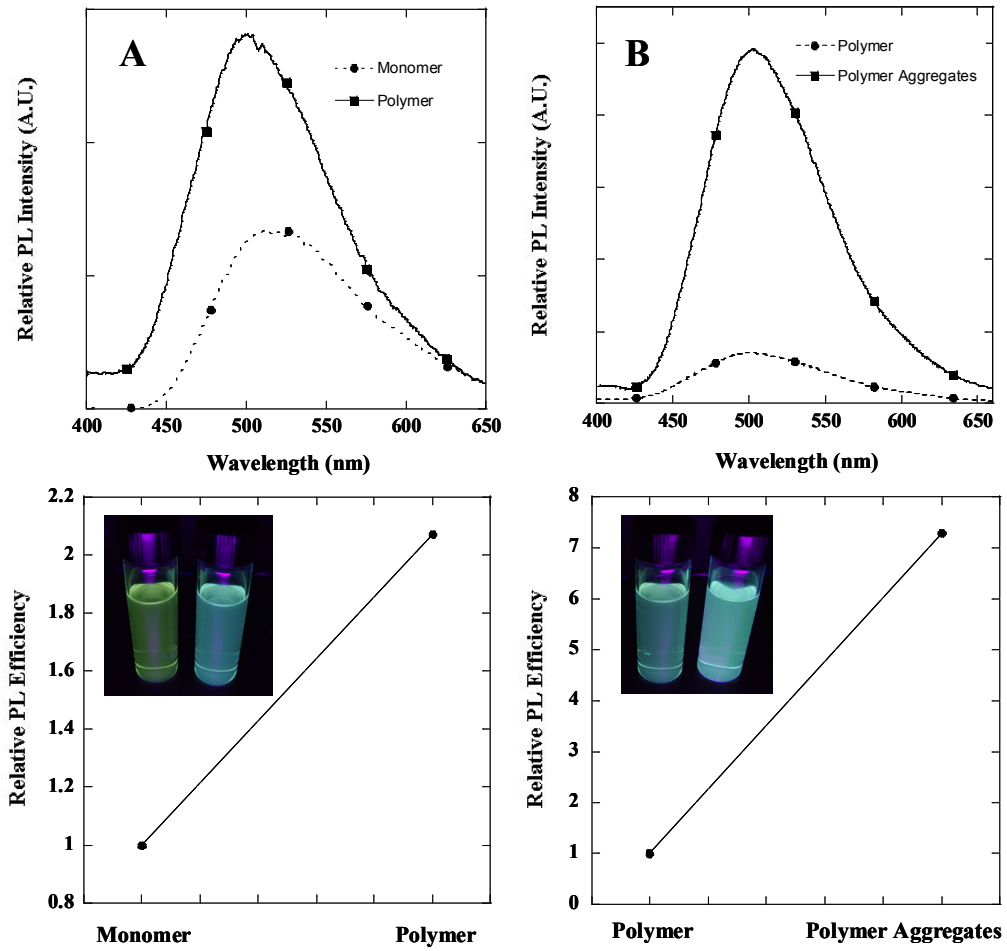

Figure 14.1. Relative PL spectra and plots of the relative intensity of monomer, polymer, and polymer nanoaggregates.

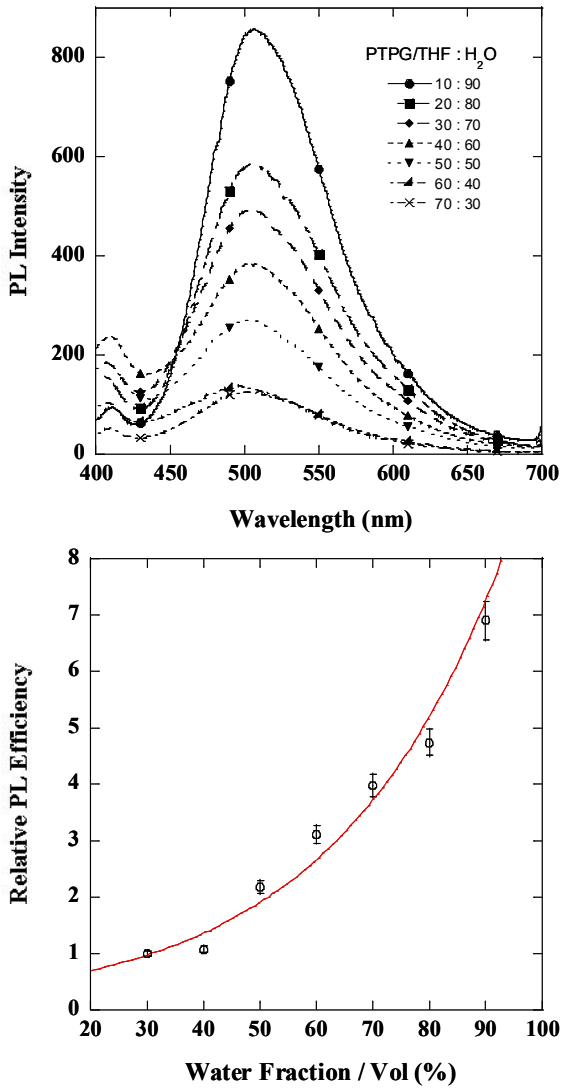

Figure 14.2. PL spectra of polygermole nanoaggregates in water-THF mixtures and plot of the relative intensity of polygermole nanoaggregates *vs* percent water by volume.

Stability of polygermole aggregates with 90% water fraction has been investigated. PL intensity of polygermole aggregates has not been changed over a month. This indicates that polygermole aggregates show neither further aggregation nor degradation. Figure 14.3 shows that particle size distributions of polygermole aggregates exhibit between a few nanometer and hundreds nanometers in the water/THF mixtures with 90%, 80%, and 70% by volumes.

FE-SEM images of polygermole aggregates with different water fraction have been obtained and shown in Figure 14.4. Sizes of polygermole aggregates with different water fraction by volume are in the range from 40 to 238 nanometers corresponding to PSA data. FE-SEM images of polygermole aggregates indicate that the higher water fraction is the smaller aggregate particles. This implies that nanoparticles of polygermole aggregate can be readily tuned by controlling the water fraction.

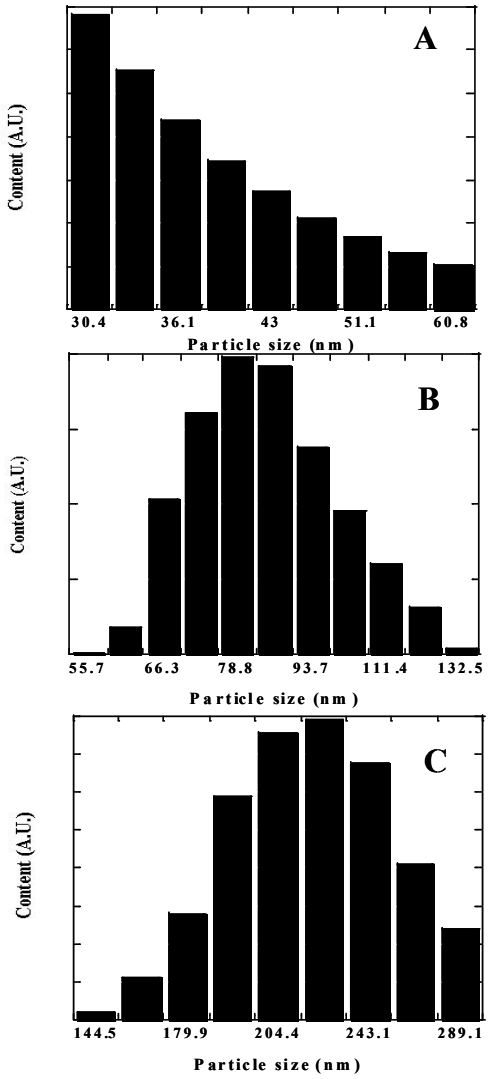

Figure 14.3. Particle size distributions of polygermole nanoaggregates in the water/THF mixtures with (A) 90%, (B) 80%, and (C) 70%.

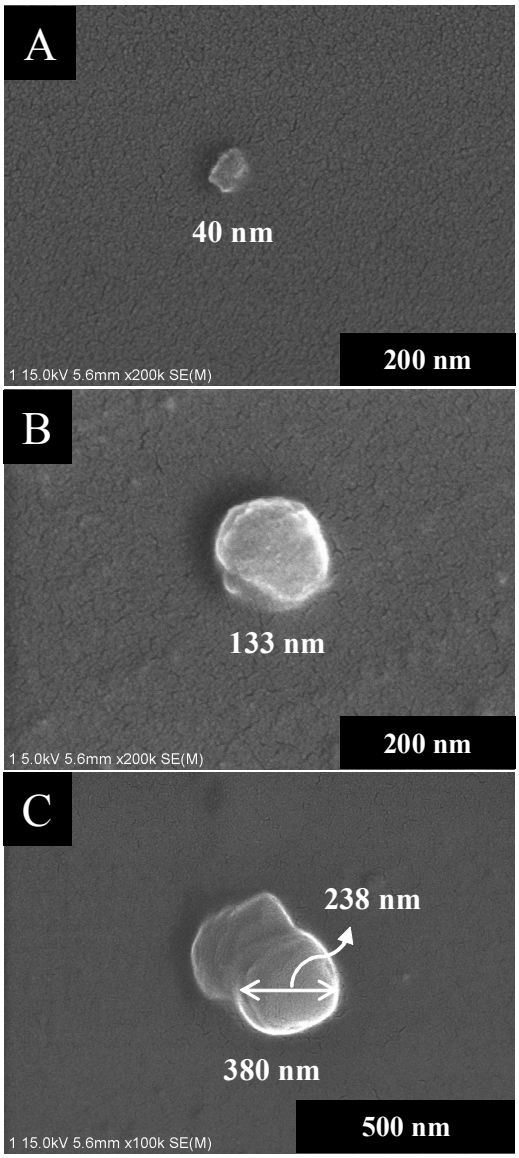

Figure 14.4. FE-SEM images of polygermole nanoaggregates in the water/THF mixtures with (A) 90%, (B) 80%, and (C) 70%.

14.4 Conclusions

Polygermole aggregates have been developed by using an aggregation-induced emission property of polygermoles. Polygermole aggregates exhibit PL intensity of emission band increases about 730% to that of normal photoluminescence when the water fraction is increased to 90% water fraction by volume. Relative PL efficiency of polygermole aggregates is exponentially increased to the percent of water fraction and particle diameter is dependent on solvent composition. PL intensity of polygermole aggregates has not been changed over a month. This indicates that polygermole aggregates show neither further aggregation nor degradation at the experimental condition.

14.5 References

[1] R. West, H. Sohn, U. Bankwitz, J. Calabrese, Y. Apeloig, and T. Mueller, *J. Am. Chem. Soc.* **117**, (1995) 11608.

[2] S. Yamaguchi and K. Tamao, *J. Chem. Soc.*, *Dalton* T*rans*. 3693 (1998).

[3] S. Yamaguchi, T. Endo, M. Uchida, T. Izumizawa, K. Furukawa, and K. Tamao, *Chem. Eur. J.* **6**, 1683 (2000).

[4] K. Tamao, M. Uchida, T. Izumizawa, K. Furukawa, and S. Yamaguchi, *J. Am. Chem. Soc.* **118**, 11974 (1996).

[5] H. Sohn, R. R. Huddleston, D. R. Powell, and R. West, *J. Am. Chem. Soc.* **121**, 2935 (1999).

[6] Y. Xu, T. Fujino, H. Naito, T. Dohmaru, K. Oka, H. Sohn, and R. West, *Jpn. J. Appl. Phys.* **38**, 6915 (1999).

[7] S. Yamaguchi, R. Z. Jin, and K. Tamao, *J. Am. Chem. Soc.* **121**, 2937 (1999).

[8] H. Sohn, R. M. Calhoun, M. J. Sailor, and W. C. Trogler, *Angew. Chem. Int. Ed.* **40**, 2104 (2001).

[9] H. Sohn, M. J. Sailor, D. Magde, and W. C. Trogler, *J. Am. Chem. Soc.* **125**, 3821 (2003) .

[10] Y. Yamaguchi, *Synth. Met.* **82**, 149 (1996).

[11] S. Yamaguchi and K. Tamao, *Bull. Chem. Soc. Jpn.* **69**, 2327 (1996).

[12] J. Luo, Z. Xie, J. W. Y. Lam, L. Cheng, H. Chen, C. Qiu, H. S. Kwok, X. Zhan, Y. Liu, D. Zhu, and B. Z. Tang, *Chem. Commun.* 1740 (2001).

[13] S. Jang, S. G. Kim, D. Jung, H. Kwon, J. Song, S. Cho, Y. C. Ko, and H. Sohn, *Bull. Korean Chem. Soc.* **27**, 1965 (2006).

[14] R. Deans, J. Kim, M. R. Machacek, and T. M. Swager, *J. Am. Chem. Soc.* **122**, 8565 (2000).

[15] L. C. Palilis, A. J. Maekinen, M. Uchida, and Z. H. Kafafi, *Appl. Phys. Lett.* **14**, 2209 (2003).

[16] B.-K. An, S.-K. Kwon, S.-D. Jung, and S. Y. Park, *J. Am. Chem. Soc.* **124**, 14410 (2002).

Chapter Fifteen
Detection of Avidin/Streptavidin Based on Biotinlyted Silole and Aggregation-induced emission (AIE)

15.1 Introduction

There has been considerable interest in the electronic properties of conduction polymers since the first discovery of a conjugated organic electroluminescent polymer by Burroughes et al. in 1988[1,2]. These conjugated polymers are organic semicondutors resulting from π-molecular orbitals delocalized along the polymer chain. Both photoluminescence and electroluminescence orinated from the radiative recombination of exciting states, in the latter by combination of oppositely charged polaons generated by injection of electrons and holes[3]. These unusual optical and electrical properties can be useful in electronic devices, such as diodes, transistors[1,4], light emitting diodes (LEDs)[2], large area light-emitting displays[5]. These unique optoelectronical properties can be used for excellent candidates for luminescent chemical sensors. Recently we have shown how luminescent polysiloles can be used as TNT and picric acid sensors[6,7]. Yang and Swager have reported luminescent conjugated organic polymers for the detection of TNT from land mines[8,9].

One of the basic componentsin a biotin-avidin-based system is the biotinylated moiety, which can be a protein, a polysaccharide, a nucleic acid, a low-Me substance, etc. To biotinylate such diverse classes of com-pounds, researchers have

developed several different
biotinylation reagents (active biotin derivatives). In addition, other biotinylation reagents have been developed for specific applications: e.g., cleavable reagents that can be used for biotinylation with the option of removing biotin at a later stage by reduction of a disulfide bond or hydrolysis of phenyl ester linkages[10-13].

In the present work, we have prepared biosensor based on biotinlyted-silole aggregate. The fabrication, optical characterization, and surface derivatization of a biotinlyted-silole aggregate are reported. For the application as a label-free biosensor, the binding interaction with avidin/streptavind has been investigated.

15.2 Experiments

15.2.1 Generals

1-Methyl-1-(3amino)propyl-2,3,4,5-teraphenylsilole has been synthesized by the procedures described in the literature[14]. All synthetic manipulations were carried out under an atmosphere of dry argon gas using standard vacuum-line Schlenk technique. All solvents were purified and degassed before use according to standard literature methods: diethylether, hexanes, tetrahydrofuran (THF), and toluene were purchased from Aldrich Chemical Co. Inc. and distilled from sodium/benzophenone ketyl. Spectroscopic grade THF from Fisher Scientific was used for the fluorescence measurements. NMR grade deuteriochloroform was stored over 4 Å molecular sieves. All other reagents (Aldrich) such as HCl, HNO_3, and H_2SO_4 were purchased and used without any purification. NMR data were collected with 300 MHz spectrometer for ^1H NMR. Chemical shifts are reported in parts per million (δ ppm); downfield shifts are reported as positive values from tetramethylsilane (TMS) standard at 0.00 ppm. UV-vis absorption spectrum and fluorescence emission spectrum were recorded with the use of a Shimadzu UV-2401 spectrophotometer and a Perkin-Elmer luminescence spectrometer LS 50B, respectively. The solvents were determined to be free of emitting impurities prior to use. To avoid changing the concentrations of the emitting compound, the experiments were carried out with solution by preparing the quencher in the same solution of the emitting compound. The concentration of aminosiloles for the fluorescence quenching measurements was 10 mg/1 L, which is about 2.4×10^{-6} M. Fluorecence spetra were immediately taken after injection of analyte.

15.2.2 Syntheses

15.2.2.1. Preparation of 1-methyl-1-hydro-2,3,4,5-tetraphenylsilole 1.

1-methyl-1-hydro-2,3,4,5-tetraphenylsilole 3 was obtained from the reduction of 1-chloro-1-methyl-2,3,4,5-tetraphenylsilole with 2 equivalent of lithium aluminum hydride ($LiAlH_4$) under dry ice bath (-78 ℃). The reaction mixture was filtered and filtrate was washed with ether. The organic layer was extracted with ether and dried over magnesium sulfate. The solvent was removed by vacuum pump. Recrystallization from ether gave a greenish-yellow powder.

^{1}H NMR (300 MHz, $CDCl_3$): δ = 6.7-7.1 (m, 20H, Ph), δ = 4.9 (s, 1H,) and δ = 0.56 (s, 3H, Me).

15.2.2.2. Preparation of 1-methyl-1-(3-amino)propyl-2,3,4,5-tetraphenylsilole 2.

Methylhydrosilole 3 (1.0 g, 2.5 mmol) dissolved in 20 mL of freshly distilled toluene was added 2 equivalent of allylamine (0.36 mL, 5.0 mmol), H2PtCl6·5H2O (2.5 mg, 5 μmol) under dry argon atmosphere and refluxed for 20 h. The solution was cooled and filtered. The solvent was evaporated to dryness. The product was dissolved in ether and precipitated with hexanes and filtered. The precipitate was collected as a yellow powder.

^{1}H NMR (300 MHz, $CDCl_3$): δ = 6.67-7.14 (m, 20H, Ph), δ = 2.62 (t, 2H), δ = 1.50 (m, 2H), δ = 1.03 (m, 2H) and δ = 0.48 (s, 3H, Me).

15.2.2.3. Synthesis of Biotinlyted-silole 3.

1-Methyl-1-(3amino)propyl-2,3,4,5-teraphenylsilole (1 g, 2.2 mmol) and NMM (0.25 mL, 2.2 mmol) in dry DMF (10 mL) were added to stirred solution of biotin (0.54 g, 2.2 mmol) and NMM (0.25 mL, 2.2 mmol) in dry DMF (10 mL). After

some minutes a solution of HATU (0.83 g, 2.2 mmol) in DMF (5 mL) was added. The reaction mixture was stirred overnight at room temperature, and precipitated to water and filtered. The precipitate biotinlyted silole was collected as a yellow powder: (1.4 g, 93%), ^{1}H NMR (300 MHz, $CDCl_3$) δ 6.73-7.3 (m, 20H, Ph), 2.64 (t, 2H), 1.53 (m, 2H), 1.01 (m, 2H), 0.49 (s, 3H), 2.05 (t. 2H), 2.54 (d, 1H), 2.74-3.15 (6H), 4.12 (m, 1H), 4.28 (m, 1H), 6.36 and 6.42 (S 2H), 6.74 (t, 1H), 7.74 (t, 1H)

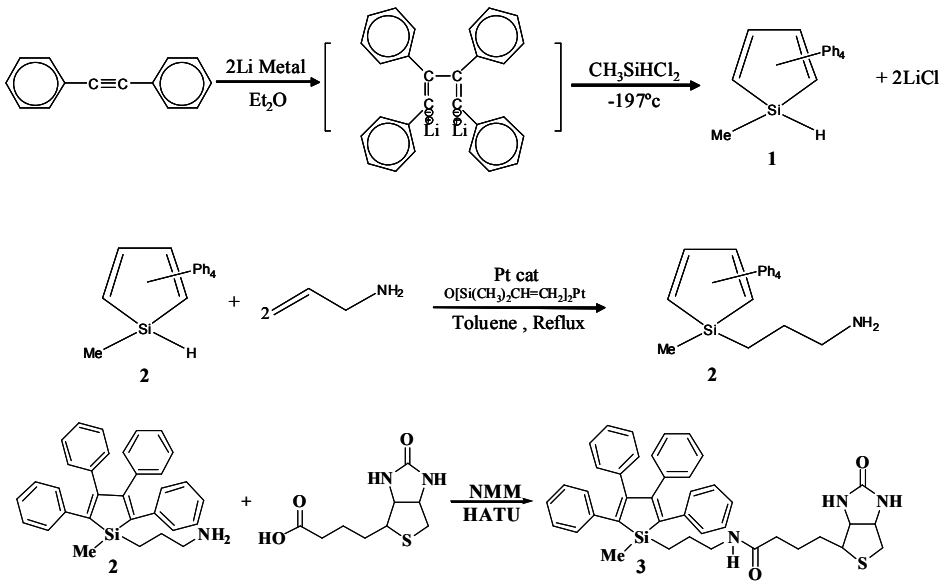

NMM : N-methylmorpholine
HATU : 1-[bis(dimethylamino)methylene]-1H-1,2,3,-triazolo(4,5b)pyridinium 1hexafluorophosphate 3-oxide

Scheme 15.1.

15.2.2.4. Preparation of Biotinylated-silole Nanoaggregates 4

Biotinylated-silole nanoaggregates of 4 are prepared by rapid precipitation from water solution by the injection of THF solution containing Biotinylated-silole. This procedure is different from the previous report [15] and gives better mono-disperse for any given water volume fraction.

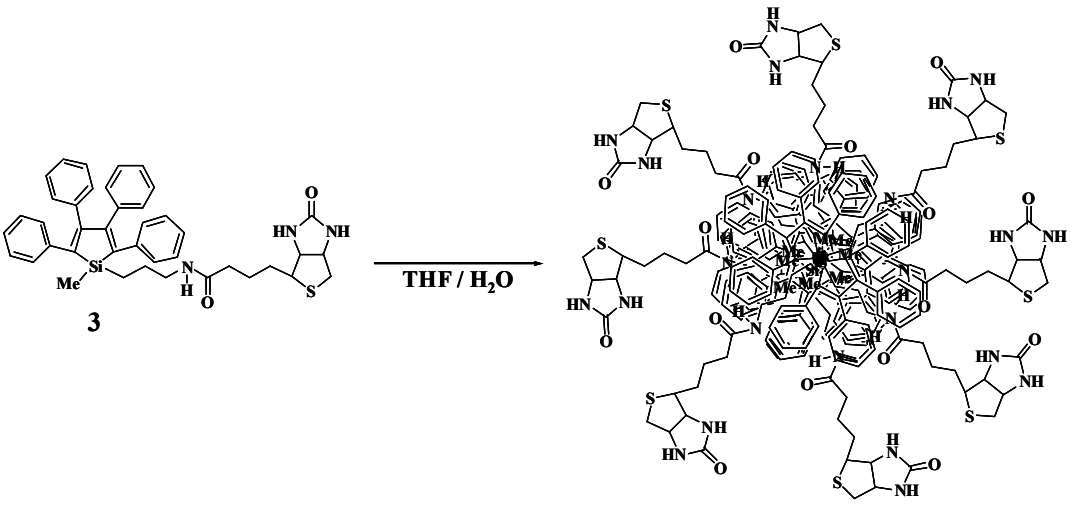

3 **4**

Scheme 15.2.

15.3 Results and Discussion

The UV-vis absorption and fluorescence spectra are measured for the Biotinlyted-silole 3 in THF, respectively as shown in Figure. 10.1. Biotinlyted-silole 3 exhibits one emission band (λ_{max}, 510 nm) when excited at 359 nm, respectively.

For Biotinlyted-silole 3 solution in pure THF, the photoluminescence (PL) intensity was very low and an emission peak near 510 nm was observed. Biotinlyted-silole aggregates 4 exhibit a nearly identical emission band, however Biotinlyted-silole aggregates are more highly fluorescent than Biotinlyted-silole at identical concentration as shown in Figure 10.2.

Aggregates of Biotinlyted-silole are prepared by rapid precipitation from water solution by the injection of THF solution dissolving Biotinlyted-silole. This procedure is different from the previous report and gives better monodisperse for any given water volume fraction. As increasing water fraction, the emission intensity of Biotinlyted-silole aggregates increases dramatically as shown in Figure 10.3. There is no shift in the emission wavelength. In the range of water fraction between 0% and 40%, the emission intensity of Biotinlyted-silole aggregates increases slightly. However, the intensity of emission band increases about 730 times, when the solution is 90% water fraction by volume.

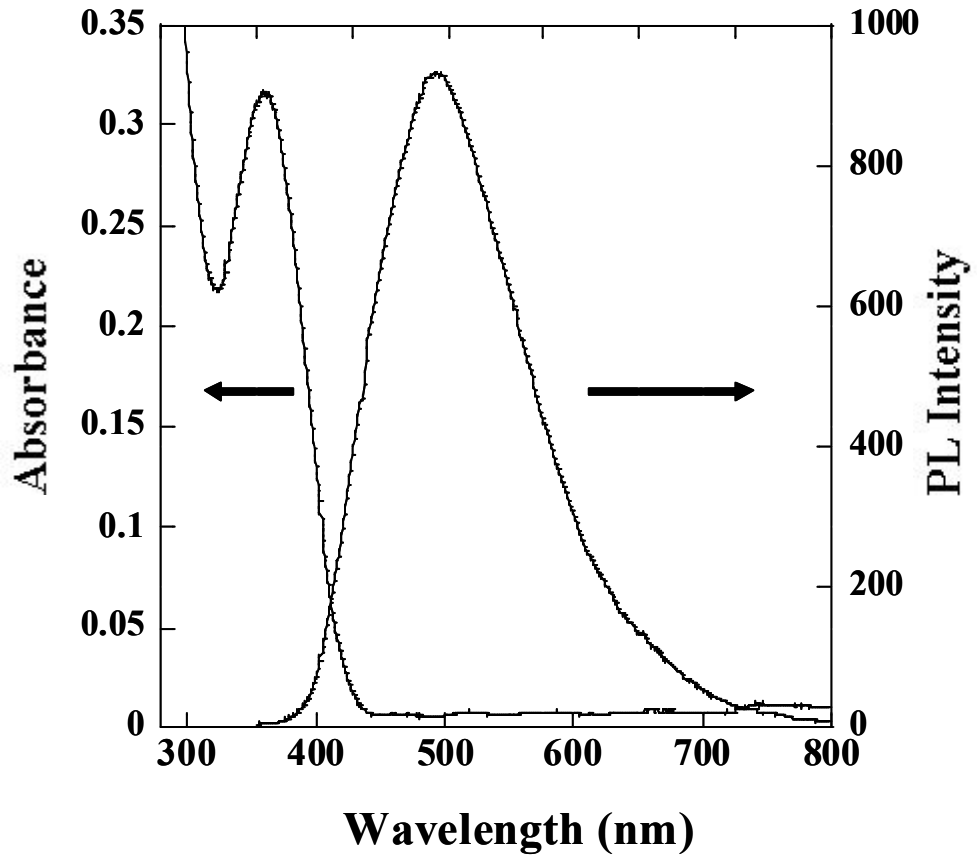

Figure 15.1 Absorption and Photoluminescence spectrum of Biotinylated-Silole.

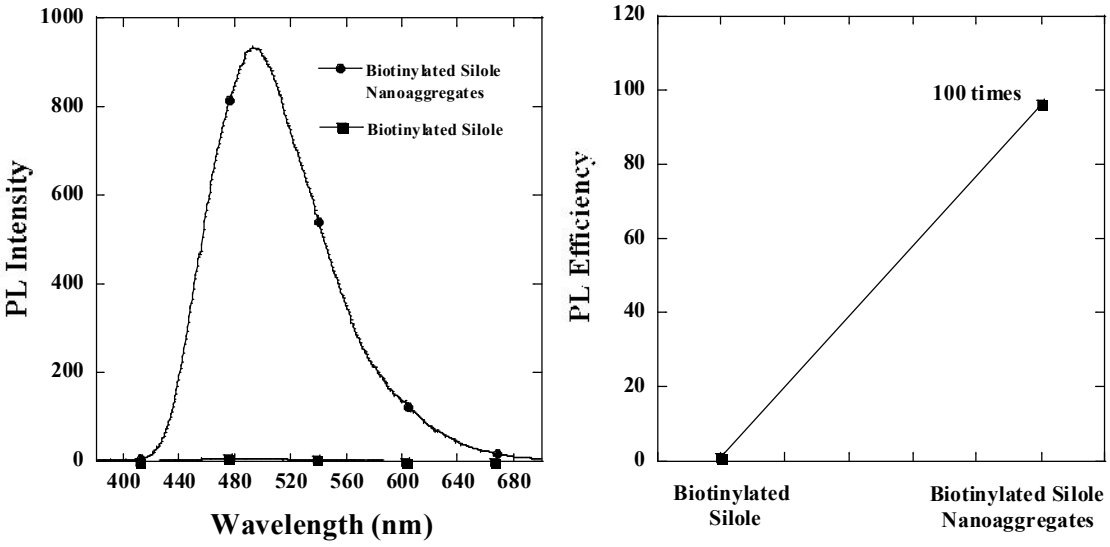

Figure 15.2. Comparison for PL Efficiency between Biotinylated-Silole and Nanoaggregate.

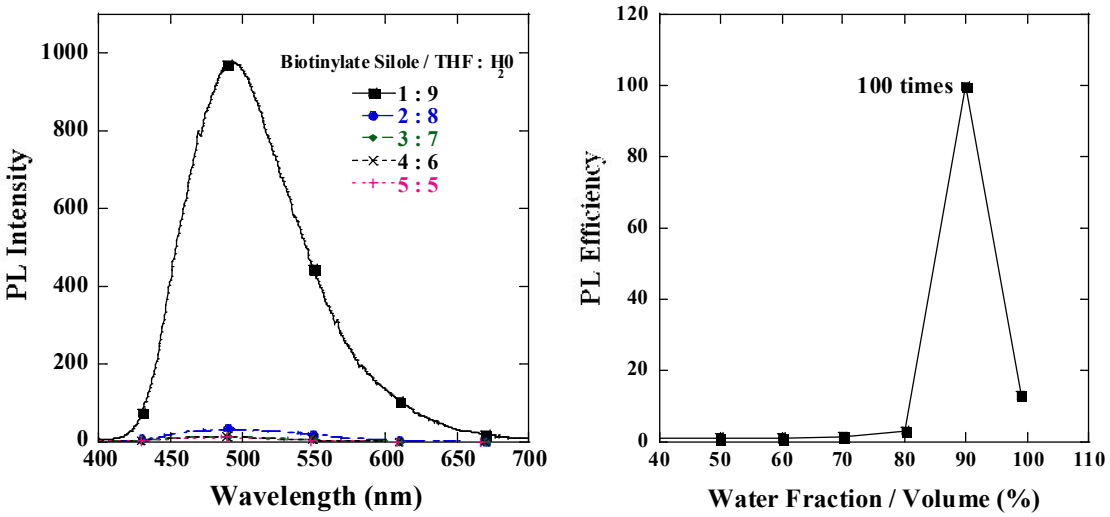

Figure 15.3. PL spectra of Biotinylated-Silole Nanoaggregates in water-THF mixtures and Plot of the Relative Intensity of Biotinylated-Silole Nanoaggregates % Water by Volume.

Stability of Biotinylated-Silole aggregates with 90% water fraction has been investigated. PL intensity of Biotinylated-Silole aggregates has not been changed over a month. This indicates that Biotinylated-Silole aggregates show neither further aggregation nor degradation. Figure 10.4. shows that particle size distributions of Biotinylated-Silole aggregates exhibit between a few nanometer and hundreds nanometers in the water/THF mixtures with 90% and 80% by volumes.

Sizes of Biotinylated-Silole aggregates with different water fraction by volume are in the range from 78.9 to 187 nanometers corresponding to PSA data. This implies that nanoparticles of Biotinylated-Silole aggregate can be readily tuned by controlling the water fraction.

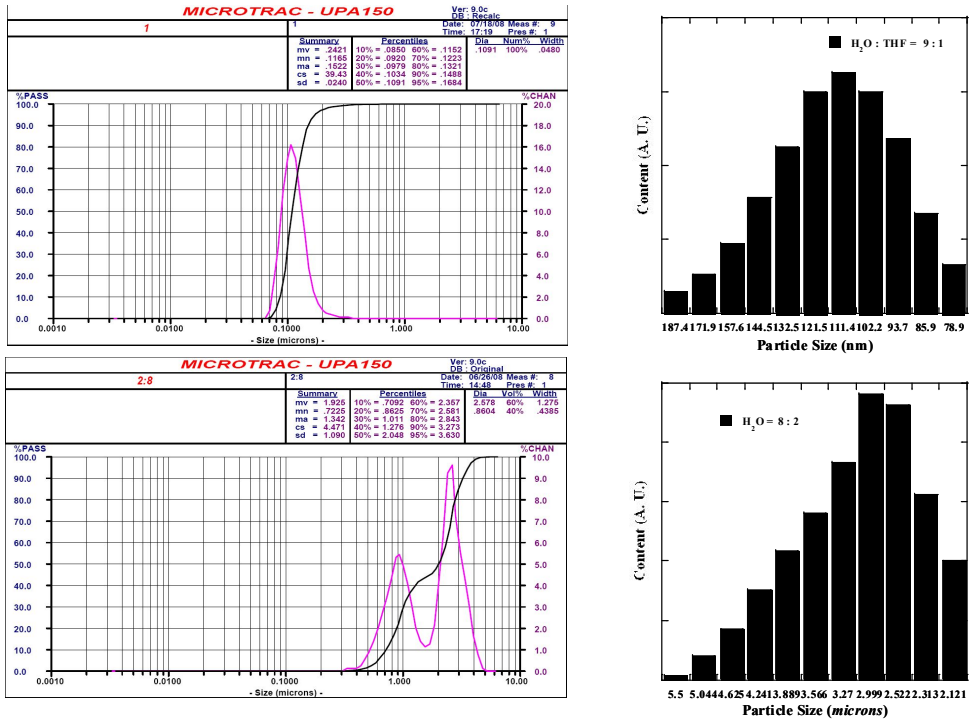

Figure 15.4. PSA Data of Biotinylated-Silole Nanoaggregate.

The Stern-Volmer equation is commonly used to quantify the differences in quenching efficiency for various analytes.

$$(I_0/I)-1 = K_{sv}[A]$$

In this equation, I_0 is the initial fluorescence intensity without analyte, I is the fluorescence intensity with added analyte of concentration [A], and K_{sv} is the Stern-Volmer constant. Figure 10.5. and 10.6. show that Stern-Volmer plots of Biotinylated-Silole Nanoaggregate **4** for the detection of avidin/streptavidin are obtained.

A linear Stern-Volmer relationship may be observed if either static or dynamic quenching process is dominant. PL may arise from either a static process, by the quenching of a bound complex, or a dynamic process, by collisionally quenching the excited state.

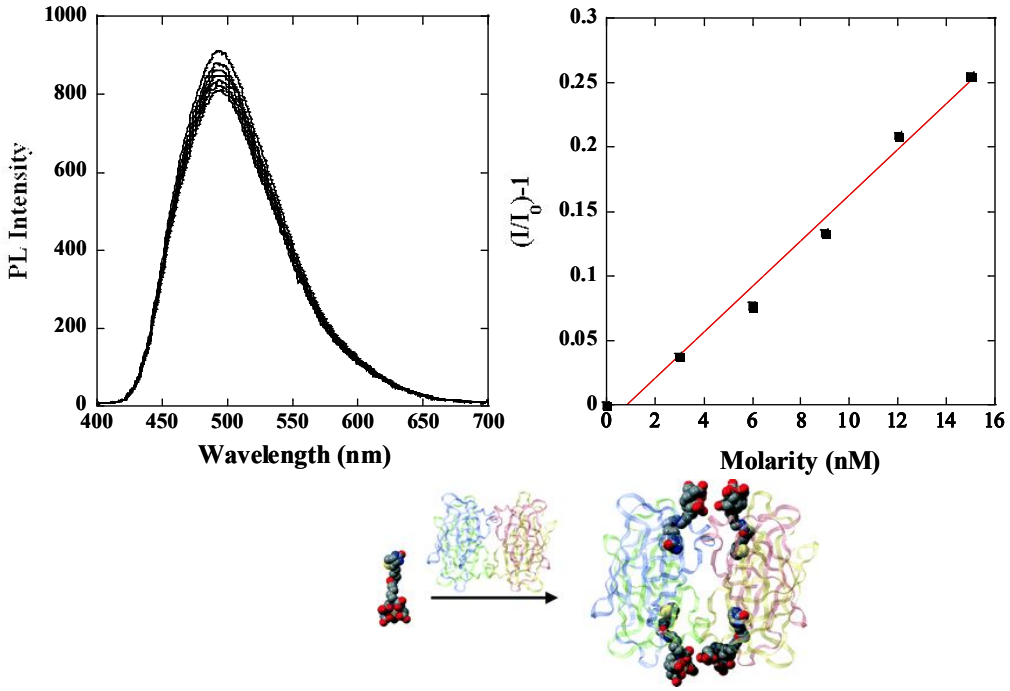

Figure 15.5. Quenching of photoluminescence spectra of Biotinylated-Silole Nanoaggregate with Avidin, from top 3 nM, 6 nM, 9 nM, 12 nM, 15 nM.

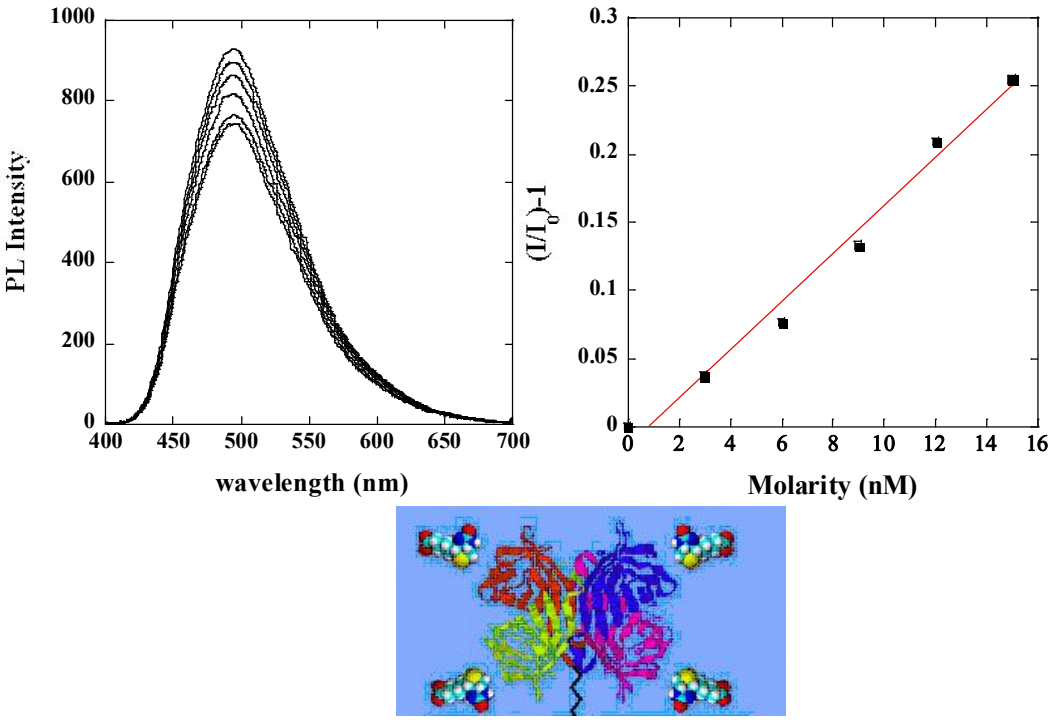

Figure 15.6. Quenching of photoluminescence spectra of Biotinylated-Silole Nanoaggregate with Streptavidin, from top 3 nM, 6 nM, 9 nM, 12 nM, 15 nM.

15.4 Conclusions

A new chemosensors for the detection of avidin/streptavidin based on photoluminescent biotinylated-Silole nanoaggregate **4**) have been developed. The detection of avidin/streptavidin acids is achieved from the measuring of quenching and enhancing photoluminescence of biotinylated-Silole nanoaggregat by adding the analytes. Photoluminescence changes of biotinylated-Silole nanoaggregat were immediately observed. Linear relationship of the Stern-Volmer plots for detection of avidin/streptavidin was obtained. The detection mechanism for quenching of photoluminescent biotinylated-Silole nanoaggregat involve that the reaction between biotinylated-Silole nanoaggregat and avidin/streptavidin is allow to be site effect, which is not photoluminescence compound. The biotinylated-Silole nanoaggregat are highly sensitive and selective to detect the avidin/stretavidin without any other interference. Our dectection limit for sensing avidin/streptavidin (Avidin, 3×10^{-12} M and Stretavidin, 3×10^{-12} M) was obtained using photoluminescence quenching technique.

15.5 References

[1] J. H. Burroughes, C. A. Jones, and R. H. Friend, *Nature*, **335**, 137 (1998).

[2] J. H. Burroughes, D. D. C. Bradley, A. R. Brown, R. N. Makers, K. Mackay, R. H. friend, P. L. Burns, and A. B. Holmes, *Nature*, **347**, 539 (1990).

[3] D. D. C. Bradley, *Chem. Brit.*, **27**, 719 (1991).

[4] Y. Yang and A. J. Heeger, *Nature*, **372**, 344 (1994).

[5] R. H.Friend, R. W. Gymer, A. B. Holmes, J. H. Burroughes, R. N. Marks, C. Taliani, d. D. C. Bradley, D. A. D. santos, J. L. Bredas, M. Logdlund, and W. R. Salaneck, *Nature*, **397**, 121 (1999).

[6] H. Shon, R. M Calhoun, M. J. Sailor, and W. C. Trogler, *Angew. Chem. Int. Ed.*, **11**, 2104 (2001).

[7] H Sohn, M. J. sailor, D. Magde, and W. C. Trogler, *J. Am. Chem. Soc.*, **125**, 3821 (2003).

[8] J.-S. Yang and T. M. Swager, *J. Am. Chem. Soc.*, **120**, 5321 (1998).

[9] J.-S. Yang and T. M. Swager, *J. Am. Chem. Soc.*, **120**, 11864 (1998).

[10] C. A. Mouton, D. Pang, C. V. Natrj, and J. A. Shater, *Arch. Biochem. Biophys.*, **218**, 101 1982.

[11] M. Shimkus, T. Levy, and T. Herman, *Proc. Natl. Acd. Sci.*, **82**, 2593 1985.

[12] D. R./ Gretch, M. Suter, and M. F. Stinski, *Anal. Biochem.*, **163**, 270, 1987.

[13] B. Ghebrehiwet and S. Bossone, *J. Immunol. Methods.*, **184**, 123 1987.

[14] S. J. Toal, K. A. Jones, D. Magde, and W. C. Trogler, *J. Am. Chem. Soc.*, **121**, 11661 2005.

[15] J. Luo, Z. Xie, J. W. Y. Lam, L. Chengm H. Chen, C. Qiu, S. H. Kwon, X.

Zhan, Y. Liu, D. Zhu, and B. Z. Tang, *Chem. Commun.*, **18**, 1740 2001.

Acknowledgments

The completion of my doctoral studies would not have been possible without the help of many people. First of all, I would like to express my sincere gratitude to my advisor respected **Professor Honglae Sohn**, for his love, guidance, patience, support and friendship both professionally and personally during the entire course of this dissertation. He allowed me many opportunities to learn and grow the course of my research. Without his help, I would not have developed the independent scientific insight. I would also like to thank to many **Professors Kidong Song**, **Sungdong Cho**, **Moonjoo Ko**, **Beomgyu Lee and Seol Ryu** in department of chemistry for their great guidance and instruction in scientific area. I would especially like to thank to **Professor Hee-Gweon Woo** from Chonnam national university for kindly accepting to be the chair of the graduation committee and also would like to thank to **Professor Hyun-Dam Jeong** from Chonnam national university.

I would also like to thank to my fellow graduate students that I have worked with over the past264 few years, my friends **Jongsun Kim**, and **Sung Gi Kim** for their sincere friendship and giving me a preasure, my juniors **Younghee Gweon**, **Jaehyun Park**, **Cheolyoung Park**, **Sung Jin Kim**, **Kyoungsun Jung**, **Sung Gi Lee**, **Jinseok Yang**, **Bomin cho**, **Tae-Eun Choi**, **Sunghoon Jin**, **Sungyong Um, Heecheol Kim, Minwoo Hwang, Boyoun Lee and Hyun Cho** for their cooperation and help to my research. Specially, I would like to thank to **Dr. Seunghyun Jang** and **Dr. Jihoon Kim** who has appreciate the reinforcement and help.

Finally, I greatly appreciate the support and endless love of **my parents**. I will always love and keep her. This thesis is dedicated to all of them.

감사의 글

2005년도 처음으로 대학원에 입학하여 어느덧 2010년이 다가오면서 저의 작은 결실을 맺게 되었습니다. 석사학위를 비롯해 박사학위를 받는 동안 조선대학교 화학과에서 너무나 많은 도움을 받으면서 여기까지 온 거 같습니다. 무엇보다도 먼저, 여러모로 부족한 저를 학문의 길로 이끌어 주시고 보다 깊은 학문적 성취를 위해 아낌없는 충고와 가르침을 주신 저의 지도교수님이신 손홍래 교수님께 맘을 담아 깊이 감사드립니다. 교수님의 크나크신 가르침을 평생 마음에 새기고 기억하겠습니다. 그리고 대학원 과정동안 각각의 분야에서 많은 학문적 가르침과 관심을 보여주신 송기동 교수님, 조성동 교수님, 고문주 교수님, 이범규 교수님, 그리고 류 설 교수님께도 깊은 감사드립니다. 또한 바쁘신 와중에도 저의 논문심사를 맡아주신 심사위원장이신 전남대학교 우희권 교수님, 심사위원이신 전남대학교 정현담 교수님께도 감사드립니다. 대학원 과정동안 저와 함께하며 고생한 우리 광나노소재연구실 선배들인 범석이형, 진우형, 형준이형, 대혁이형과 동기들인 성기, 종선이, 또한 사랑하는 후배들 용희, 재현, 철영, 성진, 경선, 성기, 진석, 보민, 태은, 성용, 성훈, 희철, 민우, 보연, 그리고 현이에게 너무나 고맙고 감사의 말을 전하고 싶습니다. 특히, 박사과정동안 함께 고생한 승현이형이랑 지훈 에게 너무나 고맙다는 말을 전하고 싶습니다.

항상 끝없는 사랑과 지지를 아껴주시지 않으신 사랑하는 부모님에게도 머리숙여 깊은 감사의 말을 전합니다. 아마 이들의 관심과 사랑이 없었더라면 힘들고 어려운 매순간마다 이겨내기 힘들었을 것입니다. 이 모든 분들의 가르침과 사랑의 빚을 평생 마음속에 간직하며 보다 더 발전되고 사회에 공한할 수 있는 사람이 되도록 노력하며 살겠습니다. 이 모든 분들께 작은 결실인 이 논문을 바칩니다.

저작물 이용 허락서

학 과	화 학 과	학 번	20077317	과 정	박사
성 명	한글: 고 영 대 한문: 高 英 大 영문: Koh, Youngdae				
주 소	광주광역시 동구 계림동 518-62				
연락처	E-mail : gobam79@naver.com				
논문제목	**한글 : 다공성 실리콘과 실리콘 나노소재를 이용한 바이오 센서의 개발** **영문 : Development of Bio Sensor Based on Porous Silicon and Silicon Nanomaterials**				

본인이 저작한 위의 저작물에 대하여 다음과 같은 조건아래 조선대학교가 저작물을 이용할 수 있도록 허락하고 동의합니다.

- 다 음 -

1. 저작물의 DB구축 및 인터넷을 포함한 정보통신망에의 공개를 위한 저작물의 복제, 기억장치에의 저장, 전송 등을 허락함.
2. 위의 목적을 위하여 필요한 범위 내에서의 편집·형식상의 변경을 허락함. 다만, 저작물의 내용변경은 금지함.
3. 배포·전송된 저작물의 영리적 목적을 위한 복제, 저장, 전송 등은 금지함.
4. 저작물에 대한 이용기간은 5년으로 하고, 기간종료 3개월 이내에 별도의 의사표시가 없을 경우에는 저작물의 이용기간을 계속 연장함.
5. 해당 저작물의 저작권을 타인에게 양도하거나 또는 출판을 허락을 하였을 경우에는 1개월 이내에 대학에 이를 통보함.
6. 조선대학교는 저작물의 이용허락 이후 해당 저작물로 인하여 발생하는 타인에 의한 권리 침해에 대하여 일체의 법적 책임을 지지 않음.
7. 소속대학의 협정기관에 저작물의 제공 및 인터넷 등 정보통신망을 이용한 저작물의 전송·출력을 허락함.

동의여부 : 동의 (○), 반대 ( )

2010년 8월 25일

저작자: 고 영 대 (서명 또는 인)

조선대학교 총장 귀하